



**HAL**  
open science

# Thermo-mechanical analyses of the solidification of electrofused alumina-zirconia-silica refractory blocks

Tiphaine Houdard

► **To cite this version:**

Tiphaine Houdard. Thermo-mechanical analyses of the solidification of electrofused alumina-zirconia-silica refractory blocks. Mechanics of materials [physics.class-ph]. Université Paris sciences et lettres, 2022. English. NNT : 2022UPSLM033 . tel-03991252

**HAL Id: tel-03991252**

**<https://pastel.hal.science/tel-03991252>**

Submitted on 15 Feb 2023

**HAL** is a multi-disciplinary open access archive for the deposit and dissemination of scientific research documents, whether they are published or not. The documents may come from teaching and research institutions in France or abroad, or from public or private research centers.

L'archive ouverte pluridisciplinaire **HAL**, est destinée au dépôt et à la diffusion de documents scientifiques de niveau recherche, publiés ou non, émanant des établissements d'enseignement et de recherche français ou étrangers, des laboratoires publics ou privés.

**THÈSE DE DOCTORAT**  
**DE L'UNIVERSITÉ PSL**

Préparée à MINES Paris PSL

**Etude thermo-mécanique  
de la solidification de produits réfractaires électrofondus  
à base d'alumine, de zircon et de silice**

Soutenue par

**Tiphaine HOUDARD**

Le 13/07/2022

École doctorale n°364

**Sciences Fondamentales  
et Appliquées**

Spécialité

**Mécanique Numérique et  
Matériaux**

Composition du jury :

M. Emmanuel de BILBAO Professeur - HDR, CEMHTI	<i>Président Rapport.</i>
M. Pierre BENIGNI Ingénieur de Recherche - HDR, Institut Matériaux Microélectronique Nanosciences de Provence	<i>Rapporteur</i>
Mme Isabelle CABODI Ingénieure - R&D Manager SEFPRO, Saint-Gobain Research Provence	<i>Examinatrice</i>
M. Julien ZOLLINGER Maître de conférence - HDR, Institut Jean Lamour	<i>Examineur</i>
M. Franck PIGEONNEAU DR Mines Paris - HDR, CEMEF	<i>Directeur de thèse</i>
M. Charles-André GANDIN DR CNRS - HDR, CEMEF	<i>Directeur de thèse</i>
M. Pierrick VESPA Ingénieur - R&D Portfolio Manager, Saint-Gobain Research Provence	<i>Invité</i>
M. Frédéric COSTES Ingénieur, Transvalor	<i>Invité</i>



---

*À Anne*  
*À Joseph*  
*À Marie*  
*À Emmanuel*



# Remerciements

L'heure de la fin de thèse est arrivée. Il est désormais temps d'écrire mes remerciements. Merci vient de *merces*, *-edis* qui signifie en latin « salaire, récompense ou prix pour qqch. » (Gaffiot en ligne, s.d.). Je tiens donc à remercier tous ceux qui ont fait "quelque chose" pour me permettre d'avancer au cours de ces trois années. Merci à vous tous pour vos conseils, votre sourire, votre soutien, vos pistes de réflexion (sur la thèse ou sur la vie), votre bienveillance et surtout pour votre soucis concernant mon régime alimentaire à base de tablettes de chocolat, de pâtes à tartiner et de glaces. Avant d'oublier, merci à toi cher lecteur pour l'intérêt qui t'a poussé à lire ce manuscrit.

Ma thèse fut réalisée au CEMEF (Sophia Antipolis, France) sous contrat CIFRE avec SGR Provence (Cavaillon, France). Je tiens à remercier, pour commencer, tous ceux qui ont permis la création de ce contrat doctoral ainsi que l'ANRT.

Je remercie tout d'abord mes deux directeurs de thèse Charles-André Gandin et Franck Pigeonneau. Merci pour vos conseils et toutes vos remarques constructives qui m'ont permis d'avancer dans ma thèse et de grandir personnellement. Merci pour nos temps d'échanges au long de ces trois années, et merci d'avoir supporté mon tempérament (et mon calendrier). Grâce à votre disponibilité et aux axes de recherche proposés, j'ai pu découvrir en profondeur les tenants et aboutissants de la modélisation numérique, développer une vision globale de la recherche, affiner mon esprit critique et surmonter les obstacles rencontrés. Merci pour votre patience quand il s'agissait de travailler sur les équations prises en compte dans les modèles, pour vos explications sur l'univers des simulations numériques et pour vos relectures assidues de mes rapports et de cette thèse.

Je tiens à exprimer ma sincère gratitude à Isabelle Cabodi et Pierrick Vespa. Votre soutien constant m'a beaucoup aidé. Merci pour votre implication dans ma thèse, votre expertise dans la fabrication des blocs électrofondus et votre pleine disponibilité malgré les confinements. Ce fut un réel plaisir que d'échanger avec vous pour approfondir ma compréhension de l'industrie réfractaire et pour refaire le monde autour d'un café.

Je remercie aussi Olivier Citti pour ses réponses initiales sur le projet de thèse et son suivi pendant ces trois années. Merci à Jean-Michel Drouin pour nos temps d'échanges qui m'ont permis de dépasser les difficultés dans mes mises en données de simulations. And a huge thanks to the different SEPR plants for welcoming me at your production lines, for your help during the trials we performed together and for all the results you shared after them. Enfin, un grand Merci à l'équipe SEFPRO de SGR Provence pour votre accueil chaleureux à chacune de mes venues sur Cavaillon et lors de mes déplacements, pour votre sourire et votre dynamisme, et pour toutes vos attentions qui m'ont permis de profiter de ces années de recherche à Cavaillon.

Un immense merci à Frédéric Costes pour l'accompagnement de ma thèse, de la prise en main de THERCAST® jusqu'aux derniers développements. Merci pour ton investissement dans

ce projet, tes encouragements et ton support dans mes simulations. Merci pour ta bienveillance, tes explications claires et pour tous ces moments passés à chercher l'erreur dans certaines mises en données erronées.

Ma reconnaissance va également vers Gildas Guillemot. Merci pour ta disponibilité et ton aide pour prendre en main PY/PATH et la CIMLib<sup>®</sup>. Merci pour ta précieuse aide et ton temps tout au long de ma thèse à reprendre le code au gré des changements de stratégie et de perspectives.

Pour qu'une thèse soit faite de hauts, il est malheureusement nécessaire de passer aussi par des bas. Merci à tous ceux qui furent présents à mes côtés dans les bons comme les mauvais moments. Je tiens à remercier les permanents des deux équipes du labo, en particulier Oriane Senninger et Edith Peuvrel-Disdier pour nos pauses déjeuner et pour votre écoute bienveillante. Je remercie également Elie Hachem et Pierre-Olivier Bouchard pour votre dévouement au sein de l'école doctorale, votre soutien permanent et vos conseils. Enfin, je tiens à remercier tout particulièrement Marie-Françoise GUENEGAN pour ta disponibilité permanente, ta bonne humeur, ta bienveillance lors de chacune de nos discussions et pour la gestion administrative de ma thèse.

Merci à toute l'administration du CEMEF, et en particulier Elisabeth Massoni, François Bay, Florence Morcamp et Coralie Fischer pour nos temps d'échange, en particulier pendant mon mandat de représentante des doctorants. Je dois également une fière chandelle au service informatique, en particulier à Hallem Ben Aissa, Carole Torrin et Sélim Kraria pour votre aide lors de ma découverte de l'univers numérique et vos réponses à toutes mes demandes informatiques. Merci enfin à tous les doctorants et surtout à celles et ceux qui assurent, à travers MSV, un esprit de convivialité sur le campus de Sophia. Merci à tous ceux avec qui j'ai eu la joie d'échanger, en particulier Christophe pendant mes pauses expérimentales, Vincent pendant nos goûters (même à distance) et mes co-bureaux Lucas et Théophile. Merci à tous pour votre soutien, nos belles discussions et pour tous ces moments partagés.

Ma gratitude va aussi vers tous ceux qui m'ont permis de vivre ces trois années à fond sur la côte d'Azur. Parce qu'une thèse c'est aussi une aventure humaine, je tiens à clore ces remerciements avec ceux qui, en dehors du boulot, ont partagé mon quotidien de doctorante. Vous m'avez permis, à votre manière, de grandir, de m'épanouir et de découvrir la vie dans le Sud. Nos temps de partage, de convivialité et de dépassement de soi furent des moments d'une grande richesse humaine, soyez-en infiniment remerciés! Merci en premier lieu à ma famille et puis à tous les autres : à la Barta, au feu-pilote, à SophiaDeo (et mes super frats!), à mes amis chanteurs, aux joueurs de hand de l'ASIE, à l'équipe du MEBC sans oublier mes amis de longue date qui ont partagé mes joies et qui m'ont réconfortée dans les temps difficiles. Pour finir, une mention spéciale à celles et ceux qui m'ont accompagnée par monts et par vaux dans l'arrière pays et le Mercantour.

# Contents

<b>Remerciements</b>	<b>iii</b>
<b>List of symbols</b>	<b>ix</b>
<b>Introduction</b>	<b>1</b>
<b>1 Industrial Processes</b>	<b>5</b>
Résumé Chapitre 1 . . . . .	6
1.1 AZS soldier block production . . . . .	7
1.1.1 History about electrofused refractory blocks in AZS . . . . .	7
1.1.2 Final application of AZS refractory blocks . . . . .	7
1.1.3 Industrial production of AZS blocks . . . . .	8
1.1.4 Recycling of AZS materials . . . . .	9
1.2 Long-term objective of this research . . . . .	11
1.3 Thermodynamic system . . . . .	12
1.3.1 Software and library used for thermodynamic properties tabulations . . . . .	12
1.3.2 Experimental observations of phase distribution at room temperature . . . . .	13
1.3.3 Phase diagram of the system . . . . .	13
1.4 Steps during solidification and annealing in an AZS refractory block . . . . .	14
1.4.1 Thermodynamic solidification path at standard composition . . . . .	14
1.4.2 Validation of mullite presence in thermodynamic equilibrium state . . . . .	16
1.4.3 Solidification path with mullite phase rejected . . . . .	18
<b>2 Solidification and heat transfer modeling</b>	<b>21</b>
Résumé Chapitre 2 . . . . .	22
2.1 Energy conservation equations considered in THERCAST <sup>®</sup> . . . . .	23
2.1.1 Liquid, solid fractions and average quantities . . . . .	23
2.1.2 Heat transfer in an homogenized fixed medium . . . . .	24
2.2 Geometries and Meshes . . . . .	25
2.3 Initial and Boundary conditions . . . . .	26
2.4 Numerical settings . . . . .	27
2.4.1 Mesh convergence . . . . .	27
2.4.2 Time step management . . . . .	29
2.4.3 Numerical values of thermal parameters involved in the computations . . . . .	29
2.5 Thermal properties in considered domains . . . . .	31
2.5.1 AZS properties . . . . .	31
2.5.2 Mold and Media properties . . . . .	33
2.5.3 Bin properties . . . . .	34
2.6 Industrial temperature history recording . . . . .	35

2.7	Temperature history results . . . . .	37
2.7.1	Thermal history at AZS nominal composition . . . . .	37
2.7.2	Simulations run for another composition . . . . .	39
2.8	Impact of thermal solver on temperature history predicted . . . . .	43
2.8.1	User solver presentation . . . . .	43
2.8.2	Tabulation of material thermal properties . . . . .	43
2.8.3	Temperature history with this second thermal solver . . . . .	46
2.9	Conclusion about temperature predictions in AZS block with THERCAST® software	47
<b>3</b>	<b>Thermo-mechanical computations of hot tears susceptibility and macro-porosity</b>	<b>51</b>
	Résumé Chapitre 3 . . . . .	52
3.1	Conservation equations . . . . .	53
3.1.1	Balance equations for thermo-mechanical computations in a single phase material ( $\varphi$ ) . . . . .	53
3.1.2	Mechanical balance equations . . . . .	54
3.2	Constitutive equations and properties specific to the AZS material . . . . .	55
3.2.1	Constitutive equations . . . . .	55
3.2.2	Interface definition in thermo-mechanical computations . . . . .	58
3.2.3	Mechanical properties of AZS . . . . .	59
3.2.4	Impact of thermo-mechanical computations in temperature history prediction . . . . .	61
3.3	Prediction of hot tears susceptibility in AZS block . . . . .	62
3.3.1	Experimental observations of hot tears along edges . . . . .	62
3.3.2	Literature review about hot tears formation . . . . .	65
3.3.3	Criteria for Hot Cracking Susceptibility (HCS) prediction . . . . .	67
3.3.3.1	Clyne-Davies criterion . . . . .	67
3.3.3.2	Yamanaka criterion . . . . .	69
3.3.3.3	Won criterion . . . . .	70
3.3.3.4	Local Strain criterion . . . . .	73
3.3.3.5	Stress criterion on AZS material . . . . .	74
3.3.4	Implementation of hot tear susceptibility prediction in THERCAST® . . . . .	75
3.3.4.1	Numerical sensors at the edge of AZS block . . . . .	75
3.3.4.2	Brittle temperature range definition for AZS at the considered composition . . . . .	76
3.3.4.3	Impact of the AZS consistency on mechanical outputs . . . . .	77
3.3.5	Impact of four geometries on hot tear susceptibility . . . . .	78
3.3.6	Conclusion about predicting the hot tears susceptibility of a block . . . . .	80
3.4	Prediction of macro-porosity in the riser . . . . .	80
3.4.1	Experimental observations of riser macro-porosity . . . . .	80
3.4.2	Impact of numerical parameters for porosity opening . . . . .	81
3.4.2.1	Open shrinkage threshold parameter . . . . .	82
3.4.2.2	Interface contact resistance at the interface Block/Media . . . . .	83
3.4.3	Impact of the composition on the riser macro-porosity . . . . .	84
3.4.4	Discussion about the potential impact of lower AZS liquid density . . . . .	85
3.5	Conclusion about mechanical outputs of numerical simulations . . . . .	88
<b>4</b>	<b>Macrosegregation</b>	<b>89</b>
	Résumé Chapitre 4 . . . . .	90
4.1	Experimental map of macro-segregation . . . . .	91

---

4.1.1	Experimental measurements of chemical heterogeneities . . . . .	91
4.1.2	Properties and solidification path of the encountered compositions . . . . .	94
4.2	Implementation of macrosegregation in THERCAST® . . . . .	98
4.2.1	Call of User-Model in THERCAST® . . . . .	98
4.2.2	PATH adaptation for concentrate alloys . . . . .	100
4.3	Focus on results from hydraulic computations . . . . .	102
4.3.1	Estimated velocity of AZS liquid with dimensionless parameters . . . . .	102
4.3.2	Convection vs Sedimentation . . . . .	104
4.3.3	Impact of density on the convection motions loops . . . . .	105
4.4	Macrosegregation inside a standard AZS block geometry . . . . .	106
4.4.1	Temperature history . . . . .	106
4.4.2	Convection predictions . . . . .	107
4.4.3	Numerical map of macrosegregation . . . . .	109
4.4.4	Impact of $\lambda_2$ parameter on permeability and macrosegregation results . . . . .	112
4.4.5	Further work . . . . .	112
4.5	Conclusion about macrosegregation . . . . .	113
	<b>Conclusion</b>	<b>115</b>



# List of symbols

## Acronyms

---

AZS	Refractory block made of Alumina-Zirconia-Silica
BTR	Brittle Temperature Range
DRX	X-Ray Diffraction
EVP	Elasto-Visco-Plastic
HCS	Hot Cracking Sensitivity
LIT	Liquid Impenetrable Temperature
OST	Open Shrinkage Threshold
PY	PhysalurgY library
RVE	Representative Element Volume
SEM	Scanning Electron Microscopy
TEM	Transmission Electron Microscopy
VP	Visco-Plastic
XRF	X-Ray fluorescence
ZDT	Zero Ductility Temperature
ZST	Zero Strength Temperature

## Greek symbols

---

$\alpha(T)$	-	Thermal dilatation coefficient
$beta$	-	Thermal shrinkage factor
$\Delta t$	s	Time step
$\Delta V$	m <sup>3</sup>	Volume occupied by domain $\Omega$
$\delta V$	m <sup>3</sup>	Variation of volume between two increments
$Delta_{max}$	K ou °C	Maximal variation of temperature for all AZS nodes
$Delta_{min}$	K ou °C	Minimal variation of temperature for all AZS nodes
$\Delta P_{sh}$	Pa	Pressure drop due to solidification shrinkage
$\Delta P_{\varepsilon}$	Pa	Pressure drop due to tensile deformations
$\Delta w_c$	wt.%	Critical variation of concentration during an increment
$\varepsilon$	-	Strain tensor
$\varepsilon_{el}$	-	Elastic contribution of strain tensor
$\varepsilon_{th}$	-	Thermal contribution of strain tensor
$\varepsilon_{vp}$	-	Viscoplastic contribution of strain tensor
$\varepsilon_r$	-	Relative emissivity
$\hat{\varepsilon}$	-	Strain rate perpendicular to temperature gradient
$\dot{\varepsilon}$	s <sup>-1</sup>	Strain rate tensor
$\dot{\varepsilon}_{el}$	s <sup>-1</sup>	Elastic strain rate tensor

## List of symbols

---

$\dot{\boldsymbol{\epsilon}}_{th}$	$s^{-1}$	Thermal strain rate tensor
$\dot{\boldsymbol{\epsilon}}_{vp}$	$s^{-1}$	Viscoplastic strain rate tensor
$\dot{\boldsymbol{\epsilon}}_{\varphi}$	$s^{-1}$	Deformation rate of the system
$\eta$	Pa s	Dynamic viscosity
$\lambda$	$W m^{-1} K^{-1}$	Thermal conductivity
$\lambda_{\varphi}$	$W m^{-1} K^{-1}$	Thermal conductivity of the phase $\varphi$
$\lambda_i$	$W m^{-1} K^{-1}$	Thermal conductivity inside Domain i
$\nu$	$m^2 s^{-1}$	Kinematic viscosity
$\nu$	-	Poisson's ratio
$\rho$	$kg m^{-3}$	Density
$\rho_{\varphi}$	$kg m^{-3}$	Density of the phase $\varphi$
$\langle \rho \rangle_{\varphi}$	$kg m^{-3}$	Average density over volume $V^{\varphi}$ of the phase $\varphi$
$\sigma_B$	$W m^{-2} K^{-4}$	Stefan–Boltzmann constant
$\boldsymbol{\sigma}$	Pa	Stress tensor
$\sigma_Y$	Pa	Yield stress value
$\boldsymbol{\sigma}_{\varphi}$	Pa	the surface forces (stresses) applied at the interface if the system
$\varphi$	-	Phase present in the system
$\Phi$	-	Global shape factor in Carman-Kozeny law
$\phi$	-	Indicator function of a phase
$\psi$	-	Generic scalar field
$\Omega$	-	Domain of the Representative Volume Element
$\Omega_{\varphi}$	-	Retriktion of $\Omega$ where only $\varphi$ is present

## Roman symbols

---

$A_0$	$MPa^{-1} s^{-1}$	Pre-exponential factor in consistency definition
$C_p$	$J kg^{-1} K^{-1}$	Specific heat capacity
$\langle D_{l;i} \rangle$	$m^2 s$	the diffusion coefficient for the component i
$d$	m	diameter of sphere
$e_{air}$	m	Air layer thickness
$E$	Pa	Young modulus
$E_a$	$J mol^{-1}$	Activation energy for consistency determination
$F$	N	Force
$F\boldsymbol{v}$	$N m^{-3}$	Volumetric force density tensor
$F\boldsymbol{v}_{\varphi}$	$N m^{-3}$	Volumetric forces in phase $\varphi$ applied on a representative volume
$g_{\varphi}$	-	Volume fraction of the phase $\varphi$
$\boldsymbol{g}$	$m s^{-2}$	Gravitational acceleration
Gr	-	Grashof dimensionless number
$H$	Pa	Strain Hardening Factor
$h_{conv}$	$W m^{-2} K^{-1}$	Exchange coefficient by convection
$h_{1/2}^{initial}$	$W m^{-2} K^{-1}$	Initial value for the exchange coefficient between domain 1 and 2
$h$	Pa	Enthalpy per unit mass
$\langle h \rangle$	Pa	averaged enthalpy per unit mass
$h_{\varphi}$	$J kg^{-1}$	Massic enthalpy of the phase $\varphi$
$h_{conv}$	$W m^{-2} K^{-1}$	Heat transfer coefficient
$\boldsymbol{I}$	-	Identity matrix
$[i]_{\varphi}$	kg/kg	Weight fraction of component i in phase $\varphi$
$\boldsymbol{j}_{\varphi}$	$W m^{-2}$	Diffusive heat flux
$K$	$Pa s^m$	Viscoplastic consistency

---

$L^{\alpha/\beta}$	$\text{J kg}^{-1}$	Mass latent heat of transformation $\beta \rightarrow \alpha$
$m$	-	Strain rate exponent in constitutive equation
$n$	-	Strain exponent in constitutive equation
$\mathbf{n}$	-	Normal vector of a surface
$P_\varphi$	Pa	Pressure inside the system $\varphi$
$P_m$	Pa	metallostatic pressure inside the block / the mesh
$Pe$	-	Péclet dimensionless number
$R_c$	$\text{K m W}^{-1}$	Reduced contact resistance at an interface
$R$	$\text{kJ mol}^{-1} \text{K}^{-1}$	Perfect gas constant
$Ra$	-	Rayleigh dimensionless number
$Re$	-	Reynolds dimensionless number
$\mathbf{s}$	Pa	Stress deviator
$T$	K or °C	Temperature
$T_\varphi$	K or °C	Temperature in phase $\varphi$
$\dot{T}$	$\text{K s}^{-1}$	Cooling/Solidification rate
$T_0$	K or °C	Initial temperature (after casting)
$T_c$	K or °C	Coherency temperature for VP to EVP transition
$T_i$	K or °C	Temperature in Domain i
$t$	s	Time
$v$	$\text{m s}^{-1}$	Velocity
$\mathbf{v}_\varphi$	$\text{m s}^{-1}$	Velocity of the phase $\varphi$



# Introduction

Glass furnaces require a container structure, in contact with the molten glass, that resists to high temperatures (above 1500 °C for silico-soda-lime glass) in continuous process for several years (up to 20 years for float furnaces that produce flat glass). Reconstruction of glass furnace [1] is a critical time period for glass makers. Furnace construction lasts a couple of months and requires a huge investment of several M€. Such action requires months of preparation to define precisely the type of glass that will be produced in order to get the longest furnace lifetime by adapting the refractories to their location inside the furnace. Each location faces specific solicitations (chemical, mechanical, thermal). Soldier blocks need to be resistant to high temperatures and to molten glass corrosion [2].

According to Begley [3], there are different families for refractory ceramics. The present work is focused on a reference that validates the requirements for glass furnaces presented above : Alumina-Zirconia-Silica ("AZS"). For materials called "AZS", there are three main components : alumina (46 to 51 wt.%), zirconia (32 to 41 wt.%) and silica (11 to 15 wt.%), to which are commonly added few percents of sodium oxide, Na<sub>2</sub>O. Refractory ceramic blocks can be produced within a wide range of dimensions. A typical block, chosen as a reference in this work, would be 1.6×0.4×0.25 m<sup>3</sup> with a mass of several hundreds of kilograms. Such soldier blocks are used to build the infrastructure of glass furnaces. Most of the soldier blocks are nowadays produced by electro-fusion process. Electro-fusion process is used to achieve low porosity inside the block (total porosity lower than 5 vol%) for better resistance to corrosion. Raw materials (alumina, zirconia, silica and soda) are melted in an Heroult-type electric arc furnace. Electro-fusion of AZS is a foundry process at extremely high temperatures. At about 1850 °C, the melt is poured into a mold laid in a steel bin. An insulating medium is interposed between the mold and the bin to control the thermal cooling. Due to the size of the blocks and the nature of the materials, controlled cooling of the ingots lasts from few days to a couple of weeks after casting. Being able to predict foundry defects occurring during solidification thanks to numerical simulation should optimize or validate the production of higher quality blocks, in order to better answer the requirements and increase furnace lifetime. A better understanding of the several phenomena that occur during the electro-fusion and the casting (pouring and annealing) processes is the first step for optimization.

To improve block quality, a "trial and error" approach implies to waste raw materials and energy to produce blocks that do not follow current standards. Numerical simulations are a good opportunity if the software forecasts well block quality indicators. The final purpose would be to validate upstream the impact of new block geometries, new alloy compositions or new industrial processes on the block quality. This PhD consists in the improvement of THERCAST<sup>®</sup> initially developed for metal alloys to AZS ceramic blocks to be able to predict, first, defects occurrences, such as hot tears and, second, solidification shrinkage for geometry optimization. Simulations of such block annealing are compared with experimental results. Typical "casting defects" are

hot tears at the edges of the block and shrinkage porosity inside the riser. A specificity of this material, due its size, is the macro-segregation (or chemical heterogeneity) within the block. The prediction by simulations of such outputs depends on the temperature history. The context of the analysis performed in the present work for the temperature history, the hot tear susceptibility, the macro-porosity simulation and the map of chemical heterogeneity is detailed below:

- **Temperature history** It exists several works in literature and in internal Saint-Gobain documents to predict the temperature history inside refractory blocks. Studies were also performed for another type of refractory ceramics, enriched in zirconia : high zirconia materials. For example, Petroni *et al.* [4] and Zhang [5] present their work to simulate high zirconia annealing with the Zebulon finite element software [6]. Some studies for AZS materials were performed with ANSYS<sup>®</sup> software at SGR Provence. In this work, the THERCAST<sup>®</sup> finite element software is considered [7], as it can performed 3D thermo-mechanical analyses in a multi-domains system.
- **Hot tears** A way to improve block quality is to prevent the occurrence of hot tears or to reduce their length at the edge of blocks. Such defect is described by Cockcroft *et al.* [8]. Studies about hot tears modeling were performed for aluminum alloys [9] or steel alloys [10]. Mechanical behavior of refractory ceramics has been studied in previous PhD theses [5, 11–14] especially on High Zirconia materials. Several criteria have been published in the literature to predict hot tear susceptibility in metallic alloys [15–18]. They have not been adapted to refractory ceramics yet. The criterion developed in this work for AZS refractories accumulates, in a defined temeparture range, the strain computed by the mechanical solver in THERCAST<sup>®</sup>. The value is used to define the hot tear susceptibility of the final product.
- **Riser porosity** To limit the porosity inside the block itself, due to solidification shrinkage, a riser is added above the block. Its volume can be up to 100% of the block volume. As it is not possible to reprocess after annealing (in case the block is not filled enough after solidification), riser and block geometries need to be optimized to validate customer expectations and to limit the economical cost of post-processing steps. Ideally, a simulation should anticipate the solidification shrinkage observed in industrial risers and the air gap layer that can open between the block and its mold [19]. THERCAST<sup>®</sup> is designed to take this air layer into account by adaptation of the mesh of the ingot. The air gap thickness can also be accounted for computation of heat exchanges. It is therefore interesting to test this option on ceramic materials.
- **Chemical heterogeneity** Simulations involving macrosegregation solvers have already been developed for metal alloys [20–25]. They return a map of compositions resulting in a so-called "macrosegregation map" at industrial block scale. Previous contributions are only partly upscaled to blocks with the dimensions considered in the PhD project. For instance, Ettroudi [23] only considers a binary alloy for a large scale (several tons) steel ingot without coupling with thermodynamic data. The tabulations of thermodynamical data are extracted using PhysalurgY<sup>®</sup> from a CALPHAD database used as an input to the Thermo-Calc<sup>®</sup> software.

The results obtained during the PhD are detailed in the present report divided in four chapters representing the different steps of an annealing simulation. First, to set-up a relevant simulation, it is important to introduce the industrial process. In a similar way, considered material data need to be validated thanks to experimental studies and from literature. A second chapter presents the validation of temperature history obtained by numerical simulations with THERCAST<sup>®</sup> in the mold and the media, to get a relevant prediction of temperature in the block

---

itself. Temperatures considered for thermal validation were recorded during the annealing of a block at Saint-Gobain SEPR plant. Adaptation of key parameters such as thermal conductivity or interface resistance have been required to achieve relevant temperature history simulation. A third chapter focuses on thermo-mechanical computations. Considering an additive constitutive equation and allowing air gap formation, simulations are optimized to predict the hot tear susceptibility and its variations depending on block geometries. However, a lack of coherency between the predicted macro-porosity inside the riser and the experimental observations was identified. Similarly, temperature incoherency remained in the riser neighborhood with respect to heat flow. The fourth chapter is therefore dedicated to macrosegregation implementation at the scale of the block as a possible explanation. Phase composition, enthalpy and density are tabulated as a function of temperature for different global system compositions. The tabulation method had to be adapted from a metallic system to an oxide alloy at standard composition that are less diluted than in the previous works of literature. Simulations were finally performed at industrial scale. A summary of the main results, the questions they rise and perspectives of the present work close this report.



# Chapter 1

## Industrial Processes

### Contents

---

Résumé Chapitre 1 . . . . .	<b>6</b>
1.1 AZS soldier block production . . . . .	<b>7</b>
1.1.1 History about electrofused refractory blocks in AZS . . . . .	7
1.1.2 Final application of AZS refractory blocks . . . . .	7
1.1.3 Industrial production of AZS blocks . . . . .	8
1.1.4 Recycling of AZS materials . . . . .	9
1.2 Long-term objective of this research . . . . .	<b>11</b>
1.3 Thermodynamic system . . . . .	<b>12</b>
1.3.1 Software and library used for thermodynamic properties tabulations .	12
1.3.2 Experimental observations of phase distribution at room temperature .	13
1.3.3 Phase diagram of the system . . . . .	13
1.4 Steps during solidification and annealing in an AZS refractory block . . . . .	<b>14</b>
1.4.1 Thermodynamic solidification path at standard composition . . . . .	14
1.4.2 Validation of mullite presence in thermodynamic equilibrium state . .	16
1.4.3 Solidification path with mullite phase rejected . . . . .	18

---

## Résumé Chapitre 1

Le chapitre 1 présente le matériau dont la solidification sera étudiée tout au long de cette étude : un bloc de cuve en céramique réfractaire composé principalement d'alumine, de zircon et de silice (AZS). Ce chapitre rappelle aussi les trois objectifs principaux des simulations. Premièrement les simulations numériques avec THERCAST<sup>®</sup> sont utilisées pour prédire le risque de formation des criques à chaud. Il s'agit de défauts de fonderie typiques, principalement observés le long des arêtes du bloc. Deuxièmement, les simulations anticipent la formation de la retassure dans la masselotte. Enfin, la distribution en composition chimique sur toute la hauteur du bloc peut être modélisée.

Dans un premier temps, le cycle de vie du matériau est présenté. Après électrofusion dans un four de type Héroult, les matières premières sont coulées dans un moule, calé dans une caisse avec un agent isolant qui limite les échanges thermiques avec l'extérieur. Après quelques semaines de refroidissement, le bloc est démoulé, la masselotte est retirée et les faces sont usinées. Les blocs sont ensuite expédiés pour construire la cuve de fusion d'un nouveau four verrier. Pour les matériaux AZS, l'augmentation de la fraction de zircon entraîne une résistance accrue à la corrosion. Après plus d'une décennie de fonctionnement, l'usure est très importante. Le four est alors déconstruit et les restes des blocs AZS peuvent être récupérés pour être recyclés.

Après avoir présenté le matériau dans son contexte industriel, l'étude s'est portée sur le matériau en tant que tel. Expérimentalement, trois phases sont observées au microscope électronique à balayage : de la zircon, du corindon et une phase vitreuse. La base de données thermodynamiques TCOX10 est choisie pour prédire le chemin de solidification et l'évolution de propriétés telles que la densité ou l'enthalpie. Lorsque le système liquide atteint le liquidus, TCOX10 prédit la formation de cristaux de zircon primaire. Cette solidification est suivie par celle d'un eutectique zircon-corindon avant l'apparition de la phase mullite. La fraction de liquide restante, fortement enrichie en silice, est assimilée à la phase vitreuse présente dans le matériau. Dans les blocs industriels, Na<sub>2</sub>O est introduit pour justement inhiber la formation de la mullite. Des traitements thermiques à 1400 °C et 1500 °C sont réalisés pour donner davantage de temps aux échantillons pour atteindre l'état d'équilibre thermodynamique. Leurs résultats valident les prédictions thermodynamiques de la base de données utilisée. Pour extraire des données cohérentes avec la réalité industrielle, la mullite est suspendue dans les calculs thermodynamiques. Le chemin de solidification et le diagramme de phases prédit dans ces conditions sont alors cohérents avec les observations expérimentales.

## 1.1 AZS soldier block production

### 1.1.1 History about electrofused refractory blocks in AZS

By definition [26], a refractory has to handle temperatures above 538°C (i.e. 1000 F). The material of interest in this work is the AZS electrofused refractories, presented in Figure 1.1, used as soldier blocks to build lateral walls in glass furnaces. They must resist to much higher temperatures: up to 1500 °C, continuously over around 15 years [27].



Figure 1.1: Photo of a new block (1600 x 400 x 250 mm).

Historically, the process for making refractories was sintering with a final porosity (open and closed) around 20 vol% (except sintering process with hot isostatic pressure) [27]. Depending on the glass furnace application (insulation, flat sheets of glass, bottles,...) and the location inside the furnace, almost every blocks are nowadays produced by electro-fusion. This process has been implemented by Corning Glass Works [28] in the 1920's to get almost fully oxidized and very dense blocks, with a porosity below 2 vol%. It implies a better resistance facing molten glass [27]. The technology of adding zirconia in alumina refractories has been developed by Fulcher and Littleton in the 1920's [29]. Zirconia crystals improve the refractory resistance against molten glass corrosion. Thanks to those innovations, furnaces lifetime increased a lot from a couple of years up to 10-20 years, depending on their final application.

### 1.1.2 Final application of AZS refractory blocks

Refractory blocks are assembled to build glass furnaces. Float furnaces are built to produce flat sheets of glass. Such process has been invented by Pilkington in the 1960's [30]. Raw materials are introduced in the entrance of the melting area (left of the yellow area in Figure 1.2). Burners are located along the side of the furnaces to heat the raw materials until molten glass is obtained. Impurities like bubbles and silica seeds get away from the glass forming liquid when the temperature in the bath reaches 1500 °C. The area colored in light blue in Figure 1 is the refining and thermal conditioning area in which the temperature decreases from 1500 to 1100 °C. On the right, the lip is the junction between the furnace and the liquid tin area, where the molten glass is spread to get perfectly flat glass strips with good optical properties. Finally, the glass cools down to room temperature in the final furnace section, called "lehr", (longer than 100 m) before being inspected, cut and shipped.

Each color in Figure 1.2 represents a type of refractory, with specifications that depend on their localization as they are facing specific solicitations (chemical, mechanical, thermal). This project focuses on soldier blocks (in orange in Figure 1.2) produced by electro-fusion process that are resistant to high temperatures and to molten glass corrosion [2]. To achieve low porosity inside the block (total porosity lower than 5 vol%), raw materials (alumina, zirconia, silica and

soda) are melted in an Heroult-type electric arc furnace. At about 1 850 °C, the melt is poured into a mold laid in a steel bin. A riser<sup>1</sup> is located above the block with a specific volume and geometry depending on the expected block quality [12]. After riser cut and surface polishing, the dimensions of the block considered in this study are  $1.6 \times 0.4 \times 0.25 \text{ m}^3$  as in Figure 1.1.

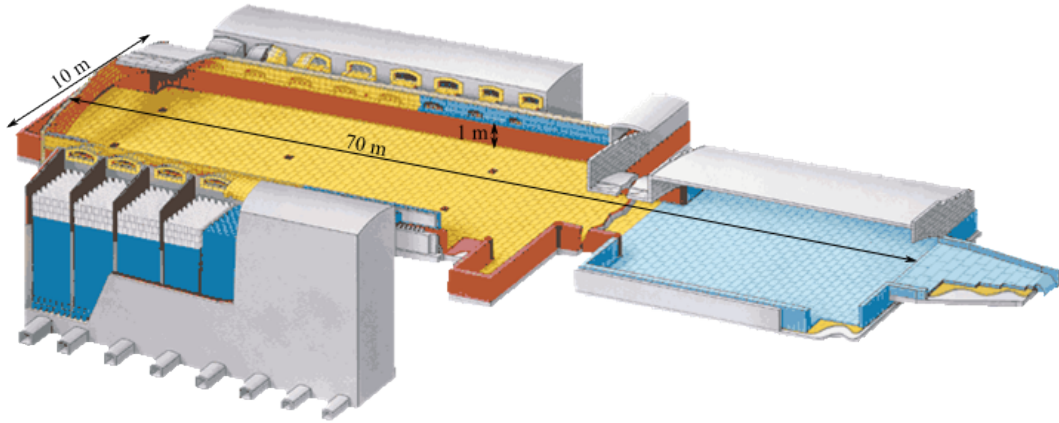


Figure 1.2: Schematics of a float furnace for flat glass production with AZS soldier blocks in orange color.

The production capacity of a float furnace is nowadays up to 900 - 1 000 t/day of flat glass (thickness 1 - 19 mm [31]). For comparison, in steel industry, a continuous-casting furnace to produce thin slab (thickness 35 - 80 mm [32]) has a capacity around 2 740 t/day. Such comparison needs to keep in mind that steel density is three times higher than glass density [33] and the slab thickness is also four times thicker than for glass sheets.

### 1.1.3 Industrial production of AZS blocks

The industrial process [8, 34] to produce AZS blocks shows similarities with some processes found in the metal casting industry and is described in Figure 1.3:

- Prepare a single used sand mold (25 - 100 mm thickness) [12] during the shaping stage;
- Insert the mold in a metal bin filled with an insulating media during the molding and shimming stages;
- Mix the raw materials (alumina - zirconia - silica - soda) to get the expected composition presented in Table 1.1;
- Melt the AZS block raw materials in a Heroult-type furnace by electro-fusion;
- Adjust the global oxidation state if needed by oxygen injection;
- Pour the melt into the mold at a temperature close to 1850 °C, i.e. the casting operation;
- Let cool down the block for several days/weeks (depending on specification and size), i.e. the annealing stage;

<sup>1</sup>Riser is the extra amount of molten refractory casted above the block to avoid the creation of shrinkage cavities inside the block itself after solidification

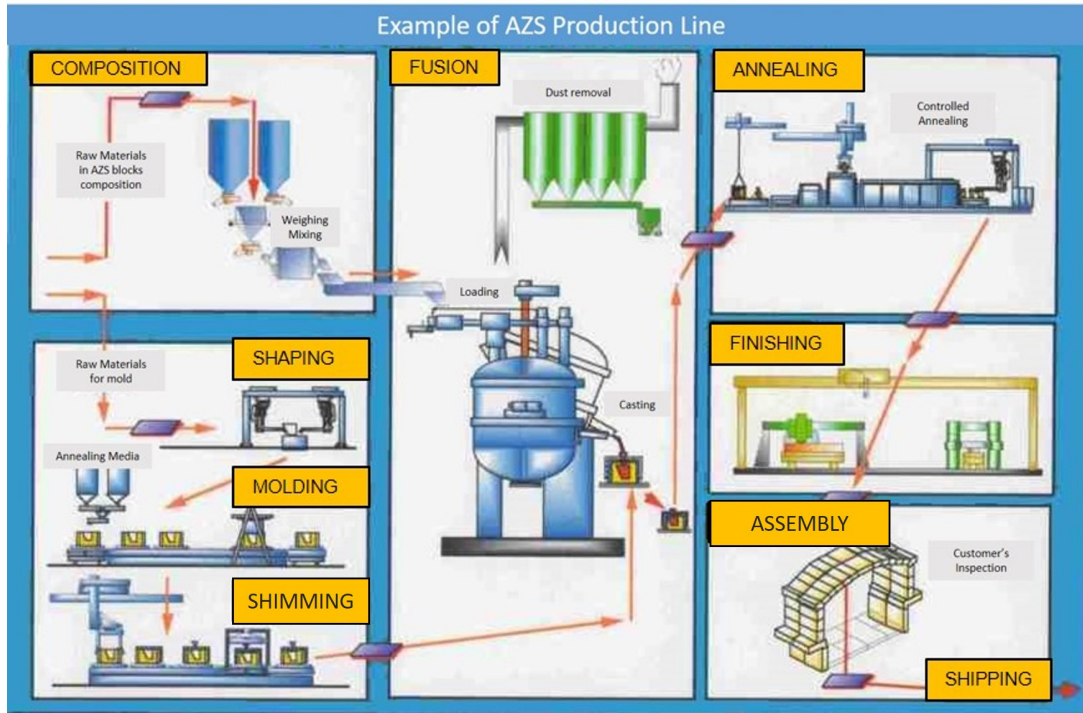


Figure 1.3: Industrial steps for AZS block Production [34].

- Finish the block (cut riser, polish lateral sides, ...);
- Furnace is assembled on the production site for customers inspection before shipment;

Raw material composition for AZS material expressed in wt.%.				
ZrO <sub>2</sub>	Al <sub>2</sub> O <sub>3</sub>	SiO <sub>2</sub>	Na <sub>2</sub> O	Other (Fe <sub>2</sub> O <sub>3</sub> , TiO <sub>2</sub> )
32-41	46-51	11-15	0.95-1.3	0.3

Table 1.1: Standard composition for an AZS refractory block.

#### 1.1.4 Recycling of AZS materials

After a short presentation of the AZS history, production process and final application, in order to get a whole idea of the AZS industry, this section presents the end-of-life of AZS blocks.

During the glass production, the soldier block undergoes a wear due to the contact with the glass forming liquid. Figure 1.4 is a photography taken from the interior of a furnace after its shutdown. Two corrosion rates are observed along the height of the block in Figure 1.4 and are documented in literature [35, 36]. First, along the block height, there is a slow dissolution of the AZS block through the molten glass depending on the fluid motion as it is clearly seen in the middle section of the blocks in Figure 1.4. Second, a high corrosion rate is localized at the top of the block, at the triple line between liquid/AZS/gas atmosphere. At this location, refractory dissolves in the molten glass but equilibrium is not reached as new molten glass is continuously coming over and replace the enriched molten glass. Hot repairs (without furnace shut down) are possible in some cases but at the end of furnace lifetime, it is required to definitely replace its blocks. While new blocks are installed, formers blocks are sent to recycling. A furnace at the end of its lifetime implies from 200 t to 600 t of refractory to recycle, the exact tonnage depends on furnace application (bottle, flat glass, insulation...). Used blocks are ground on furnace site

before shipping the gravels by train or boat [37]. In Europe, there are around 30 furnaces (all applications being considered) to recycle per year. The extended producer responsibility in Europe promotes the recycling of refractories used in furnaces as any other construction materials. This is not the case worldwide yet.



Figure 1.4: Blocks installed in a furnace at the end of its life.

As the soldier blocks are in contact with molten glass, most are contaminated by oxides that are present in the glass composition [37]. Up to 40 different quality segments are defined depending on the block initial composition and the pollutants it has been exposed to (fuel-gaz from furnace energy source, dusts, glass composition,...) [38].

Section of the soldier blocks can be recycled mostly in refractory concrete. They are ground in small pieces that will be used directly as gravels for concrete and refractory mortar [38]. Gravels are sized in three categories : fine (0-1 mm), medium (1-3 mm) and coarse (3-6 mm) [39]. The composition variations between blocks and the possibility to find glass residue stuck to gravels lead different references of secondary raw materials. At the end of the recycling process, more than 85% of refractory waste from glass furnace has a second life. The remaining (mostly super-structure composed of pure silica) is buried in accredited sites that use them as reinforcement structure between waste layers.

A better way to recycle waste is to avoid producing it. The riser is by definition a piece that will be removed after annealing. In production plant, they are ground and reintroduced in the Heroult-type furnace. Optimizing their shape would reduce the volume of remaining material inside the riser that needs to be processed.

## 1.2 Long-term objective of this research

Refractory producers need to produce more than 200 blocks just for the fusion section of a float furnace. Usual casting defects can be found inside soldier blocks such as hot tears along the block edges. Casting specificities such as macro-porosity or macro-segregation (i.e. chemical heterogeneity) are also observed within the block and in the riser.

To increase block quality, a better understanding of hot tears formation is required. One way to improve block quality is to perform tests at industrial scale changing process settings (mold shape or thickness, annealing media, ...). This option implies wasting raw materials and requires lots of energy to melt those raw materials before casting. A second way is to develop theoretical model which can be solved numerically to estimate the hot tears susceptibility. Several modeling approaches have been published in the literature to predict hot tear susceptibility in metallic alloys depending on the accumulated strain [17] or the cavitation pressure [10]. Despite contributions about ceramics that focused on thermal stress analyses [8], reliable numerical predictions of hot tears applied to the fused cast refractory products are still missing.

Macro-porosity due to solidification shrinkage must be localized in the riser, to be removed after annealing. Several qualities of block filling exist [12, Chap. 2] : RT (total filling - without remaining porosity inside the block - considered in this study), RR (reinforced filling - with only a small part of macro-porosity that remains in the block section), RN (normal filling - with a significant part of the macro-porosity remaining in the block section). To increase environmental efficiency and economical efficiency of the AZS block production process, the riser geometry can be optimized to condense macro-porosity and hence limit its presence inside the AZS block section. As zirconia crystals are the first to solidify and with higher density, the bottom of the block contains higher concentration of zirconia that increases the block resistance toward corrosion. Therefore, in glass furnaces, blocks are installed upside down for those two reasons. The first is to avoid the presence of porosity at the triple line where corrosion is the most effective. The second is to get the section of the block with higher zirconia content (bottom of the produced block) at the triple interface to increase the corrosion resistance of the block in this area. Such an objective requires a software able to simulate the location of macro-porosity.

THERCAST<sup>®</sup> is a 3D finite-element simulation software, commercialized by the company Transvalor. One of the objectives of this project is to consider a hot tear susceptibility criterion that could predict quality impact introduced by a change in the process. The second objective is to model the shrinkage to optimize riser geometries depending on the expected block quality defined by its filling. The highest the "filling", the less porosity remains in the block. Relevant computations of macro-porosity require to take real density into account and therefore to model macrosegregation.

Such objectives start by a good prediction of the temperature history inside the AZS block. Standard simulations on THERCAST<sup>®</sup> consider thermo-mechanical properties tabulated as a function of temperature. To retrieve relevant temperature history, it is necessary to get relevant tabulated properties. Such properties can be obtained experimentally or determined thanks to software such as thermodynamic databases made accessible by Thermo-Calc<sup>®</sup>. An industrial casting has been followed in temperature and composition. It will be used as reference to validate the software outputs.

## 1.3 Thermodynamic system

### 1.3.1 Software and library used for thermodynamic properties tabulations

#### Thermo-Calc<sup>®</sup> software and its TCOX10 database

Thermo-Calc<sup>®</sup> is a software developed to calculate the properties of a thermodynamic system based on the CALPHAD method [40]. Such solver can predict properties of multi-component alloys by ab-initio calculated data validated thanks to the extrapolation of experimental data. It is a phase-based approach that requires to define the amount of all chemical elements considered, as well as the description of all phases encountered in the system. To define an equilibrium, the exact composition of the global system is given with physical properties (size of the system, temperature, pressure). It is possible to consider "pseudo-thermodynamic" equilibrium, at a higher level of energy compare to the thermodynamic one, by removing the presence of some phases expected in the thermodynamic equilibrium state. Thermodynamic parameters for a system composed of  $\text{Al}_2\text{O}_3\text{-ZrO}_2\text{-SiO}_2$  are detailed by Kwon *et al.* [41].

Parameters used with the CALPHAD method are stored in a database. In this study, the thermodynamic database created in 2020, TCOX10 [42], is considered. This version of the metal oxide solutions database is adapted for metal slags and oxides. It returns the amount and composition of the phases but also the phase fraction at equilibrium and the phase diagram. It is also possible to extract phase enthalpy, entropy, heat capacity and density to get thermodynamic properties of a system in a given state. Among the 29 elements in this database, there are the main element of the AZS refractories : aluminum (Al), zirconium (Zr), silicon (Si), sodium (Na) and oxygen (O).

#### Physalurgy<sup>®</sup> and its tool PATH

Physalurgy<sup>®</sup> (PY) is a library that has been developed at CEMEF [43]. Thanks to the TQ interface of Thermo-Calc<sup>®</sup>, it is possible to call thermodynamic and kinetic databases to retrieve data for material evolution simulations coupled with thermodynamic equilibrium state properties. Among the several tools developed in this library, PATH is considered to obtain thermodynamic phase properties in a format ready-for-use in finite-element solvers such as those called in THERCAST<sup>®</sup>, as detailed in § 2.8.

The PY library works with Thermo-Calc<sup>®</sup> databases using its TQ interface. It tabulates temperature dependent properties (phase fractions and phase compositions but also enthalpy and density) at a given global composition. It can combine results for several global compositions to get a global tabulation, used for heat flow and macrosegregation computations.

The PATH tool [43] has been developed for metal alloys. Adaptations were required to take oxide components into consideration. If four solute compounds are defined with specific proportion, e.g.  $\text{Al}_2\text{O}_3\text{-ZrO}_2\text{-SiO}_2\text{-Na}_2\text{O}$ , five elements (Al - Zr - Si - Na - O) need to be used. In the initial definition of the system, only chemical elements are defined. When computing equilibrium, Thermo-Cal<sup>®</sup> allows the consideration of component (oxide, for example  $\text{Al}_2\text{O}_3$ ) instead of "single" chemical element (for example Al) at condition that the amount of elements is kept (5 in our study). Oxygen is then defined as a fifth component but it should not be included in tabulation, as a second main element. Oxygen activity is set to 1, as if oxygen was a solvent which contains the four other components.

The method was initially available for diluted alloys. Because AZS material contains solutes at high nominal concentrations and macrosegregation implies deviations up to 20-30% from the nominal composition, more adaptations were required. They are presented in § 4.2.2.

### 1.3.2 Experimental observations of phase distribution at room temperature

Figure 1.5 depicts an Scanning Electron Microscopy (SEM) observation taken from an AZS block at room temperature. The chemical composition of the AZS block is given in Table 1.1. Observations are similar to images presented by Asokan *et al.* [44]. Three phases can be identified: zirconia (mainly composed of  $ZrO_2$  with a slight solubility of  $Al_2O_3$ ) in white, corundum (pure  $Al_2O_3$ ) in light gray and a glassy phase in dark gray (containing  $SiO_2$ ,  $Na_2O$  and a significant fraction of  $Al_2O_3$ ). Zirconia can be dispersed as coarse crystals in the glassy phase or as laths in a eutectic structure with corundum.

At room temperature, the zirconia crystal family is monoclinic as detailed by Gouraud [13]. The phase distribution, determined by X-Ray Diffraction (DRX) at room temperature is detailed in Table 1.2.

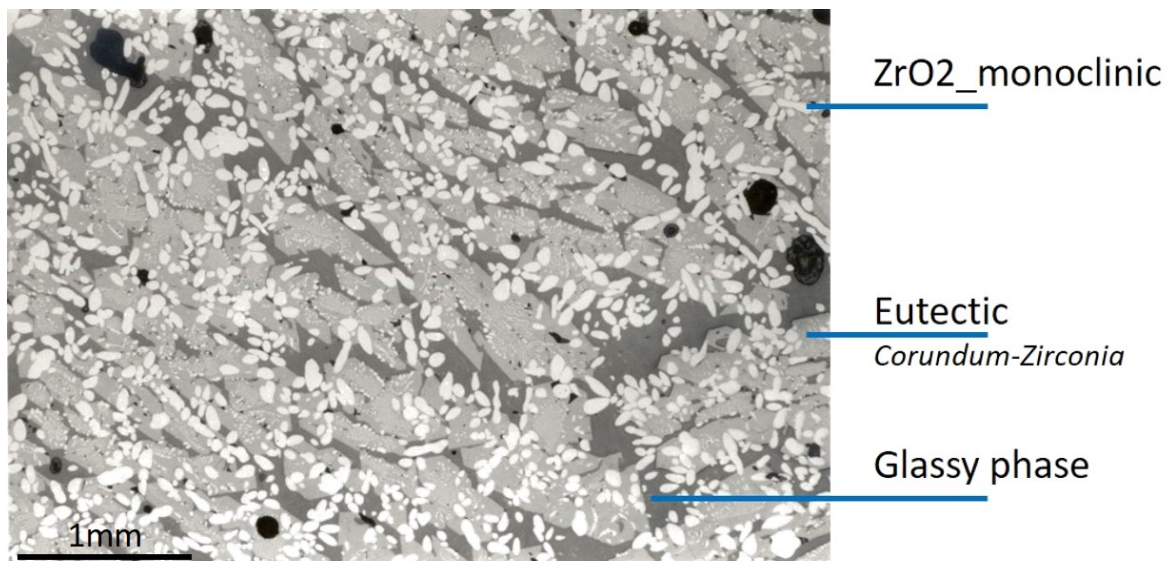


Figure 1.5: SEM observation of phase distribution in AZS sample with 41% of  $ZrO_2$ .

Crystallographic analysis on AZS (wt%)		
Corundum	Zirconia phase	Glassy phase
43	40	(Remaining = 17)

Table 1.2: Composition of AZS products [12].

### 1.3.3 Phase diagram of the system

Phase diagram for  $Al_2O_3-ZrO_2-SiO_2$  system has been studied as early as 1939 by Rea [45], without investigating the section of the diagram where mullite can be observed. Several revisions have since been done, especially in 1972 by Greca [46] by extending the domain of stability of the primary zirconia phase, by increasing the alumina content of mullite solid solution and by modifying the position of the invariant point in terms of temperature and composition. The implementation of such phase diagram in thermodynamic database is still to be improved as recorded by Kwon [41] or Vorozhtcov [47].

With the TCOX10 database, it is possible to obtain a map of liquidus projection depending on composition for an  $Al_2O_3-ZrO_2-SiO_2$  system (see Figure 1.6). The mullite domain is shorter than the one predicted by Greca [46] but the primary zirconia domains are quite similar. AZS

family with composition close to Table 1.1 are at bottom center of the phase diagram. Solidification path of AZS is plotted in pink, it ends at the invariant point where mullite, corundum and tetragonal zirconia phases solidify. Except the liquid phase that contains all the components, the solid phases are almost pure (a single component) or a binary of two components (for example : mullite is composed of  $\text{Al}_2\text{O}_3$  and  $\text{SiO}_2$ )

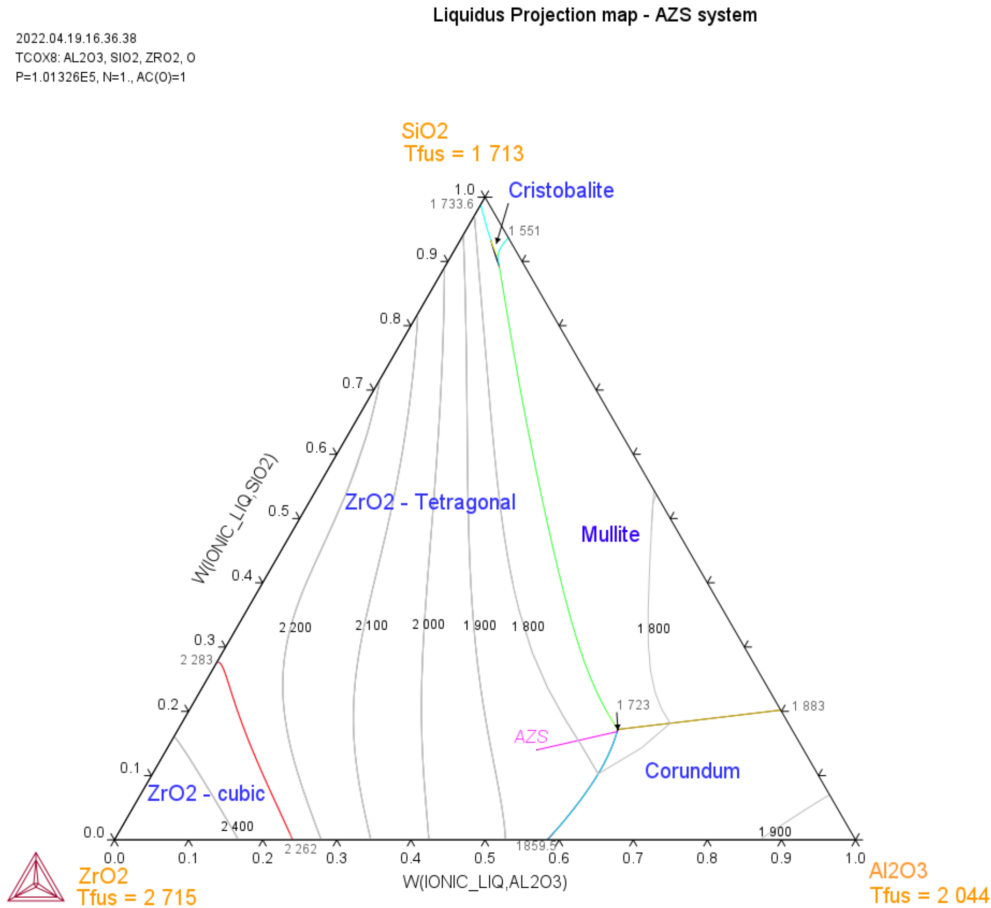


Figure 1.6: Liquidus projection map obtained with TCOX10 database for an AZS system with: (blue) the first solid phase formed below the liquidus and (pink) the solidification path for AZS.

## 1.4 Steps during solidification and annealing in an AZS refractory block

### 1.4.1 Thermodynamic solidification path at standard composition

In order to solve the energy conservation equation, THERCAST<sup>®</sup> needs to get a tabulation with temperature of heat capacity and latent heat during solidification. Thermo-Calc<sup>®</sup> is able to produce such tabulation for a system at thermodynamic equilibrium state.

AZS refractory family has a composition contained in range presented in Table 1.1. The specific block composition that will be considered all along this project is determined by X-Ray fluorescence (XRF) characterization and is detailed in Table 1.3.

Thermo-calc<sup>®</sup> predicts a solidification path as presented in Figure 1.7 for a system at a composition as in Table 1.3. Just below 1 900°C, liquidus is reached and zirconia crystals start

wt.%	Al <sub>2</sub> O <sub>3</sub>	ZrO <sub>2</sub>	SiO <sub>2</sub>	Na <sub>2</sub> O
AZS41	45.01	41.53	12.40	1.06
AZS36	48.6	36	14	1.4

Table 1.3: Composition of the both AZS specifications considered for thermal data extraction.

to solidify. At 1 771°C, an eutectic structure starts to solidify combining corundum crystals with zirconia crystals that will solidify at such temperature. Mullite phase (in purple) is predicted thermodynamically when the system reaches 1 723°C. Below 1 650°C almost all the refractory has solidified.

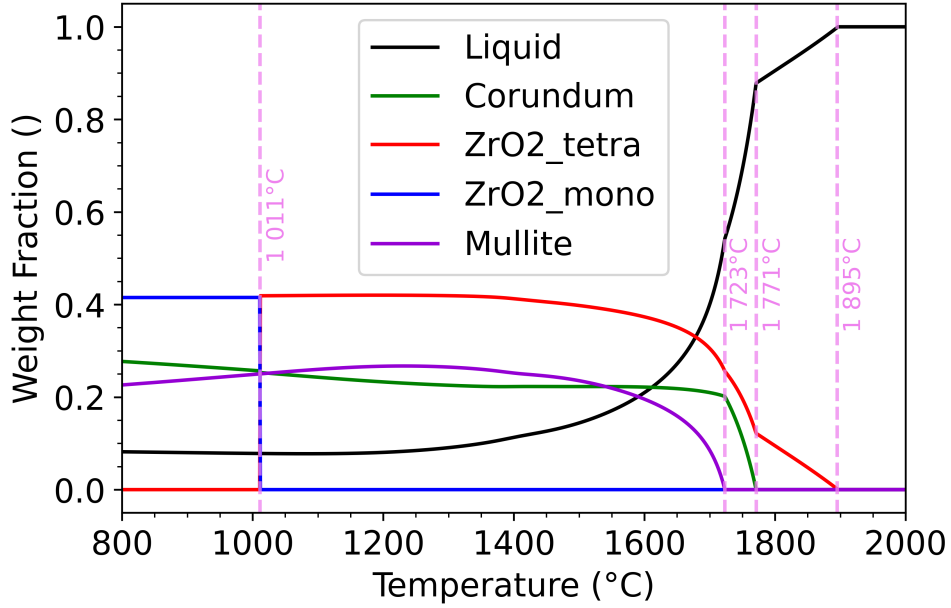


Figure 1.7: Solidification path for the AZS41 as computed by the TCOX10 thermodynamic database assuming full equilibrium with mullite phase allowed.

At 1 011°C, zirconia phase transition results in a 4% volumetric expansion of Zirconia crystals. For a block with 33 wt.% of zirconia, it implies a global expansion of 1.3%, that impact the properties of the entire system [48]. Cockcroft *et al.* [49] showed that such martensitic phases transformation might lead to cracks, more than initial quenching of the surfaces during casting. Below 780°C, after the glass transition temperature [12], the system presents an elastic behavior.

Micro-probe measurements of glassy phase returns a composition as detailed in Table 1.4. The ratio Al<sub>2</sub>O<sub>3</sub>/SiO<sub>2</sub> goes from 3.8 in the liquid state to 0.2 in the glassy phase. Mullite is an alumina-silicate solid-solution with several end members : mullite 3:2 composed of 3Al<sub>2</sub>O<sub>3</sub> – 2SiO<sub>2</sub> or mullite 2:1 2Al<sub>2</sub>O<sub>3</sub> – SiO<sub>2</sub> [50]. Mullite is more stable than the glassy phase and its crystallization will reduce the energy of the system.

wt.%	SiO <sub>2</sub>	Al <sub>2</sub> O <sub>3</sub>	Na <sub>2</sub> O	others
AZS41	77.1	16.6	4.3	2

Table 1.4: Composition of the glassy phase in the AZS block determined by micro-probe (WDS element analysis).

### 1.4.2 Validation of mullite presence in thermodynamic equilibrium state

As shown in Figure 1.6, mullite is predicted for a ternary  $\text{ZrO}_2 - \text{Al}_2\text{O}_3 - \text{SiO}_2$  system. At the skin of the AZS block (around  $500 \mu\text{m}$  from surface), the system is almost a ternary  $\text{Al}_2\text{O}_3 - \text{ZrO}_2 - \text{SiO}_2$  system as  $\text{Na}_2\text{O}$  concentration is lower than inside the core of the block. In such case, mullite can be observed as detailed by Wisniewski *et al.* [51] from 0.4 to 1.5 mm below the block surface. Experimental observations (Figure 1.5) retrieve conclusions found by Gaubil [50] after DRX measurements that adding few weight percents of  $\text{Na}_2\text{O}$  inhibits mullite phase formation.

The determination of temperature dependent properties can be divided in three parts. First, thermodynamic equilibrium state must be validated thanks to heat treatments for several days. Then, solidification path with rejection of the mullite phase is computed with the TCOX10 database. Finally, relevant temperature dependent properties are extracted at a single composition, corresponding to the global composition detailed in Table 1.3.

With a global concentration of  $\text{Na}_2\text{O}$  higher than 1.8 wt.%, thermodynamic results show that mullite phase appears at high temperature but dissolves at lower temperatures [42]. When  $\text{Na}_2\text{O}$  concentration is over 2.3 wt.%, no mullite is predicted at all during solidification, the energy of such phase is above the thermodynamic equilibrium state. In this case,  $\text{Na}_2\text{O}$  can be considered as a thermodynamic inhibitor for mullite. According to Table 1.3, only 1 wt.%  $\text{Na}_2\text{O}$  is added and no mullite is observed in DRX measurements. Transmission Electron Microscopy (TEM) observations on industrial block samples have been performed in 2021 by Pons [52]. Few nano-crystals of mullite have been detected in the glassy phase as shown in Figure 1.8. Their diameter is around 20 nm with some reaching 80 nm. Mullite growth has been completely inhibited due to the presence of  $\text{Na}_2\text{O}$ , the exact mechanism has not been determined.

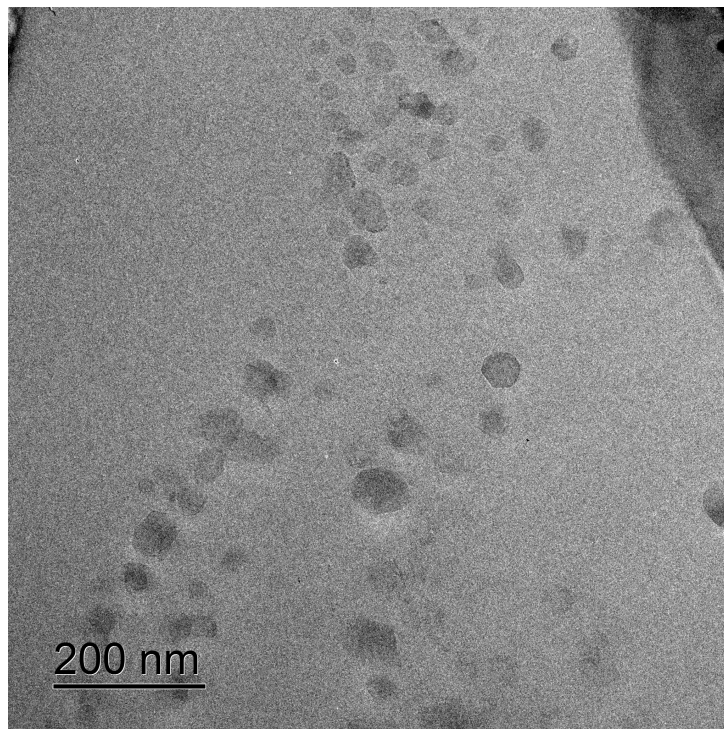


Figure 1.8: TEM observation of glassy phase at nanometric scale of a sample before heat treatment.

In order to validate the kinetic inhibitor effect of  $\text{Na}_2\text{O}$  at low concentration rate, heat treatment are performed for several days to give more time to the system to reach thermodynamic equilibrium state. Samples are thermally treated for up to 4 days at 1 400 °C (black in Figure 1.9). A second set of samples is thermally treated at 1 500 °C (green in Figure 1.9). Each spot represents one sample result. To be sure that microstructure has no impact, samples are taken closer to the skin of the block (square in Figure 1.9), with a finer microstructure, and others are taken at the center of the block (circle in Figure 1.9), with coarser microstructure. Chemical composition was measured after treatment to validate that  $\text{Na}_2\text{O}$  is still present as it is a volatile component. The averaged composition are detailed in Table 1.5. Crystalline phase proportion is determined by DRX after cooling down the sample to room temperature on D8 Endeavor equipment commercialized by BRUKER [53]. Qualitative information was retrieved with DIFFRAC.EVA software and its ICDD2016 database after acquisition ( $2\theta$ ) from  $5^\circ$  to  $80^\circ$  (step  $0.01^\circ$ ) [54], then analyzed by HighScore Plus software by Rietveld refinement [55].

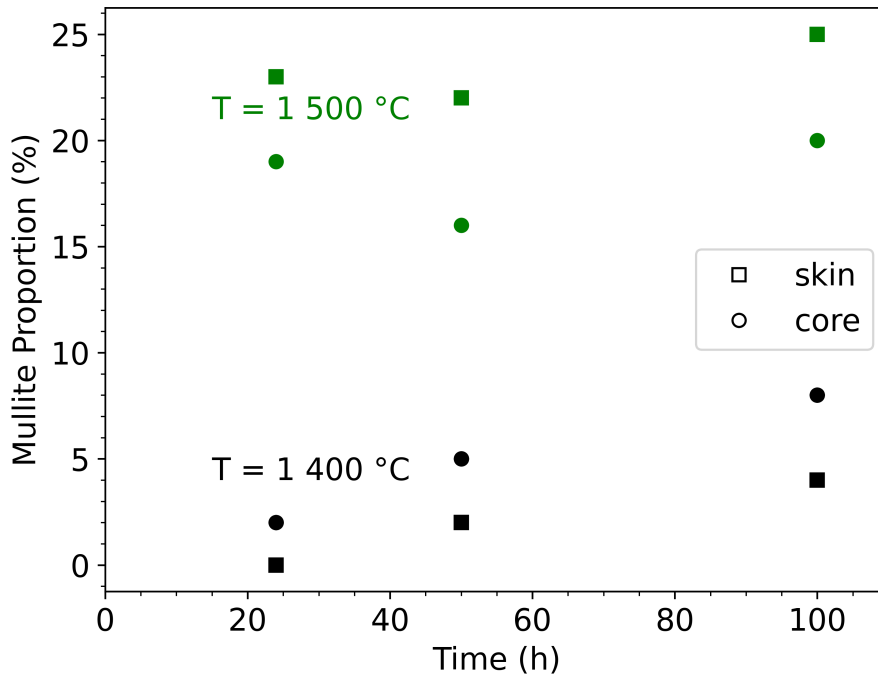


Figure 1.9: Evolution of mullite proportion measured by DRX (without measuring glassy phase proportion) over time at two holding temperatures and for samples at two locations on the block.

wt.%	$\text{Al}_2\text{O}_3$	$\text{ZrO}_2$	$\text{SiO}_2$	$\text{Na}_2\text{O}$
Average	42.2	43.9	11.6	1.04
Standard Deviation	0.9	1.3	0.3	0.03

Table 1.5: Averaged compositions of AZS41 samples after heat treatment.

Thanks to results presented in Figure 1.9, it is shown that with enough time at high temperature, mullite crystals have time to growth and their proportions for samples at 1 500 °C are close to the range predicted (above 20 wt.%) at thermodynamic equilibrium state, as presented in Figure 1.7. SEM observations, as presented in Figure 1.10, show that mullite crystals are indeed present inside the glassy phase. Their gray color is in between the light gray of silica and the darker gray of alumina (Corundum) as mullite composition contains a mixture of such components.

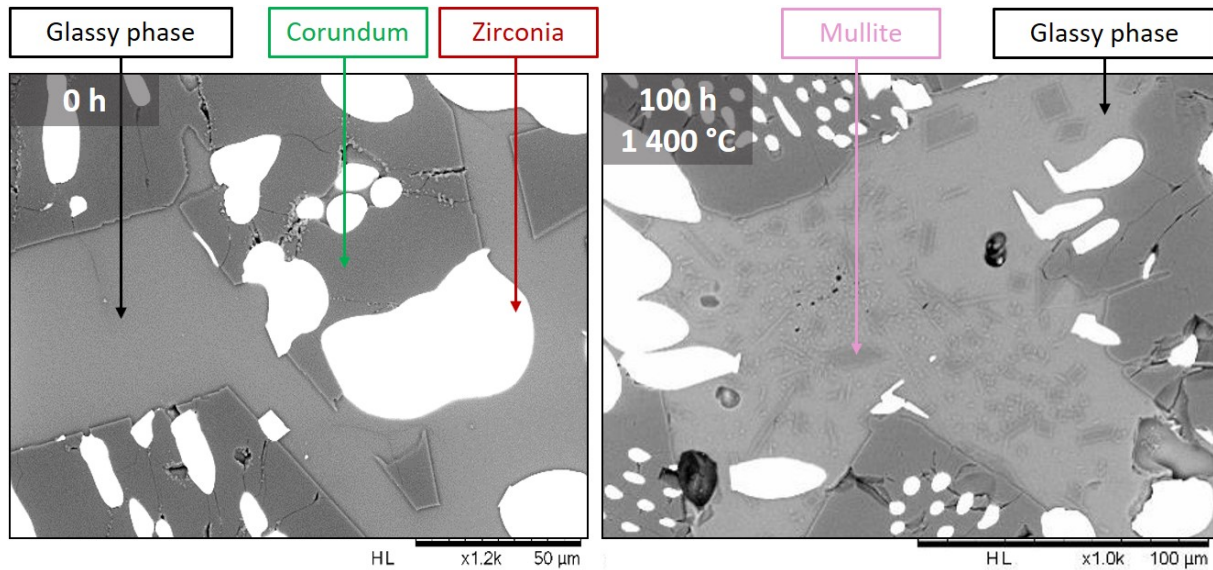


Figure 1.10: As-cast (0h) and heat treated at 1 400 °C (100h) AZS samples.

### 1.4.3 Solidification path with mullite phase rejected

To retrieve the experimental solidification path, it is therefore required to reject the mullite phase formation in Thermo-Calc<sup>®</sup> TCOX10 database. The solidification path of AZS41 is presented in Figure 1.11. A liquidus projection map for the system without mullite is presented in Figure 1.12. The solidification path gets the following steps during casting and annealing :

- the liquidus is at 1 887 °C, zirconia (tetragonal) crystals solidify; the system reaches the liquidus map at the left of the pink line in Figure 1.12;
- the eutectic valley with corundum - zirconia crystals is reached at 1 762 °C, on the pink line in Figure 1.12 between temperature points 1800 and 1710;
- solidification of the system following the eutectic pink line in Figure 1.12;
- phase transformation of zirconia from tetragonal to monoclinic takes place at 1 012 °C as explained by Yeugo-Fogaing [14];
- remaining SiO<sub>2</sub>-rich liquid solidifies as glassy phase with a composition detailed in Table 1.4. Glass-phase transition temperature is around 780 °C [12].

Lever and Gulliver-Scheill rules return similar solidification paths as the segregation coefficients in the solid phases are close to 0 for the considered system. After the validation of the solidification path, it is possible to extract the temperature dependent data such as the enthalpy, the density and phase compositions.

Having the right solidification path allows the extraction of relevant tabulations properties. Indeed, Figure 1.13 shows, for a given AZS composition, different tabulations depending on the status of the mullite phase. Figure 1.13a shows that a denser material is obtained when mullite phase is rejected compare to the density expected at the thermodynamic equilibrium state. Figure 1.13b shows, in the case mullite phase is formed, two peaks of latent heat released corresponding to the crystallization of the eutectic and the mullite phases whereas only a single peak is expected when mullite phase is rejected.

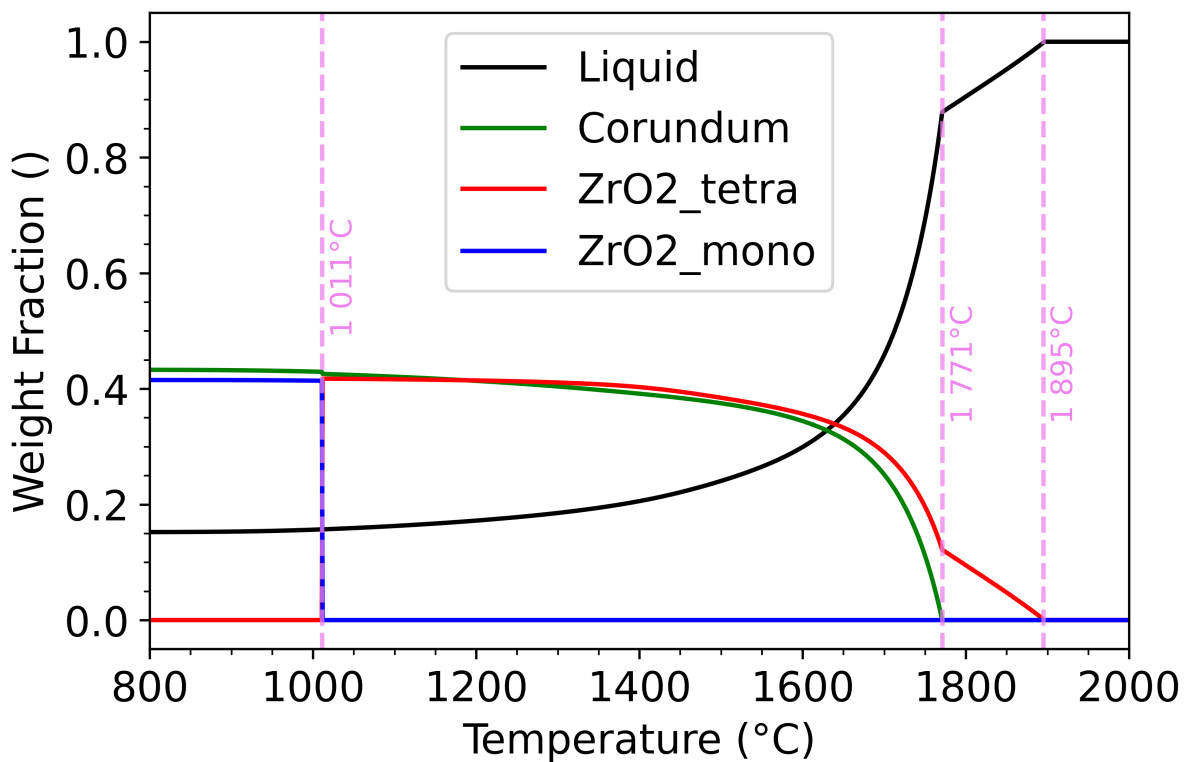


Figure 1.11: Solidification path for the AZS41 as computed by the TCOX10 thermodynamic database assuming full equilibrium with mullite phase rejected.

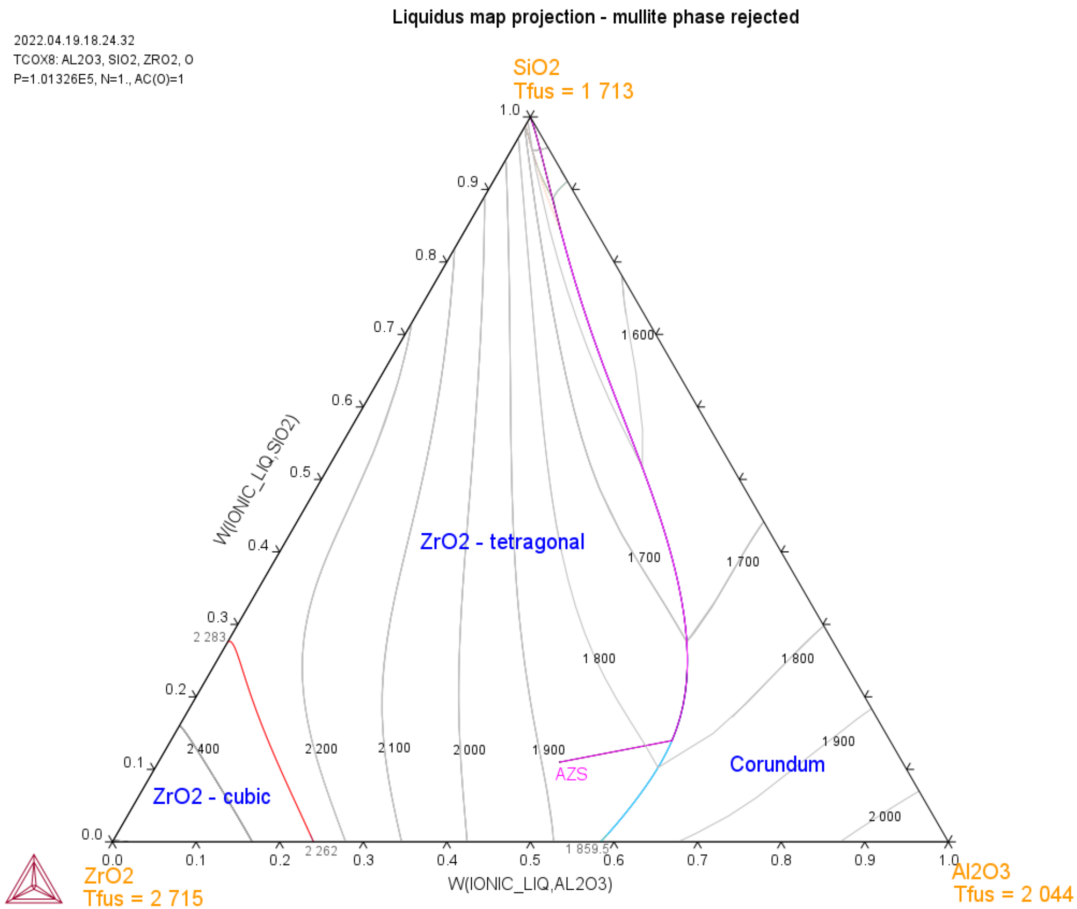


Figure 1.12: Liquidus projection map obtained with TCOX10 database with mullite phase rejected with: (blue) the phases in presence and (pink) the solidification path for AZS.

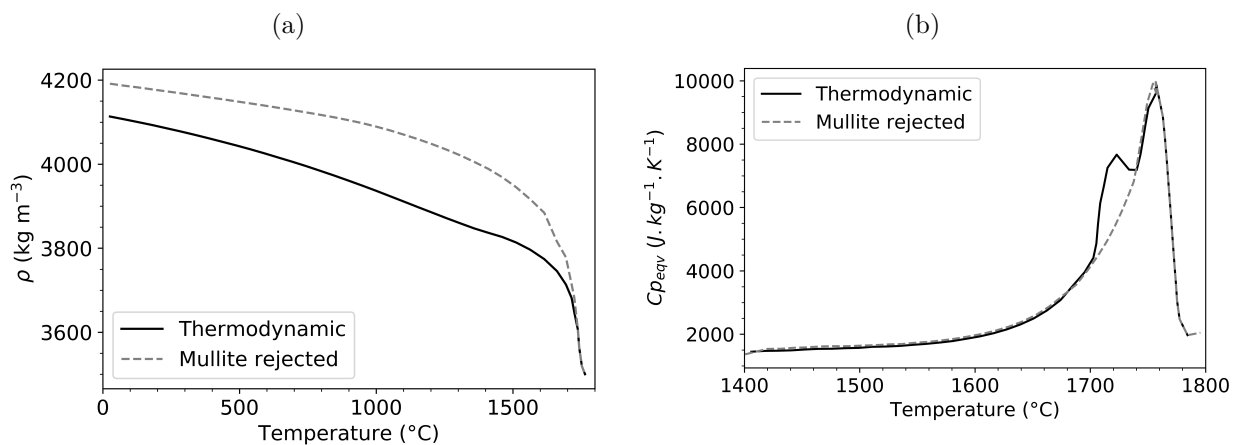


Figure 1.13: Comparison of properties extrated from TCOX10 database for a system containing mullite phase (thermodynamic equilibrium state) and the experimental one (mullite rejected) for: (a) density and (b) equivalent specific heat.

## Chapter 2

# Solidification and heat transfer modeling

### Contents

---

Résumé Chapitre 2 . . . . .	<b>22</b>
2.1 Energy conservation equations considered in THERCAST® . . . . .	<b>23</b>
2.1.1 Liquid, solid fractions and average quantities . . . . .	23
2.1.2 Heat transfer in an homogenized fixed medium . . . . .	24
2.2 Geometries and Meshes . . . . .	<b>25</b>
2.3 Initial and Boundary conditions . . . . .	<b>26</b>
2.4 Numerical settings . . . . .	<b>27</b>
2.4.1 Mesh convergence . . . . .	27
2.4.2 Time step management . . . . .	29
2.4.3 Numerical values of thermal parameters involved in the computations . . . . .	29
2.5 Thermal properties in considered domains . . . . .	<b>31</b>
2.5.1 AZS properties . . . . .	31
2.5.2 Mold and Media properties . . . . .	33
2.5.3 Bin properties . . . . .	34
2.6 Industrial temperature history recording . . . . .	<b>35</b>
2.7 Temperature history results . . . . .	<b>37</b>
2.7.1 Thermal history at AZS nominal composition . . . . .	37
2.7.2 Simulations run for another composition . . . . .	39
2.8 Impact of thermal solver on temperature history predicted . . . . .	<b>43</b>
2.8.1 User solver presentation . . . . .	43
2.8.2 Tabulation of material thermal properties . . . . .	43
2.8.3 Temperature history with this second thermal solver . . . . .	46
2.9 Conclusion about temperature predictions in AZS block with THERCAST® software . . . . .	<b>47</b>

---

## Résumé Chapitre 2

Le chapitre 2 est consacré à l'étude du refroidissement du bloc.

Le système étudié comprend le (futur) bloc AZS et sa masselotte mais aussi le moule, l'agent de calage, et la caisse de cuisson avec un fond en béton réfractaire. Dans un premier temps, l'équation de conservation de l'énergie, appliquée à tous les domaines, est présentée. Par défaut, dans THERCAST<sup>®</sup>, le solveur thermique prend en compte la chaleur spécifique équivalente (et non l'enthalpie) des matériaux au cours du refroidissement.

L'état initial et les conditions aux interfaces sont ensuite présentés. Le remplissage du moule lors de la coulée n'est pas modélisé, le domaine relatif au bloc AZS commence entièrement rempli à 1900 °C alors que les autres domaines sont à température ambiante. La convergence en fonction du maillage et du pas de temps est vérifiée pour assurer la cohérence des résultats obtenus dans les simulations numériques. Pour limiter le temps de calcul, le pas de temps est adapté à la variation de température au cours de l'incrément. Ainsi, au démarrage il est restreint avec une valeur initiale de 5 s avant d'augmenter progressivement lorsque le refroidissement est plus lent. Une autre partie est consacrée à la description des propriétés thermiques appliquées dans les simulations. La densité, la chaleur spécifique et la conductivité thermique, pour les différents domaines, sont tabulées avec la température. Des ajustements au niveau de la conductivité thermique du moule et du médium ont été réalisés.

Des coulées industrielles ont été suivies à l'aide de 18 thermocouples. Les thermocouples sont installés dans ou au contact du moule, à différentes hauteurs du bloc et de la masselotte. Des capteurs numériques sont positionnés au même endroit dans les simulations. L'histoire thermique simulée peut alors être comparée avec les mesures. Le refroidissement de deux compositions d'AZS a été simulé et comparé aux enregistrements. Les histoires thermiques simulées au milieu et en haut du bloc suivent très bien les valeurs expérimentales. Pour la masselotte, les résultats numériques sont moins pertinents.

Une dernière partie est consacrée à l'intégration d'un second solveur thermique issu de la librairie CIMLib<sup>®</sup> qui prend en compte les propriétés de chacune des phases présentes au cours du refroidissement et non une chaleur spécifique équivalente globale pour l'AZS. L'outil PATH de PhysalurgY<sup>®</sup> a été utilisé pour extraire de la base de données thermodynamique TCOX10 les évolutions de l'enthalpie et de la densité des phases liquide, zircon et corindon avec la température et la composition en alumine, silice et oxyde de sodium. L'histoire thermique simulée avec ce nouveau solveur est cohérente sur les premières heures seulement. Une nouvelle étape d'ajustement des paramètres thermiques serait nécessaire pour retrouver les tendances expérimentales. Les capteurs situés au niveau de la masselotte présentent à nouveau l'histoire thermique la plus éloignée des données expérimentales.

In the previous chapter, the solidification path was provided assuming thermodynamic equilibrium state. This means that, at a given temperature, the phase proportions and their compositions can be defined. Modeling of the solidification process is a hard task requiring to write balance equations about heat and mass transfer with phase change. Since the material will have an heterogeneous microstructure, modeling requires to write balance equations using a homogenization technique. This method is grounded on the consideration of balance equations in a Representative Volume Element (RVE) as presented in [56, 57]. In this chapter, the AZS domain is thus considered as a unique material with properties depending on the fractions of phases. The motion of the liquid phase is first ignored and hence shrinkage flow is not modeled. This level of modeling is presented in § 2.1.

THERCAST® is a multi-domain 3D finite element computation software. This chapter focuses on heat transfer during casting and annealing (after pouring). The system is presented with the geometries and numerical models considered at the interfaces. The materials properties involved are summed up in § 2.5. Temperatures recorded at a Saint Gobain SEPR plant are compared with the simulated temperature history. To further optimize temperature predictions, some options were considered. Among them, the consideration of a second thermal solver is presented in § 2.8.

## 2.1 Energy conservation equations considered in THERCAST®

### 2.1.1 Liquid, solid fractions and average quantities

Before writing the heat balance equation, few definitions have to be presented. First, equations are written in a RVE sufficiently small to consider the medium as a continuum but sufficiently large to be representative which means containing the liquid and several solid phases, the latter being combined into a global solid medium [56, Chap. 4].

As mentioned by Ishii and Hibiki [58] and Ni and Beckermann [59] and Sun [60], the main difficulties in description of multi-phase systems are the presence of multiple moving interfaces and the property discontinuities across those. But, in the multi-phase system, some of these rules are not verified like the average of the derivative which is different from the derivative of the average [61]. Here, only the useful relations are presented.

If  $\Delta V$  is the volume of the RVE domain  $\Omega$ , the liquid and the equivalent global solid phase occupy  $\Delta V_l$  and  $\Delta V_s$  volumes, respectively. Assuming that the interfaces between phases are sharp interfaces, i.e. without volume, the following relation is obtained:

$$\Delta V = \Delta V_l + \Delta V_s \quad (2.1)$$

The volume fractions of liquid and solid phases are simply defined by

$$g_l = \frac{\Delta V_l}{\Delta V}, \quad (2.2)$$

$$g_s = \frac{\Delta V_s}{\Delta V}, \quad (2.3)$$

with using (2.1),  $g_l + g_s = 1$ .

Using a volume averaging method, the average value of a generic scalar field  $\psi$  is defined by

$$\langle \psi \rangle = \frac{1}{\Delta V} \int_{\Omega} \psi dV. \quad (2.4)$$

If  $\Omega_l$  is the restriction of the domain in which only the liquid phase is present and  $\Omega_s$  the same restriction for the solid phases such that  $\Omega = \Omega_l \cup \Omega_s$ , indicator functions are then defined by

$$\phi_l = \begin{cases} 1 & \text{if } x \in \Omega_l, \\ 0 & \text{if } x \notin \Omega_l, \end{cases} \quad (2.5)$$

and

$$\phi_s = \begin{cases} 1 & \text{if } x \in \Omega_s, \\ 0 & \text{if } x \notin \Omega_s, \end{cases} \quad (2.6)$$

The phase average in phase  $\alpha$  of a scalar field  $\psi$  is then defined by (2.7) with  $\alpha$  equal to  $l$  or  $s$ :

$$\langle \psi \rangle_\alpha = \frac{1}{\Delta V} \int_\Omega \psi \phi_\alpha dV, \quad (2.7)$$

The intrinsic average in the phase  $\alpha$  is defined as (2.8) with the definition of  $g_\alpha$  given in (2.2):

$$\langle \psi \rangle_\alpha = \langle \psi \rangle_\alpha / g_\alpha = \frac{1}{\Delta V_\alpha} \int_\Omega \psi \phi_\alpha dV, \quad (2.8)$$

For instance, applied to the density,  $\rho$ ,  $\langle \rho \rangle_\alpha$  corresponds to the partial density while  $\langle \rho \rangle_\alpha$  is similar to  $\rho_\alpha$  when  $\rho_\alpha$  is uniform over  $V_\alpha$ .

### 2.1.2 Heat transfer in an homogenized fixed medium

Only heat transfer is first considered. AZS block is taken as a mixture of phases (solids & liquid) without motion (no shrinkage and no convection in the domain). As shown in [56, Chap. 6], the energy balance in enthalpy form writes:

$$\frac{\partial \langle \rho h \rangle}{\partial t} = \nabla \cdot (\langle \lambda \rangle \nabla T), \quad (2.9)$$

with  $h$  the enthalpy per unit mass and  $\lambda$  the thermal conductivity. The averages  $\langle \rho h \rangle$  and  $\langle \lambda \rangle$  are defined by [56, Chap. 6]

$$\langle \rho h \rangle = g_l \langle \rho \rangle_l \langle h \rangle_l + g_s \langle \rho \rangle_s \langle h \rangle_s, \quad (2.10)$$

$$\langle \lambda \rangle = g_l \langle \lambda \rangle_l + g_s \langle \lambda \rangle_s. \quad (2.11)$$

In the RVE, it is possible to neglect the energy transfer due to pressure variation ( $\frac{\partial P_\varphi}{\partial t} + \nabla P_\varphi \cdot \mathbf{v}$ ). No energy source term is considered as there is no chemical reaction or Joule effect. The energy due to the deformation power ( $\sigma_\varphi : \dot{\epsilon}_\varphi$ ) is also neglected [57].

To solve equation (2.9), thermodynamic data obtained by ThermoCalc<sup>®</sup> is used. As thermodynamic equilibrium state is assumed locally in each point of  $\Omega$ ,  $\langle \rho h \rangle$  is only function of  $T$ . PhysalurgY<sup>®</sup> uses the TCOX10 database in Thermo-Calc<sup>®</sup> to tabulate the liquid phase fraction and the equivalent specific heat of the system (deduced from the derivative of  $\langle \rho h \rangle$  with temperature) [43]. Properties used by the default thermal solver in THERCAST<sup>®</sup> are detailed in § 2.4.3. Then, in § 2.8, the enthalpy and density for the three phases present at high temperature in Figure 1.11 are tabulated.

The following hypotheses are further considered in numerical simulations in THERCAST<sup>®</sup>:

- The average volumetric enthalpy is divided into two components : the average specific heat and the volumetric latent heat of solidification  $l \rightarrow s$  ( $(\rho L)^{l/s}$ ) [57, Chap. 5].

$$\langle \rho h \rangle = g_l \int_{T_0}^T (\rho c_p)_l d\theta + g_s \int_{T_0}^T (\rho c_p)_s d\theta + g_l (\rho L)^{l/s} = \int_{T_0}^T \langle \rho c_p \rangle d\theta + g_l (\rho L)^{l/s} \quad (2.12)$$

- $\langle \rho c_p \rangle = g_l \langle (\rho c_p)_l \rangle + g_s \langle (\rho c_p)_s \rangle$  considering the solid phase  $s$  as a global solid medium that combines corundum and zirconia domains :  $g_s \langle (\rho c_p)_s \rangle = g_{zirconia} \langle (\rho c_p)_{zirconia} \rangle + g_{corundum} \langle (\rho c_p)_{corundum} \rangle$ .
- The equivalent specific heat per unit of volume can be defined [16] as (2.13). Equation (2.12) writes then as (2.14):

$$\langle \rho c_p \rangle_{eq} = \left( \frac{\partial \langle \rho h \rangle}{\partial T} \right)_P = \langle \rho c_p \rangle + (\rho L)^{l/s} \frac{dg_l}{dT} \quad (2.13)$$

$$\langle \rho h \rangle = \int_{T_0}^T \langle \rho c_p \rangle_{eq} d\theta \quad (2.14)$$

In THERCAST<sup>®</sup>, only the AZS domain considers the phase transformation from liquid to solid. In all the other parts, only the heat transfer is considered. The energy conservation equation as considered in THERCAST<sup>®</sup> with fixed phases writes:

$$\langle \rho c_p \rangle_{eq} \frac{\partial T}{\partial t} - \nabla \cdot (\langle \lambda \rangle \nabla T) = 0 \quad (2.15)$$

## 2.2 Geometries and Meshes

Due to symmetries, only a quarter of the whole system is considered. Pouring operation, detailed in Figure 1.3, consisting in pouring the molten AZS in the mold in a couple of minutes is not modeled here. Only the annealing stage is considered. The annealing simulation involves six domains, shown in Figure 2.1, with the mesh parameters detailed in Table 2.1:

- AZS block (gray color in Figure 2.1) with the geometry for which casting was recorded (shared by Saint Gobain SEPR plant);
- Mold (blue color) made of sand agglomerated with resin, with walls 7 cm thick and the bottom 8 cm thick;
- Insulating media (sand color) that controls heat exchanges with the environment, by insulating the block from plant environment and slowing its cooling down;
- Concrete base that holds the mold and the media (brown color);
- Steel bin (red color) that contains the entire system and allows the system to be moved in the plant.

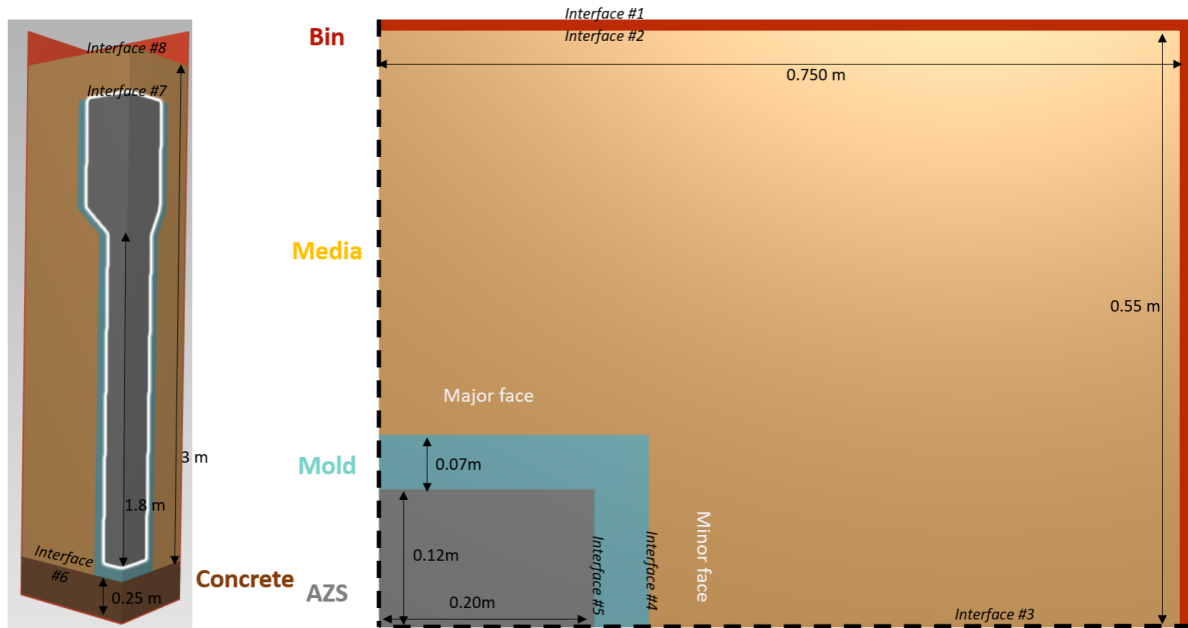


Figure 2.1: Geometries considered in THERCAST® simulations with the dimensions of the different domains and the interfaces numbering.

Domain	AZS	Mold	Media	Concrete	Bin	Total
Number of tetragonal meshes	450 974	391 664	2 423 688	205 889	240 734	3 712 949
Mesh size (mm)	12	12	12-25	12-25	25	

Table 2.1: Mesh sizes and repartition of the 3 712 949 elements considered.

## 2.3 Initial and Boundary conditions

### Initial conditions

Upon casting (see Figure 1.3), the mold is filled with molten AZS during about 2 min 30 s. This step is not considered. In numerical simulations, the AZS block is initially completely filled, entirely liquid, at temperature  $T_0$ . The mold and all the other parts are initially at room temperature,  $T_{ext}$ , neglecting pre-heating occurring during casting itself as it will only reduce the initial quenching.

### Thermal boundary conditions with the exterior of the domain

The external faces of the bin and the upper face of the media domain (interfaces #1 and #8 in Figure 2.1) are in contact with the external environment. According to Costes [19], the thermal boundary conditions can be written as follows:

$$-\lambda \nabla T \cdot \mathbf{n} = h_{conv}(T - T_{ext}) + \epsilon_r \sigma_B (T^4 - T_{ext}^4), \quad (2.16)$$

in which  $h_{conv}$  is the conducto-convective heat transfer coefficient,  $\epsilon_r$  the radiative emissivity of the material in contact with the exterior,  $\sigma_B$  the Stefan-Boltzmann constant,  $T_{ext}$  the far-field exterior temperature and  $\mathbf{n}$  the outward normal vector of the interface.

### Interfaces between two objects

In the general flowchart developed in THERCAST, the balance equations are solved separately in each domain. The thermal balance at each interface between a domain  $i$  and a domain  $j$  has to be written. Under a perfect contact, the thermal flux through each interface must be conserved. In presence of non-perfect contact, a thermal resistance appears. In the general case, the boundary condition is written as follows:

$$\lambda_i \nabla T_i \cdot \mathbf{n} = \lambda_j \nabla T_j \cdot \mathbf{n}, \quad (2.17)$$

$$\lambda_i \nabla T_i \cdot \mathbf{n} = h_{ij} (T_j - T_i), \quad (2.18)$$

with  $h_{ij}$  is the heat transfer coefficient between the two domains  $i$  and  $j$  and  $\mathbf{n}$  is the unit normal directed toward the domain  $j$ .

Interfaces not in contact with the AZS block have the same heat transfer coefficient while those in contact with the AZS block, labeled #5 and #7 in Figure 2.1, have another value given in Table 2.3.

### Symmetry conditions

Two planes of symmetries (interface #3) are defined as only a quarter of the block is modeled. Such plane implies adiabatic conditions for heat transfer computations.

## 2.4 Numerical settings

### 2.4.1 Mesh convergence

Before tests at industrial scale, the numerical convergence (mesh and time step) is investigated. To limit the CPU time, tests are performed on a 100 mm high slice. Top and bottom faces are adiabatic. Four sensors were located at locations identified by the red dots in Figure 2.2 corresponding to thermocouple location around the block during an industrial casting that has been recorded in temperature. The constitution of the different domains is identical to the one used in Figure 2.1 with AZS in gray, mold in blue, media in sand, and bin in red color. Computations simulate the annealing of the slice during the first 9 hours. The time step is set at 0.5 s for all computations.

Test #	AZS & Mold	Media	Bin
Coarse	20	20-60	60
Fine	15	15-30	30
Finest	5	5-20	20

Table 2.2: Mesh sizes (in mm) tested to reach numerical convergence, using a time step of 0.5 s.

Three computations are done with different meshes as indicated in Table 2.2. Since none analytical solution is known, the numerical solution obtained with the finest mesh is considered as the reference solution. For the same CPU configuration (architecture and number nodes), the finer mesh is, the longer computation is. More than 1% error is only observed during a short period of time when large variation of enthalpy takes place due to the solidification process. The test with the fine mesh is four times faster than the reference for an acceptable relative temperature error as shown in Figure 2.3. Temperature outputs with the coarse mesh show strong variations compare to the reference mesh.

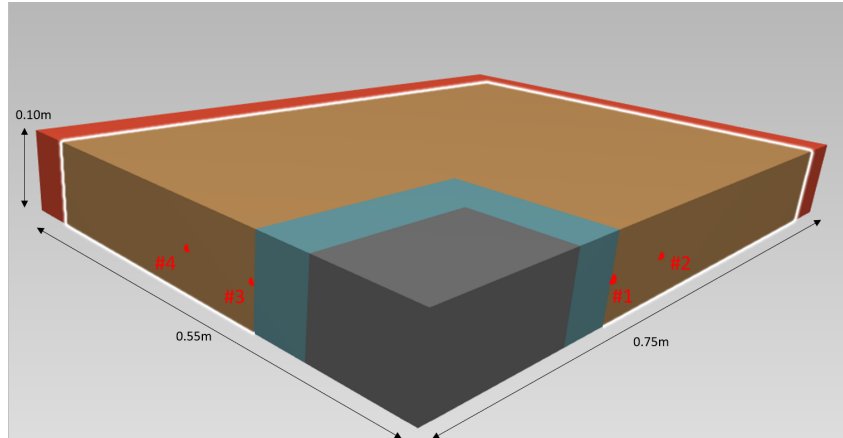


Figure 2.2: Slice of material used to validate the mesh and time step convergences with in red the four sensors used to validate the convergence.

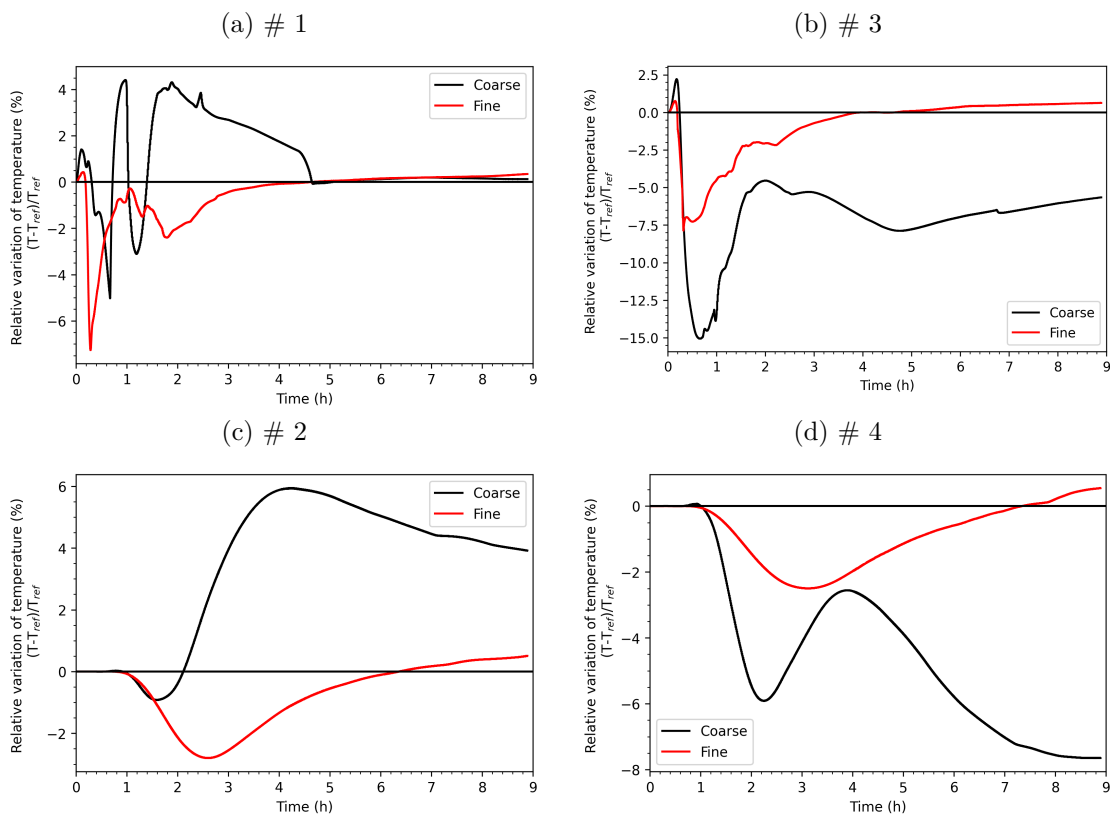


Figure 2.3: Comparison of temperature outputs over time with reference mesh size using (black) a coarse mesh size and (red) a fine mesh size for the four sensors detailed in Figure 2.2: (a) #1 at the minor face close to the mold, (b) #3 major face close to the mold, (c) #2 minor at 10 cm from the mold, (d) #4 major at 10 cm from the mold.

The mesh sizes considered in computations when the block is at industrial scale (see Table 2.1) are slightly smaller than the one considered in the test with the fine mesh in the convergence test. This is done to avoid checking again mesh convergence when a parameter is slightly modified at industrial block scale.

### 2.4.2 Time step management

The casting and annealing of a block spends a couple of weeks. At the beginning, just after the pouring, the heat release of the hot AZS liquid leads to the enhancement of the temperature in the mold and in the annealing media. A time step around 2 s is required to keep a relevant map of temperature variations. After 1 day, temperature decreases with an exponential trend-line. However, keeping the same time step would imply longer computation duration without improving the relevance of numerical outputs. An adaptive time step is therefore considered to adjust the duration of the time step depending on the temperature variations [62].

An "initial time step" is defined. Then, at each node, the absolute temperature difference between two successive time steps is determined as follows:  $|T_n - T_{n-1}|$ . A minimal and maximal variation of temperature during an increment are defined, respectively  $\Delta_{\min}$  and  $\Delta_{\max}$ . If the condition in (2.19) is valid for the entire system, the time step is kept, otherwise, a new time step is calculated as in (2.20):

$$\Delta_{\min} < \max(|T_n - T_{n-1}|) < \Delta_{\max} \quad (2.19)$$

$$\Delta t_n = (0.2\Delta_{\max} + 0.8\Delta_{\min}) \cdot \frac{\Delta t_{n-1}}{\max(|T_n - T_{n-1}|)} \quad (2.20)$$

By default, the initial time step is  $1 \times 10^{-3}$  s and the temperature gap is 2-5°C. Over the first day of annealing, temperature outputs obtained with such default settings present less than 2 % of variations with outputs considering an initial time step = 5 s and a temperature gap using  $\Delta_{\min} = 10^\circ\text{C}$  and  $\Delta_{\max} = 20^\circ\text{C}$ . The limit of the time step value is set at 120 s to avoid too wide time step at the end of the cooling down. Those new settings, given in Table 2.3, implies faster results. For an industrial scale block, to compute the first 24 h of annealing, simulation runs with an adaptive time step in 1 h 4 min 48 sec considering 32 cores in a processor Intel(R) Xeon(R) Gold 6148 CPU @ 2.40GHz.

### 2.4.3 Numerical values of thermal parameters involved in the computations

$T_0$	1 900 °C
$T_{ext}$	20 °C
$h_{conv}$	3 W m <sup>-2</sup> K <sup>-1</sup>
$h_{ij}$ with $i,j \neq \text{AZS}$	10 <sup>3</sup> W m <sup>-2</sup> K <sup>-1</sup>
$h_{AZS/Media}$	3 W m <sup>-2</sup> K <sup>-1</sup>
$h_{AZS/Mold}$	56 W m <sup>-2</sup> K <sup>-1</sup>
Initial time step	5 s
$\Delta_{min}$	10 °C
$\Delta_{max}$	20 °C

Table 2.3: Numerical values of different parameters considered in THERCAST<sup>®</sup> thermal computations.

$T_0$  is an approximation of the initial temperature for the AZS material.

Globally, after a stage of heating, the mold and annealing materials cold down. A macroscopic balance of energy can be done as described in the textbook of Bird et al. [63]. By defining the volume average, temperature on the whole domain writes as follows:

$$\langle T \rangle = \frac{1}{V} \int_{\Omega} T dV, \quad (2.21)$$

the macroscopic energy balance writes:

$$\frac{d\langle T \rangle}{dt} = -\frac{h_{\text{conv}} S}{\langle \rho C_p \rangle V} (\langle T \rangle - T_{\text{ext}}). \quad (2.22)$$

In this equation,  $h_{\text{conv}}$  is the heat transfer coefficient between the domain and the surrounding air,  $S$  the external surface in contact with air,  $\langle \rho C_p \rangle$  the volume average of the  $\rho C_p$  over the entire system and  $T_{\text{ext}}$  the far field temperature of air.

By reducing the temperature under the form

$$\theta(t) = \frac{\langle T \rangle - T_{\text{ext}}}{T_0 - T_{\text{ext}}}, \quad (2.23)$$

and by defining the characteristic cooling time as follows

$$\tau = \frac{\langle \rho C_p \rangle V}{h_{\text{conv}} S}, \quad (2.24)$$

the energy balance becomes

$$\frac{1}{\theta} \frac{d\theta}{dt} = -\frac{1}{\tau}. \quad (2.25)$$

By this simple analysis, the logarithmic derivative of the average temperature is simply a negative constant meaning that the temperature decreases exponentially with the time. As it will be described later, in § 2.6, after 10 h of annealing, the temperature sensors follow an exponential trend in agreement with the simple model presented above. The opposite logarithmic derivative of the temperature, written  $\alpha$ , varies from  $3.5 \times 10^{-6} \text{ s}^{-1}$  to  $7.5 \times 10^{-6} \text{ s}^{-1}$  with a mean at  $5.7 \times 10^{-6} \pm 1.2 \times 10^{-6} \text{ s}^{-1}$ . These coefficients have been found by regression for which a mean correlation coefficient  $R^2$  is above 0.98.

Using these data, the heat transfer coefficient  $h_{\text{conv}}$  can be estimated by

$$h_{\text{conv}} = \frac{\langle \rho C_p \rangle V}{S \alpha}. \quad (2.26)$$

The whole volume is equal to  $5.36 \text{ m}^3$  and external surface in contact with air,  $S$ , is  $20.2 \text{ m}^2$ . The value of  $\langle \rho C_p \rangle$  has been estimated by volume average for all parts of the domain by taken the tabulated data of the density and specific heat capacity at  $600^\circ\text{C}$ . The value is then equal to  $1.42 \times 10^6 \text{ J m}^{-3} \text{ K}^{-1}$ .

With such mean parameters,  $h_{\text{conv}} = 2.15 \text{ W m}^{-2} \text{ K}^{-1}$ . If only the vertical faces are considered for heat transfer by convection, the surface to consider drops at  $16.9 \text{ m}^2$ . Sensors located at the middle height of the block get an exponential factor closer to  $7 \times 10^{-6} \text{ s}^{-1}$ . In this case,  $h_{\text{conv}} = 3.16 \text{ W m}^{-2} \text{ K}^{-1}$ . In the computations,  $h_{\text{conv}}$  is defined constant during the entire annealing and over the height of the block.  $h_{\text{conv}}$  is defined equal to  $3 \text{ W m}^{-2} \text{ K}^{-1}$ .

## 2.5 Thermal properties in considered domains

Properties are considered for a system at a single composition. As presented in the previous chapter, some AZS properties can be extracted from the TCOX10 database of Thermo-Calc<sup>®</sup> to get tabulations over temperature. Other properties, for the AZS block and for the other domains, are determined experimentally or retrieved from literature. All properties are summed-up in Table 2.4 and the corresponding figures.

Domain	AZS	Mold	Media	Concrete	Bin
Thermal conductivity $\text{W m}^{-1} \text{K}^{-1}$	Fig. 2.4	Fig. 2.7	0.9	1.28	Fig. 2.10
Specific Heat $\text{J kg}^{-1} \text{K}^{-1}$	Fig. 2.5	Fig. 2.9	Fig. 2.9	881.82	Fig. 2.10
Density $\text{kg m}^{-3}$	Fig. 2.6	1 600 [64]	727 [65]	2 200	Fig. 2.10
Emissivity	0.9	0.75	0.75	0.9	0.8

Table 2.4: Thermal properties for the different materials.

### 2.5.1 AZS properties

#### Thermal conductivity

Thermal conductivity is presented in Figure 2.4. It was initially detailed in [12], and tests have been performed since at Saint Gobain Research Provence to confirm such results with the reference considered in this study. Its value decreases with temperature until 800°C, close to the glass transition temperature of the glassy phase, before increasing again. In this first approach, in which only the heat transfer by conduction is accounted for, the heat transport by the liquid convection at high temperature can be artificially added by increasing the thermal conductivity. This is why the thermal conductivity is set at  $15 \text{ W m}^{-1} \text{K}^{-1}$  at the liquidus temperature equal to 1875°C. Such optimization was necessary to better fit the experimental temperature history.

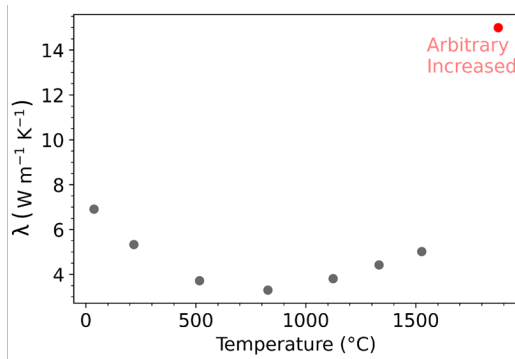


Figure 2.4: AZS thermal conductivity from [12] for AZS with an extra value at 1 875°C to compensate the heat exchange by liquid convection neglected in the present simulations.

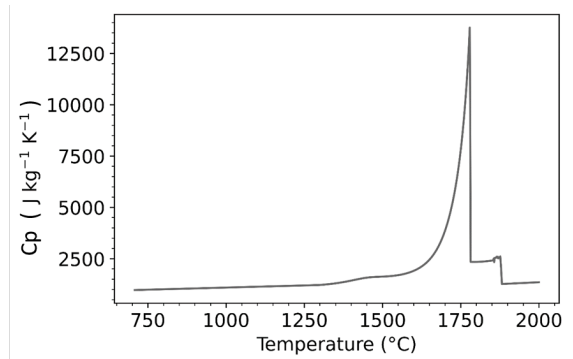


Figure 2.5: AZS specific heat from Thermo-Calc<sup>®</sup> for AZS composition system with mullite phase rejected considering Gulliver-Scheil rule for solute diffusion.

#### Specific heat capacity

Specific heat capacity tabulation is extracted from the TCOX10 database in Thermo-Calc<sup>®</sup>,

with mullite phase rejected as detailed in Chapter 1. Such extraction was performed thanks to the PY<sup>®</sup> library [43] with the tool PY/PATH, it is possible to extract the phase distribution and the specific heat of the AZS material with a temperature increment equal to 1 °C. Tabulations obtained with PY/PATH combine specific heat of each phase with latent heat released during the solidification of crystalline phases. Such value, called equivalent specific heat, is presented in Figure 2.5 and has the advantage of a single tabulation over temperature which summarizes the thermal stages from casting to annealing up to room temperature.

### Density

Density of the entire system can be determined experimentally and thanks to the TCOX10 database as in Figure 2.6. Experimental data are plotted with dot symbols and the solid line corresponds to the density extracted from ThermoCalc (TCOX10 database). At temperatures below 1 500°C, experimental tests are performed by dilatometry on a solid sample. Above 1700 °C CEMHTI lab (Orléans, France) performed measurements considering the variations of the shadow area of liquid, obtained by heating (thanks to lasers) pills in atmospheric levitation. Five samples, with a mass around 20 mg, are collected by cracking an AZS cube with an edge length of 50 mm. Density obtained by Thermo-Calc<sup>®</sup> is extracted every Celsius, as for the specific heat tabulation, for a system at the standard composition detailed in Table 1.3. Some numerical artifacts can be observed for a couple of temperature values.

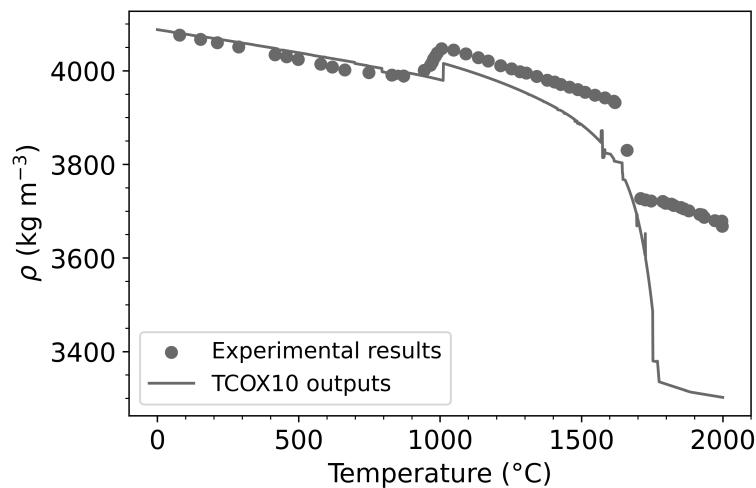


Figure 2.6: AZS density from experimental measurements and from TCOX10 database predictions.

As detailed in previous PhD thesis on high zirconia refractory ceramics [5, 11–14, 66] and according to Heidrich [48], zirconia phase transition is a reversible phase transition (from tetragonal to monoclinic crystal family) occurring at around 1 000°C during the cooling down. This martensitic transition imposes a dilatation of zirconia crystals of 4 vol%. Such expansion leads to a global volume expansion of around 1.5 vol% that can lead to cracks according to Cockcroft [49]. Zirconia phase transition is considered in numerical computations as a step in density tabulations around 1 000°C as shown in Figure 2.6.

Measurements at low temperatures are close to thermodynamic data. Both methods show the expansion of Zirconia phase transition. At high temperatures, measured density seems shifted upward compared to the thermodynamical data with a similar slope over temperature. The slope is obtained by the variations of the shadow surface, that is well estimated (same slope as theoretical value). The value of the density depends on the initial density value obtained from

the shadow surface (to retrieve the volume), the temperature measured and the mass considered. There is almost no variations between the five density evolutions measured.

Due to the significant variations between numerical predictions by TCOX10 database and experimental results, a new sample from the same cube was taken and measured. Its results are in the same order of magnitude of previous samples and data treatment method was checked. In THERCAST<sup>®</sup>, the experimental data have been considered. A comparison of temperature outputs using the two densities at high temperature (experimental and thermodynamic) has not been performed.

## 2.5.2 Mold and Media properties

### Composition of mold and media

Mold is composed of sand grains, with a diameter below 500  $\mu\text{m}$ , that are mainly composed of silica and are agglomerated by resin. Such polymer resin burns during the first hours of annealing. Mold properties are tabulated over temperature during the entire annealing (from casting to room temperature), without mold degradation consideration. Mold geometry remains constant and impenetrable for other domains.

Media is mainly composed of silica and alumina. Its shape goes from fine powder (up to 5  $\mu\text{m}$ ) to coarse grains (5-18 mm) depending on the thermal insulation properties expected and the mechanical resistance required for media as it holds the mold (and liquid AZS) during casting. Impurities inside the gravels used as annealing media give it a color from cream to dark-brown.

### Thermal conductivity

Thermal conductivity has been determined experimentally at Saint-Gobain Research labs. However, to better fit experimental temperature history recorded in the mold, it has been required to adjust arbitrarily the mold and media thermal conductivity. The values considered in THERCAST<sup>®</sup> can be more than twice the experimental one. Properties considered are presented in Figure 2.7 and Figure 2.8. Such increases were required to fit temperature outputs. For the media, it can be related to air convection and thermal radiation in these domains that can occur during the controlled cooling stage. At high temperature, the mold is burning and its combustion is not modeled. The increased values for the mold can be related to the heat release during the mold degradation.

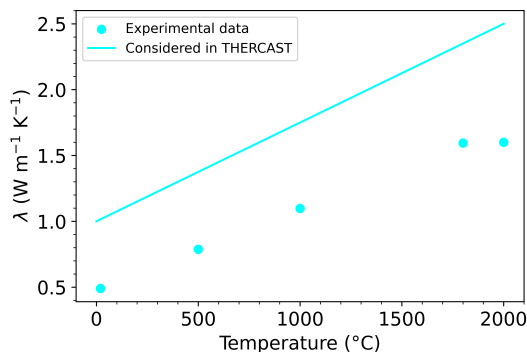


Figure 2.7: Mold thermal conductivity from experimental results (dots) and values considered for relevant numerical computations of temperature (line).

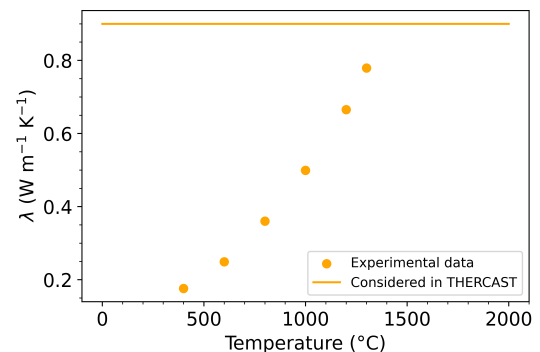


Figure 2.8: Media thermal conductivity from experimental results (dots) and values considered for relevant numerical computations of temperature (line).

### Specific heat capacity

The properties for media domain is the average value of the granular system considered. Specific heat capacity can be determined from its composition and the size of the particle (compacity) [5]. Mold is single-use as resin disintegrates at high temperatures. Such combustion is not considered and the mold specific heat is related to sand specific heat, as reported in Figure 2.9.

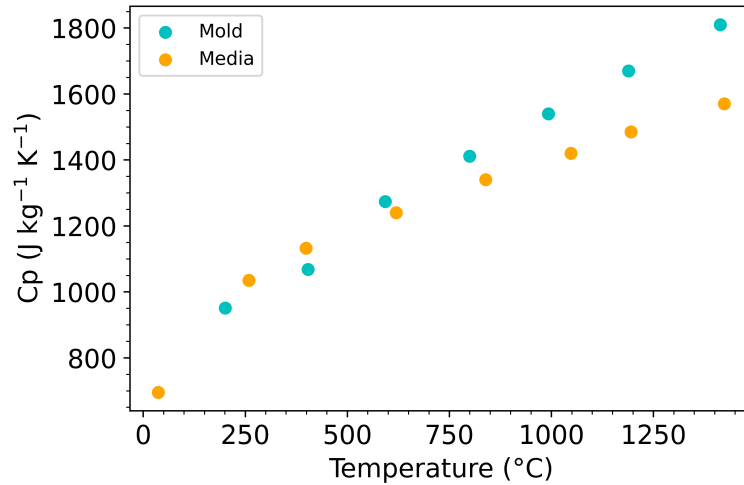


Figure 2.9: Specific heat capacity considered in simulation for mold and media.

### Density

For mold and media, density is considered as constant with temperature. Values have been determined experimentally in Saint Gobain labs. For mold, density is 1 600 kg m<sup>-3</sup> and for media 727 kg m<sup>-3</sup>.

### 2.5.3 Bin properties

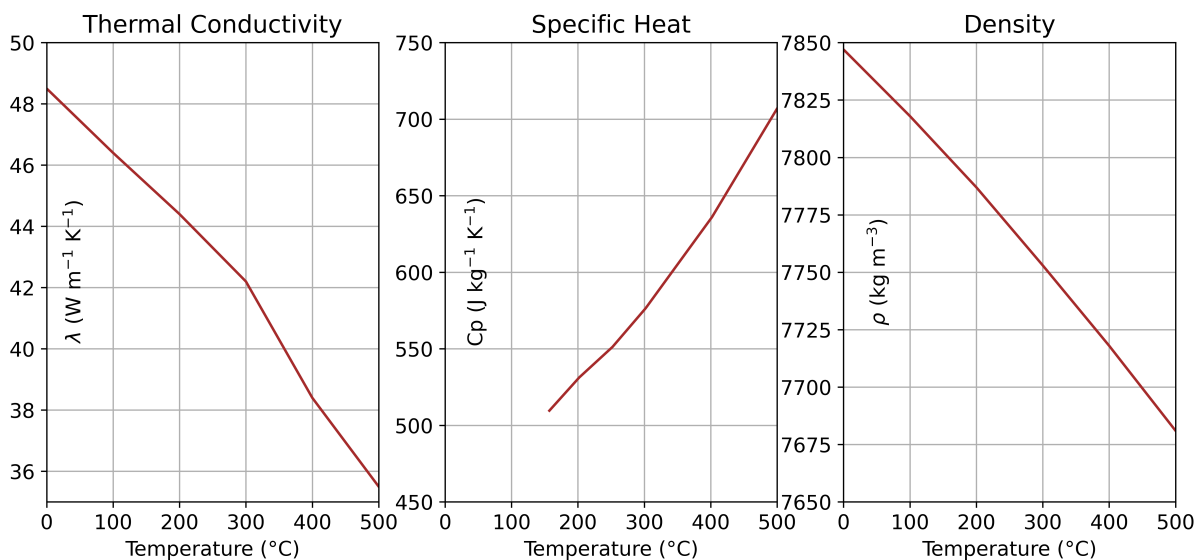


Figure 2.10: Properties of the bin in steel that contains the entire system during annealing.

The bin that contains the system is in steel. A material data sheet called "Steel" is implemented in THERCAST®. Such file was considered for the last domain of the industrial system. Only properties for temperatures below 500 °C are presented in Figure 2.10 as bin temperature stays "cold" during annealing.

## 2.6 Industrial temperature history recording

During industrial casting, it is not possible to record temperature inside the AZS itself as liquid temperature is too high for available sensors. In the mold, temperature stays in measurable range and it is therefore possible to record its temperature during an industrial block casting. Such data serve to validate the mold temperature history predicted by numerical simulations. Temperature evolution in AZS will be consequently considered as relevant and be validated for mechanical consideration.

Before a casting at SEPR Saint-Gobain plant, 18 thermocouples had been installed for the entire cooling duration. Sensors are protected inside a thin alumina shell that crosses straight (horizontally) the bin and media. Temperature acquisition is done each 15 minutes. They are located outside (surface contact) or inside (midway) of the mold at different heights as presented in Figure 2.11. For feasibility reasons, it has not been possible to implement the thermocouples parallel to the isotherms, thermocouples enters from the lateral walls of the bin. The frame reference being chosen at the center of the bottom face of the block, sensors are positioned as follows (in m):

- Inside the mold, centered under the block [#11 (0; 0; -0.05)], with origin (0; 0; 0) centered at the base of the AZS block,
- Inside the mold at the middle of the major face and at different heights (bottom [#1 (0; 0.161; 0.17)], middle [#3 (0; 0.161; 0.77)] and top [#5 (0; 0.161; 1.37)] of the block section),
- Outside of the mold at the middle of the major face and at different heights (bottom [#2 (0; 0.196; 0.27)], middle [#4 (0; 0.196; 0.87)] and top [#6 (0; 0.196; 1.47)] of the block section),
- Inside the mold at the middle of the minor face and at different heights (bottom [#12 (0.245 ; 0; 0.17)], middle [#14 (0.245; 0; 0.77)] and top [#16 (0.245; 0; 1.37)] of the block section),
- Outside of the mold at the middle of the minor face and at different heights (bottom [#13 (0.280 ; 0; 0.27)], middle [#15 (0.280; 0; 0.87)] and top [#17 (0.280; 0; 1.47)] of the block section),
- Outside of the mold along the edge of the block at different heights (bottom [#8 (0.190 ; 0.196; 0.17)], middle [#9 (0.190 ; 0.196; 0.77)] and top [#10 (0.190 ; 0.196; 1.37)] of the block section),
- Outside of the mold at the bottom of the cylindrical riser (major face [#7 (0 ; 0.357; 2.03)] and minor face [#18 (0.375 ; 0; 2.03)]).

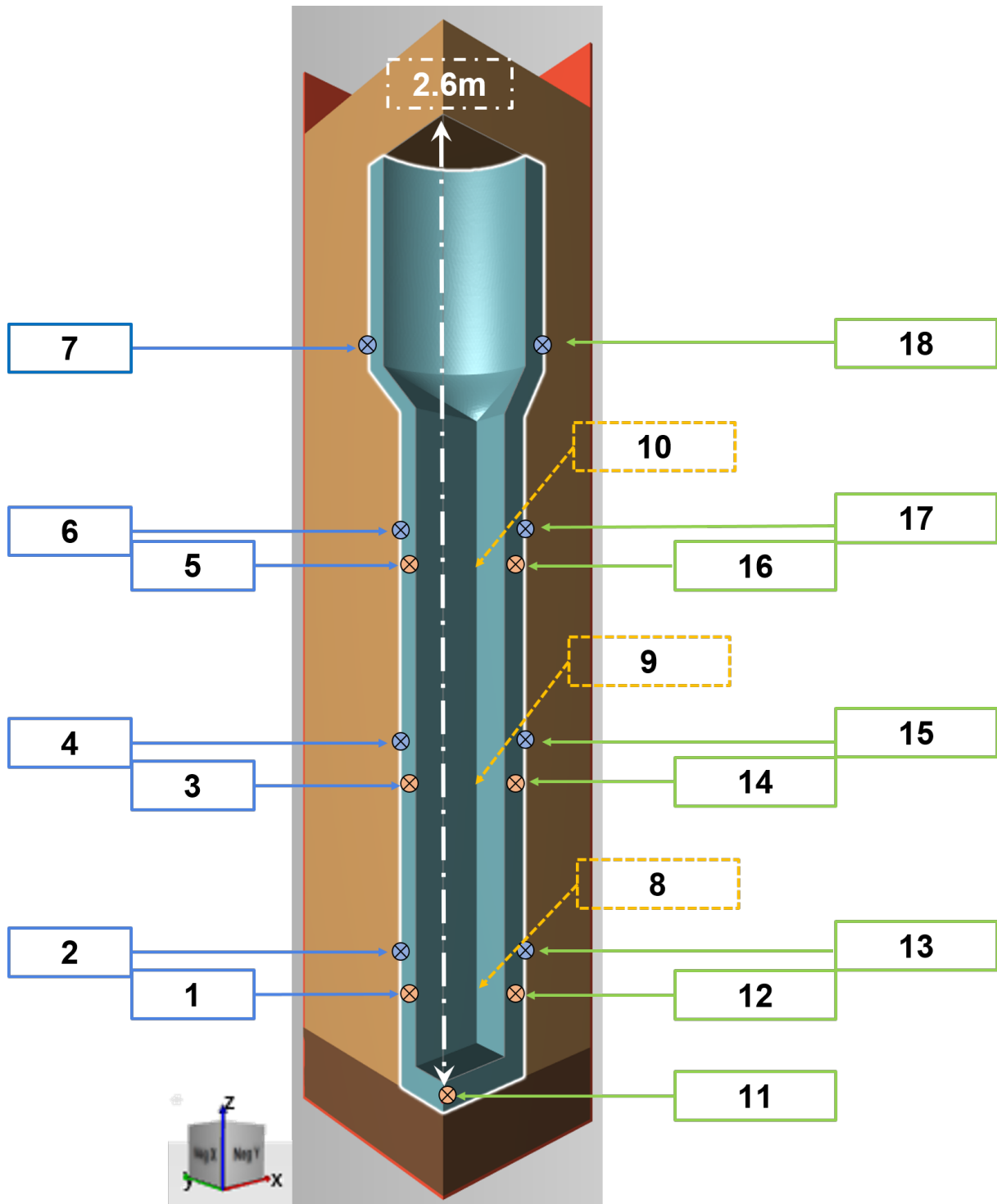


Figure 2.11: Casting configuration of (transparent) AZS block surrounded by (blue) a mold, (orange) an insulating media and (brown) a concrete base. Those objects are contained in (red) a steel bin. Thermocouples installed around the AZS block are displayed depending on their position: (orange circle with cross) inside the mold (midway) and (blue circle with cross) outside the mold. Position of the thermocouples close to the edge of the block are shown by dashed arrows.

## 2.7 Temperature history results

### 2.7.1 Thermal history at AZS nominal composition

Figure 2.14 gathers temperature as a function of time for all thermocouples over 28 h of annealing. This map is built according to the location in the domain. Black solid lines are the experimental data. Roughly, the trend of temperature is the same for all thermocouples and can be summarized in Figure 2.12 with four sensors located at the bottom (#12), at the middle (#14), at the top of the block (#16) and at the riser (#18). The temperature increases quickly at the short times due to the heat release of the AZS block. A maximum of temperature is observed with an amplitude and a time depending on the thermocouple location. At long times, the temperature decreases approximately exponentially with time.

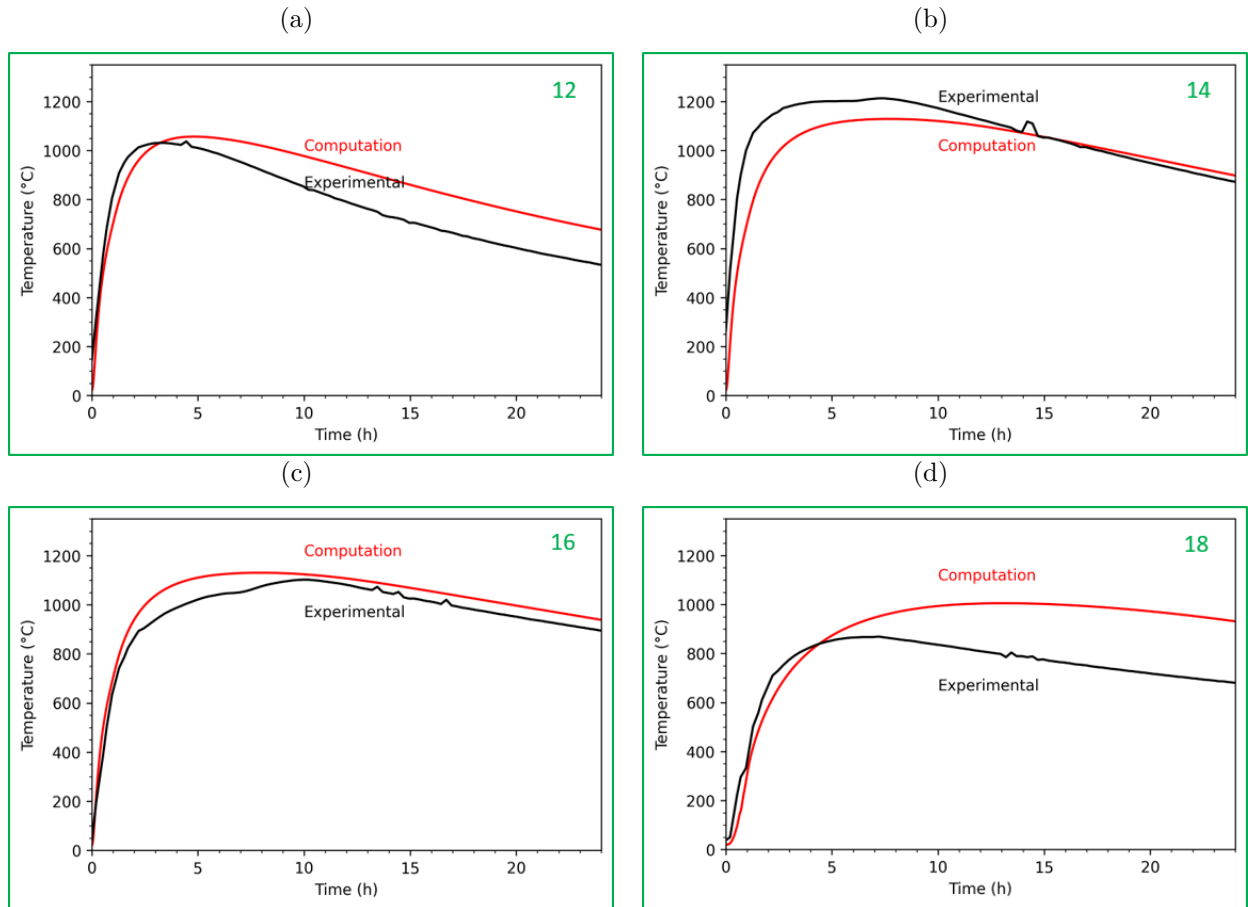


Figure 2.12: Comparison of (black) recorded and (red) computed temperature histories at different locations (see Figure 2.11) : (a) #12 bottom of the block, (b) #14 middle of the block, (c) #16 top of the block, (d) #18 riser.

In Figure 2.14, red solid lines correspond to the numerical results. This solution has been found after an adaptation of properties and boundary conditions as already reported above. Globally, the trend at long times is well reproduced numerically, especially at mid-height and at the top of the block. The overall behaviors for the thermocouples #3, 4, 5, 6, 9, 10, 11, 14, 15, 16 and #17 are well captured numerically. For thermocouples #1, #2, #7, #8, #12, #13 and #18, the numerical solution overestimates the temperature at long times. The predictions of the maximums of temperature are delayed in time. This serial of thermocouples are either located on the bottom (#1, 2, 8, 12 and 13) or on the riser (#7 and 18).

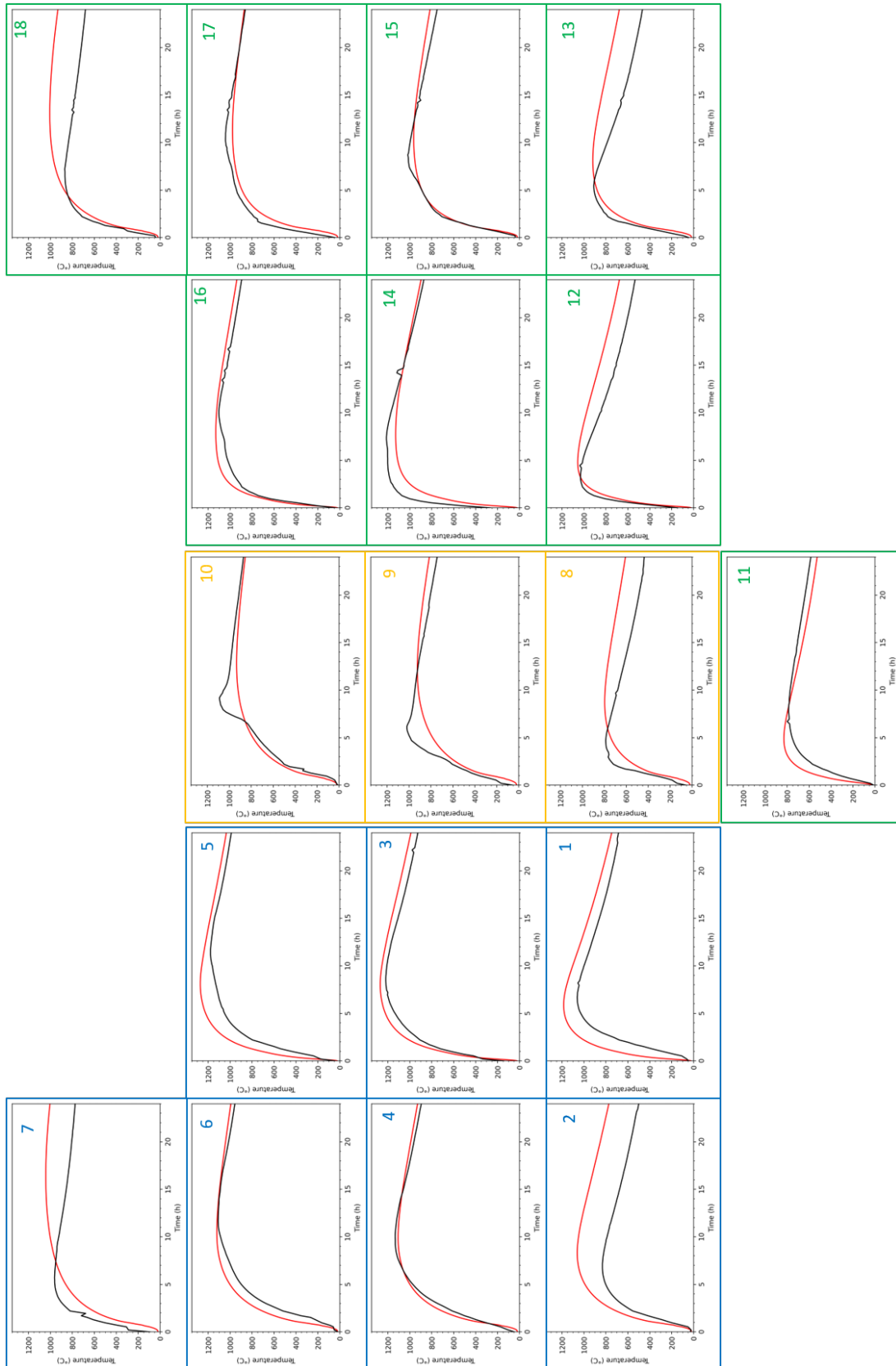


Figure 2.13:  $T$  ( $^{\circ}\text{C}$ ) as a function of  $t$  (h) for all thermocouples located in the domain shown in Figure 2.11 for an AZS composition given in Table 1.3. Experimental data are plotted in black solid line and numerical predictions are in red solid line. This map reproduced the location in the mold and in the annealing media.

Data recorded at the edge of the AZS block with thermocouples #8, #9 and #10 present a sharper temperature peak compared to simulation, as presented with a yellow border in Figure 2.13.

### 2.7.2 Simulations run for another composition

Simulation can be transposed to another composition of AZS by changing the thermal properties of the AZS block. The mold, media, concrete and bin properties are kept similar to the one used for an AZS with composition given in Table 1.3.

New composition is AZS36 detailed in Table 1.3.

#### Thermal properties of this second material

Thermal properties of this second material is compared with properties of AZS41, previously considered. Thermal conductivity can be considered as equal between both references as shown in Figure 2.14. That is why the same extra value ( $15 \text{ W m}^{-1} \text{ K}^{-1}$ ) has been considered for thermal conductivity at  $1875 \text{ }^\circ\text{C}$  (liquidus), three times larger than the last experimental point around  $1500 \text{ }^\circ\text{C}$ .

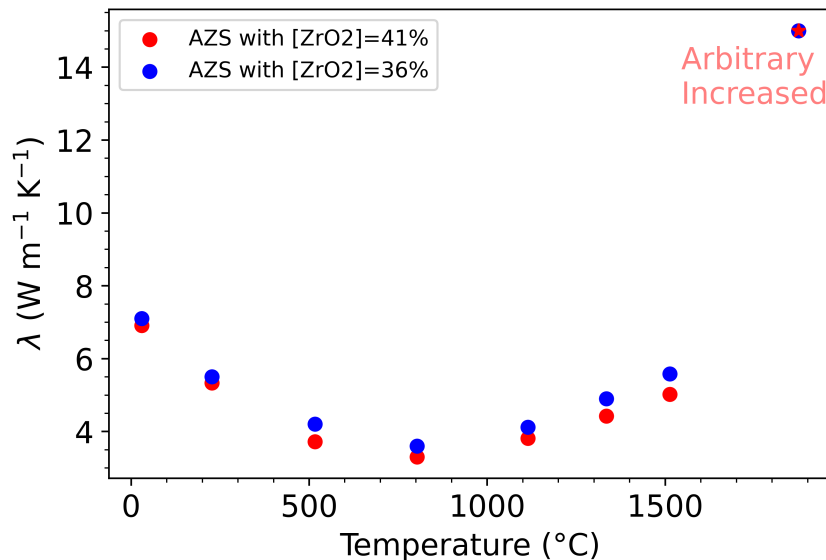


Figure 2.14: Thermal conductivity,  $\lambda$  in  $\text{W m}^{-1} \text{ K}^{-1}$ , as a function of  $T$  in  $^\circ\text{C}$  for the two compositions. Red dots are for the AZS41 composition and blue dots represent the AZS36 composition given in Table 1.3. An extra value at  $1875 \text{ }^\circ\text{C}$  is considered to compensate the heat exchange by liquid convection neglected in the present simulations.

The heat capacity at constant pressure is represented for the two compositions in Figure 2.16. These data have been extracted from the thermodynamic computation using the TCOX10 database and the PY/PATH tool. The liquidus temperature for AZS36 is  $100 \text{ }^\circ\text{C}$  below liquidus for AZS41. As  $\text{ZrO}_2$  is the component with the highest melting temperature (see phase diagram in Figure 1.12), reducing its proportion AZS36 implies a lowered liquidus temperature for AZS36.

Figure 2.16 depicts the density as a function of temperature. These data come from experimental determination achieved by the aerodynamic levitation of small pills heated by a laser. The decrease of the amount of  $\text{ZrO}_2$  in the second composition leads to an overall reduction of the density. Both compositions present a similar behavior at low temperature, especially

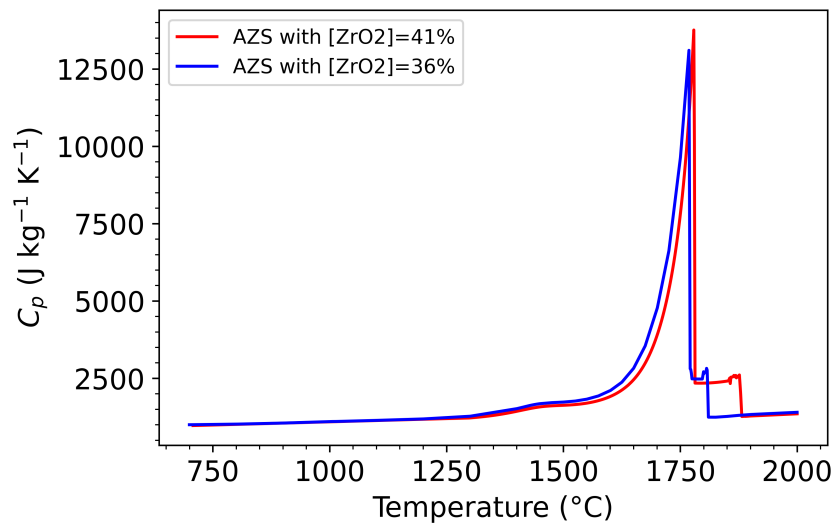


Figure 2.15: Heat Capacity  $C_p$  in  $\text{J kg}^{-1} \text{K}^{-1}$ , as a function of  $T$  in  $^{\circ}\text{C}$  for (red) the nominal composition AZS41 and (blue) a second composition AZS36 given in Table 1.3.

for zirconia phase transition around 1 000 $^{\circ}\text{C}$ . The experimental density gap at the beginning of eutectic structure solidification is not retrieved for AZS36. The density gap between liquid and solid phase is also higher for this composition.

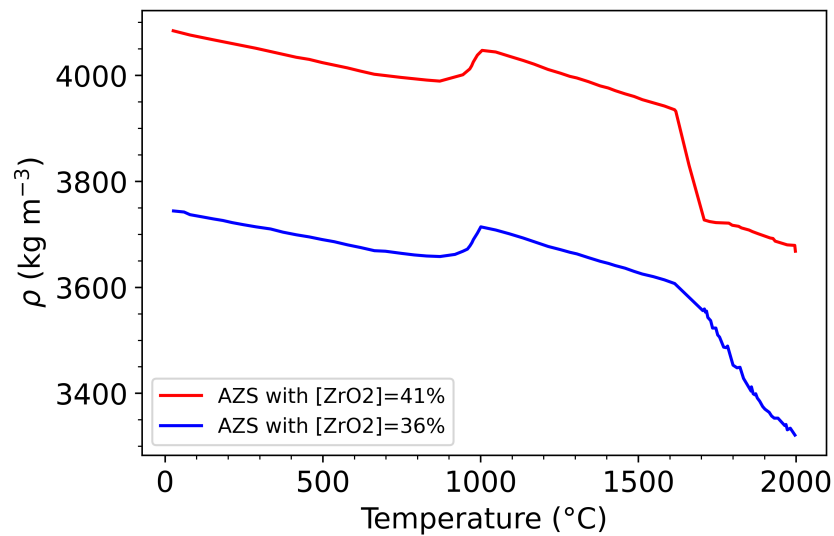


Figure 2.16: Block density  $\rho$  in  $\text{kg/m}^3$  as a function of  $T$  in  $^{\circ}\text{C}$  for AZS41 in red and AZS36 in blue.

### Impact on temperature history prediction

A second industrial trial recorded temperature history for AZS36. Figure 2.18 gathers the temperature behaviors for all thermocouples located as it is shown in Figure 2.11. The solid lines represent the experimental data over 24 h. Numerical predictions are plotted in blue dashed lines.

As for the AZS41 case, the agreement between numerical and experimental predictions is quite good for the thermocouples distributed in the middle of the block. The trend of temperature is also the same for all thermocouples and can be summarized in Figure 2.17 with four sensors located at the bottom (#12), at the middle (#14), at the top of the block (#16) and at the riser (#18). In this second case, the numerical predictions reproduce very well the decrease at long times on the riser, thermocouples #7 and #18. The largest disagreements are observed on thermocouples #11, #12 and #13.

The numerical computation for these second case has been done without changing the numerical parameters found in the first case. Only the properties of the AZS material have been changed. The overall good agreement is noticed.

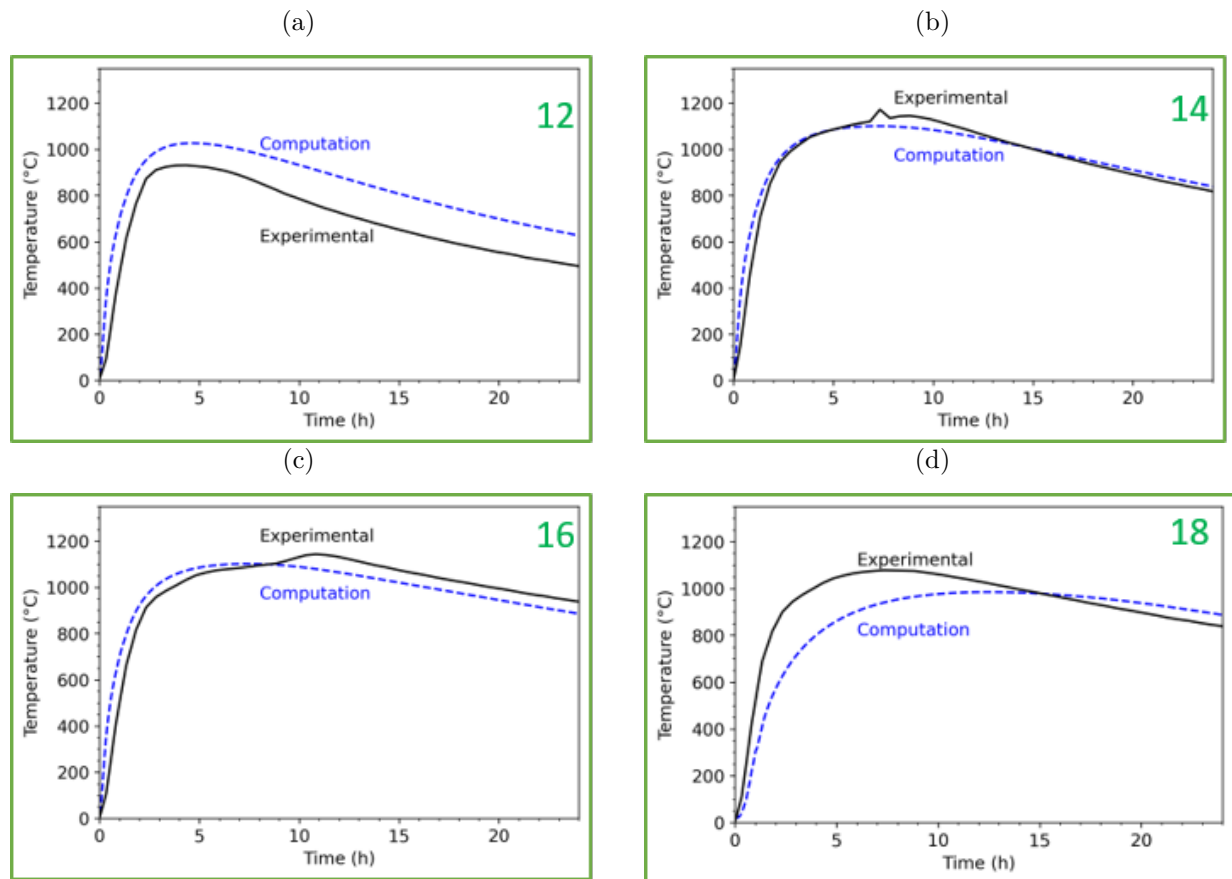


Figure 2.17: Comparison of (black) recorded and (blue dotted) computed temperature histories at different locations (see Figure 2.11) for the AZS36: (a) #12 bottom of the block, (b) #14 middle of the block, (c) #16 top of the block, (d) #18 riser.

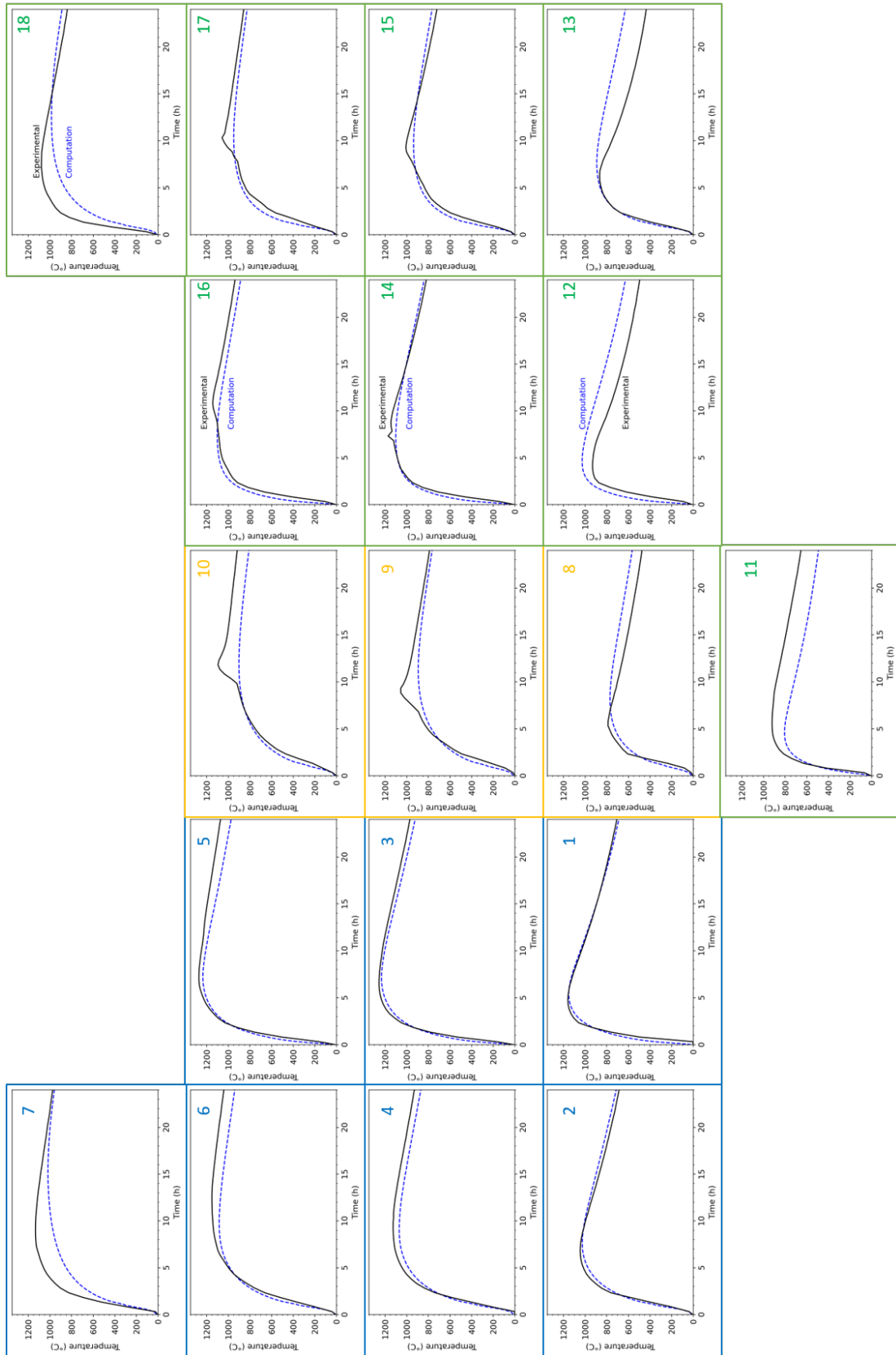


Figure 2.18:  $T$  ( $^{\circ}\text{C}$ ) as a function of  $t$  (h) for all thermocouples located in the domain shown in Figure 2.11 for an AZS36. Experimental data are plotted in black solid line and numerical predictions are in bleu dashed line. This map reproduced the location in the mold and in the annealing media.

## 2.8 Impact of thermal solver on temperature history predicted

### 2.8.1 User solver presentation

For this approach, properties are tabulated by phase with temperature. All phases remain fixed. A non linear temperature solver is considered and is presented in [67]. This solver considers enthalpy of each phase weighted by phase fraction and not an equivalent specific heat tabulated for the entire AZS composition as detailed in (2.27), for an element with fixed density  $\rho$ :

$$\frac{\partial \langle \rho h \rangle}{\partial t} = \nabla \cdot (\langle \lambda \rangle \nabla T) \quad (2.27)$$

As detailed in [20], for each iteration  $\nu$  at mesh node  $j$  the solver determines thanks to the enthalpy tabulation the following equivalent heat capacity using the finite difference formulation (2.28).

$$\left( \frac{\partial \langle \rho h \rangle}{\partial T} \right)_j^\nu = \frac{\langle \rho h \rangle_j^\nu - \langle \rho h \rangle_j^{\nu-1}}{T_j^\nu - T_j^{\nu-1}} \quad (2.28)$$

At the beginning of the increment, when temperature is known, a model reads a microsegregation tabulation file and returns for each phase its fraction, its composition and its thermal properties. Those values are updated at each solver iteration of the time step and used for the new temperature determination by the thermal solver at the considered increment. To limit the duration of computations, it is possible to define them only once, at the first iteration of the time step.

Liquid convection is also expected to take place during casting, hence transporting heat. THERCAST<sup>®</sup> has been used considering an extra value ( $15 \text{ W m}^{-1} \text{ K}^{-1}$ ) for thermal conductivity at  $1\ 875^\circ\text{C}$  (liquidus), three times larger than the last experimental point around  $1\ 500^\circ\text{C}$ . The same thermal conductivity tabulation is used with this user solver.

### 2.8.2 Tabulation of material thermal properties

Microsegregation tabulation file initially contains general information about the considered materials in terms of structure and zone as explained in [67]. Different structures can be considered if it is important to separate a phase in dendrites from the same phase that is located in a eutectic structure for example. A zone is defined to consider a global system and can contain one or more structures: mushy zone (partially solidified region), fully solidified zone,...

It is possible to simplify the system by considering a single zone, that contains a single structure, composed of three phases (as defined by Thermo-Calc<sup>®</sup> at high temperatures) with a distribution as detailed in Table 1.2. Glassy phase is modeled as remaining liquid phase. Zirconia transition is not taken into account as in Thermo-Calc<sup>®</sup> TCOX10 database, the transition implies a switch from zirconia<sub>tetragonal</sub> toward zirconia<sub>monoclinic</sub>. With such simplified system, no separation are done neither between zirconia that solidifies first and nor zirconia that solidifies in a eutectic structure with corundum. Yet the zirconia fraction with temperature follows the two reactions and thus the increase due to the dendrites solidification plus the one due to the eutectic solidification. Thermal properties are tabulated for each phase in two different blocks. The first about the phase fraction and composition over temperature and the second about phase density and enthalpy over temperature. More details are given below.

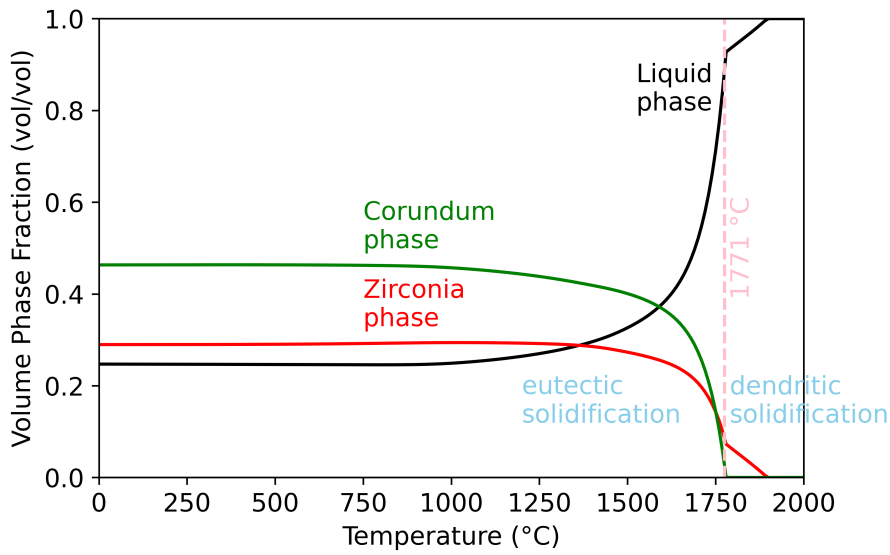


Figure 2.19: Volume phase fraction tabulated over temperature for a system composed of 46 wt.% of  $\text{Al}_2\text{O}_3$ , 11 wt.% of  $\text{SiO}_2$ , 1 wt.% of  $\text{Na}_2\text{O}$  and remaining fraction for  $\text{ZrO}_2$ : (black) liquid phase (green) corundum and (red) Zirconia phase.

Thermo-Calc<sup>®</sup> imposes to get the same amount of chemical elements and components for equilibrium state computations. For the quaternary system considered, five chemical elements are considered : Al – Zr – Si – Na – O. After the definition of the four oxide components measured experimentally ( $\text{Al}_2\text{O}_3 - \text{ZrO}_2 - \text{SiO}_2 - \text{Na}_2\text{O}$ ), free oxygen, O, has to be also defined as a component to define the system. O is defined with an activity set as 1 and Thermo-Calc<sup>®</sup> equilibrium state computations returns a concentration for "free oxygen" below  $1 \times 10^{-15}$  wt% that is not presented in the tabulations.  $\text{ZrO}_2$  is the first component to solidify to form the zirconia phase. It is therefore considered as main element and its proportion is not tabulated as it is defined as the remaining fraction.

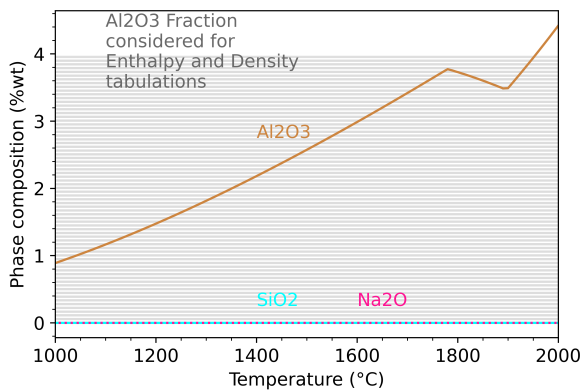


Figure 2.20: Zirconia phase composition over temperature considering (blue)  $\text{SiO}_2$  (brown)  $\text{Al}_2\text{O}_3$  and (pink)  $\text{Na}_2\text{O}$ . Each horizontal gray lines represents an  $\text{Al}_2\text{O}_3$  concentration considered for the second set of tabulations

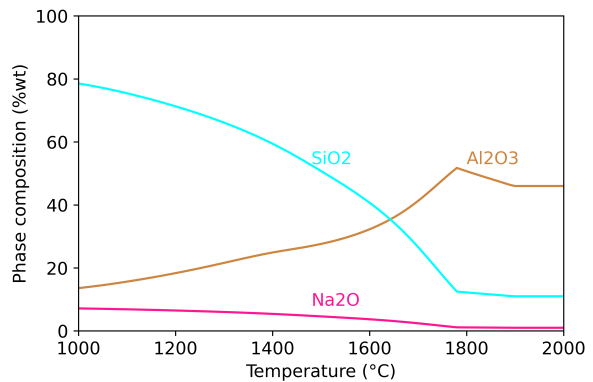


Figure 2.21: Liquid phase composition over temperature considering (blue)  $\text{SiO}_2$  (brown)  $\text{Al}_2\text{O}_3$  and (pink)  $\text{Na}_2\text{O}$ . For each component, 72 concentrations are considered for the second set of tabulations.

A first tabulation focuses on phase fraction for a standard AZS system composed of 46 wt.% of  $\text{Al}_2\text{O}_3$ , 11 wt.% of  $\text{SiO}_2$ , and 1 wt.% of  $\text{Na}_2\text{O}$ , close to AZS41. Considering the global concentration of the different elements defined in Table 1.3 and temperature, it returns the volume phase fraction (see Figure 2.19 combined for the three phases computed as a single structure and a single zone) and the composition of those phases. (see Figure 2.21 for liquid composition). A temperature step of 10 °C is considered for this first tabulation.

A second tabulation defines thermal properties of the phase at the different compositions encountered in the first tabulations when the phase is present (phase fraction > 0 wt.%). PATH tool is able to concatenate the tabulations of temperature dependent properties obtained for the different phases. As detailed by Carozzani [67], every set of values has to be tabulated in order to be readable by the solver. The first column needs to be sorted from the smallest to the largest value and so on as explained with Table 2.5.

	Component 1	Component 2	T (°C)
Min	1	10	0
Max	2	20	2000

Table 2.5: Example of data tabulations.

implies the following tabulation:

- 1 10 0
- 1 10 2000
- 1 20 0
- 1 20 2000
- 2 10 0
- 2 10 2000
- 2 20 0
- 2 20 2000

Thermal properties (density, enthalpy) being mostly linear over temperature at a given composition, a temperature step of 200°C is considered for this second tabulation, as shown by the evolution over temperature for dots with the same color in Figure 2.22 and Figure 2.23. As Corundum is pure alumina, only a single composition is tabulated over temperature. In Zirconia phase,  $\text{ZrO}_2$  is almost pure with a slight solubility of  $\text{Al}_2\text{O}_3$ . 72 different fraction values, encountered during annealing, for each components are tabulated over temperature. Such tabulation gets four inputs : the weight phase fraction inside the phase in the three components ( $[\text{Al}_2\text{O}_3]^\varphi$ ,  $[\text{SiO}_2]^\varphi$  and  $[\text{Na}_2\text{O}]^\varphi$ ) and temperature (in °C). This tabulation returns two outputs: weight phase enthalpy (see Figure 2.23 for Zirconia phase) and density (see Figure 2.22 for Zirconia phase).

Even if phase composition depends only on temperature and therefore phase properties too, thermal properties are tabulated for each set of compositions encountered at different temperatures, as represented by gray lines in Figure 2.20. For liquid phase, the composition of the phase over temperature is presented in Figure 2.21. The extrema values obtained during the annealing are detailed in Table 2.6. As the sum of the maximum encountered for each component along

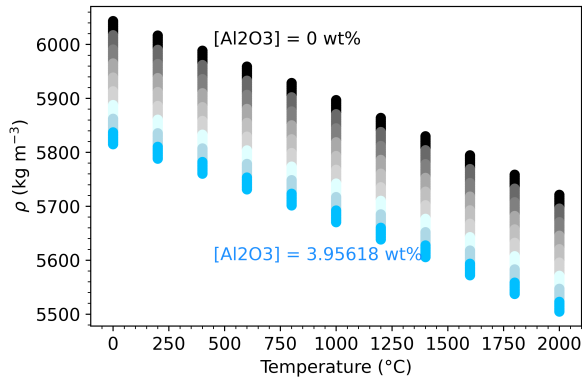


Figure 2.22: Zirconia phase density tabulated over temperature for different set of compositions are encountered during annealing. Each color represents 8 sets of composition.

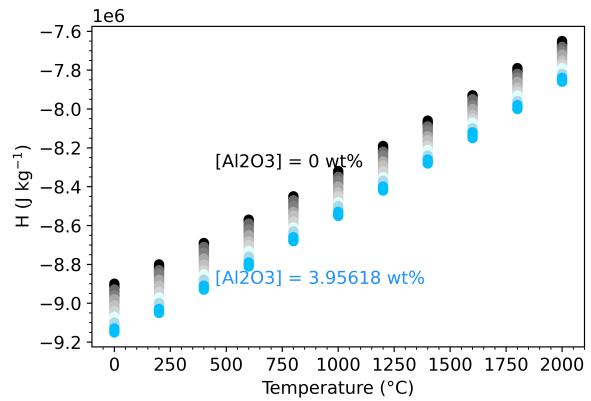


Figure 2.23: Zirconia phase enthalpy tabulated over temperature for different set of compositions are encountered during annealing. Each color represents 8 sets of composition.

the annealing (139,69%) is over 100%, adjustments of PATH tool has been required to get relevant tabulations without negative concentrations of  $\text{ZrO}_2$ . They are detailed in Chapter 4 when macrosegregation will be considered in section § 4.2.2. As corundum is pure alumina, a single set of composition is tabulated over temperature. Zirconia phase contains a slight fraction of  $\text{Al}_2\text{O}_3$ , below 5%, that can be easily tabulated by PATH tool.

	$\text{Al}_2\text{O}_3$	$\text{SiO}_2$	$\text{Na}_2\text{O}$
Min	12.05%	11.00%	1.00%
Max	51.74%	80.62%	7.33%

Table 2.6: Minimal and maximal concentrations in liquid phase tabulated by PY/PATH when temperature is included between 0 °C and 2 000 °C.

### 2.8.3 Temperature history with this second thermal solver

For these computations, properties for all other domains were considered identical.

Temperature outputs with such solver (orange dotted lines in Figure 2.24) is less relevant compared to the results obtained with the solver by default in THERCAST<sup>®</sup> (red line in Figure 2.24) when comparison is done with experimental temperature history.

Even if results are not well adapted compared to experimental data, the first hours of annealing are well computed for sensors located in the block section. The sensor located in the riser (Figure 2.24d) is again the worse predictive sensor as even the first hours are not close to past results with THERCAST<sup>®</sup> default solver. This study confirms that the gap between experimental data and numerical temperature outputs are not due to the solver. Another phenomenon occurring (such as macro-porosity) in the riser should be taken into account to adjust sensors predictions in this region.

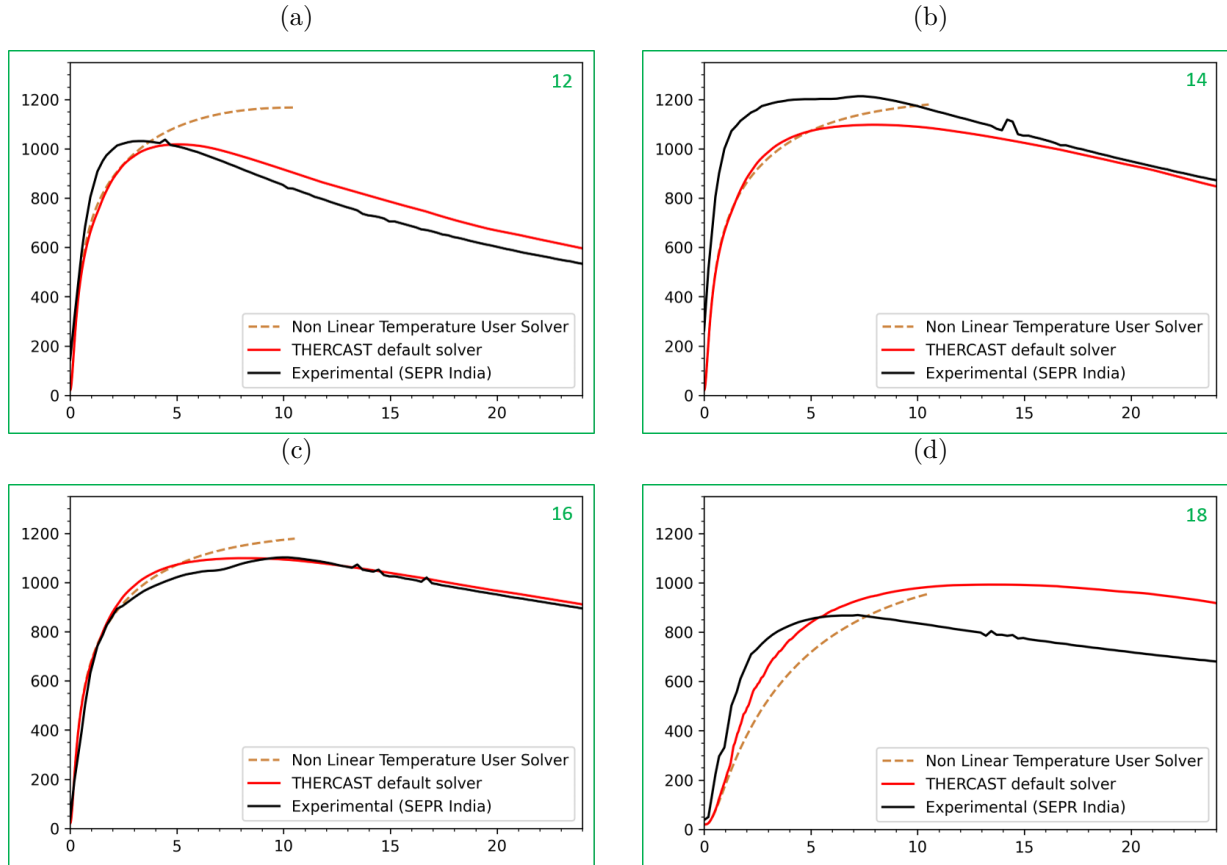


Figure 2.24: Comparison of temperature histories at different locations (see Figure 2.11) for (black) experimental recorded data, (red) computed with default THERCAST® solver and (orange, dotted line) computed with another thermal solver : (a) at the bottom of the block, (b) middle of the block, (c) top of the block, (d) in the riser.

## 2.9 Conclusion about temperature predictions in AZS block with THERCAST® software

THERCAST® is a multi-domain 3D finite-element computation software. The system studied in this project is composed of five domains : AZS block, Mold, Media, Concrete, Bin. Each domain is associated with material properties. First the energy conservation equation was presented, assuming fixed phases, then thermal properties considered for each domain have been presented and finally the numerical settings such as the heat exchanges at the interfaces or the initial conditions for computations.

Eighteen thermocouples have recorded temperature inside the mold during industrial annealing in a Saint Gobain SEPR plant. Temperatures simulated inside the mold fit well experimental results along the block section. Numerical sensors located close to the riser predict less relevant temperature histories. This means that temperature annealing inside the AZS riser is not well simulated by THERCAST® whereas temperature evolution predicted inside the AZS block itself is relevant.

At the mold/AZS interface, a heat exchange coefficient is considered as constant over the entire block height. As the heat transfer coefficient is also constant over time, it means that the mold combustion is not modeled and the energy released by the resin combustion has not been

determined. However, as the temperature history is well reproduced by computations over the first day of annealing, it is not required to take this phenomenon into consideration.

In order to improve temperature prediction inside the riser, different options are detailed here:

- Numerical adjustments of parameters in a defined region close to the riser:

This option consists in defining a region (including almost only the riser) and adjusting thermal exchanges or properties in this region only. It will be then possible to shorten the duration between pouring (beginning of the computation) and the peak of temperature to get closer to what is observed experimentally. If this option would improve only the less relevant temperature outputs, it would have a huge drawback: it does not try to understand why this region is not well predicted compared to the block. This option is therefore not recommended.

- Consideration of convection flow inside the media:

Air convection in the porous media was considered only by increased values for thermal conductivity, identical over the entire media domain. To determine the impact of convection, a new set of numerical simulations focused on media needs to be created. As the media is like granular media, air can move all around the block due to the natural convection. Close to the riser, the temperature is the hottest as (a) hot air comes from the bottom of the block that rises up and as (b) the riser is the hottest region in the block and heats for a longer time the media around it. Feasibility of such computations have been done for a 2D case but some software adjustments are required before switching to industrial geometries. The quantitative impact of convection in media on temperature history is consequently not determined in this project. With an hotter air regions, natural convection is stronger. Heat release is then dependent on the system height but this specificity is not taken into account. The adjustments of media and mold thermal conductivity are currently done for the entire domain, as well as the heat exchange coefficients at the interfaces.

- Thermal solver validation:

A second thermal solver is considered. This solver requires to tabulate enthalpy for each phase instead of an equivalent specific heat as required in THERCAST<sup>®</sup> default thermal solver. Implementation of such solver has been performed, keeping the same optimized properties for media and mold. Temperature predictions with this second solver are relevant for the first hours of annealing but after 5h, the trend of simulated annealing is too slow compare to experimental data. The temperature peak is not reached after 12h of computation whereas it is obtained after 5h experimentally. A new adaptation of parameters (for example, of the mold and media thermal properties) would be required to fit experimental results but such adaptation was not performed during this PhD project for time saving reasons.

- Consideration of other phenomena that occur inside AZS domain during its annealing, such as macro-porosity opening:

Air inside the block releases less energy as the same volume filled with hot AZS solidifying. Considering real AZS block shrinkage during annealing might have an impact on temperature history. Macro-porosity opening is modeled in thermo-mechanical simulations in THERCAST<sup>®</sup> as it will be presented in Chapter 4.

In this chapter, temperature history is validated inside the block section with the thermal solver by default in THERCAST®. With this calibration, it will be possible to consider stress and strain generation, especially along the edges of the block where hot cracks occur. In order to optimize riser geometry, macro-porosity inside the riser will also be studied. This thermo-mechanical aspect is detailed in the next chapter.



## Chapter 3

# Thermo-mechanical computations of hot tears susceptibility and macro-porosity

### Contents

---

Résumé Chapitre 3 . . . . .	<b>52</b>
3.1 Conservation equations . . . . .	<b>53</b>
3.1.1 Balance equations for thermo-mechanical computations in a single phase material ( $\varphi$ ) . . . . .	53
3.1.2 Mechanical balance equations . . . . .	54
3.2 Constitutive equations and properties specific to the AZS material . . . . .	<b>55</b>
3.2.1 Constitutive equations . . . . .	55
3.2.2 Interface definition in thermo-mechanical computations . . . . .	58
3.2.3 Mechanical properties of AZS . . . . .	59
3.2.4 Impact of thermo-mechanical computations in temperature history prediction . . . . .	61
3.3 Prediction of hot tears susceptibility in AZS block . . . . .	<b>62</b>
3.3.1 Experimental observations of hot tears along edges . . . . .	62
3.3.2 Literature review about hot tears formation . . . . .	65
3.3.3 Criteria for Hot Cracking Susceptibility (HCS) prediction . . . . .	67
3.3.4 Implementation of hot tear susceptibility prediction in THERCAST® . . . . .	75
3.3.5 Impact of four geometries on hot tear susceptibility . . . . .	78
3.3.6 Conclusion about predicting the hot tears susceptibility of a block . . . . .	80
3.4 Prediction of macro-porosity in the riser . . . . .	<b>80</b>
3.4.1 Experimental observations of riser macro-porosity . . . . .	80
3.4.2 Impact of numerical parameters for porosity opening . . . . .	81
3.4.3 Impact of the composition on the riser macro-porosity . . . . .	84
3.4.4 Discussion about the potential impact of lower AZS liquid density . . . . .	85
3.5 Conclusion about mechanical outputs of numerical simulations . . . . .	<b>88</b>

---

## Résumé Chapitre 3

Le chapitre 3 présente les résultats mécaniques des simulations numériques. La mécanique est appliquée uniquement sur le domaine AZS. Les quatre domaines sont résolus en thermique uniquement, comme pour le chapitre précédent.

Dans un premier temps, les équations relatives à la mécanique sont présentées : les équations de conservation de la quantité de mouvement et de la masse ainsi que la loi de comportement adaptée au matériau d'intérêt. Les propriétés mécaniques de l'AZS ont été mesurées expérimentalement ou extraites de précédentes thèses sur des céramiques réfractaires à haute teneur en zircon, les données du comportement de l'AZS à très hautes températures étant limitées voire inexistantes.

Dans un deuxième temps, l'étude s'est portée sur la prédiction des criques à chaud sur les arêtes du bloc. L'histoire thermique étant bien prédite, le comportement mécanique du matériau sur l'arête du bloc peut être étudié. La première étape fut l'observation expérimentale des déchirures pour confirmer leur occurrence à des températures où la phase liquide est encore présente et assez fluide. Différents critères existent dans la littérature pour quantifier le risque de formation de criques à chaud, principalement pour les aciers et les alliages d'aluminium. Plusieurs critères ont été testés pour les AZS : celui de Clyne-Davies, celui de Yamanaka et celui de Won. Un critère en contrainte a également été testé mais ne sera pas retenu par la suite. Le critère en déformation retenu, ayant une plus forte susceptibilité de fissuration à chaud sur les arêtes du bloc comparé au reste du bloc, est celui intégrant la déformation cumulée au cours de l'intervalle de température fragile (BTR). Le BTR et la loi de comportement sont des paramètres clés qui influencent fortement la valeur du critère. Après les avoir optimisés, il a été possible de valider la mise en données avec un cas d'étude expérimentale comparant plusieurs géométries ayant différentes susceptibilités à la fissuration à chaud.

Dans un troisième temps, l'analyse mécanique se porte sur la masselotte pour définir les paramètres clés expliquant les écarts observés entre l'histoire thermique expérimentale et les simulations présentées au chapitre 2. A nouveau, la première étape fut l'analyse de masselottes expérimentales et notamment la forme de sa retassure qui occupe quasiment tout son volume. Après l'étude de paramètres numériques relatifs à l'ouverture de la retassure dans les simulations numériques, l'impact de la composition du matériau a été mis en avant. Le point critique qui influence fortement l'ouverture de la retassure est le saut de densité subi par le matériau lors de la solidification. Or dans la masselotte, le liquide est enrichi en  $\text{SiO}_2$  et en  $\text{Na}_2\text{O}$  à cause de la macroségrégation avec une densité autour de  $3\,000\text{ kg m}^{-3}$ , inférieure à la densité initiale au moment de la coulée qui est davantage autour de  $3\,700\text{ kg m}^{-3}$ .

Pouvoir prédire la forme de la retassure à la fin du refroidissement ainsi que le risque de défaut sont des attentes fortes de la part des industriels. Cela permet en effet de pouvoir optimiser des géométries ou des paramètres du procédé de façon numérique pour limiter les tests à l'échelle industrielle.

To anticipate foundry defect formations such as hot tears located at the edge of the block, it is required to consider mechanical responses of the material. Temperature history is well modeled in the AZS block region by the calibrated default thermal solver in THERCAST<sup>®</sup> as detailed in Chapter 2. It is then possible to investigate hot tears formation, also called "crack" in this chapter. To quantify stress and strain, it is required to know the temperature history, the constitutive equation used and the tabulation of the AZS mechanical properties over temperature.

This chapter first presents the balance equations solved for mechanical computations. A second section focuses on data specific to the AZS material: the constitutive equation considered and the mechanical properties of this refractory material. Then hot tears at the edge of the AZS blocks are analyzed with experimental observations, literature about criteria to predict their susceptibility to form and comparison between numerical and experimental results. Finally, as mechanical computations also include solidification shrinkage, the resulting macro-porosity in the riser is compared with experimental macro-porosity and several possible adjustments are presented.

## 3.1 Conservation equations

### 3.1.1 Balance equations for thermo-mechanical computations in a single phase material ( $\varphi$ )

The three equations of conservation of mass, momentum and energy in a single phase material read [57]:

$$\frac{\partial \rho_\varphi}{\partial t} + \nabla \cdot (\rho_\varphi \mathbf{v}_\varphi) = 0, \quad (3.1)$$

$$\rho_\varphi \frac{D\mathbf{v}_\varphi}{Dt} = (\mathbf{F}_V)_\varphi - \nabla P_\varphi + \nabla \cdot \mathbf{s}_\varphi, \quad (3.2)$$

$$\frac{\partial \rho_\varphi h_\varphi}{\partial t} + \nabla \cdot (\rho_\varphi h_\varphi \mathbf{v}_\varphi) = \frac{\partial P_\varphi}{\partial t} + \mathbf{v}_\varphi \cdot \nabla P_\varphi + \mathbf{s}_\varphi : \dot{\boldsymbol{\varepsilon}}_\varphi + \dot{Q}_\varphi - \nabla \cdot \mathbf{q}_\varphi, \quad (3.3)$$

with

- $\rho_\varphi$  the density of the phase  $\varphi$ ;
- $\mathbf{v}_\varphi$  the velocity of the phase  $\varphi$ ;
- $(\mathbf{F}_V)_\varphi$  the volumetric forces in phase  $\varphi$ ;
- $\mathbf{s}_\varphi$  the deviatoric of the Cauchy stress tensor of phase  $\varphi$ ;
- $h_\varphi$  the enthalpy of phase  $\varphi$ ;
- $P_\varphi$  the pressure inside phase  $\varphi$ ;
- $\dot{\boldsymbol{\varepsilon}}_\varphi$  the deformation rate of phase  $\varphi$ ;
- $\dot{Q}_\varphi$  a source term involving phase  $\varphi$ ;
- $\mathbf{q}_\varphi = -\lambda_\varphi \nabla T_\varphi$  the diffusive heat flux, with  $\lambda_\varphi$  the thermal conductivity in phase  $\varphi$  and  $T_\varphi$  the temperature of phase  $\varphi$ .

### 3.1.2 Mechanical balance equations

Thermo-mechanical simulations solve, at each time increment, the heat transfer equation for all domains. As explained in Chapter 2, solidification is considered only in the AZS domain. Mass and momentum balance equations are also solved only in the AZS domain. A volumetric average method explained in § 2.1.1 is used for a given REV, made of an assembly of different phases ( $\varphi = \{liquid; solid\}$ ).

#### Mass balance equation

The following definitions are used to get a general expression of mass conservation for a system with two phases (liquid and solid). The average density,  $\langle \rho \rangle$  and momentum  $\langle \rho \mathbf{v} \rangle$  are over the REV given by

$$\langle \rho \rangle = \langle \rho_l \rangle + \langle \rho_s \rangle = g_l \langle \rho \rangle_l + g_s \langle \rho \rangle_s \quad (3.4)$$

$$\langle \rho \mathbf{v} \rangle = \langle \rho_l \mathbf{v}_l \rangle + \langle \rho_s \mathbf{v}_s \rangle = g_l \langle \rho \mathbf{v} \rangle_l + g_s \langle \rho \mathbf{v} \rangle_s \quad (3.5)$$

The solid phase combines all the solid phases present (i.e. zirconia and corundum as detailed in Chapter 1). Therefore, for a generic scalar field  $\psi$ , its average can be expressed as :

$$\begin{aligned} \langle \psi_s \rangle &= \sum_{\varphi \neq l} \langle \psi_\varphi \rangle \\ &= \langle \psi_{\text{ZrO}_2} \rangle + \langle \psi_{\text{corundum}} \rangle \\ &= g_{\text{ZrO}_2} \langle \psi \rangle_{\text{ZrO}_2} + g_{\text{corundum}} \langle \psi \rangle_{\text{corundum}} \end{aligned}$$

The mass balance equation averaged over all phases in volume  $V$  reads [56, 57] :

$$\frac{\partial \langle \rho \rangle}{\partial t} + \nabla \cdot \langle \rho \mathbf{v} \rangle = 0 \quad (3.6)$$

The average procedure leads to the introduction of a fluctuation part. According to Ni and Beckermann [59], the correlation between the fluctuation contributions of  $\rho$  and  $\mathbf{v}$  is neglected. This means that  $\langle \rho \mathbf{v} \rangle$  is simply written as follows:

$$\langle \rho \mathbf{v} \rangle = \langle \rho \rangle \langle \mathbf{v} \rangle. \quad (3.7)$$

Alternatively, it is possible to introduce a density-weighted average as it is classically done in turbulent compressible flow [68] and in multiphase flow [69] to avoid the fluctuation correlation in the average mass conservation balance. However, the resulting form of the mass balance equation is the same.

$$\nabla \cdot (\langle \rho \rangle \langle \mathbf{v} \rangle) = \nabla \langle \rho \rangle \cdot \langle \mathbf{v} \rangle + \langle \rho \rangle \nabla \cdot \langle \mathbf{v} \rangle \approx \langle \rho \rangle \nabla \cdot \langle \mathbf{v} \rangle. \quad (3.8)$$

Mass conservation equation solved in THERCAST<sup>®</sup> [19], applied only on the AZS domain, writes:

$$\frac{1}{\langle \rho \rangle} \frac{\partial \langle \rho \rangle}{\partial t} + \nabla \cdot \langle \mathbf{v} \rangle = 0 \quad (3.9)$$

### Momentum balance equation

Using the same procedure of averaging, the momentum balance equation reads as follows:

$$\langle \rho \rangle \frac{D \langle \mathbf{v} \rangle}{Dt} = \langle \rho \rangle \mathbf{g} - \nabla \langle P \rangle + \nabla \cdot \langle \mathbf{s} \rangle, \quad (3.10)$$

in which the first term of the right-hand side is the volumetric force due to the gravity, the average pressure  $\langle P \rangle$  and the deviator of the Cauchy stress tensor are given by

$$\langle P \rangle = g_l \langle P \rangle_l + g_s \langle P \rangle_s, \quad (3.11)$$

$$\langle \mathbf{s} \rangle = g_l \langle \mathbf{s} \rangle_l + g_s \langle \mathbf{s} \rangle_s. \quad (3.12)$$

Similarly to the mass balance equation, the acceleration of the fluid is simplified under the form:

$$\langle \rho \rangle \frac{D \langle \mathbf{v} \rangle}{Dt} \approx \langle \rho \rangle \frac{\partial \langle \mathbf{v} \rangle}{\partial t}, \quad (3.13)$$

meaning that the quadratic term in velocity is neglected.

## 3.2 Constitutive equations and properties specific to the AZS material

As detailed in [57], whatever the system, the conservative equations are the same. Constitutive equations are therefore required to detail the specificities of the AZS41. AZS material is initially fully liquid, with a Newtonian behavior. Creep is observed when temperature is above 1 300°C. Here, AZS material behaves like a temperature dependent elasto-visco-plastic material. As solidification shrinkage is tracked by an adaptive domain size, interface parameters are then detailed before presenting the mechanical properties of the AZS material.

### 3.2.1 Constitutive equations

The modeling of thermo-mechanical behavior in casting process must take into account the phase change due to the cooling of the material. At the beginning, the material is liquid behaving like a Newtonian fluid. In this state, the Cauchy stress tensor is simply linked to the rate-of-strain tensor. When the temperature decreases, a solid phase appears changing dramatically the mechanical behavior of the material. Finally, when the material is fully solid, the elastic behavior prevails. According to Bellet *et al.* [70], a clear distinction between the “liquid-like” and the “solid-like” constitutive equations is mandatory. The change between the liquid-like to the solid-like behaviors is determined as a function of temperature. Above a critical temperature,  $T_c$ , the material behaves like a liquid while below  $T_c$ , the material is seen as a solid. The critical temperature is taken close to the coherency point corresponding to the state of continuous skeletal dendritic network [71]. Beside the phase transformation, the change of density with temperature must be accounted for.

**Liquid-like constitutive equation:** This behavior is applied both in the pure liquid state and also in the mushy state. According to Bellet *et al.* [70], the constitutive equations are written under inverse form. This means that the rate-of-strain tensor is given in function of the stress tensor, thermal rate. The reason is due to the fact that the strain is additive. In the liquid state, the total rate-of-strain tensor is written as follows

$$\dot{\boldsymbol{\epsilon}} = \dot{\boldsymbol{\epsilon}}_{\text{vp}} + \dot{\boldsymbol{\epsilon}}_{\text{th}}. \quad (3.14)$$

The first contribution is due to the visco-plastic or pseudo-plastic deformation described by a power law as follows

$$\dot{\boldsymbol{\epsilon}}_{\text{vp}} = \frac{1}{2K(T)} \left( \sqrt{3}\dot{\epsilon}_{\text{eq}} \right)^{1-m(T)} \mathbf{s}. \quad (3.15)$$

The scalar  $\dot{\epsilon}_{\text{eq}}$  is the von Mises norm

$$\dot{\epsilon}_{\text{eq}} = \sqrt{\frac{2}{3} \dot{\boldsymbol{\epsilon}}_{\text{vp}} : \dot{\boldsymbol{\epsilon}}_{\text{vp}}}. \quad (3.16)$$

$K(T)$  is the consistency and  $m(T)$  the pseudo-plastic exponent of the material. These two parameters are function of the temperature to take into account the change of the material with  $T$ . In liquid state,  $m$  is equal to one and  $K$  should be equivalent to the viscosity of the liquid. To describe the increase of the viscosity occurring when the solid fraction is not equal to zero (mushy zone),  $K$  increases strongly with  $T$ . The data used in our case will be given below.

The thermal expansion and shrinkage is given by

$$\dot{\boldsymbol{\epsilon}}_{\text{th}} = \left( \alpha \dot{T} + \frac{1}{3} \dot{g}_l \frac{\rho_l - \rho_s}{\rho_l} \right) \mathbf{I}, \quad (3.17)$$

with  $\alpha$  the linear thermal dilatation coefficient given by

$$\alpha = -\frac{1}{3\langle \rho \rangle} \left( \frac{\partial \langle \rho \rangle}{\partial T} \right)_P. \quad (3.18)$$

The shrinkage contribution, second term in the right-hand side of (3.17), is different to zero in the mushy zone, i.e. when  $\dot{g}_l \neq 0$ . The two quantities  $\dot{T}$  and  $\dot{g}_l$  are the thermal rate and liquid phase rate determined by the computation of the point-wise partial derivative of  $T$  and  $g_l$ .

**Solid-like constitutive equation** When the temperature of the material is less than  $T_c$ , the mechanical behavior must be changed. Since the material is close to solid state an elastic contribution is added. To take into account the plastic deformation a yield stress is also introduced. The elastic-visco-plastic material can be seen like a generalized standard material clearly defined in the thermodynamic framework as presented by Halphen and Nguyen [72], see also [73, Chap. 5]. Notice also that the total deformation is considered small. This means that the convective contributions in any temporal derivative are neglected.

As previously, the total rate-of-strain tensor is written as follows

$$\dot{\boldsymbol{\epsilon}} = \dot{\boldsymbol{\epsilon}}_{\text{el}} + \dot{\boldsymbol{\epsilon}}_{\text{vp}} + \dot{\boldsymbol{\epsilon}}_{\text{th}}, \quad (3.19)$$

with the three contributions given by

$$\dot{\boldsymbol{\varepsilon}}_{\text{el}} = \frac{1+\nu}{E}\dot{\boldsymbol{\sigma}} - \frac{\nu}{E}\text{tr}(\dot{\boldsymbol{\sigma}})\mathbf{I}, \quad (3.20)$$

$$\dot{\boldsymbol{\varepsilon}}_{\text{vp}} = \frac{\sqrt{3}}{2s_{\text{eq}}}\max\left(0, \frac{s_{\text{eq}} - \sigma_y - H\varepsilon_{\text{eq}}^n}{K\sqrt{3}}\right)^{1/m} \mathbf{s}, \quad (3.21)$$

$$\dot{\boldsymbol{\varepsilon}}_{\text{th}} = \alpha\dot{T}\mathbf{I}. \quad (3.22)$$

The elastic deformation follows a linear behavior with  $\nu$  the Poisson coefficient and  $E$  the Young modulus. The tensor  $\dot{\boldsymbol{\sigma}}$  in (3.20) is the temporal derivative of the Cauchy stress tensor.

The visco-plastic contribution presents a non-continuous behavior with the occurrence of the yield stress  $\sigma_y$  completed by a strain hardening modeling by  $H$  and the strain-hardening exponent  $n$ . The operator  $\max(0, x)$  means that when the equivalent stress defined by

$$s_{\text{eq}} = \sqrt{\frac{3}{2}\mathbf{s} : \mathbf{s}} \quad (3.23)$$

is less than  $\sigma_y + H\varepsilon_{\text{eq}}^n$ , the visco-plastic rate-of-strain tensor vanishes. The two other parameters  $K$  and  $n$  are the same physical meaning as on the previous paragraph. The equivalent strain,  $\varepsilon_{\text{eq}}$ , is determined by the temporal integration as follows

$$\varepsilon_{\text{eq}}(\mathbf{x}, t) = \int_{t/T=T_c}^t \dot{\varepsilon}_{\text{eq}}(\mathbf{x}, t') dt', \quad (3.24)$$

only computed in the range of temperature below  $T_c$ , i.e. in the elasto-visco-plastic domain.

In THERCAST<sup>®</sup>, all parameters of the constitutive equations are defined point-wise and function of the temperature. Data for the AZS are presented below. As already indicated, the critical temperature should be close to the coherence point. According to Bellet et al. [70],  $T_c$  is taken close to the solidus temperature. However, for oxide materials like AZS, a large amount of a glassy phase,  $\sim 20\%$  leads to that the solidus is never reached. The critical temperature is taken equal to  $1600^\circ\text{C}$  corresponding to the "end of crystallization". As shown in Figure 1.11, below  $1600^\circ\text{C}$ , the fraction that has not solidified yet is around  $10\%$ . Such critical temperature is still widely above the glass transition temperature of the glassy phase around  $780^\circ\text{C}$ [12]

Numerically, such behavior is solved with the pressure and the velocity as primitive variables. The finite element method requires a weak form of the mass balance and the momentum balance equations. In the mixed formulation, the stabilization requirement, Ladyzhenskaya-Babuška-Brezzi (LBB) condition [74], needs to enlarge the velocity space. Both the pressure and the velocity are linear functions in each element but one degree of liberty is added for the velocity: the "bubble" in the center of the element. The simplest element verifying the LBB condition is  $\mathbb{P}_1$  – bubble/ $\mathbb{P}_1$  and it defines an element in THERCAST<sup>®</sup>. More details in the numerical formulation can be found in [70].

**ALE formulation:** Since the density is not constant, the material is not iso-volume. When the temperature decreases, the contraction appears. In the case of a mold fully rigid, an air gap is formed between the mold and the AZS block. In THERCAST<sup>®</sup>, the numerical method used to describe this contraction is the Arbitrary Lagrangian Eulerian method. The main idea of this method is to move the nodes of each element according to the material velocity. Recall that the Lagrangian description follows the material in its motion. This means that

the mesh velocity is equal to the material velocity. Conversely, the Eulerian description works in immobile domain. In this case, the mesh velocity is equal to zero. In THERCAST<sup>®</sup>, the solidified regions are described as Lagrangian description. The liquid-like regions are considered as a Lagrangian-Eulerian description for which the mesh velocity is determined to respect the divergence conservation through each element but the material is transported by the Eulerian velocity in relative motion to the mesh displacement. Details about this formulation is provided in [70].

### 3.2.2 Interface definition in thermo-mechanical computations

#### Interfaces between all objects except the AZS block

As in Chapter 2, a constant heat transfer coefficient,  $h_{ij}$ , is considered between two domains  $i$  and  $j$  with  $i, j \neq \text{AZS}$  as detailed in (2.18).

#### Interface AZS-Mold

An air gap is modeled at the AZS-Mold interface due to solidification shrinkage. Its thickness is  $e_{air}$  and the air thermal conductivity is  $\lambda_{air}$  defined with two values presented in Table 3.1.

0 °C	0.025 W m <sup>-1</sup> K <sup>-1</sup>
1500 °C	0.16 W m <sup>-1</sup> K <sup>-1</sup>

Table 3.1: Air thermal conductivity depending on temperature in THERCAST<sup>®</sup>.

An initial value for the contact resistance ( $1/h_{AZS/Mold}^{initial}$ ) is defined identical to the one defined in Table 2.3. At each time step, a comparison is done between this initial resistance and the resistance implied by the air layer [19]. The thermal resistance due to air layer is detailed in (3.27).

$$\begin{cases} \lambda_{AZS} \nabla T_{AZS} \cdot \mathbf{n} = \lambda_{Mold} \nabla T_{Mold} \cdot \mathbf{n} \\ \lambda_{AZS} \nabla T_{AZS} \cdot \mathbf{n} = \frac{1}{R_c} (T_{Mold} - T_{AZS}) \end{cases} \quad (3.25)$$

$$\text{with} \quad \frac{1}{R_c} = \min \left( h_{AZS/Mold}^{initial}, h_{radiation} + \frac{\lambda_{air}}{e_{air}} \right) \quad (3.26)$$

$$\text{and} \quad h_{radiation} = \epsilon_{AZS} \sigma_B (T_{AZS} + T_{Mold}) (T_{AZS}^2 + T_{Mold}^2) \quad (3.27)$$

#### AZS-Media interface

At the top of the AZS block, an interface between AZS and Media is observed (# 8 in Figure 2.1). It models the fact that after casting, extra amount of annealing media can cover the AZS and hence limit heat exchanges by the top.

For such interface, resolved equations (3.28) are the same than for AZS/Mold interface (Eq.3.25) but with a specific initial contact resistance  $h_{AZS/Media}^{initial}$  as presented in Table 2.3:

$$\begin{cases} \lambda_{AZS} \nabla T_{AZS} \cdot \mathbf{n} = \lambda_{Media} \nabla T_{Media} \cdot \mathbf{n} \\ \lambda_{AZS} \nabla T_{AZS} \cdot \mathbf{n} = \frac{1}{R_c} (T_{Media} - T_{AZS}) \end{cases} \quad (3.28)$$

$$\text{with} \quad \frac{1}{R_c} = \min \left( h_{AZS/Media}^{initial}, h_{radiation} + \frac{\lambda_{air}}{e_{air}} \right) \quad (3.29)$$

$$\text{and} \quad h_{radiation} = \epsilon_{AZS} \sigma_B (T_{AZS} + T_{Media}) (T_{AZS}^2 + T_{Media}^2) \quad (3.30)$$

### Symmetries

In mechanical computations, a symmetry plane implies sliding conditions besides their adiabatic conditions for thermal computations.

In numerical simulations, the mold geometry is fixed and impenetrable. Therefore when the block shrinks, an air layer of few centimeters is modeled at the bottom of the block as presented in Figure 3.1. The block is hold at the neck of the riser in the simulations, just above the block when the horizontal section increases. As mold burns, the block can go down due to gravity and this phenomenon is not reported in the literature or detailed in industrial feedbacks. To avoid such numerical artifact, a sliding condition is set between the AZS and the mold. It forces locally the contact between the plane attached at the bottom face AZS and the plane defining the upper section of the mold domain. As the mold is fixed, this sliding condition inhibits vertical motions of the bottom face of the AZS domain (separation of both plane previously defined) but it allows an horizontal deformation to model the air layer formation between the AZS block and the side walls of the mold.

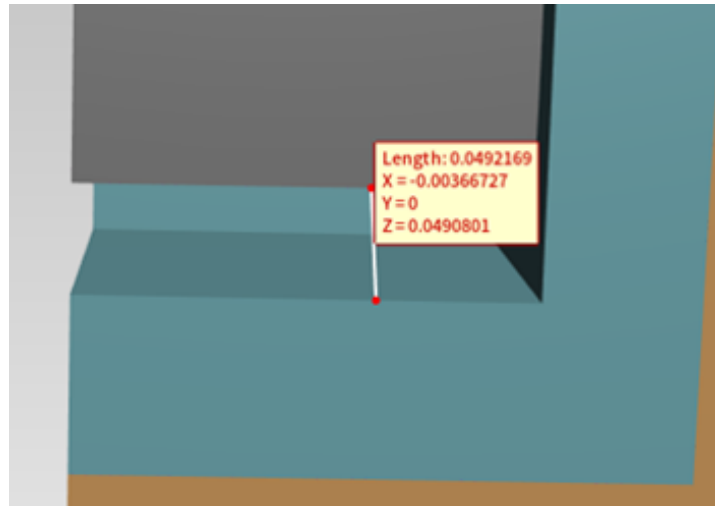


Figure 3.1: Air layer of 5 cm height formed at the bottom of the block due to the solidification shrinkage as the neck of the riser holds the block.

### Air-AZS interface : opening of macro-porosity due to solidification shrinkage

THERCAST<sup>®</sup> can represent solidification shrinkage with an opening inside the domain that can grow as the block continues to shrink after the opening. A parameter called "Open Shrinkage Threshold" (OST) [19] is set to determine the internal cavity opening. By default, this value is at 0.6. The impact of this parameter is detailed in § 3.4.2.1. The internal AZS/Air interfaces are defined as adiabatic.

### 3.2.3 Mechanical properties of AZS

As the numerical values for the constitutive equations (3.21) and (3.20) have been determined for high zirconia in previous PhD. theses [5, 66], similar settings are considered for AZS as specific values have not been experimentally tested for this AZS composition. Mechanical properties of AZS materials are summed up in Table 3.2.

Mechanical tests have been done at temperature below 1500 °C, when solidification can be considered as fulfilled. Values have therefore to be artificially defined at high temperatures otherwise THERCAST<sup>®</sup> keeps the last value tabulated.

Property	E	$\nu$	$\sigma_y$	SH	K
Unit	GPa		MPa	MPa	Pa s
Value	Figure 3.2a	0.14	Figure 3.2b	1 150	Figure 3.3

Table 3.2: Mechanical properties for the different materials.

### Elastic properties

Young modulus and yield stress have been determined by 3 points bending tests in isothermal conditions on AZS 150x25x15 mm<sup>3</sup> samples. Yield stress is the stress value above which visco-plastic deformations are observed, without considering the strain hardening. Results are presented in Figure 3.2 where each dot represents an experiment. When glass transition temperature of the glassy phase is crossed (at around 780 °C), the Young modulus and yield stress decrease. Measurements could not be performed until  $T_c$ . If temperature is out of tabulated range (for example above 1200 °C), the Young modulus and yield stress values used in the simulation are the last values tabulated.

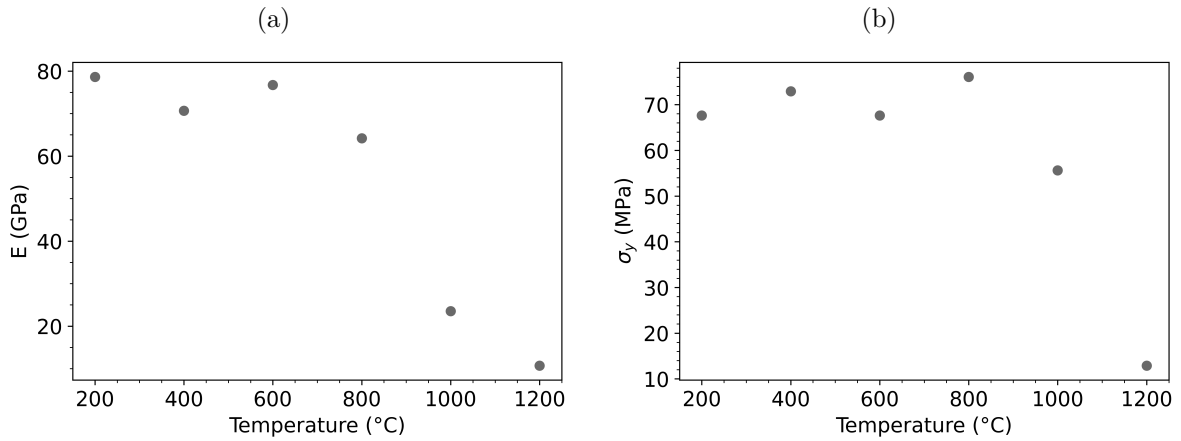


Figure 3.2: (a) Young Modulus and (b) Yield Stress tabulated over temperature for AZS material where each dot represents an experiment.

### Viscoplastic properties

Experimental creep tests have been performed at different temperatures below the liquidus temperature [11]. Massard [12] and Petroni [66] performed experimental creep test. Consistency from stationary stage (when the strain rate is constant) can be retrieved considering  $A_0$  the pre-exponential factor,  $E_a$  the activation energy,  $R$  the perfect gas constant and  $T$  the temperature. Experimental data (purple in Figure 3.3) gives  $A_0 = 2.8 \times 10^{-5} \text{ MPa}^{-1} \text{ s}^{-1}$  and  $E_a = 8.5 \times 10^4 \text{ J mol}^{-1}$ . With (3.31), it is possible to extrapolate at any other temperatures the value of consistency (square in Figure 3.3). In the mushy zone (above  $T_c$ , blue line in Figure 3.3), as liquid phase is present, material resistance drops. Such variation is not quantified experimentally and the decrease is therefore arbitrary defined.

$$\dot{\epsilon} = A_0 \sigma^n \exp\left(-\frac{E_a}{RT}\right). \quad (3.31)$$

$$K = A_0^{-1/n} \exp\left(\frac{E_a}{nRT}\right). \quad (3.32)$$

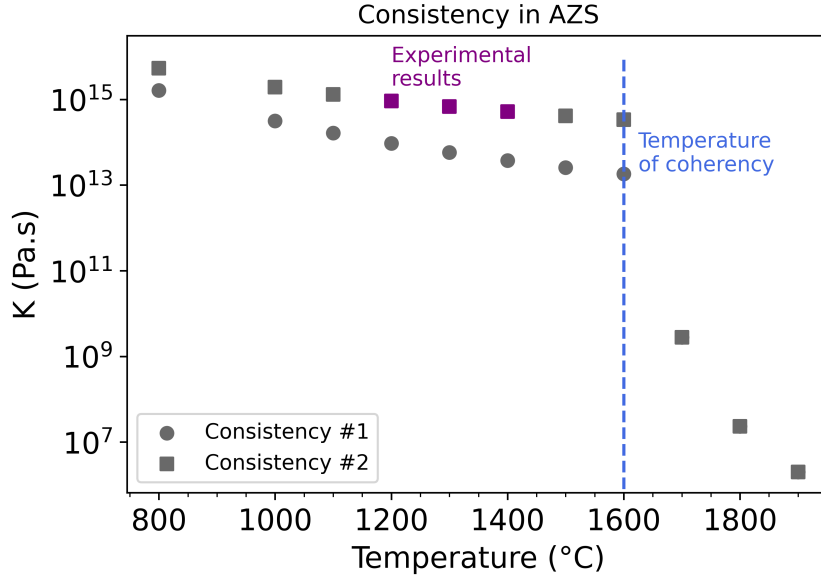


Figure 3.3: (Square) AZS consistency (purple) determined experimentally thanks to creep tests and (gray) extrapolated for temperatures below  $T_c$  or arbitrary decreases above, (circle) arbitrary soften material to quantify the impact of consistency on mechanical outputs.

Lu *et al.* [75] have shown a strong variation of behavior when the refractory receives a solicitation in compression or in tension at the same temperature and same strain rate. In literature [5, 12, 13, 66] most of the tests are possible in compression or bending conditions until 1 500°C and focused on high zirconia refractory materials. No experimental data are available in the mushy zone, when hot tears opens. Liquid viscosity is simulated at around  $10^6$  Pa.s, far from experimental results at around 40-60 mPas. The mechanical solver is solid-oriented and numerical liquid viscosity is increased to avoid a too wide range of visco-plastic consistency. Such increased viscosity inhibits motions inside AZS domain. Consequently, convection is not modeled as it could be with a fluid oriented solver.

To quantify the impact of the consistency on mechanical results, two consistency tabulations are considered. Consistency #1 (circles in Figure 3.3) implies a less viscous material than consistency #2 (squares in Figure 3.3). It is then possible to model a block more than 10 times softer than the viscosity properties obtained by the experimental results at temperatures inside glass furnaces but not in the mushy zone. The impact of the consistency tabulation are detailed later in § 3.3.4.3.

### 3.2.4 Impact of thermo-mechanical computations in temperature history prediction

The temperature history is checked in the presence of thermo-mechanical deformations. Considering results in Figure 3.4, almost no variation of temperature is observed for sensors at the middle and top sections of the block, even if an air layer is computed between the block and the mold. At the bottom of the block, the simulations are slightly better in thermo-mechanical computations. The predictions of the riser are not improved, even if a macro-porosity is now predicted inside the riser.

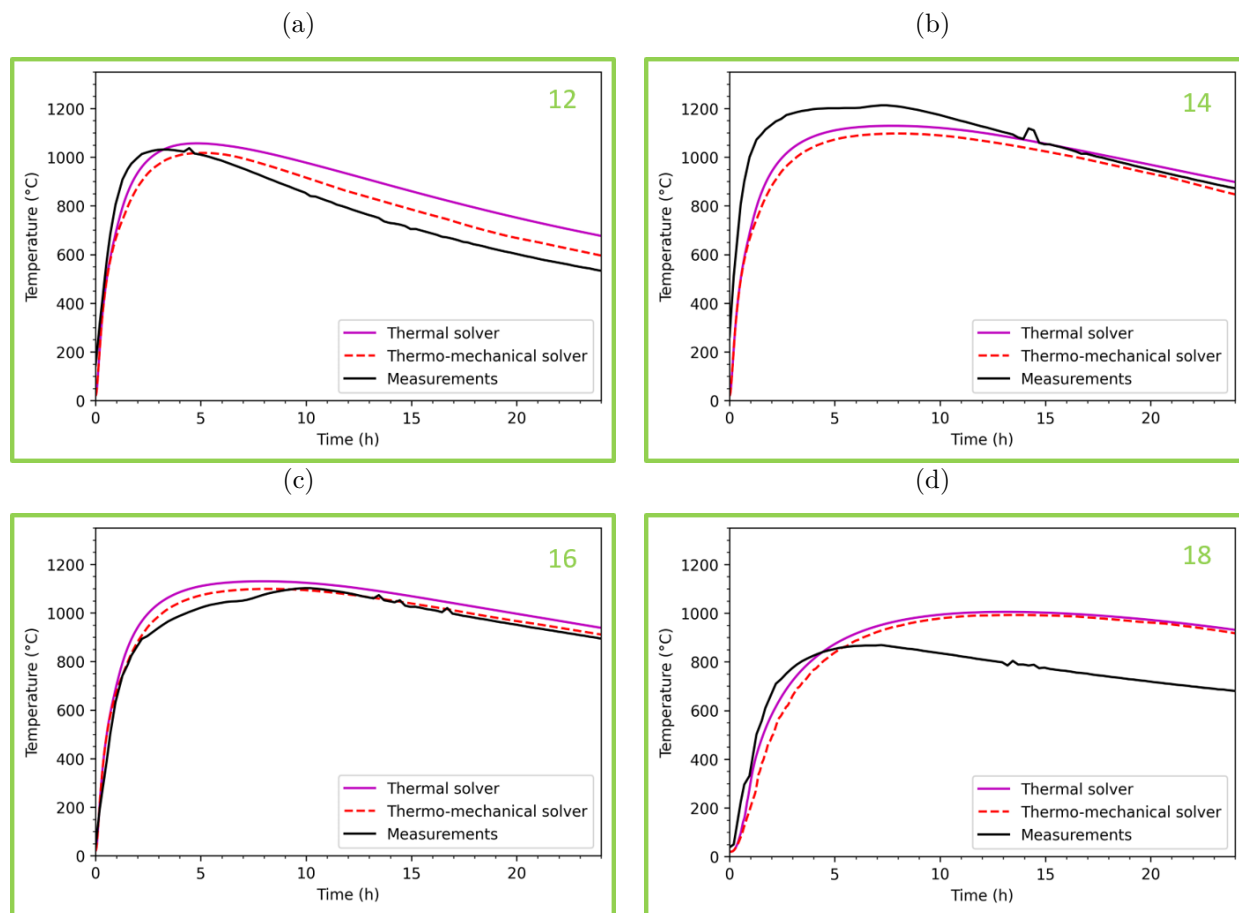


Figure 3.4: Comparison of temperature histories at different locations (see Figure 2.11) for (black) experimental recorded data, (dashed red) computed with default THERCAST<sup>®</sup> thermal solver and (pink) default THERCAST<sup>®</sup> thermo-mechanical solver : (a) #12 bottom of the block, (b) #14 middle of the block, (c) #16 top of the block, (d) #18 riser.

### 3.3 Prediction of hot tears susceptibility in AZS block

Running the mechanical solver increases a lot the computation duration as the first day of annealing is computed in a couple of days over 32 cores as for thermal computations. The objective of mechanical computations is to predict the hot tears occurrence at the edge of the block. The industrial observations of blocks presented by Cockcroft [8] show that more than one block over two present edge tears.

In a first subsection, observations of hot tears are presented. In a second one, a literature review sums up hypothesis about hot tears formation and criteria developed for metal alloys to predict the Hot Cracking Susceptibility (HCS). Then, the adaptations of the Yamanaka criterion are presented. Such criterion considers cumulated strain over a Brittle Temperature Range (BTR) which needs to be defined for the AZS material. Finally, a case study comparing several industrial geometries is used to validate the results of HCS obtained with such criterion.

#### 3.3.1 Experimental observations of hot tears along edges

On some industrial blocks, hot tears are visible along edges as in Figure 3.5a. Those cracks are easily detectable by visual inspection of the block. The color around the tear is orangish

compared to the other regions of the block, as in Figure 3.5c. The color is due to a higher level of oxidation of impurities such as  $\text{Fe}_2\text{O}_3$ . Healed cracks, as the one in Figure 3.5b, are cracks that have been refilled by liquid before the end of the solidification process.

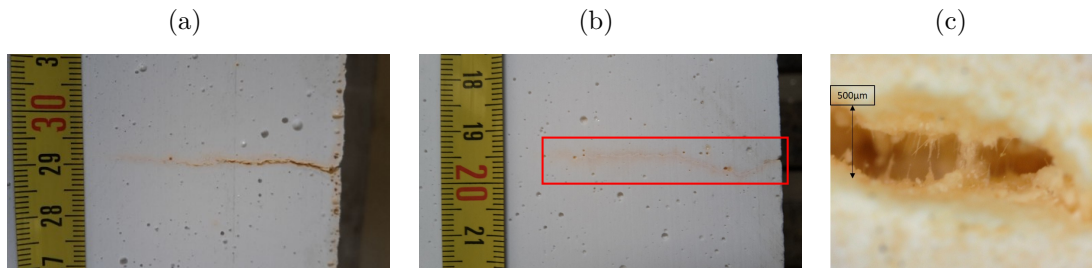


Figure 3.5: Photo of hot tears in industrial blocks taken during a trial in SEPR plant with (a) a photo of an edge crack taken with a phone camera (8 Mpx), (b) a photo of an healed crack taken along the polished face of the block with a phone camera (8 Mpx) and (c) the photo of the inside of a hot tear obtained with a DinoLite USB camera [76] from a polished face of the block.

Hot tears are observed on the entire height of the edge but in a proportion slightly more important at the center section of the block.

Some hot tears from industrial block from SEPR plant have been cut, mounted on with epoxy resin and polished for SEM observations. Figure 3.6 reveals the micro-structure. At the very skin of the AZS block, the microstructure is extremely fine compared to the one few millimeters further inside the block. Similar observations are reported by Wisniewski [51] with EBSD analyses over the first 24 mm of an AZS sample (with 40 wt.% of  $\text{ZrO}_2$ ) without crack.

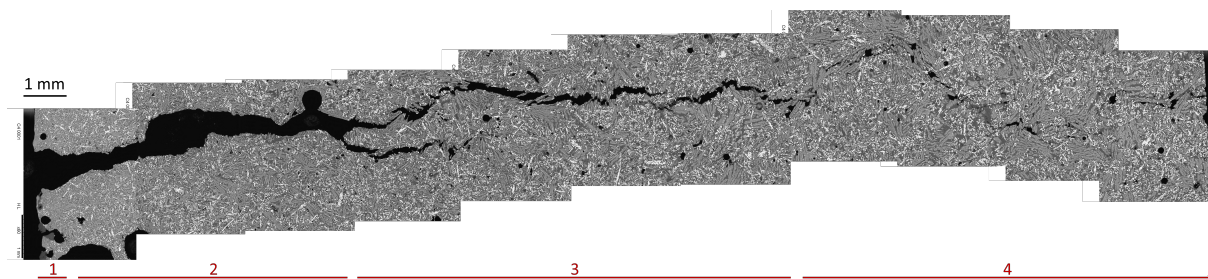


Figure 3.6: SEM observations of hot tears revealing different regions for the crack numbered #1 to #4.

Different hot tears were observed with SEM. They present a similar morphology within the four regions that can be described as follows from the skin to the core of the block:

1. Opening of the tear at the skin of the block. The very skin, with an extremely fine microstructure, has a thickness around roughly 200-400  $\mu\text{m}$ . [51].  
Crack dimensions in Figure 3.6 : length 0.59 mm & opening width 1 mm
2. Wide opening without remaining strings of vitreous phase.  
Crack dimensions in Figure 3.6 : length: 5.47 mm & opening width 500  $\mu\text{m}$
3. Thinner opening with remaining strings of vitreous phase.  
Crack dimensions in Figure 3.6 : length 8.68 mm & opening width 200  $\mu\text{m}$

4. Very thin and unjoined openings (like cavitation) inside the glassy phase.  
 Crack dimensions in Figure 3.6 : length more than 8 mm & opening width  $< 100 \mu\text{m}$

When observing closely the crack in region 3 (Figure 3.7), the liquid strings between both faces of the crack are still visible. No crystal or micro-crystal are observed inside those strings. The cracks seems to occur when all the zirconia and corundum crystals have solidified and before the remaining liquid has become a solid vitreous phase. The glassy phase viscosity is presented by Lataste [11] for a synthetic glassy phase enhanced in soda for casting feasibility.

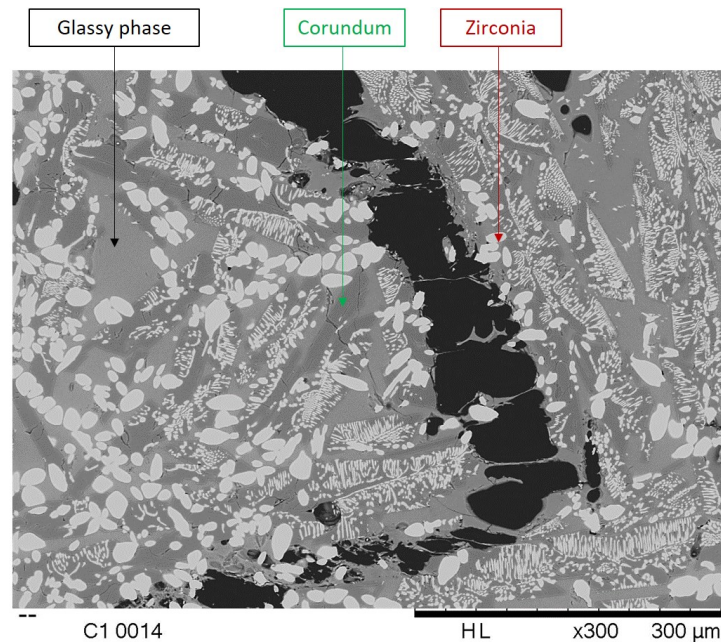


Figure 3.7: SEM observation of a hot tear showing the presence of solidified liquid strings and the distribution of phases.

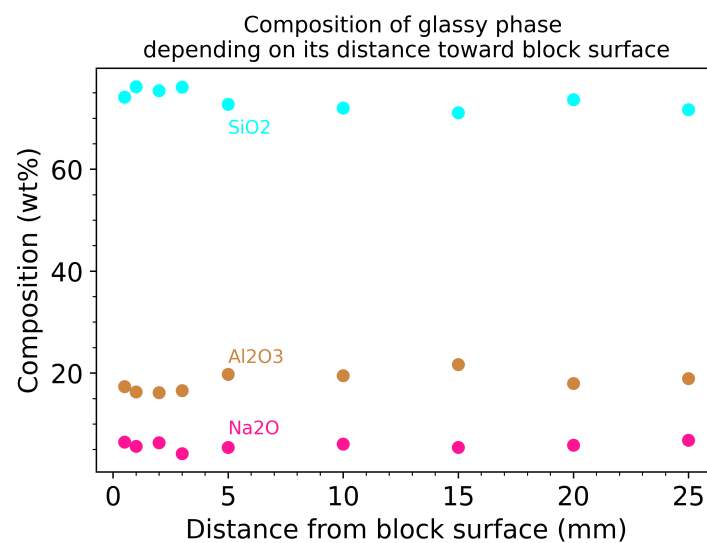


Figure 3.8: Composition of the glassy phase close to the opening of the crack at different depths from the skin by EPMA at room temperature.

Composition of the glassy phase along the opening of the crack has been measured by micro-probe. Analyses performed at SGR Provence return similar compositions all along the crack (from 0.5 mm to 25 mm deep) as shown in Figure 3.8. Closer to the interface (0.1 mm), glassy phase is detected but its dimensions are smaller than  $1 \mu\text{m}$  and chemical analyses are not possible because of a too strong sodium migration submitted to electron beam.

### 3.3.2 Literature review about hot tears formation

According to Cockcroft [8], horizontal cracks on AZS blocks are divided into three categories presented in Figure 3.9: the large horizontal cracks, the smile-shaped ones located at the bottom (first 20-30 cm) and the edge tears. Horizontal cracks distribution is all along the block except at the bottom and in the riser. Close to the bottom face ( $z = 0$  to  $z = 254$  mm), isotherms are curved and zirconia transition can lead to smile-shaped cracks. Maximal axial stresses evidenced by modeling in [49] are predicted in the middle of the block, after almost 1 day of annealing, when the temperature is around  $1000 \text{ }^\circ\text{C}$  (corresponding to the zirconia martensitic transition from tetragonal to monoclinic). Increasing the zirconia content should increase the strain generation during its phase transition to monoclinic. However, no industrial feedback reports a strong impact on hot tears when comparing the two compositions presented in Chapter 2 at 36 wt.% and 41 wt.% of  $\text{ZrO}_2$ .

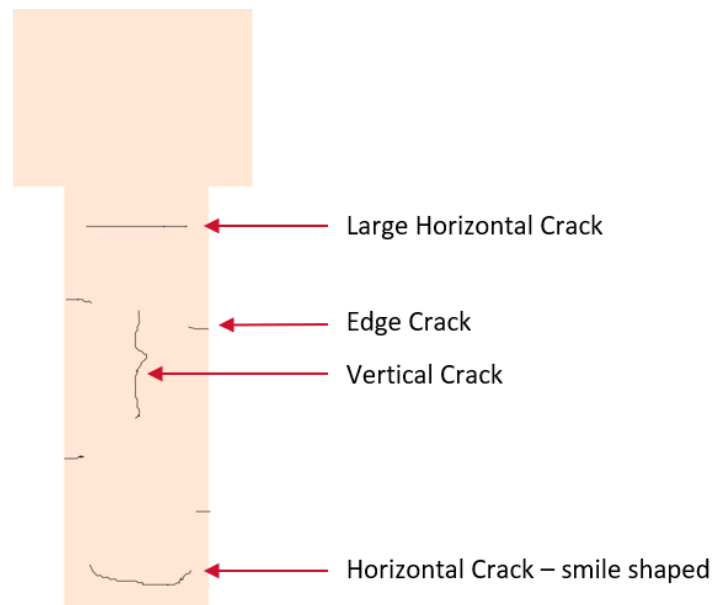


Figure 3.9: Schematic of different types of cracks that can be observed on AZS blocks : vertical cracks and the three types of horizontal cracks : large horizontal cracks, smiled-shaped cracks and edge tears [8].

During solidification of the block, the permeability of the mushy zone decreases, leading to a lack of liquid feeding. Locally, the pressure drops and the region is facing tensile stresses. The strain rate perpendicular to temperature gradient is written  $\hat{\epsilon}$ , in purple in Figure 3.10. The strength of the mushy zone is still reduced compared to a fully solidified area due to the presence of an intergranular liquid film. As a consequence, stresses perpendicular to the temperature gradient can lead to the formation of hot cracks, also called " hot tears ". The shape of the cracks is different from regular shrinkage porosity (cavities observed in the riser) or gaseous porosity (bubble due to lower gaseous solute solubility at lower temperature) [56].

Two combined reasons are considered to explain the edge tears formation [56]:

- Lack of liquid feeding due to the decrease of permeability into solid channels;
- Tensile stresses, induced by temperature gradient during annealing, accumulates tensile strain in the material until it reaches its critical resistance;

During casting, the stresses due to quenching (skin of the block) are simulated by Cockcroft at a lower level compared to the stress generated by zirconia phase transition [49]. No critical value is determined specifically for AZS. However, such critical value might depends on microstructure and therefore be different between the skin and the core of the block. Indeed, the surface presents a finer microstructure (see Figure 3.6) and also variations in composition due to volatile components (such as  $\text{Na}_2\text{O}$ ). Mechanical properties of the material retrieved at block surface have not been characterized as a single constitutive equation is considered all over the block.

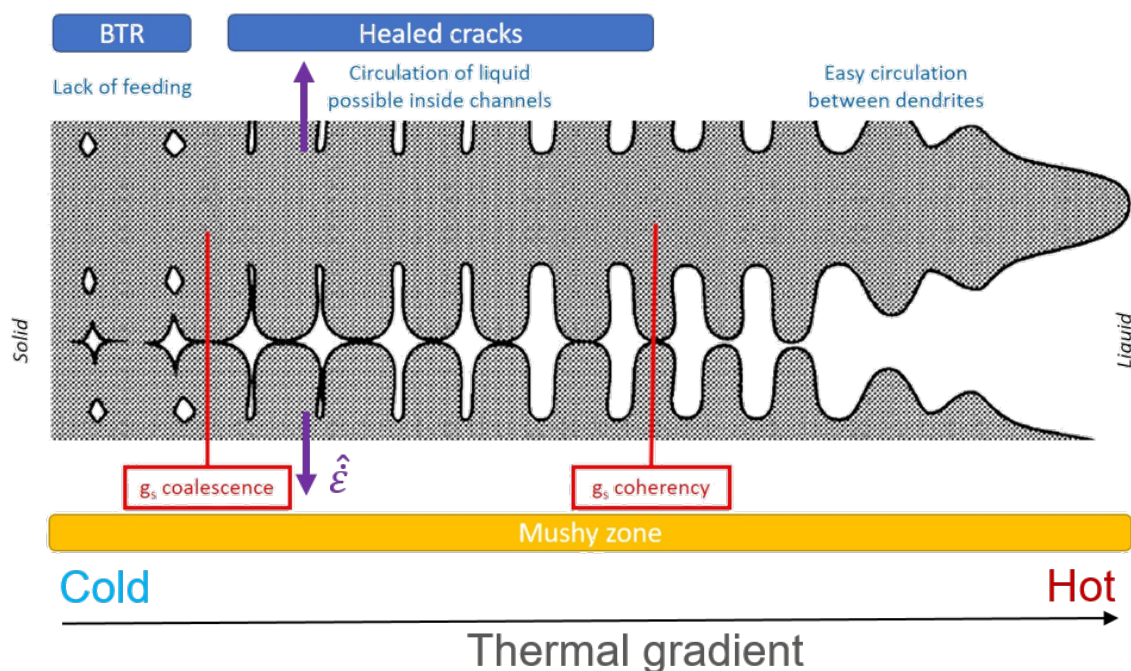


Figure 3.10: Schematic growth of dendrites, adapted from [57].

Just after dendrites coalescence (at solid fraction higher than  $g_s coalescence$  in Figure 3.10), the whole structure is connected and it can propagate stress. However, liquid channels are now closed, liquid feeding is not possible anymore. In case of high temperature gradient (along the edges) the solidification could be too fast and liquid feeding could not compensate the strain to avoid a crack opening. The Brittle Temperature Range (BTR) [17, 56] is defined as the interval between the coalescence of solid dendrites and the solidus temperature when permeability drops and the intergranular film might crack. For steels, BTR is when the solid fraction is defined between 0.9 and 0.99 [10, 18]. Below 90 vol.% of solid phase, the stresses can still be relaxed with a crack that will be filled by remaining liquid after its opening (Figure 3.5b). Healed cracks are typically observed when solid fraction is between 0.4 and 0.9.

As there is 20 vol.% of vitreous phase in the AZS final micro-structure, the BTR definition needs to be adjusted for ceramics and no BTR for AZS is already available in literature. In THERCAST<sup>®</sup>, a study with several temperature intervals is detailed in § 3.3.4.2.

### 3.3.3 Criteria for Hot Cracking Susceptibility (HCS) prediction

Cerri [15] sums up several HCS criteria depending on the mechanical outputs considered (strain or stress). Stress-oriented criteria have been considered historically and the most recent criteria are more strain-oriented. Some criteria consider a critical value that can depend on composition, strain rate, BTR length,... Currently, no critical value is retrieved for refractory ceramics such as AZS in literature.

Several criteria, such as the Rappaz-Drezet-Gremaud criterion [16], were developed to quantify HCS in steels or Al-Cu metal alloys but not all of them are implemented in THERCAST<sup>®</sup>. Criterion implemented in THERCAST<sup>®</sup> (such as the Won criteria [17]) are mostly based on the cumulated strain with a critical value usually defined for steels [77].

#### 3.3.3.1 Clyne-Davies criterion

##### Main principle:

Such criterion was initially defined by Clyne and Davies in 1979 [18] for Al-Cu alloys. This criterion is a non-mechanical criterion as it is based only on thermal consideration. It is the ratio between the time spent in the BTR (left on Figure 3.10) and the time spent in the "healed cracks" zone (middle on Figure 3.10) [78].

The Hot Cracking Sensitivity (HCS) is expressed by (3.33) [15]. Typical HCS values observed for Al-Cu alloys are between 0 and 1 [16].

$$HCS = \frac{t_{99} - t_{90}}{t_{90} - t_{40}} \quad (3.33)$$

This criteria was adapted by Katgerman in 1982 [15], replacing in the equation the specific fractions by times related to physical phenomena as presented in (3.34)

$$HCS = \frac{t_{\text{solidus}} - t_{\text{coalescence}}}{t_{\text{coalescence}} - t_{\text{coherence}}} \quad (3.34)$$

##### Results for AZS material:

For AZS material, as the glassy phase is modeled as remaining liquid phase, the solidus is not reached. The fraction are adapted by removing the 20 % of glassy phase from the previous equation and presented in (3.35).

$$HCS = \frac{t_{80} - t_{71}}{t_{71} - t_{21}} \quad (3.35)$$

Five horizontal planes are defined in the block section at 0.3, 0.6, 0.9, 1.2 and 1.5 m height. On each plane, five sensors are defined with coordinates : (0,0) at the center of the block, (0,0.128) at the middle of the major face, (0.203,0) at the middle of the minor face, (0.203,0.128) at the edge of the block and (0.15,0.1) inside the block. The averaged HCS values and standard deviations over the different heights are plotted in Figure 3.11 depending on their (x,y) coordinates.

For a given (x,y) position, the HCS predictions thanks to Clyne & Davies criterion are similar for the five horizontal planes as the standard deviation values are quite small. For the sensors located at the edge of the block, the specific solid fraction are reached at the same increment which implies the same HCS prediction exactly. The region with the most risks of

hot tears is predicted to be the center of the major face with a HCS at 2.73. In comparison, at the center of the block, HCS is estimated at 0.47. The edge gets a HCS of 1.72, below the center of major face value whereas the hot tears are observed experimentally along the edge. This criterion does not seem well adapted for hot tears prediction in AZS material.

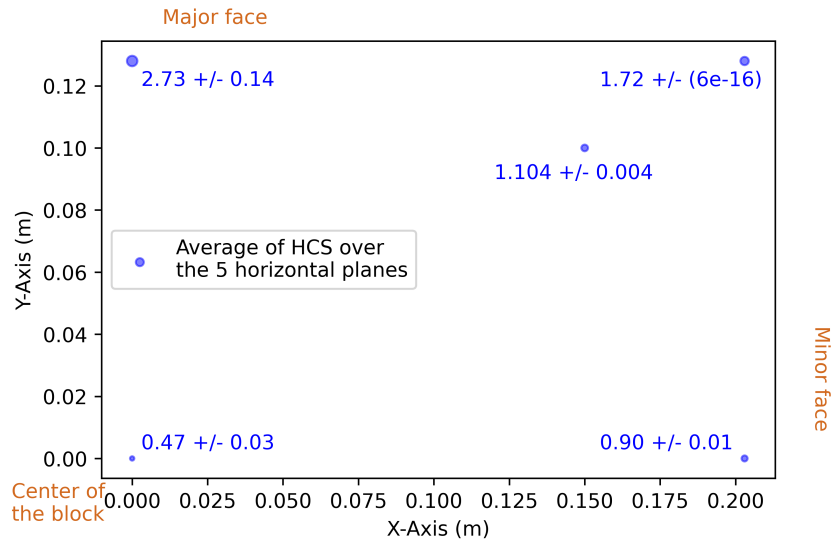


Figure 3.11: Averaged HCS prediction for the five horizontal planes with Clyne & Davies criterion for AZS material considering consistency #1 mentioned in Figure 3.3.

**Pros:**

- HCS value easy to determine from such a basic approach. Knowing the solidification path, the three different time values considered can be retrieved;
- Lambda-shaped curves<sup>1</sup> observed experimentally for metal alloys can be retrieved by simulations [18].

**Cons:**

- Consider only the temperature field and not the uniaxial tensile deformations applied on dendrites that are responsible of the tear;
- This criterion was developed for Al-Cu experiments, updated for other alloys and steel but not for ceramics (and its glassy phase);
- Accuracy is not perfect. For Al-Cu alloys, the HCS changes depending on the concentration in Cu (lambda curves). The critical composition, experimentally observed at around 0.5 wt.% Cu, is simulated at around 5.7 wt.% Cu.

<sup>1</sup>The curve of HCS as function of the solute concentration will result in a lambda-shaped curve with a maximal Hot Cracking Sensitivity for a critical composition

### 3.3.3.2 Yamanaka criterion

#### Main principle:

Yamanaka *et al.* [79] estimated the internal cracking risk in continuous casting in 1995 thanks to tensile tests and solidification analyses. Tensile tests are performed on cylindrical samples with a liquid core.

Yamanaka criterion can be expressed as a strain-based criterion, considering only the strain perpendicular to the temperature gradient  $\hat{\epsilon}$ .

$$HCS = \int_{ZST}^{ZDT} \hat{\epsilon} dt \quad (3.36)$$

Two specific temperatures are considered that overlapped the BTR and the "healed cracks" temperature range:

- Zero Ductility Temperature (ZDT), set at  $g_s=0.99$  for steels, corresponding to the end of solidification, when the material starts to present plastic deformation instead of brittleness,
- Zero Strength Temperature (ZST), set at  $g_s=0.8$  (instead of 0.4 in Clyne and Davies criteria), corresponding to coherency temperature in Figure 3.10.

When the strain rate is above  $2.0 \text{ s}^{-1}$  for a given steel composition, every sample will present cracks above the same strain value : 1.9%. At lower strain rate, an increased deformation has to be reached to observe cracks experimentally.

#### Results for AZS material:

Yamanaka *et al.* defined a critical strain value for steel. Such value has not been determined for AZS material. As for the former criterion,  $g_{ZST}=0.7$  and  $g_{ZDT}=0.79$ . Computations with consistency #1 defined in Figure 3.3 return HCS predictions as detailed in Figure 3.12. The standard deviation between the values obtained for sensors with the same (x,y) but at different height is in the same order of magnitude than the average value as mentioned in Figure 3.12. This criterion is not stable along the height of the block except at the center of the major face where the HCS results are more similar between the different horizontal planes considered. The region with the highest risk of cracks is at the center of the major face instead of the edge of the block as observed experimentally.

#### Pros:

- This criterion takes in consideration solidification stages (coherency, solidus) to determine the BTR
- It considers the strain applied on the system and not only the temperature history of the material

#### Cons:

- This criterion predicts HCS values that evolves a lot along the height of the block section
- For AZS, the accumulated strain at the edge of the block is close to 0.01 % whereas for steel the strain is between 1-2 % [79].

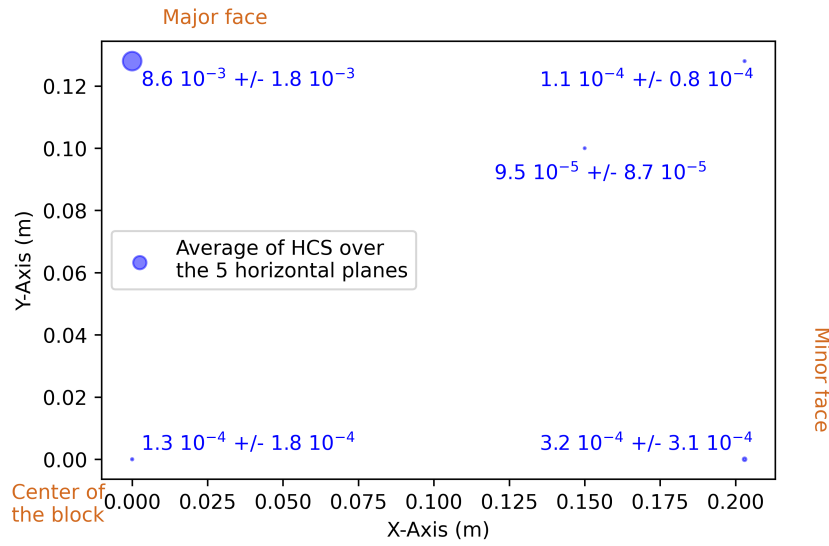


Figure 3.12: Averaged HCS prediction for the five horizontal planes with Yamanaka criterion for AZS material considering consistency #1 mentioned in Figure 3.3.

### 3.3.3.3 Won criterion

#### Main principle:

Won *et al.* presented their Hot Cracking Susceptibility criterion in 2000 [17]. This criterion improves the Yamanaka criterion by adding a critical value dependent of process and material solidification history. It was defined for continuous steel casting, considering two phases : liquid and solid in a columnar dendrites zone. This criterion focuses on steel with carbon content lower than 1 wt.% in continuous casting processes. It considers the cumulated strain deformation energy along the BTR as expressed in (3.38) and compares it to a critical value. If the energy is higher than the critical value that can be handled by the steel, hot tears occur. The released energy is divided into surface energy of the crack and kinetic energy at its extremities.

The BTR and the strain rate are the main parameters integrated over time of this criterion, for comparison with the critical strain value,  $\varepsilon_c$ , defined in (3.37). This critical strain expression is determined after experimental results from various compositions of steels and different strain rates.

$$\varepsilon_c = \frac{\phi}{\dot{\varepsilon}^{m^*} (BTR)^{n^*}} \quad (3.37)$$

$$\phi = 0.02821 \text{ (in } K^n \text{ s}^{-m}\text{)}, m^* = 0.3131, n^* = 0.8638, \text{ and } \dot{\varepsilon} \text{ strain rate}$$

In this criterion, ZST is set at  $g_s=0.75$  (instead of 0.4 in Clyne and Davies criteria), ZDT is set at  $g_s=0.99$ . A third specific temperature can be mentioned : Liquid Impenetrable Temperature (LIT) that is set at  $g_s=0.9$  for steels. It defines the temperature after coalescence of the system when liquid feeding is not possible anymore.

Won *et al.* consider a mushy zone behavior identical to the liquid behavior above the ZST [17]. Between ZST and LIT, the material is porous and the cracks can be healed by liquid feeding as represented in the middle region of Figure 3.10. This temperature interval (ZST-LIT) is not considered to determine the Hot Cracking Sensitivity of the material.

Won *et al.* [17] define the BTR as the interval of temperatures between the LIT and the ZDT. The BTR depends on the cooling rate and the material composition. In current simulations, only nominal composition is considered as no macrosegregation is taken into account. This implies that a single BTR is considered for such system. Inside the BTR, the accumulated deformation energy,  $W_{BTR}$ , can be used to predict the crack propagation, as expressed in (3.38) below. Increasing the change of deformation energy between the boundaries of BTR increases the probability of cracks.

$$W_{BTR} = \int_0^{\varepsilon_c} (\sigma_{ZDT} - \sigma_{LIT}) d\varepsilon \quad (3.38)$$

$W_{BTR}$  = (ductile fracture - brittle fracture) deformation energy

Stresses in the block are generated by thermal contraction, external mechanical loads and phase transformation stresses ( $\delta/\gamma$  for steel and tetragonal/monoclinic for  $ZrO_2$  crystals). The stresses  $\sigma_{ZDT}$  and  $\sigma_{LIT}$  are defined in (3.39) [17]. Won criterion gives therefore a quantitative solution of the stresses in continuous casting steel processes, for a wide range of temperatures (BTR) and for the different test conditions ( $\dot{\varepsilon}$ ).

$$\dot{\varepsilon} = A \exp\left(-\frac{Q}{RT}\right) \left[ \sinh\left(\beta \frac{\sigma}{\varepsilon^n}\right) \right]^{1/m} \quad (3.39)$$

with

- A,  $\beta$  material constants
- R perfect gas constant
- T in K
- n strain hardening exponent
- Q activation energy of the deformation
- m constant related to strain-rate sensitivity

The highest value of  $W_{BTR}$  is obtained by combining the effective strain rate definition (3.39) with the critical strain handled by the system (3.37). Typical strain rate for steel in continuous casting is around  $10^{-4}$  to  $10^{-3}$  s<sup>-1</sup>. For steel, the critical strain is reported between 0.5% and 3.8%. It is then possible to get the critical stress that can be obtained in each phase ( $\varphi$ ) as detailed in (3.40).

$$\sigma_{\varphi;c} = \frac{\varepsilon_{\varphi;c}^{n_{\varphi}}}{\beta_{\varphi}} \operatorname{arcsinh} \left\{ \left[ \frac{\dot{\varepsilon}}{A_{\varphi}} \exp\left(\frac{Q_{\varphi}}{RT}\right) \right]^{m_{\varphi}} \right\} \quad (3.40)$$

Won criterion can then be expressed also as a strain-based criterion, considering only the strain perpendicular to the temperature gradient  $\hat{\varepsilon}$ .

$$HCS = \int_{BTR} \hat{\varepsilon} dt - \hat{\varepsilon}_c \quad (3.41)$$

**Results for AZS material:**

The AZS coefficients for critical strain determination are unknown. They will be first considered as identical than for steel material even if the AZS material is a more concentrated alloy compared with the steel reference used in [17].

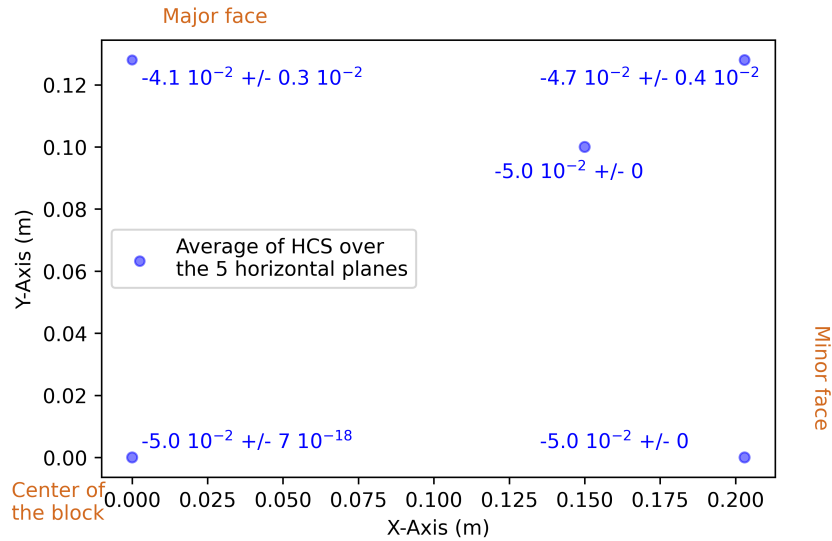


Figure 3.13: Averaged HCS prediction for the five horizontal planes with Won criterion for AZS material considering consistency #1 mentioned in Figure 3.3.

Won criterion predicts HCS values more stable in along the height of the block as the standard deviation are below 10% of the HCS averaged value along the height of the block, as mentioned in Figure 3.13. For the five sets  $(x, y)$  considered, the Won HCS values are negative, meaning that the critical strain is not reached. However, as the real critical strain is unknown, a comparison of values between each others can be performed to get an idea of the region with the highest risk of cracking. As for the former criteria presented, the center of the major face presents the highest HCS value (-0.041) as presented in Figure 3.13. The edge of the block arrive in second position (-0.047) a bit above the three other set of coordinates that are all at (-0.05).

**Pros:**

- Microsegregation of solute element could be taken into account as impacting the critical BTR value;
- Prediction for several experimental conditions by adjusting the strain rates;
- Criterion related to crack propagation;

**Cons:**

- Coefficients have been calculated for steel and limitations have been found for the ultra-low carbon steels. The extrapolation to AZS is not granted;

### 3.3.3.4 Local Strain criterion

#### Main principle:

Criteria presented in former sections gets a HCS value higher for the center of the major face than the edge of the block. As this study focuses on hot tears observed experimentally along the edge of the block, another strain-based criterion is considered. Instead of considering the strain perpendicular to the temperature gradient ( $\hat{\epsilon}$ ), this criterion considers the deformation rate  $\dot{\epsilon}$  whatever its direction.

Adjustment of Won critical strain value has not been done for the AZS material. To compare AZS processes between each others, in a first approximation, only the cumulated deformation is considered (without considering a critical value). The criterion considered call "local strain" is determined with (3.42).

$$HCS = \int_{BTR} \dot{\epsilon} dt \quad (3.42)$$

#### Results for AZS material:

With such criterion, process conditions are taken into account thanks to the BTR as they impacts the temperature history. Mechanical behavior of the material impact the  $\dot{\epsilon}$  value over the cooling down of the block. The HCS values obtained with this criterion are similar over the height of the block as the standard deviation are much smaller than the average value over the five horizontal planes considered. As mentioned in Figure 3.14, the standard deviation over the five horizontal planes considered is around 4% of the average value predicted numerically at the edge of the block.

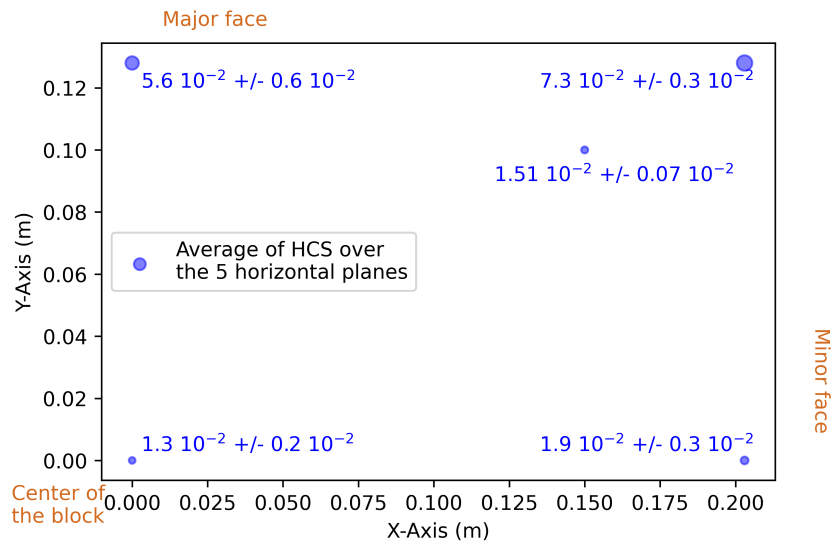


Figure 3.14: Averaged HCS prediction for the five horizontal planes with Local Strain criterion for AZS material considering consistency #1 mentioned in Figure 3.3.

With this criterion, the highest value obtained is well at the edge of the block, close to the surface with a HCS at  $7.3 \times 10^{-2}$ . The sensor inside the block shifted toward the edge corner presents a HCS at  $1.51 \times 10^{-2}$  close to the value at the center of the block  $1.3 \times 10^{-2}$  as in Figure 3.14. The center of the major face is close to the edge HCS value but slightly below it with and HCS at  $5.6 \times 10^{-2}$ .

This criterion will be considered for this mechanical study of AZS material. It seems indeed the most adapted to predict the formation of hot tears at the edge of the block as expected in the initial objectives of this project.

### 3.3.3.5 Stress criterion on AZS material

The Clyne-Davies criterion is based on temperature history only. The local strain deformation of the block is taken into consideration. A simplified stress criterion was also tested on AZS material. A critical stress was defined  $\sigma_c = \sigma_y$ , the strain hardening is not considered in first approximation. Yield stress is determined experimentally only until 1 200°C, the value is keep constant in the mushy zone. At each increment, the stress predicted numerically by THERCAST® is compared with the critical value as detailed in (3.43). The maximal value obtained is however also obtained at the edge of the block with a HCS at 63.7 compare to a HCS at 8.0 at the center of the block.

$$HCS = MAX\left(\frac{\sigma_{increment}}{\sigma_{c;increment}}\right) \quad (3.43)$$

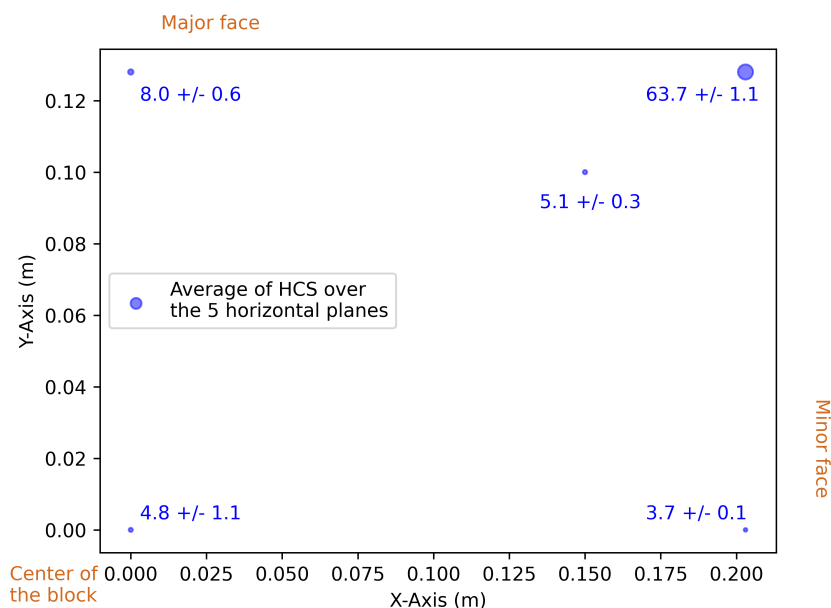


Figure 3.15: Averaged HCS prediction for the five horizontal planes with simplified stress criterion for AZS material considering consistency #1 mentioned in Figure 3.3.

HCS results with this criterion are presented in Figure 3.15. Values predicted numerically are stable along the height of the block. An averaged value above unity was expected to predict a risk of hot tears (as the critical value is overcome). As the entire domain is at risk, this criterion was rejected at the beginning. However, as for Won criterion, a relative comparison can be performed. The edge presents a stress ratio that is 10 times larger than the rest of section. This criterion could also have been considered for HCS predictions in AZS materials, but it is not the case in the computations presented in the further sections.

An adaptation of the critical stress value should be implemented before applying such criterion for AZS material hot tears prediction. Strain hardening can occur during the solidification, leading to a shift of the yield stress. It could impacts the critical stress value that have to be

defined along the solidification. However, experimental data are lacking at high temperatures (close to the coherency temperature). A way of improvement of such stress criterion could be to get experimental values of yield stress at temperature where the system is partially liquid (in the mushy zone). A stress criteria seems already adapted for fully solidified system and it could be used to predict the formation of cold cracks, with a different morphology than hot tears and that are not considered in this project.

#### 3.3.4 Implementation of hot tear susceptibility prediction in THERCAST®

##### 3.3.4.1 Numerical sensors at the edge of AZS block

In order to get a better resolution of the mechanical state at the edge of the block, mesh grid is refined along the edge as presented in Figure 3.16. Sensors are located at a node of the block edge every 10 cm along the height. They are the red dots in Figure 3.16. Other sensors are considered close to the edge at 1 and 2 cm along both faces and every 20 cm along the height (purple, green, light blue and dark blue dots in Figure 3.16), not necessarily at a node of the mesh. Sensors are defined as Lagrangian markers, following the displacement of AZS material from its initial position to its final position after shrinkage and air gap layer formation between the AZS block and the mold. All sensors recorded numerical outputs from thermal and mechanical computations at each increment.

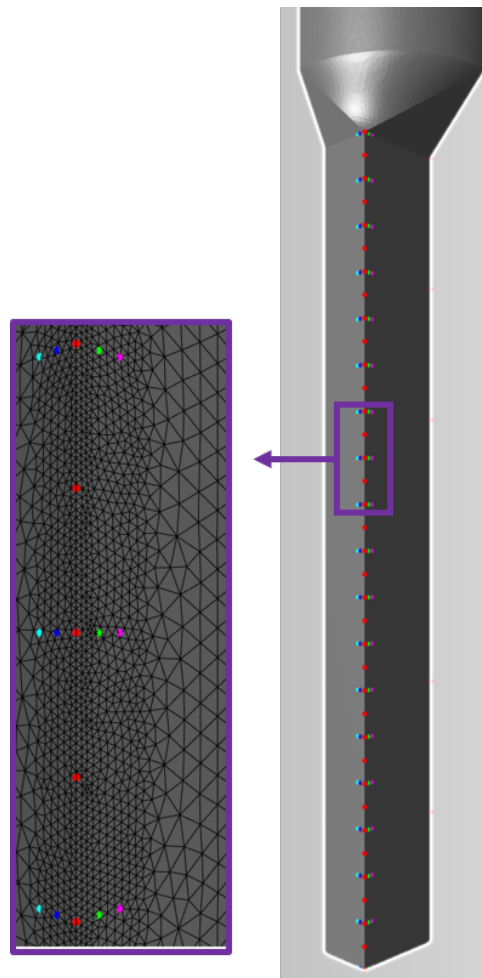


Figure 3.16: Sensors location and mesh refinement at the edge of the AZS block.

Industrial teams are looking for a quantitative HCS criterion to compare blocks and processes between each others. Each sensor returns cumulated local strain criterion defined in (3.42). The value over the height is not averaged anymore to follow the evolution of this criterion over the height of the block. HCS can be compared between each other even if no "critical" value has been determined for AZS material. Such quantification method, of great interest to determine the impact of process or material changes over the HCS, is detailed in § 3.3.5.

It is also important to keep in mind that Yamanaka value (also called "cumulated local strain") is influenced by thermal and mechanical properties of the material. For example, changing the temperature of coherency (and therefore considering or not elastic stress in the domain) influences the final value of the parameter.

### 3.3.4.2 Brittle temperature range definition for AZS at the considered composition

In this study, the BTR is defined in temperature and not in solid fraction. This definition has no impact on current results as a single solidification path is considered. This would not be the case if solid mechanics (hot tears predictions) is coupled with macrosegregation. Adjustment was required to separate materials just after solidification with glass forming liquid phase (i.e. around 1600 °C) from a system with the same glassy phase fraction but at lower temperature when glass behavior is much more viscous.

For metal alloys, the BTR is defined as  $g_s = 0.9 - 0.99$ . In the AZS material, a glassy phase is observed in proportion around 20 vol.%. This imposes a new definition of the BTR. Three temperature intervals are considered as detailed in Figure 3.17a.

- 1500 - 1800 °C : Hot tears might form when the eutectic structure (zirconia tetragonal with corundum) solidifies. The BTR stops when the solidification can be considered as over.
- 1300 - 1650 °C : Hot tears might form at the end of solidification of crystals. Such interval starts when 90% of crystals are formed, in a similar way that the value  $g_s = 0.9$  considered for metal. The lower boundary is when the viscosity of a synthetic glassy phase reaches 500 mPa.s [11]. Such synthetic phase was enriched in Na<sub>2</sub>O, that reduces a lot the viscosity measured as materials enriched in SiO<sub>2</sub> present a really high viscosity [80].
- 900 - 1400 °C : Hot tears might form during zirconia phase transition and only when glassy phase remains.

Tests were done with Consistency #1 presented in Figure 3.3. Cumulated local strains presented in Figure 3.17b show an important impact of the BTR definition. If the BTR is focused after the end of solidification (red), almost any strain is cumulated during the BTR. The majority of strain is cumulated at the end of the solidification as 1500 - 1800 °C (green) and 1300 - 1650 °C (blue) present similar values of cumulated deformations. With such consideration, to get as close to metal HCS definition, the 1300 - 1650 °C interval is considered as the relevant BTR for this study. Only the first hours of annealing are relevant and cracks due to zirconia phase transition are not modeled.

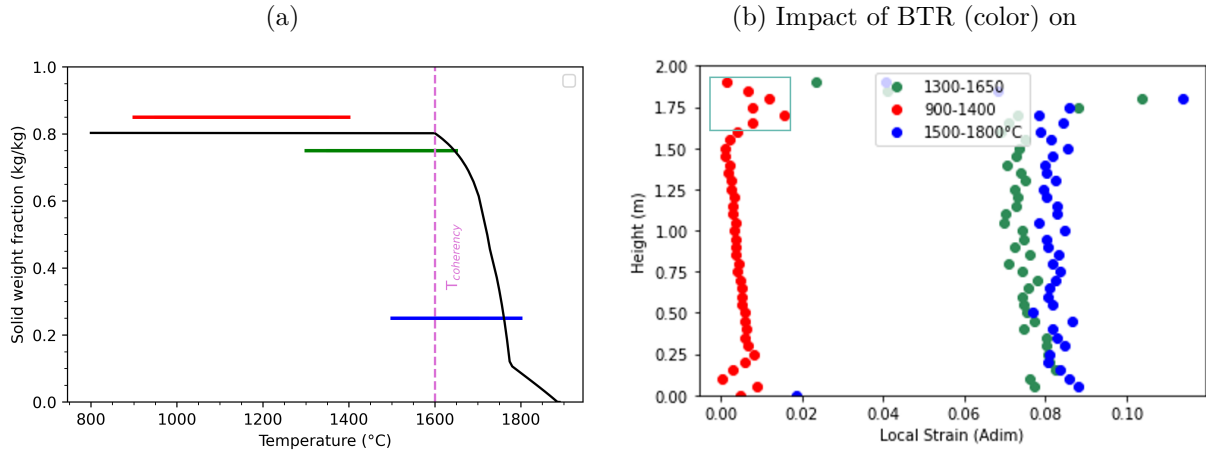


Figure 3.17: Three different BTR are considered with (a) the 3 different BTR (color) that will cumulate the strain at the edge over different periods of the (black) solidification path. The impact of (color) the BTR on mechanical outputs is measured considering cumulated local strain over the height of AZS block. The green rectangle for the higher red dots indicates that those sensors are still above 900°C (inside the BTR), their local strain value can still increase over annealing.

### 3.3.4.3 Impact of the AZS consistency on mechanical outputs

Two different consistencies were tabulated for the AZS material in Figure 3.3. Local strain is cumulated in the BTR 1 300-1 650°C for both computations. Each dots in Figure 3.18 represents a sensor (red dots in Figure 3.16).

At first glance, cumulated local strain seems constant over the height of the block, when neglecting results at the very top of the block. With Consistency #1 (softer material), cumulated strain is between 0.069 and 0.088. With Consistency #2, deformation is much lower with values between 0.008 and 0.018. According to Koshikawa, cumulated strain for steel ingots is between 0.01 and 0.03 [81]. The order of magnitude for AZS material seems therefore relevant. Variations over the height for the test with consistency #1 implies less visco-plastic deformation and the HCS values are straighter over the height of the block compare to consistency #2.

At the very top of the block region, the cooling down is lower due to the proximity with the riser. The time spent inside the BTR is longer and the deformation is more important. The sensors located at the bottom of the block presents almost no deformation as the annealing is too fast at the corner of the block and BTR is crossed in only a few increments.

As no test is done in traction but only in compression and bending, the visco-plastic deformation to expect is more important than results with Consistency #2 obtained from experimental measurements. The real constitutive equation should return results between both outputs presented in Figure 3.18. For next simulations, consistency #1 will be considered to get a soften material with larger values of deformation.

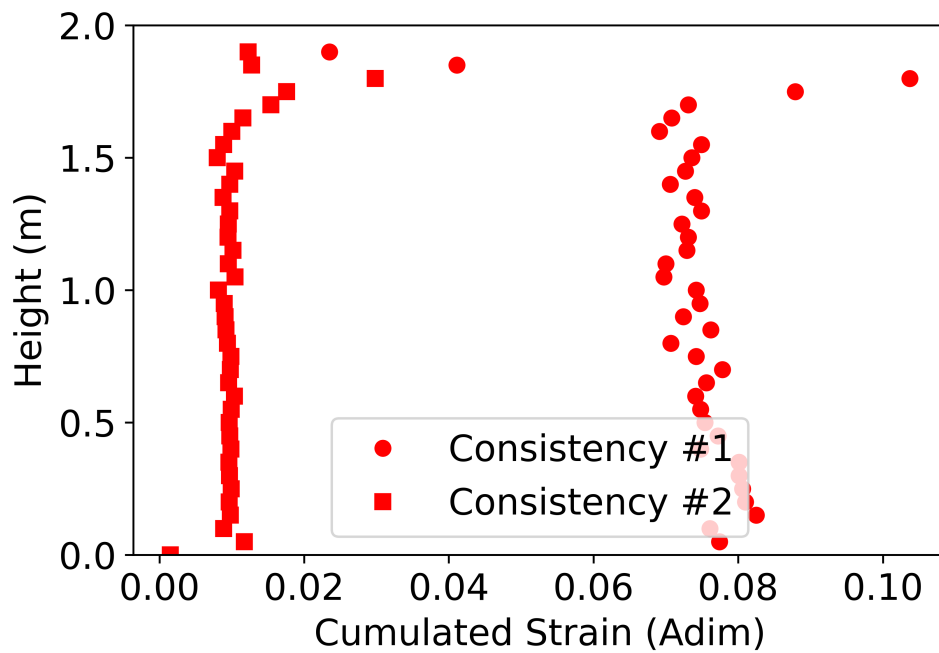


Figure 3.18: Strain cumulated during the range 1 300 °C - 1650 °C at the edge of the block for both consistency tabulations presented in Figure 3.3.

### 3.3.5 Impact of four geometries on hot tear susceptibility

#### Geometries considered:

Four different computations have been performed in order to visualize the impact of the block geometry on the hot tears predictions. The final objective is the determination of a quantitative criterion that retrieve industrial feedbacks about hot tears susceptibility for each geometry considered, as explained in Table 3.3.

Geometry	Industrial feedback about HCS	Duration of post processing stage to obtain a block at the expected standard geometry
Geo. #1	Several hot tears	short
Geo. #2	Few hot tears	short
Geo. #3	No hot tears	much longer
Geo. #4	No hot tears	much longer

Table 3.3: Industrial feedbacks about hot tears susceptibility depending on geometry considered.

#### Comparison of mechanical outputs:

As observed on industrial blocks, numerical simulations retrieve that edges are the region with the highest risk for hot tears. The contact between the block and its riser is also simulated as a critical spot, with the highest value for the equivalent strain parameter, and this could be observed experimentally at the junction between block and riser.

Considering a cross section at the middle height of the block region (for geometry #1), edges are the region where the more strain is cumulated as presented in Figure 3.19. The center of the face is also a region of strain concentration. There, the deformation present the widest gap between the AZS block surface and the mold (gray in Figure 3.19).

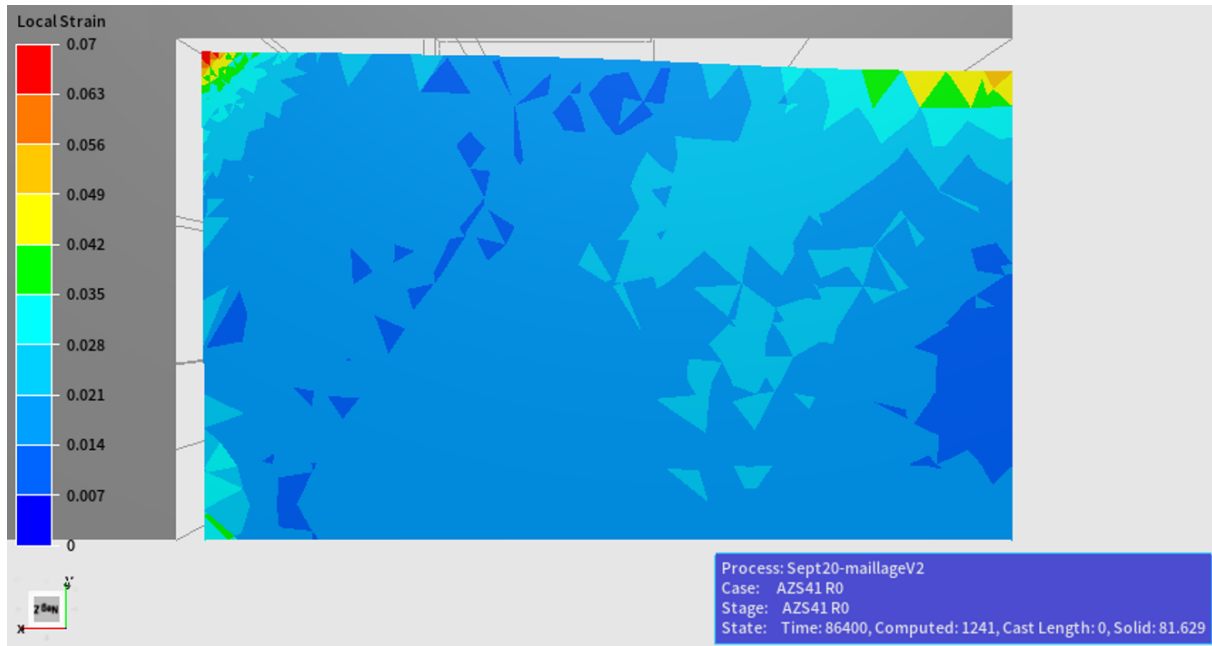


Figure 3.19: Strain cumulated for Geometry #1 during the range 1650 °C - 1300 °C in a section of the block at 0.8 m height of the block with the mold object in gray color.

Local strain can be extracted for the 4 geometries in Figure 3.20 after the firsts 6 h of the simulations. At this time, each sensor is below 1300 °C and surfaces of the block present a liquid fraction around 0.2 corresponding to the glassy phase.

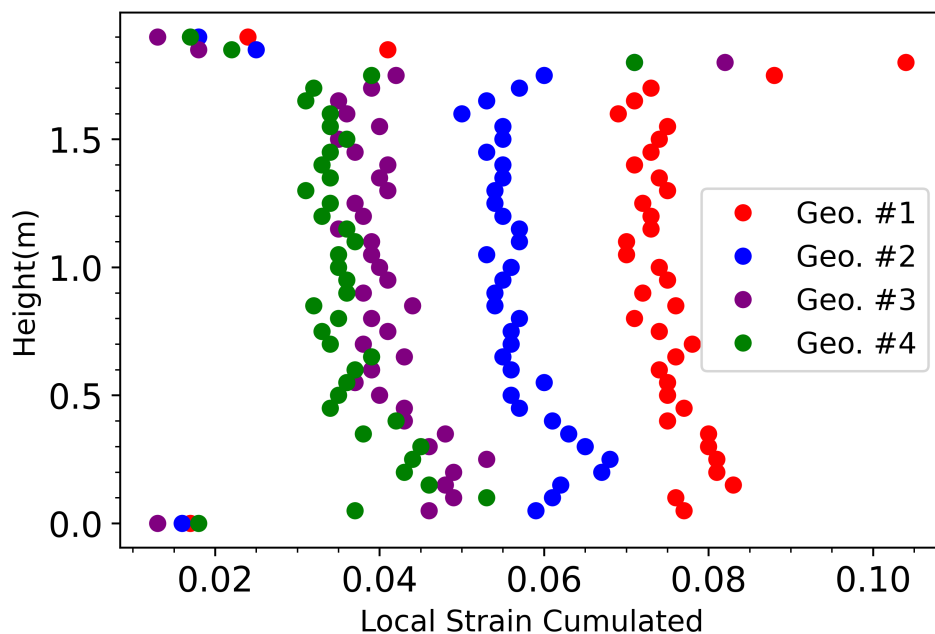


Figure 3.20: Strain cumulated for four different geometries along the edge of the AZS block at several heights with a BTR 1300 °C - 1650 °C.

For the four geometries, cumulated local strain is almost constant over the height of the block. The results show significant variations between the highest values obtained for geometry

#1 and the smallest for geometries #3 and #4, as observed in plants.

Such criterion seems therefore to be able to predict hot tears susceptibility. If the second consistency is considered for AZS, some adjustments will be required to get an even thinner range of local strain over the height. Indeed, as the deformation is around 1% only, the outputs variations due to geometry will be smaller. Numerical noise might induce overlapped results.

### 3.3.6 Conclusion about predicting the hot tears susceptibility of a block

Hot tears are typical foundry defects that can be observed at the edge of AZS blocks. They are due to the thin intergranular liquid film that opens. Experimental observations and chemical measurements validates that hot tears are created at the end of the solidification, when only glassy phase remains. Hot tears stop to propagate when liquid phase becomes too viscous and can sustained more stress without breaking.

Several criteria have been detailed in literature to predict HCS in metal alloys. Cumulated local strain is considered for AZS materials. Experimental observations where used to adjust such criterion to a material with almost 20% of glassy phase. An adaptation of the BTR by considering the viscosity of the remaining liquid phase could have been an option but its implementation was too difficult and a temperature range at the end of crystallization was defined.

As constitutive equation is not fully detailed experimentally in the mushy zone, numerical adjustments were required. In a similar way, the temperature of transition between VP to EVP behavior is arbitrarily defined and can be adjusted if a study is done in the future with better experimental fit. After mechanical adjustments, four different geometries are considered. Industrial feedbacks return a strong variation of behavior for the three first geometries considered and similar behavior for the third and fourth geometries. Numerical results are compared between each others and retrieve such industrial behavior. A value of local accumulated strain around 0.06 with in the considered material and numerical conditions could be considered as a critical value for hot tears susceptibility in AZS block.

The considered criterion seems adapted in our specific case with a decrease of consistency arbitrary defined in the mushy zone and the  $T_c$  parameter set at 1 600°C. Changing an input data such as  $T_c$ , AZS consistency at high temperature or the BTR range will impact the outputs and the predictability of hot tears susceptibility. A new adjustment study will be required. If it requires time, no significant numerical problem is to be expected.

## 3.4 Prediction of macro-porosity in the riser

In thermo-mechanical resolution, stress and strain are determined at each increment. This allows the prediction of tears but it leads also to the formation of an air layer between the mold and the AZS block. The mesh also opens inside the AZS domain if necessary. It is then possible to model a macro-porosity in the riser. As riser is an extra amount of liquid material cast above the block, it is important to optimize its volume and shape in order to keep for the longest possible duration this material reserve in liquid state. It is also important to predict the size of the macro-porosity to avoid casting too much material that will be removed during the post-processing steps.

### 3.4.1 Experimental observations of riser macro-porosity

Experimental riser for AZS41 has been cut in half. The shape of the macro-porosity inside the riser is presented in Figure 3.21. The objective is to retrieve similar shape of macro-porosity

inside the riser.

Macro-porosity can be divided in two main sections :

- Upper section presents several layers of AZS material well defined that spread over almost all the width of the riser. Each layers are separated by few centimeters of air;
- Lower section shape is like a sponge with interlacing walls of AZS material and small cavities. This section is centered inside the riser and cover the half of the riser width. Its porosity is determined experimentally at SGR Provence around 40 vol.%.

As air occupies a quarter of the riser volume, numerical computations should target the largest macro-porosity as possible.



Figure 3.21: Macro-porosity inside an industrial riser of an AZS block with 41 wt.% of  $ZrO_2$ .

#### 3.4.2 Impact of numerical parameters for porosity opening

The small volume of air predicted in the riser compared to the experimental observations could explain that macro-porosity has no impact yet on temperature history predictions.

Two numerical parameters get a major role in the opening of macro-porosity. The Open

Shrinkage Threshold (OST) parameter that controls the mesh opening inside AZS domain and the interface resistance with the media that controls the heat transfer at the top of the block.

### 3.4.2.1 Open shrinkage threshold parameter

At each increment, the mechanical laws are applied and contraction will modify the surface of the AZS domain (including the evolution of the internal cavities). The next stage is to test an opening condition to determine if an internal (closed) cavity needs to be opened [62]. Open Shrinkage Threshold (OST) is the solid fraction used to set the volume of the mushy zone where the test condition (3.44) is applied, called here "shrinkable volume". A mesh element is in this "shrinkable volume" if its solid fraction is between 0 (fully liquid) and this OST fraction.

This OST parameter rules the internal closed cavity opening. If the value is equal to 1, the volume for the test will be every mesh element with a solid fraction between 0 and 1, i.e. the entire AZS domain. Therefore, no internal cavity can be created, as shown on the right of Figure 3.22. If  $OST = 0$ , the volume is not defined and the condition detailed in (3.44) is not tested implying that no internal cavity is opened neither.

As the system solidifies, the shrinkage leads a lowered pressure. If the pressure is below the pressure threshold (1 300 Pa by default), an internal cavity is created with a volume defined thanks to (3.45). Such equation combines the solidification shrinkage and the thermal contraction [62] during the increment  $\Delta t$ .

$$\text{Opening condition:} \quad -\frac{1}{3}tr(\boldsymbol{\sigma}) \leq 1\,300 \text{ Pa} \quad (3.44)$$

$$\text{Contraction:} \quad \frac{\delta V}{V} = \int_{\Delta t} -\left(\frac{\rho_l - \rho_s}{\rho_l} \frac{\partial g_s}{\partial t} + \frac{1}{\rho} \frac{\partial \rho}{\partial T} \frac{\partial T}{\partial t}\right) dt \quad (3.45)$$

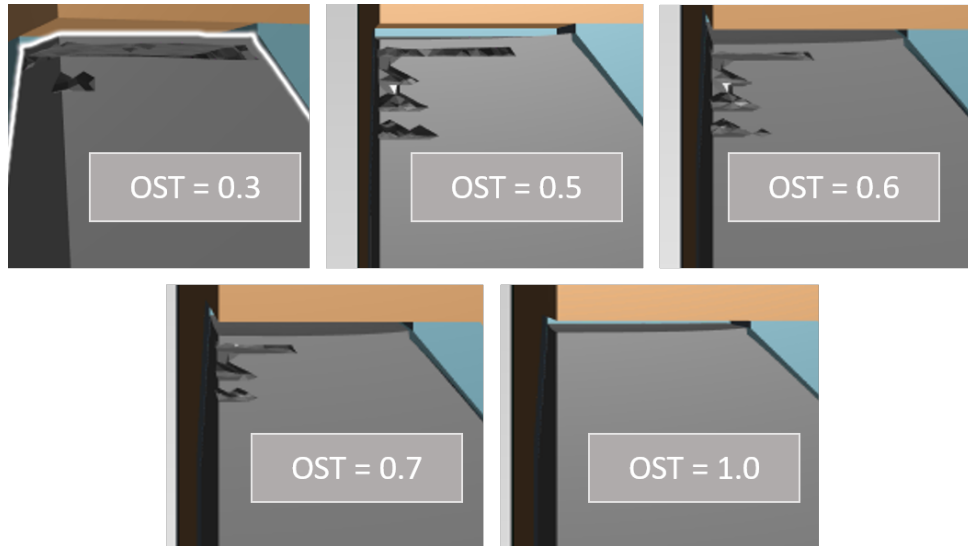


Figure 3.22: Impact of OST parameter on macro-porosity predicted after few hours of annealing.

When the OST value is too low (i.e.  $g_s=0.3$ ), the "shrinkable volume" is an internal domain with liquid fraction between 0.7 and 1. As it represents only the beginning of the solidification, the drop of pressure, quantified as  $\frac{1}{3} tr(\boldsymbol{\sigma})$ , is too small in this solid fraction interval and the opening threshold condition is not reached. This explains the small internal volume opening as on the left of Figure 3.22.

When the OST value is too high, a mesh at the surface of the domain is almost always included as the shrinkable volume is wide. As the surface is included, no internal cracks can be formed and just the surface will move. As the glassy phase in AZS material is modeled as the "remaining liquid phase", at the end of the computations, the lowest liquid fraction reached is  $g_L = 0.21$  (i.e.  $OST = g_S = 0.79$ ). This implies that an OST value between 0.79 and 1 cannot create an internal cavity.

A parameter study was performed about the lowest allowed pressure in (3.44). Three pressure were considered : 650 Pa, 1 300 Pa and 2 600 Pa. The simulations predict the same shape of macro-porosity in the three cases.

For the THERCAST<sup>®</sup> computations presented in the next sections, OST parameter is set at  $g_s = 0.6$ . Such value is equal to the default value for metal alloys such as steel [62]. The opening pressure is also kept at THERCAST<sup>®</sup> default value: 1 300 Pa.

### 3.4.2.2 Interface contact resistance at the interface Block/Media

AZS block presents an interface with medium for its upper face, two tests with extremal values of heat exchanges are considered  $h_{AZS/Media}^{initial} = 32 \text{ W m}^{-2} \text{ K}^{-1}$  and  $h_{AZS/Media}^{initial} = 0.1 \text{ W m}^{-2} \text{ K}^{-1}$ . Results are presented in Figure 3.23. The resistance with the mold is unchanged and similar to the one presented in § 2.4.3.

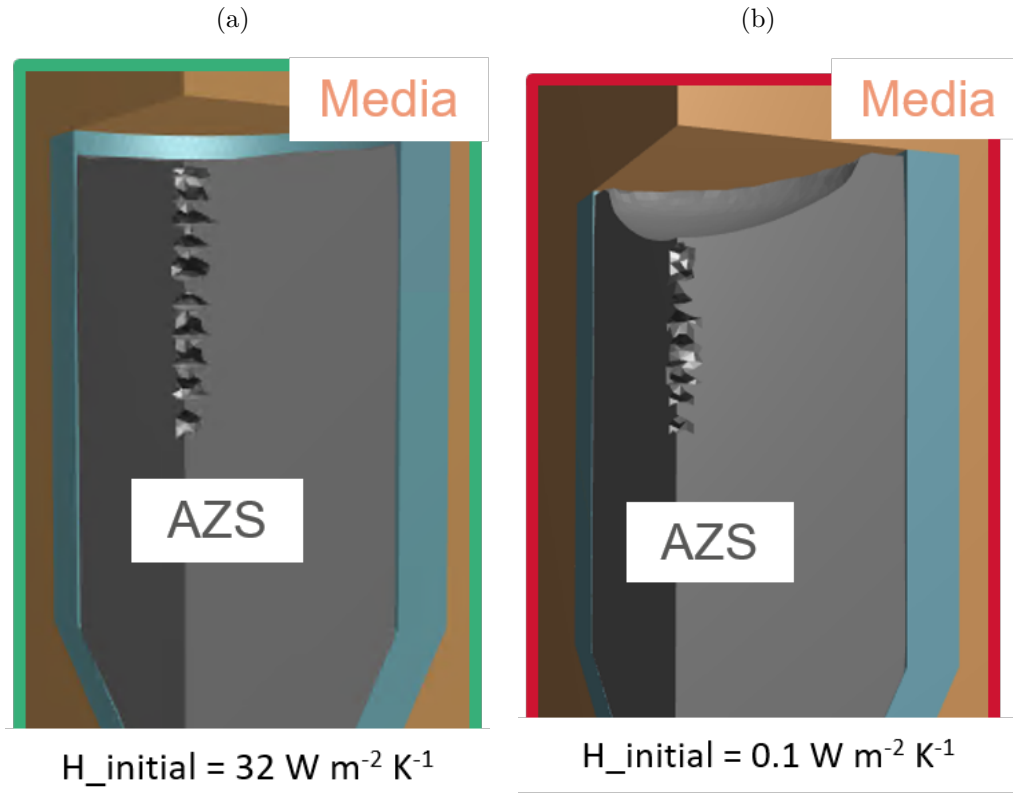


Figure 3.23: Impact of the AZS-Media interface resistance at the end of solidification with the heat exchange coefficient (a)  $h_{AZS/Media}^{initial} = 32 \text{ W m}^{-2} \text{ K}^{-1}$  and (b)  $h_{AZS/Media}^{initial} = 0.1 \text{ W m}^{-2} \text{ K}^{-1}$ .

If such parameter has no impact on temperature history at the bottom of the riser (# 7 and #18), it changes a lot the shape of the macro-porosity at the top of the riser. As presented in Figure 3.23, the open macro-porosity is smaller in the case where the contact resistance is

the highest (and the heat exchange coefficient the smallest). However, this parameter does not modify the width of the secondary air layers present in the simulations and observed experimentally. In order to keep a relevant value, further computations will keep an intermediate resistance value:  $h_{AZS/Media}^{initial} = 3 \text{ W m}^{-2} \text{ K}^{-1}$  and further investigations are required to increase the width and depth of macro-porosity below the block surface inside the riser.

### 3.4.3 Impact of the composition on the riser macro-porosity

Additional computations were run for the first hours with the second AZS composition AZS36 detailed in Table 1.3. Similar mechanical properties are kept for this second composition. The thermal properties are detailed in § 2.7.2.

For this second composition, the riser geometry prediction is presented in Figure 3.24c. The air layer thickness between the block and the mold is reduced. The macro-porosity shape presents two categories. A first one is a single coarse open macro-porosity with trapezoidal shape at the top of the block. The second category presents layers of AZS materials between air layers in a V-shape. The final depth of porosity is predicted at the middle of the riser, whereas experimentally the entire riser present macro-porosity.

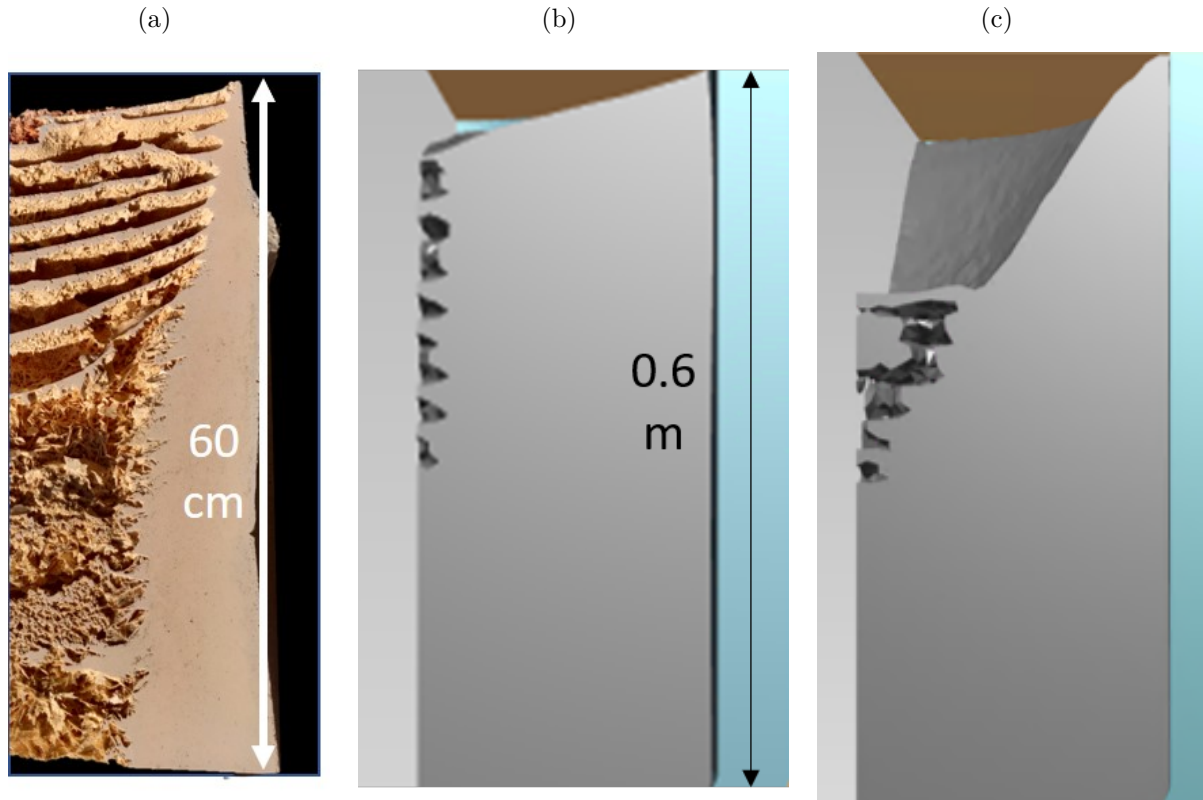


Figure 3.24: Riser macro-porosity shapes at AZS41 composition for (a) the experimental riser, (b) the predicted macro-porosity in a block considering AZS41 properties detailed in § 2.5.1 and (c) the predicted macro-porosity in a block considering AZS36 properties detailed in § 2.7.2.

Predicted macro-porosity in the riser is deeply impacted by this change of composition as presented in Figure 3.24. The only variations between both computations are the thermal properties of both AZS materials. As presented in § 2.7.2, the strongest variations between thermal properties are with density tabulations. The AZS36 presents the strongest density change between solid and liquid phases as shown in Figure 2.16. It becomes therefore important

to validate the impact of density change during solidification with a dedicated computation that will be presented in details in the next part.

### 3.4.4 Discussion about the potential impact of lower AZS liquid density

In order to validate the impact of density variation during solidification, a test was performed with artificially lowered liquid density. All other properties (thermal and mechanical properties) are kept identical between both computations.

New liquid density is set at  $3\,000\text{ kg m}^{-3}$ , as presented in Figure 3.25, corresponding to the density observed in the riser due to macrosegregation inside the block. The experimental measurements are presented in § 4.1.1. This density is tabulated all along the block as a single material composition. This means that the bottom of the block will also present such density tabulation even if density at the bottom is known to be higher experimentally.

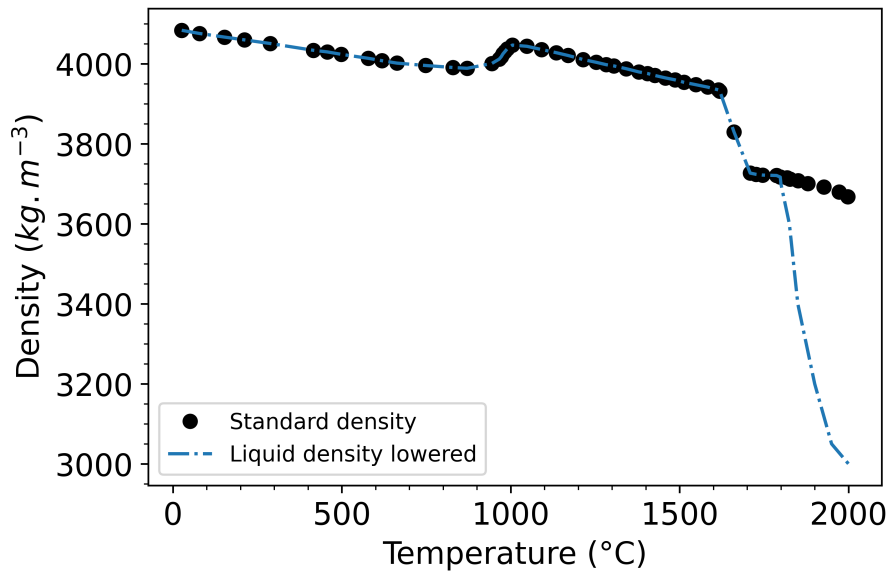


Figure 3.25: Density tabulated over temperature for (black dot) the AZS41 and (dashed blue line) a test with liquid at lower density.

The impact of density change during solidification on macro-porosity shape is clearly presented in Figure 3.26. The two categories observed with the AZS36 are also observed in this artificial case : the first category presents a coarse open macro-porosity for a thickness around the first quarter of the riser. The second presents the superposition of air and AZS layers in a V shape. The final depth of macro-porosity reaches more than the three quarters of the block height.

The air layer thickness at the interface between AZS and Mold is also increased. Experimental sensors to record temperature are located in the mold and not directly in the AZS. As the air layer reduces heat exchanges with the mold, temperature predicted at sensors locations are lower than the experimental recorded data as presented in Figure 3.27. Temperature in the riser (Figure 3.27d) is better predicted at the end of the solidification but the first hours of annealing are still not well predicted.

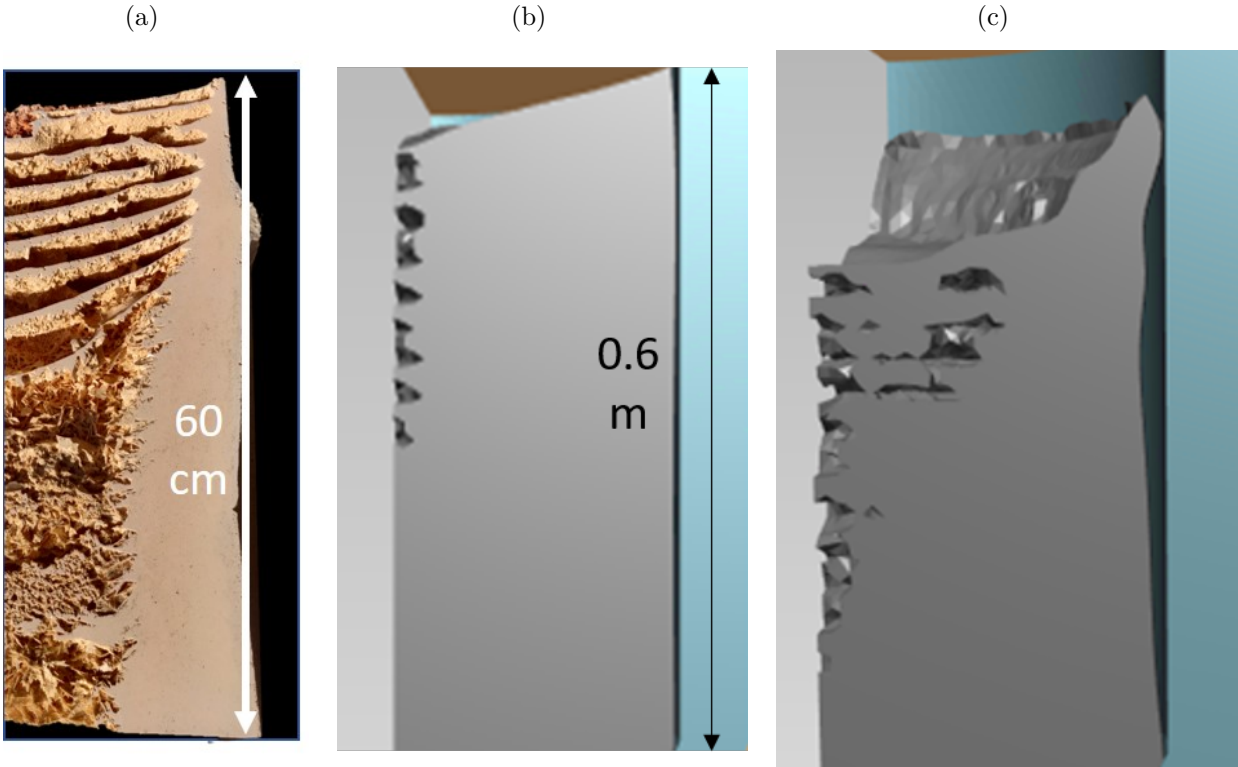


Figure 3.26: Riser macro-porosity shapes at AZS41 composition for (a) the experimental riser, (b) the predicted macro-porosity in a block considering AZS41 properties detailed in § 2.5.1 and (c) the predicted macro-porosity in a block considering AZS41 properties with a lower liquid density detailed in Figure 3.25.

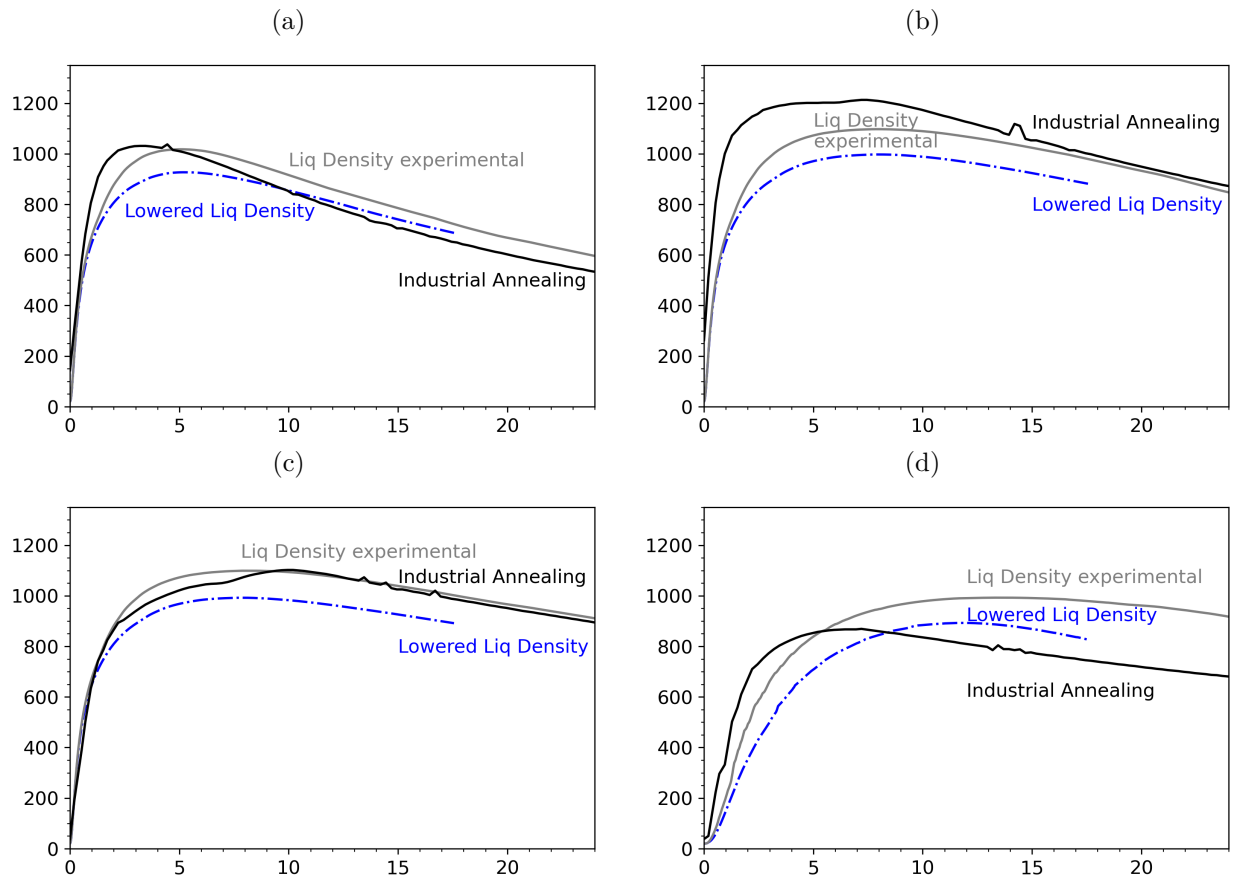


Figure 3.27: Comparison of temperature histories at different locations (see Figure 2.11) for (black) experimental temperature history, (dashed blue) temperature history computed with lowered liquid phase density and (gray) temperature history computed with experimental AZ material density : (a) at the bottom of the block, (b) middle of the block, (c) top of the block, (d) in the riser.

### 3.5 Conclusion about mechanical outputs of numerical simulations

After the validation of temperature history with THERCAST<sup>®</sup>, mechanical balance equations have been resolved. This study focuses initially on hot tears susceptibility prediction then on macro-porosity shape inside the riser.

SEM observations of hot tears confirm that those cracks appear at high temperatures, when liquid film is present and not too viscous and at the end of the crystallization of corundum and zirconia. Several criteria are detailed in literature to quantify hot tears susceptibility in metals. Few adjustments were required to adapt one of them, the cumulated local strain inside a defined BTR. Indeed, as ceramics present a high proportion of glassy phase at the end of solidification, the BTR had to be adjusted. Mechanical balance equations requires to get relevant mechanical properties tabulation. For AZS material, properties in the mushy zone, above 1 500°C, are not well determined experimentally. Consistency had to be artificially tabulated and it impacts a lot the strain accumulation at the edge of the block. An industrial case study with four different geometries used in Saint-Gobain plants retrieve the feedback collected about their hot tears susceptibility.

The macro-porosity was initially predicted as several gas bubbles located at the center of the riser. Such predictions do not match the experimental observations of a macro-porosity occupying the entire riser with an alternation of AZS and air layers above a spongy region. After numerical adjustments and tests for another composition in the AZS family, it has been proven that the density gap during solidification is a key parameter to well predict the shape of macro-porosity. A well predicted macro-porosity shape impacts as expected temperature history. The air located inside the macro-porosity reduces the heat exchanges with the environment.

To improve the relevance of simulations, especially in the riser, it is important to get a right prediction of macro-porosity. Density, especially the density gap during solidification, is proven to be a key parameter to determine the shape of macro-porosity. To avoid the drawback of a lowered liquid density for the entire block, real composition evolution should be considered to determine local density. The size of the block allows chemical heterogeneity (also called "macrosegregation") over the height of the block, which impacts density. The next chapter presents the macrosegregation implementation in THERCAST<sup>®</sup>.

# Chapter 4

## Macrosegregation

### Contents

---

Résumé Chapitre 4 . . . . .	<b>90</b>
4.1 Experimental map of macro-segregation . . . . .	<b>91</b>
4.1.1 Experimental measurements of chemical heterogeneities . . . . .	91
4.1.2 Properties and solidification path of the encountered compositions . . . . .	94
4.2 Implementation of macrosegregation in THERCAST® . . . . .	<b>98</b>
4.2.1 Call of User-Model in THERCAST® . . . . .	98
4.2.2 PATH adaptation for concentrate alloys . . . . .	100
4.3 Focus on results from hydraulic computations . . . . .	<b>102</b>
4.3.1 Estimated velocity of AZS liquid with dimensionless parameters . . . . .	102
4.3.2 Convection vs Sedimentation . . . . .	104
4.3.3 Impact of density on the convection motions loops . . . . .	105
4.4 Macrosegregation inside a standard AZS block geometry . . . . .	<b>106</b>
4.4.1 Temperature history . . . . .	106
4.4.2 Convection predictions . . . . .	107
4.4.3 Numerical map of macrosegregation . . . . .	109
4.4.4 Impact of $\lambda_2$ parameter on permeability and macrosegregation results . . . . .	112
4.4.5 Further work . . . . .	112
4.5 Conclusion about macrosegregation . . . . .	<b>113</b>

---

## Résumé Chapitre 4

Le chapitre 4 porte sur la prise en compte de la macroségrégation dans les modélisations. Pour ce faire, l'approche thermo-mécanique par défaut de THERCAST<sup>®</sup> n'est plus considérée mais est remplacée par une approche thermo-hydraulique, basée sur l'appel d'un solveur thermique et d'un solveur de mécanique des fluides, complétée par un solveur de conservation des solutés. Tous ces solveurs sont issus de la librairie CIMLib<sup>®</sup> et appelés depuis THERCAST<sup>®</sup>. Seul le domaine AZS est concerné par cette nouvelle approche, la thermique par défaut de THERCAST<sup>®</sup> étant appliquée aux autres domaines (moule, agent isolant, caisse).

Dans un premier temps, plus d'une vingtaine d'analyses chimiques sont réalisées sur la face médiane d'un bloc AZS pour définir une cartographie expérimentale de la macroségrégation. Les fortes variations autour de la composition de coulée, de l'ordre de 20-30% pour chacun des composants, ont pour conséquence de fortes variations dans la tabulation des propriétés thermiques (densité, liquidus, enthalpie, chemin de solidification).

Dans un deuxième temps, l'implémentation de la macroségrégation est présentée avec les différentes équations résolues à chaque incrément du temps. Les simulations n'utilisent pas le solveur thermique par défaut mais celui présenté à la fin du chapitre 2 qui modélise correctement les premières heures, lorsque la macroségrégation fait évoluer localement la composition de la phase liquide. Ce solveur est basé sur les tabulations des propriétés de chacune des phases progressivement formées au cours du refroidissement. Les proportions de  $\text{Al}_2\text{O}_3$  et de  $\text{ZrO}_2$  dans un bloc d'AZS sont supérieures à 40%. L'adaptation de l'outil PATH pour les alliages concentrés est présentée. Il a ensuite été possible d'extraire, de la base de données thermodynamiques TCOX10, la composition, la fraction, la densité et l'enthalpie des trois phases observées expérimentalement (zircone, corindon et phase vitreuse). Les tabulations obtenues pour différents sets de compositions globales, qui incluent les compositions mesurées expérimentalement, sont concaténées dans un seul fichier de tabulation lu par CIMLib<sup>®</sup>.

Les simulations sont désormais orientées par la mécanique des fluides. Les résultats relatifs à la convection dans le bloc AZS sont présentés. Il n'y a pas de mesure expérimentale de la vitesse du liquide dans un bloc AZS au cours du refroidissement. Il a donc été nécessaire de définir des valeurs théoriques dans le cas d'un liquide idéal pour valider la cohérence des résultats obtenus dans les simulations de l'ordre de plusieurs  $\text{mm s}^{-1}$ . La sédimentation des cristaux de zircone n'est pas prise en compte, seule la convection thermo-solutale est considérée pour expliquer l'enrichissement de la masselotte en phase vitreuse composée principalement de  $\text{SiO}_2$  et  $\text{Na}_2\text{O}$ . L'étude s'est ensuite portée sur la direction des vecteurs vitesse considérés. L'évolution de la densité du liquide au cours du refroidissement avec un pic au liquidus entraîne une inversion du sens de la convection après plusieurs minutes, une fois le processus de solidification entamé. L'impact de la perméabilité de la zone pâteuse sur la cartographie finale de composition est estimé par une étude de sensibilité de la distance inter-dendritique secondaire.

Enfin, les résultats finaux obtenus pour un bloc AZS sont présentés en détails avec son histoire thermique, l'évolution de la convection et les cartes de compositions finales comparées aux données expérimentales. Cette étude est réalisée pour un domaine actuellement incompressible. Elle doit être poursuivie pour répondre pleinement aux objectifs initiaux en couplant la compressibilité avec la macroségrégation. De même, un couplage avec la mécanique du solide pourrait aider les industriels à prévoir les conséquences de la macroségrégation sur les défauts de fonderie qui peuvent être observés.

In this chapter, the entire volume (solid phases + liquid) is considered as incompressible and the sedimentation of equiaxed zirconia grains, first to solidify, is not taken into account: only solute convection is considered. Composition of phases and their associated density are retrieved from tabulations. The liquid depleted in zirconia is lighter and rises toward the riser. The density of liquid during solidification first increases by cooling from the initially high temperature to the liquidus. The liquid composition remains at nominal composition. Below the liquidus, the liquid density decreases with temperature due to a higher proportion of lighter solute compounds due to macrosegregation.

This chapter first presents the chemical heterogeneities over the height of a block. Macro-segregation is measured at the center of the block. The extremal compositions are used to define the impact of macrosegregation on properties such as density or enthalpy of the system. An incompressible fluid-oriented solver is called for such study. Macro-segregation development is detailed for a simplified case study before shifting toward industrial conditions.

## 4.1 Experimental map of macro-segregation

### 4.1.1 Experimental measurements of chemical heterogeneities

Experimental map of  $ZrO_2$  segregation is presented by Massard [12] and shows elliptical distribution of the iso-concentration on an horizontal plane at mid-height of the block. The  $ZrO_2$  proportion is quantified and presents a constant increase from the skin to the core of the block.

To get the composition of the four components ( $Al_2O_3 - ZrO_2 - SiO_2 - Na_2O$ ), an AZS41 electrofused refractory block was analyzed at SGR Provence. It has been cut in half to sample it at the center. Samples are small cores collected at several height of the block. Each sample (around  $1\text{ cm}^3$ ) is ground in powder, which is mixed to homogenize the powder to get relevant chemical composition measurements of the sample. A small portion is agglomerated to form a specimen pill analyzed in the X-Ray Fluorescence (XRF) spectrometer to measure an average composition,  $w_i$ , with  $i = [Al_2O_3, ZrO_2, SiO_2, Na_2O]$ . 18 samples are analyzed : 10 in the block section or at the junction with the riser plus 8 in the riser.

A sample was taken closer to the skin of the block at 0.15 m height. Close to the skin, the cooling rate is the highest and the measured composition is found similar to the nominal composition  $w_{0,i}$  defined in Table 1.3 and measured by the production team. At the center of the block, macrosegregation is present with higher amplitude especially at 0.15m height. By comparison with the nominal alloy composition, relative variations can be calculated. Extremal variations in relative scale,  $100\frac{w_i - w_{0,i}}{w_{0,i}}$ , are detailed in Table 4.1.

	$Al_2O_3$	$ZrO_2$	$SiO_2$	$Na_2O$
Min	-17%	-28%	-33%	-34%
Max	14%	24%	53%	48%

Table 4.1: Extremal variations in relative scale for the composition in an AZS block over height.

Composition measurements have been previously done by SGR Provence [82] on 5 other AZS41 blocks. Similar results were obtained. For samples at the skin of the block, composition at 0.2, 0.6, 1.0 and 1.4 m return identical composition over the height of the block and equal to the nominal AZS41 composition. At the center of the block, 4 samples are measured at the same heights than the samples at the skin. The results present similar relative variations of composition than for the block detailed in Table 4.1.

The chemical compositions of the 18 samples located at the center of the block are presented in Figure 4.1 depending on their height inside the block. As  $\text{SiO}_2$  and  $\text{Na}_2\text{O}$  are present only in glassy phase, the macrosegregation maps for both components are similar over the height of the block. The riser is enriched in  $\text{Al}_2\text{O}_3$ ,  $\text{SiO}_2$  and  $\text{Na}_2\text{O}$  and depleted in  $\text{ZrO}_2$ . On the contrary, the block section is depleted in  $\text{Al}_2\text{O}_3$ ,  $\text{SiO}_2$  and  $\text{Na}_2\text{O}$  and enriched in  $\text{ZrO}_2$ . Two specific compositions can be selected : inside the riser (open red symbol in Figure 4.1) and at the foot of the block (open blue symbol in Figure 4.1) and are defined in Table 4.2.

wt.%	$\text{Al}_2\text{O}_3$	$\text{ZrO}_2$	$\text{SiO}_2$	$\text{Na}_2\text{O}$
$w_{0,i}$	45.0	41.5	12.4	1.06
$w_{\text{riser},i}$	48.6	29.7	19.0	1.57
$w_{\text{foot},i}$	37.4	51.6	10.2	0.89

Table 4.2: Composition of three specific samples mentioned in this study.

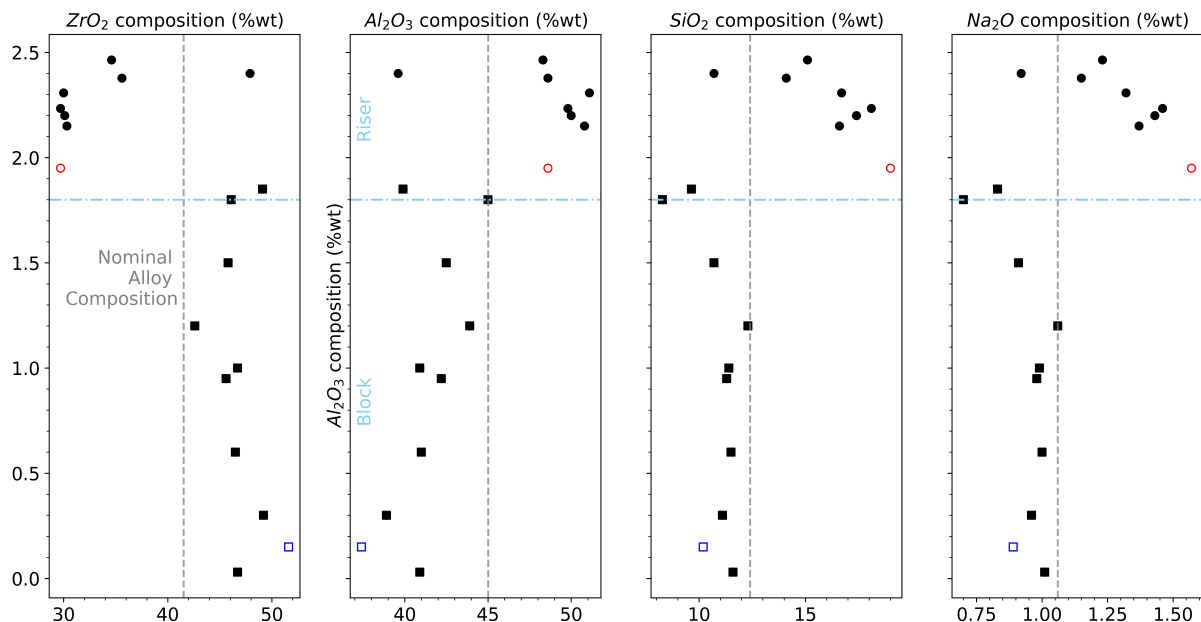


Figure 4.1: Measured composition profiles along the height at the center of the block. The limit with the riser (at 1.80 m height) is outlined by an horizontal dashed blue line. The nominal AZS composition is marked by a vertical dashed gray line corresponding to the composition detailed in Table 1.3. Density and mass enthalpy for the compositions : nominal, blue square and red circle are presented in Figure 4.4 and Figure 4.5.

Each composition is plotted in a ternary diagram in Figure 4.2. In purple is plotted the solidification path for the nominal AZS composition. The solidification paths of the compositions in the riser (red line) and at the foot of the block (blue line) are also plotted. The compositions observed all along the block present similar solidification path. When a liquid phase, at  $w_{\text{foot},i}$  composition solidifies, the liquid will first form zirconia crystals, as shown in Figure 4.3a. This will deplete the liquid in zirconia. The proportion of primary zirconia crystal will be larger at the foot and the solidification path will then follow exactly the same solidification path than the one for nominal composition  $w_{0,i}$ . Inside the riser, corundum crystals will form the primary phase as the composition is highly depleted in zirconia and enriched in alumina. The absence of primary zirconia crystals is shown in Figure 4.3b. The solidification path reaches quickly the eutectic valley, where it follows the same end of the solidification path than the samples located

in the block region.

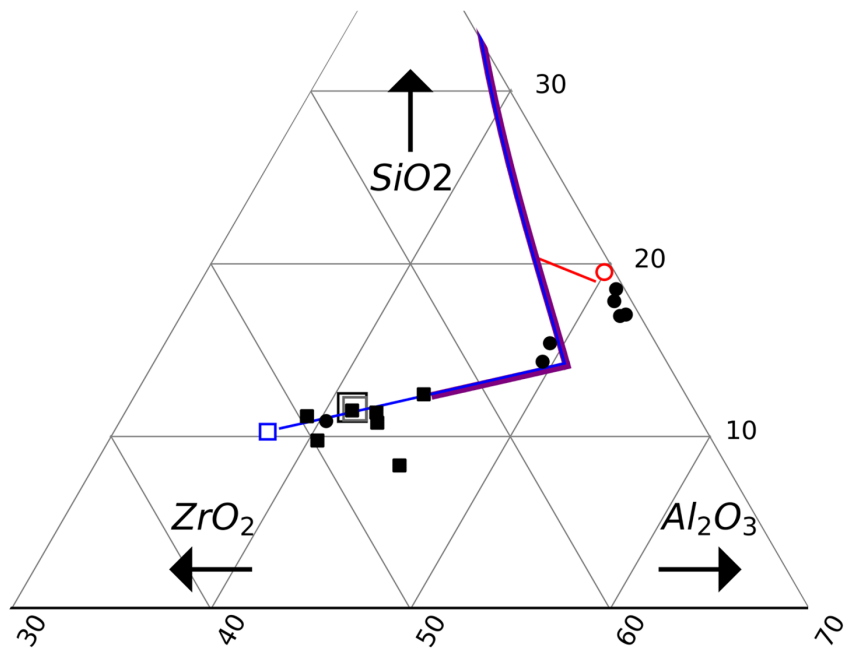
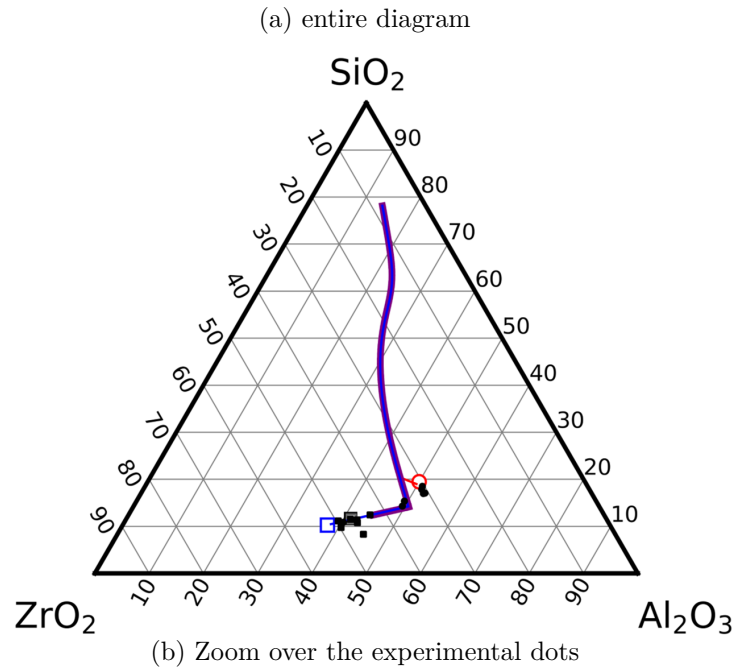


Figure 4.2: Composition on a ternary diagram assuming  $\text{Na}_2\text{O}$  composition is fixed at 1 wt.% of the samples measured on the AZS (circle) riser and (square) block sections. (lines) Solidification paths are plot for nominal, (open red symbol) riser and (open blue symbol) foot compositions detailed in Table 4.2. Compositions of samples at 0.6 and 1.0 m height are overlapping the square of sample results at 0.03 m, they are plotted with larger open gray symbols for visibility reasons.

As the segregation coefficients for all solute compounds are close to 0 as almost a single compound is present is the crystalline phases. Therefore, the compositions of the several samples in the block (square in Figure 4.2b) are aligned on the phase diagram. Compositions of samples

at 0.3, 0.6 and 1.0 m are almost identical as they are on the same vertical line in Figure 4.1, they are plotted with larger open symbols for visibility reasons on the ternary diagram in Figure 4.2.

The objective is to be able to reproduce such composition map inside a block at the end of solidification in THERCAST<sup>®</sup>.

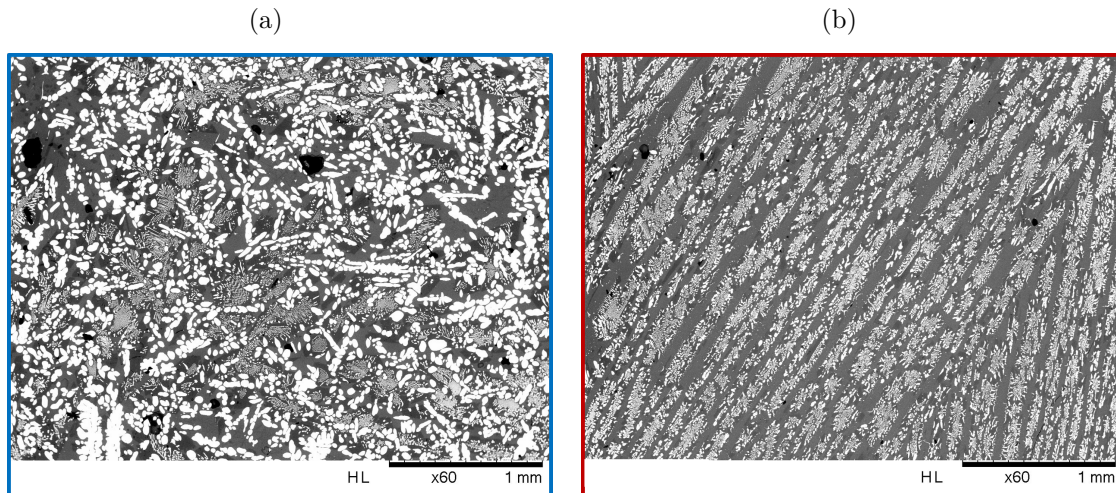


Figure 4.3: SEM observations of the phase distribution for AZS samples located in (a) the foot and (b) the center of the riser.

#### 4.1.2 Properties and solidification path of the encountered compositions

Chemical heterogeneity is observed along the height of the block. Macroseggregation seems to be a key parameter for solidification computation as it impacts a lot temperature dependent properties such as density, enthalpy and also possibly viscosity. Such variations are plotted for the three compositions detailed in § 4.1.1 : nominal, riser and block composition.

Density plotted in Figure 4.4 shows that liquidus depends on composition. Above liquidus, density increases due to thermal contraction for the three set of compositions. At liquidus temperatures, 2 041°C for the foot and 1 895°C for the nominal compositions, zirconia crystals solidify. In the riser, primary corundum crystals start to solidify at 1 775°C. After the macroseggregation had time to established, liquidus has therefore a variation of 266°C between the riser (the lowest liquidus) and the foot (the highest liquidus) compositions. The eutectic valley is reached at 1 771°C for the samples at composition  $w_0$  and  $w_{\text{foot}}$  but only at 1 737°C for the sample at  $w_{\text{riser}}$  composition. In thermo-mechanical solver presented in Chapters 2 and 3, a single liquidus (at nominal composition) was tabulated. The convection inside the riser is therefore expected to be active for a longer time as the riser stays liquid at lower temperature than the liquidus temperature at nominal composition,  $T_L(w_0)$  in Figure 4.4.

The highest density value for the liquid phase is obtained for nominal and foot compositions at the liquidus temperature as observed in Figure 4.4. For the riser composition, the maximal value is obtained when the system reaches the eutectic valley at 1 737.5°C. The maximal value is reached when the proportion of  $\text{ZrO}_2$  is the highest over the solidification path, as  $\text{ZrO}_2$  is the heaviest compound in the quaternary system  $\text{Al}_2\text{O}_3 - \text{ZrO}_2 - \text{SiO}_2 - \text{Na}_2\text{O}$ . In the foot of the block, density at liquidus is at 3 546  $\text{kg m}^{-3}$ , whereas it reaches 3 317  $\text{kg m}^{-3}$  at nominal composition. After macroseggregation had time to established, in the riser, the maximal liquid density is at 3 066  $\text{kg m}^{-3}$  and density at the liquidus is 3 042  $\text{kg m}^{-3}$ .

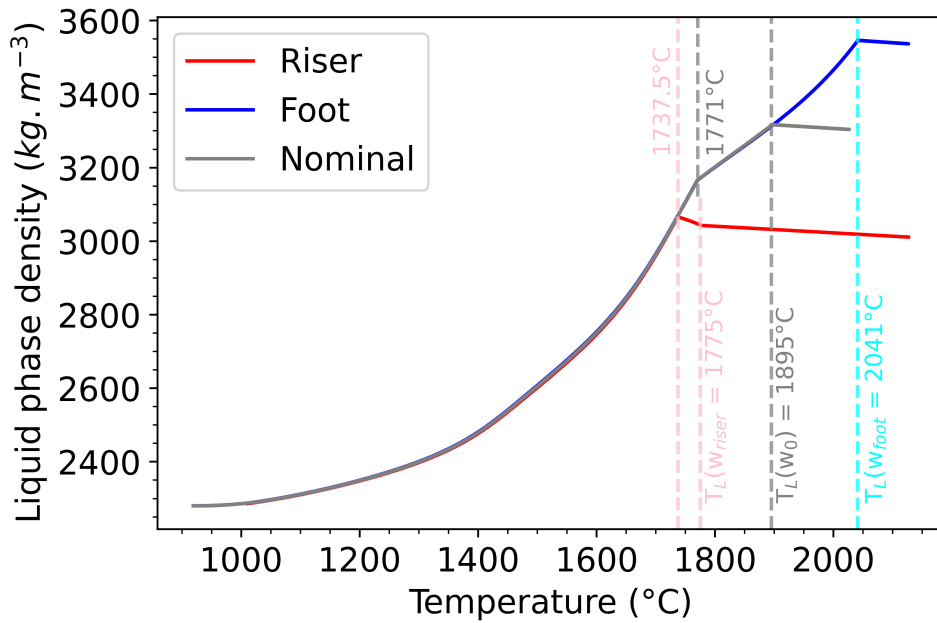


Figure 4.4: Liquid density as a function of  $T$  for the nominal composition and two others observed in the riser and in the bottom of the block.

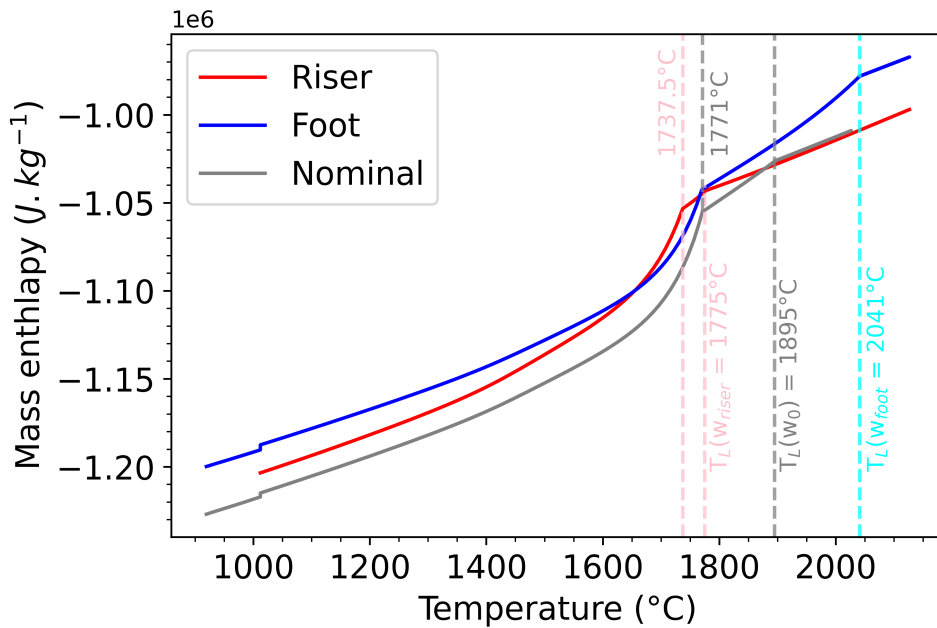


Figure 4.5: Mass enthalpy as a function of  $T$  for the nominal composition and two others observed in the riser and in the bottom of the block.

Enthalpies for the three compositions detailed in Table 4.2 are plotted in Figure 4.5. The evolutions over temperature between enthalpies in the riser (red) and in the foot (blue) are different at high temperatures. The eutectic zirconia-corundum, for nominal and foot composition, implies a change of slope at 1771  $^{\circ}\text{C}$  when corundum starts to solidify. In the riser, corundum is the only solid phase until 1737.5  $^{\circ}\text{C}$ . At lower temperature, the same sharp slope is observed when eutectic with zirconia starts to solidify. For the three compositions of Table 4.2, reach-

ing the eutectic valley implies a strong variation in the enthalpy slope. At their own liquidus temperature, the three compositions present a change of slope as shown in Figure 4.5.

The evolutions of liquid composition over the temperature for the three compositions of Table 4.2 are detailed in Figure 4.7. Between 1000 °C et 1900 °C, as the solidification paths at the foot and the nominal compositions match, the evolution of liquid composition is exactly the same as detailed in Figure 4.7c. In the riser, with the macrosegregation measured experimentally, the liquidus is at 1775 °C and the concentrations remain constant at higher temperature. At lower temperature, corundum crystals solidify and the  $\text{Al}_2\text{O}_3$  concentration (orange line in Figure 4.7) drops in the liquid that becomes progressively enriched in the remaining components.

As presented in § 2.8.2, the properties can be tabulated thanks to the PATH tool of PhysalurgY<sup>®</sup> (PY/PATH). The current system is still defined in a single zone, a single structure and three phases. The zirconia transition at low temperature is still not taken into account as macrosegregation occurs only at the beginning of solidification and little effect of the corresponding enthalpy and density variations is expected on macrosegregation.

In the former tabulation, a single global composition was defined at  $w_0$ . It is possible thanks to PY/PATH to concatenate the tabulation for different global compositions. In Figure 4.6, the different compositions of the tabulation are represented in orange. For each orange dot, 4 tabulations are defined to take into account the variations of  $\text{Na}_2\text{O}$  between 0.5 and 2 wt.% with a step of 0.5 wt.%. Temperature varies from 0 to 2000°C with a step of 10°C. Tabulations are built for all phase fractions and phase properties. The exact value for computation is obtained by intrapropagation between the closest neighbours tabulated.

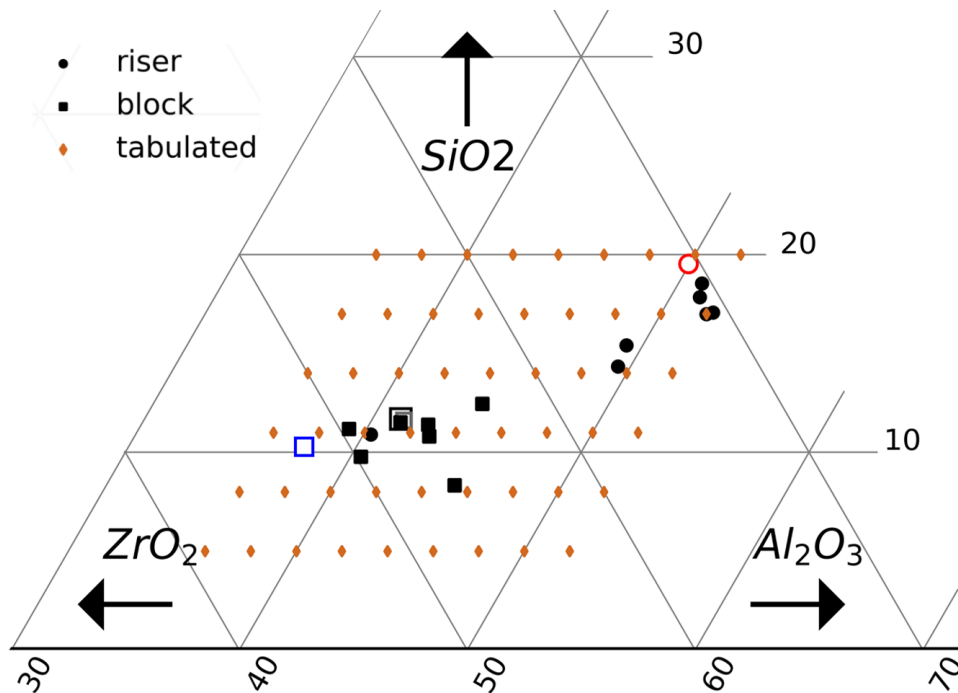


Figure 4.6: Compositions on ternary diagram comparing (orange) those tabulated with PATH tool and (black) those measured experimentally.

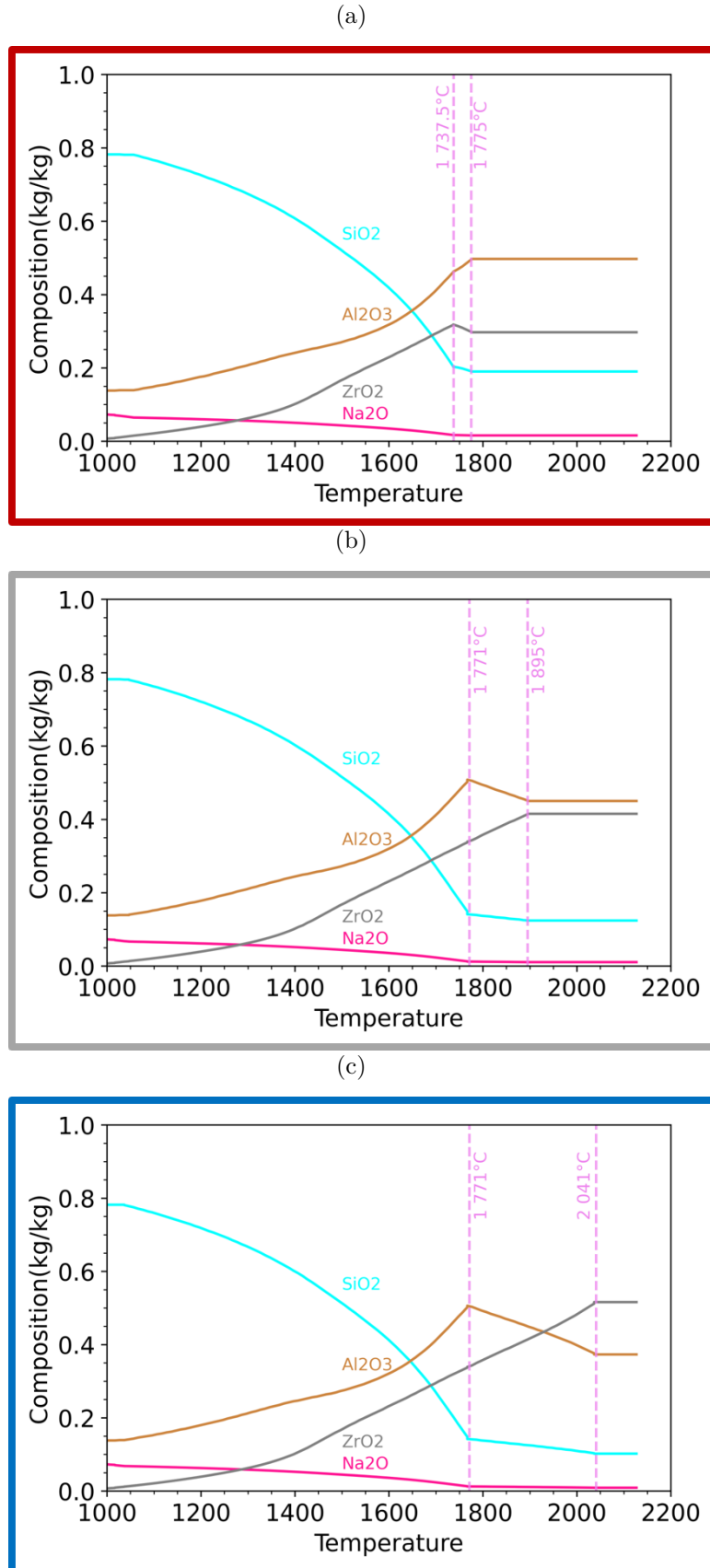


Figure 4.7: Composition of the liquid phase for the compositions detailed in Table 4.2 respectively (a) in the riser, (b) at nominal composition and (c) in the foot of the block.

## 4.2 Implementation of macrosegregation in THERCAST®

As observed in previous subsection, it is obvious that the AZS block is not uniform in composition. This composition field in the AZS block is due to the macrosegregation. This latter is the consequence of the convection at long ranges due to the relative motion of liquid during the solidification [83]. The different origins of the fluid motions are listed by Beckermann [83] and by Dantzig and Rappaz [56, Chap. 14]. The solidification shrinkage, natural and forced convection, grain motion and deformation of the mushy solid are the main causes of the macrosegregation. The numerical computations of the macrosegregation requires to describe the motion at large scale.

### 4.2.1 Call of User-Model in THERCAST®

In THERCAST®, it is possible to call User-models (orange in Figure 4.8). Their function is to by-pass the THERCAST® default solver (blue in Figure 4.8) or to add an extra action. The objective is to use the three solvers presented afterwards to obtain a numerical prediction of the map of composition. Such map will then be compared with the one obtained experimentally presented in § 4.1.1.

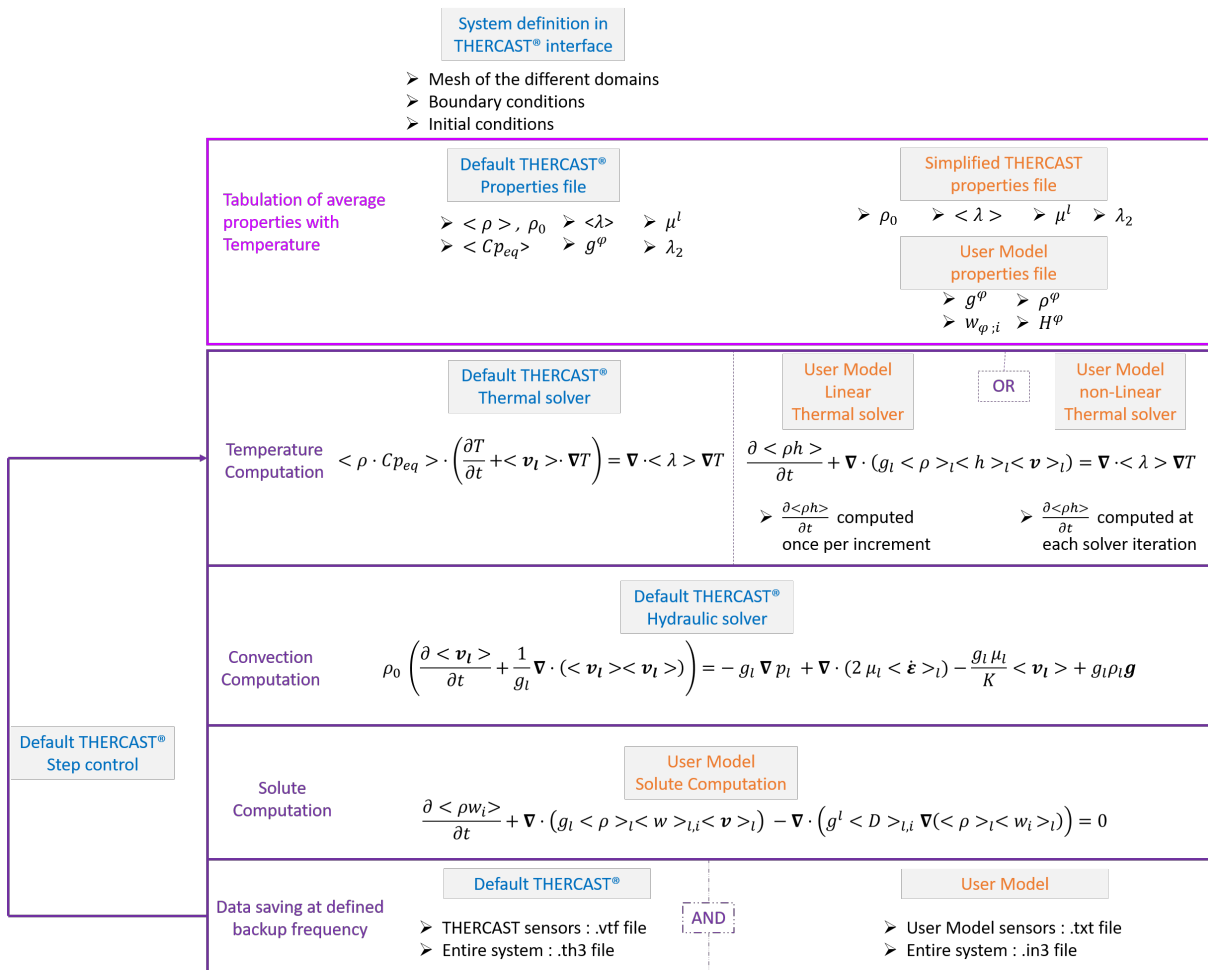


Figure 4.8: Steps of numerical computations with (blue) actions done by default THERCAST® and (orange) actions called thanks to user models.

### Thermal solver

A default thermal solver is implemented in THERCAST®. A second thermal solver considering the enthalpy of each phase can be called instead of the default solver. It is possible to execute such solver in a linear or non-linear manner for the enthalpy derivative computation. Linear method will compute enthalpy derivation only once when the solver is called (at each increment) whereas non-linear method compute enthalpy derivation at each iteration of the solver. Tests were performed to validate that linear and non-linear temperature solvers return similar outputs in our case. As annealing is slow (overall annealing over several days), properties are tabulated every 10°C, linear computations are up to 10 times faster than non-linear computations.

### Convection

In THERCAST®, as detailed by Costes in [19], momentum balance equation combines Navier-Stokes and Darcy equations. Saad [20] details the incompressible Navier-Stokes equation in the mushy zone considering the solid phase as fixed:

$$\begin{cases} \rho_0 \left( \frac{\partial \langle \mathbf{v}_l \rangle}{\partial t} + \frac{1}{g_l} \nabla \cdot (\langle \mathbf{v}_l \rangle \langle \mathbf{v}_l \rangle) \right) &= -g_l \nabla p_l + \nabla \cdot (2\mu_l \langle \dot{\boldsymbol{\epsilon}} \rangle_l) - \frac{g_l \mu_l}{K} \langle \mathbf{v}_l \rangle + g_l \rho_l \mathbf{g} \\ \nabla \cdot \langle \mathbf{v}_l \rangle &= 0 \end{cases} \quad (4.1)$$

with  $p_l$  the liquid pressure,  $K$  the mushy zone permeability ( $\text{m}^2$ ),  $\langle \mathbf{v}_l \rangle$  the average liquid velocity and  $\mu_l$  the dynamic viscosity of the liquid phase ( $\text{kg m}^{-1} \text{s}^{-1}$ ).

In mushy zone, solid crystals limit the convective flows of the liquid phase. The Carman-Kozeny law [84] is used to predict the drop of permeability in the isotropic porous domain, representative of the solid crystals, made of a mixture of solid and liquid. Permeability inside the mushy zone, written in (4.2), depends on a global shape factor  $\Phi$ , the liquid fraction  $g^l$  and the secondary dendrite arm spacing  $\lambda_2$  [56].

$$K = \Phi \frac{\lambda_2^2 \cdot g_l^3}{180 \cdot (1 - g_l)^2} \quad (4.2)$$

Only the buoyancy term ( $g_l \rho_l \mathbf{g}$ ) computes the exact density, where  $\rho_l$  varies with the temperature and the liquid phase composition  $w_{l,i}$ . This member of the equation drives the convection. Density at liquidus of the nominal alloy composition is used as a reference,  $\rho_0$ , for the other terms of the equation

### Macrosegregation

Solute conservation solver is called three times per increment: once for each component ( $\text{Al}_2\text{O}_3 - \text{SiO}_2 - \text{Na}_2\text{O}$ ) considering  $\text{ZrO}_2$  as the main element as it is the first to solidify. Solute equation computes the variation of composition over time (due to the solidification) and the transfer due to the liquid convection and diffusion. Macroseggregation solvers are properly defined in previous PhD. theses written by Rivaux [85], Saad [20] and Carozzani [67]. The solute conservation equation reads :

$$\frac{\partial \langle \rho w_i \rangle}{\partial t} + \nabla \cdot (g_l \langle \rho \rangle_l \langle w \rangle_{l,i} \langle \mathbf{v} \rangle_l) = \nabla \cdot (g_l \langle D_i \rangle_l \nabla (\langle \rho \rangle_l \langle w \rangle_{l,i})) \quad (4.3)$$

with  $\langle w_i \rangle$  the global composition of component  $i$  in the system,  $\langle w_i \rangle = \sum_{\varphi} g_{\varphi} \langle w \rangle_{\varphi,i}$ , where  $\langle w \rangle_{\varphi,i}$  is the composition of component  $i$  in the  $\varphi$  phase,  $\langle D \rangle_{l,i}$  is the diffusion coefficient in the liquid for the component  $i$  and  $\langle w \rangle_{l,i}$  the liquid composition.

Two safety controls are implemented to avoid numerical divergences of the solute solver:

- The allowed results for global concentrations and the phases concentrations are delimited by the minimal and the maximal values present in the tabulations;
- If the variation of component concentration during an increment evolves too quickly, the previous concentration is conserved. A critical variation concentration,  $\Delta w_c$  is defined.

Computations are stabilized with the Streamline Upwind / Petrov-Galerkin (SUPG) method for linear convection equation considering the incompressible Navier-Stokes equations [86] and [57, Chap. 7]. This method is used to avoid non-physical oscillations, considering a domain with only small variations of the solution (no abrupt or too large variations). The discretization of the solute equation over the mesh elements is governed by the Galerkin method where each parameter inside an element is a linear combination of the basis vectors in the element domain.

$\rho_0$	3 300	kg m <sup>-3</sup>	defined with Figure 2.6
$\lambda_2$	200	$\mu\text{m}$	arbitrary
$\langle D \rangle_{l,i}$	$1 \times 10^{-13}$	m <sup>2</sup> s <sup>-1</sup>	adapted from [87] and [88]
$\Delta w_c$	1	wt.%	arbitrary

Table 4.3: Numerical values of different variables considered in THERCAST<sup>®</sup> macrosegregation computations.

#### 4.2.2 PATH adaptation for concentrate alloys

Computing macrosegregation implies that locally, the global concentration,  $\langle w \rangle_i$ , in a RVE varies. Global concentration has to be known to tabulate phase fraction and composition with PATH as explained previously. In Chapter 2 § 2.8.2, the first tabulation (for phase fraction and composition) had a single global set of concentration  $\langle w \rangle_0$ . In the second tabulation (for phase density and enthalpy), PY/PATH concatenates already the properties predicted by Thermo-Calc<sup>®</sup> for different phase compositions encountered. Similar method is used when macrosegregation is applied. PY/PATH is now used to concatenate even for the first tabulations several sets of global compositions. The second tabulation continues to tabulate properties for encountered compositions.

Tabulation grid for the quaternary system is detailed in Table 4.4, with ZrO<sub>2</sub> as main element and O defined with an activity set as 1 (as in Chapter 2). The sum of the different component compositions has to be below 100 (to get positive concentration of ZrO<sub>2</sub>). The sum of the maxima in Table 4.4 is 74 wt.%.

	Al <sub>2</sub> O <sub>3</sub>	SiO <sub>2</sub>	Na <sub>2</sub> O	T (°C)
Min	36%	5%	0.5%	0
Max	52%	20%	2%	2000
Step	2	3	0.5	10

Table 4.4: Range of compositions in an AZS41 block for tabulations with PY/PATH that contained the global composition variations measured experimentally over the height of an AZS block.

The second tabulation considers sets of compositions encountered in the phase along the solidification path as detailed in Chapter 2 § 2.8.2. In Figure 2.21, the sum of the maximum for each component concentration in the liquid phase encountered during the annealing is above

100% as the liquid composition varies a lot when the temperature decreases during annealing. As the concentration of  $ZrO_2$  has to be positive, an adaptation of PY/PATH for concentrated alloys was required.

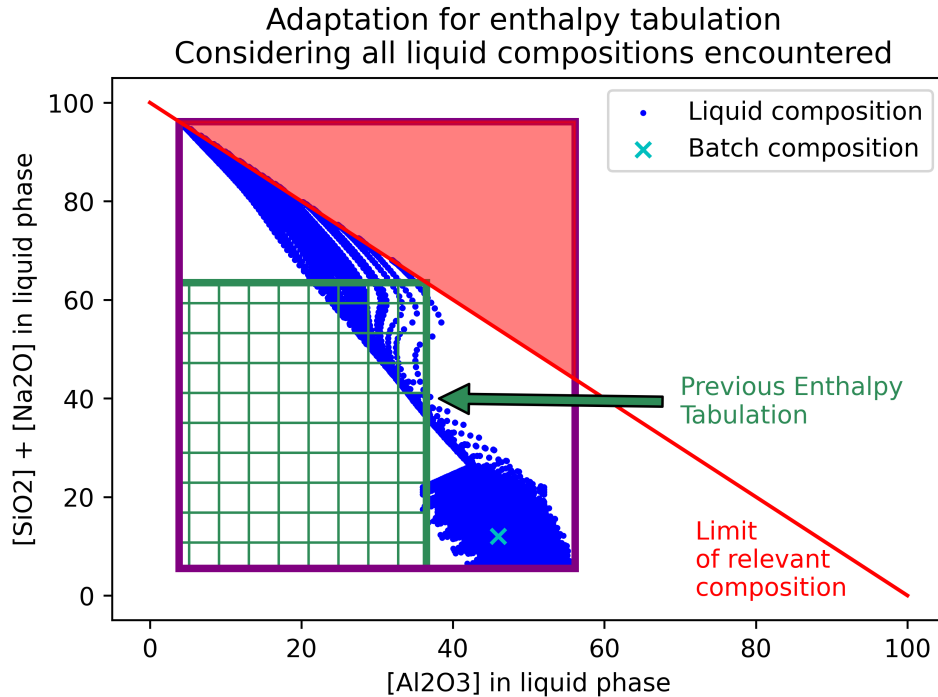


Figure 4.9: Range of compositions for the tabulation of liquid phase properties (i.e. enthalpy and density) in the PY/PATH tool. The purple rectangle represents the required range of compositions that needs to be tabulated to cover the entire solidification path. The green rectangle represents the previous PY/PATH range of composition included in tabulation to avoid having to test a set of composition which requires to return data inside the red triangle where sum of the three solute is above 100%. The blue dots represent liquid composition obtained in the first tabulation and the light blue cross represents the initial composition, when the entire block is at the batch composition  $w_0$ .

In Figure 4.9, the liquid composition encountered is plotted as a distribution between  $Al_2O_3$  (x-axis) and the sum  $SiO_2 + Na_2O$  (y-axis). The blue spots represent liquid compositions obtained in the first tabulation. It is then mandatory to tabulate the properties (density and enthalpy) for the different sets of compositions defined by min and max compositions. Assuming a general combination of all min and max, this corresponds to the purple rectangle in Figure 4.9. Some sets of composition imply irrelevant compositions, where  $ZrO_2$  is negative, represented by the upper red triangle. A safety control is implemented in PY/PATH to tabulate only in the possible range defined by the lower left section in Figure 4.9. This safety step had no impact for diluted alloys that were considered before in PY/PATH. For AZS, such control implies that only the compositions contained in the green square of Figure 4.9 were tabulated. The blue dots represent encountered compositions during the solidification path and most of them are not included in the green rectangle. This means that such tabulation does not necessarily return properties during the entire solidification path. The light blue cross is the nominal alloy composition, representing the system at its initial stage when it is fully liquid. Even this symbol is not included in the enthalpy and density tabulations. The solute solver will consider the closest concentration tabulated in the green square but the variations over the annealing

will not be relevant. It was therefore required to adjust the PY/PATH tool to consider the entire domain of the general combination of all min and max (purple rectangle) and not only the relevant sets of combinations with only positive  $ZrO_2$  concentrations (green rectangle).

The CIMLib<sup>®</sup> user solute solver imposes to get a full tabulation with each component concentration tabulated with all the other component concentrations observed. A tabulation over a domain that includes only the blue dots in Figure 4.9 is not readable by the solver. It has been decided to adapt the PY/PATH tool to get full tabulation instead of adapting the tabulation reading method in the solver. The objective is then to get values of density and enthalpy over the entire purple rectangle in Figure 4.9. Arbitrary values for irrelevant compositions (red triangle in Figure 4.9) are defined :  $h = 10^6 \text{ J kg}^{-1}$  and  $\rho = 10^3 \text{ kg m}^{-3}$ .

In the former version of PY/PATH, the same number of sets of composition is expected for both tabulations. For the first tabulation, with the range of global composition and the step presented in Table 4.4, 9 different compositions are tested for  $Al_2O_3$ , 6 for  $SiO_2$  and 4 for  $Na_2O$ , leading to a total of  $9 \times 6 \times 4 = 216$  sets of composition. There will also be 216 sets of compositions in the second tabulation that returns phase properties for encountered phase composition. For a given phase, the minimal and the maximal concentrations for each element are defined, values for the liquid phase is in Table 2.6. The tabulation rule implies therefore that 9 different values are between 12.05wt.% and 51.74wt.% for the proportion of  $Al_2O_3$  in the liquid phase and so on for the two others components

To get the data at a given composition, the solver interpolates the values with its closest tabulated neighbors. To limit the risk of having to interpolate an obtained composition with a set of composition with arbitrary properties if its closest neighbor is located in the red triangle in Figure 4.9, the tabulation for enthalpy and density has to be refined. A multiplying factor is defined (set at 8) to increase the amount of composition tested for each components. It leads to  $(9 \times 8) \times (6 \times 8) \times (4 \times 8) = 110\,592$  sets of compositions tabulated. A cleaning step is used to delete set of compositions that are identical. For example, as zirconia is mainly  $ZrO_2$  with a slight solubility of  $Al_2O_3$ , the minimal and maximal values for  $SiO_2$  and  $Na_2O$  are both 0. The second tabulation for properties will then test only the variations over  $Al_2O_3$ , i.e.  $9 \times 8 = 72$  sets of compositions.

Each sets of composition are tabulated over temperature with a defined step :  $10^\circ\text{C}$  for the first tabulation (201 increments) and  $200^\circ\text{C}$  for the second (11 increments). It means that, just for the liquid phase, PY/PATH calls Thermo-Calc<sup>®</sup> to compute  $216 \times 201 = 43416$  equilibria for the first tabulation and  $110592 \times 11 = 1216512$  equilibria for the second tabulation. Each phase has to get its own couple of tabulations and our system takes in account three phases : liquid, zirconia and corundum. This method implies extremely heavy tabulation file (63.2 MB) that limits the initial range of compositions that can be tabulated. A way to simplify it would be to linearise over time and compositions the properties to obtain data without such heavy tabulation.

## 4.3 Focus on results from hydraulic computations

### 4.3.1 Estimated velocity of AZS liquid with dimensionless parameters

Dimensionless values are used to get an order of magnitude of the velocity if the system was ideal and completely liquid.

**The Rayleigh number** compares the time scale needed for thermal transport between thermal diffusion and thermal convection at a given velocity of the fluid

$$Ra = \frac{\beta_T \cdot \Delta T \cdot l^3 g}{\nu \cdot \alpha} \sim 1.3 \cdot 10^7 \quad (4.4)$$

Considering the following numerical values

- $\beta_T$  : thermal expansion coefficient obtained from data presented in Figure 2.6.  

$$\beta_T = 5 \cdot 10^{-5} \text{ K}^{-1}$$
- $\alpha = \frac{\lambda}{\rho \cdot C_p}$  : thermal diffusivity obtained from data presented in Figure 2.4 to Figure 2.6.  

$$\alpha = \frac{8}{3800 \cdot 2000} = 10^{-6} \text{ m}^2 \text{ s}^{-1}$$
- $\nu$  : kinematic viscosity obtained from data presented in Figure 2.6 and dynamic viscosity measured at CEMHTI lab [89].  

$$\nu = 2.83 \cdot 10^{-5} \text{ m}^2 \text{ s}^{-1}$$
- $g$  : gravitational acceleration.  

$$g \simeq 10 \text{ m s}^{-2}$$
- $l$  : characteristic length chosen as the minor face of the block as presented in Figure 2.1.  

$$l = 0.2 \text{ m}$$
- $\Delta T$  : temperature variation within a segment  $l$  estimated by thermal computations presented in Chapter 2.  

$$\Delta T = 100 \text{ K}$$

**Grashof number** is characterizing the ratio between the buoyancy force that induces motion when there are density variations and the viscous forces that constrain the displacements in natural convection.

The Grashof number has been defined using the numerical values presented for the former section about the Rayleigh number determination.

$$Gr = \frac{g \cdot \beta_T \cdot \Delta T \cdot l^3}{\nu^2} = \frac{Ra \cdot \alpha}{\nu} \sim 5 \cdot 10^5 \quad (4.5)$$

**The Reynolds number** is used to predict the transition between laminar to turbulent flow in forced convection systems. It is defined as the ratio between inertia and viscous forces within a fluid.

$$Re = \frac{v \cdot l}{\nu} \quad (4.6)$$

### Estimated velocity

In inertial regime, the buoyancy term could be balanced with the inertia.

$$\rho \frac{v}{l} \sim \Delta \rho g \quad (4.7)$$

The Reynolds number can then be related to the Grashof number :  $Re \sim \sqrt{Gr} = 7.1 \times 10^2$ . It is then possible to retrieve an estimation of the liquid velocity inside a fully liquid domain.

$$v = \frac{\sqrt{Gr} \cdot \nu}{l} \quad (4.8)$$

The order of magnitude for the velocity inside the AZS liquid should be around:  $v = 0.1 \text{ m s}^{-1}$ . As the system is not fully liquid, an order of magnitude for velocity in AZS is expected to be around  $1 \text{ cm s}^{-1}$  in THERCAST® simulations. Yet, liquid pouring was not modeled, the velocity at the initial stage was null.

### 4.3.2 Convection vs Sedimentation

Lesoult [90, Chap. 10] presents a map of segregation of a steel ingot where an accumulation of equiaxed grains at the bottom of the block is clearly identified as the result of sedimentation. In THERCAST®, only solute convection is computed to get a map of macrosegregation. The model considers fixed solid phases. It means that the sedimentation of zirconia crystals is not taken into account in the simulations.

This section presents the determination of the falling speed of a sphere in a liquid. Stokes law is applied to a sphere of solid zirconia in AZS liquid at  $1860^\circ\text{C}$  for an arbitrary mean diameter of zirconia crystals, chosen after SEM observations presented in Figure 4.3a.

$$v = \frac{(\rho^{\text{ZrO}_2} - \rho^l) \cdot (d^{\text{ZrO}_2})^2 \cdot g}{18 \cdot \mu^l} \sim 0.13 \text{ mm s}^{-1} \quad (4.9)$$

Considering the following numerical values

- $\mu$  : dynamic viscosity measured at CEMHTI lab [89]
 
$$\mu = 94 \text{ mPa s}^{-1}$$
- $d^{\text{ZrO}_2}$  : arbitrary defined diameter of the solid sphere at  $1860^\circ\text{C}$ 

$$d = 100 \mu \text{ m}$$
- $g$  : gravitational acceleration
 
$$g \simeq 10 \text{ m s}^{-2}$$
- $\rho^{\text{ZrO}_2}$  : density of solid zirconia at  $1860^\circ\text{C}$ 

$$\rho^{\text{ZrO}_2} = 5559 \text{ kg m}^{-3}$$
- $\rho^l$  : density of AZS liquid at  $1860^\circ\text{C}$ 

$$\rho^l = 3319 \text{ kg m}^{-3}$$

Convection in a fully liquid domain is estimated 1000 times larger than sedimentation and in a first approximation, sedimentation may be neglected. However, this analysis was performed considering only the thermal convection ( $\beta_T$ ) and not the impact of the solute convection ( $\beta_w$ ).

Sedimentation might also have an impact as the real convection velocity is expected to be lower than  $0.1 \text{ m s}^{-1}$  and the flow could broke dendrites and carry them to the bottom of the block due to the orientation of the convection loops detailed in the next part.

### 4.3.3 Impact of density on the convection motions loops

The order of magnitude of the flow velocity is a first indication. A second aspect is the orientation of the convection loops.

Above liquidus, density increases when temperature decreases due to thermal contraction. By considering the gravitation acceleration perpendicular to temperature gradient, it implies that cooler liquid goes down and warmer liquid goes up as the red loop in Figure 4.10. Below liquidus, cold liquid, depleted in zirconia is lighter, creating an inversion in the orientation of the convection loop as represented by the blue loop in Figure 4.10.

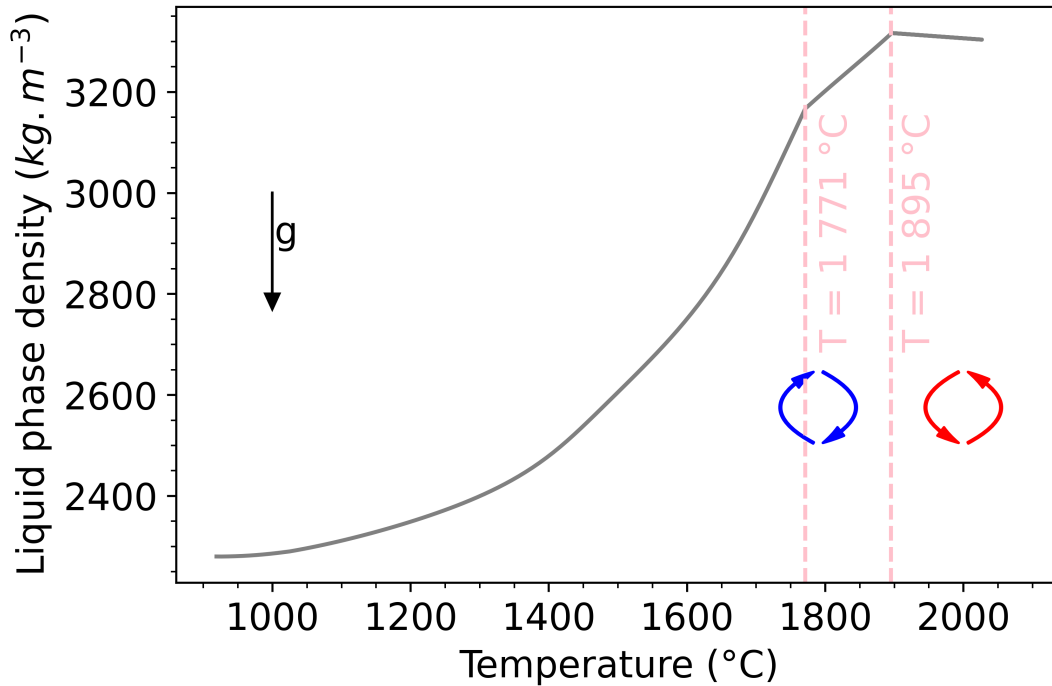


Figure 4.10: Impact of the liquid density variation on convection loops orientation (blue below liquidus and red above liquidus).

Such situation is retrieved in the simulation as shown in Figure 4.11 four minutes after the beginning of the cooling down. In a fully liquid domain, before the solidification front (represented by the  $g_l=0.99$  line), warmer liquid goes up (orangish color of z-velocity vector) at the center of the block and goes down before the solidification front. When the liquidus is reached, the lighter liquid goes up inside the mushy zone and a second loop is observed with upward z-velocity vectors at the right of the figure. Close to the skin of the block, especially at the edge of the block (bottom right of the figure), temperature is below liquidus and the velocity is close to 0, with a yellow color in Figure 4.11. This is modeled thanks to the Darcy law involving the mushy zone permeability detailed in equation (4.1).

After 4 min of annealing, the highest velocity observed inside the quarter of the block is  $11.3 \text{ mm s}^{-1}$ , in agreement with the velocity expected in § 4.3.1. The thermo-hydraulic results present therefore a relevant order of magnitude of velocity and relevant orientation for the convection loops.

After half an hour, the loop due to solute convection imposes its orientation over the whole block. As represented in Figure 4.12, a single loop is observed inside the block.

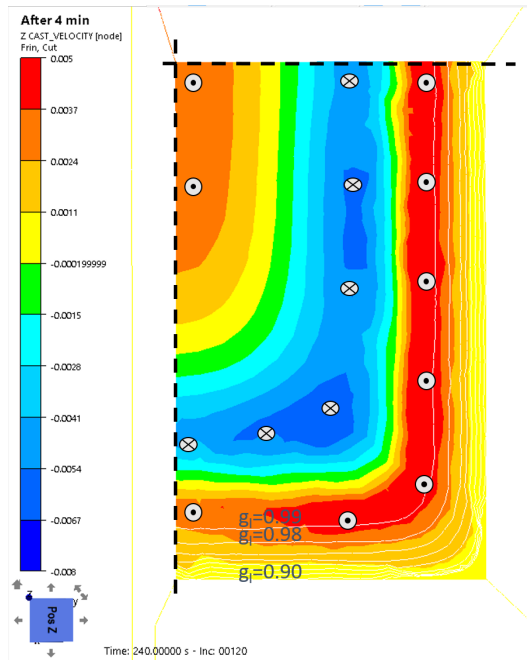


Figure 4.11: Horizontal cutting plane at 0.8 m height in the block with (color) the value of velocity vector over z-axis, (lines) the iso-fractions of liquid phase between 0.9 and 0.99 and (symbols) a summary of vector orientation after 4 min of annealing.

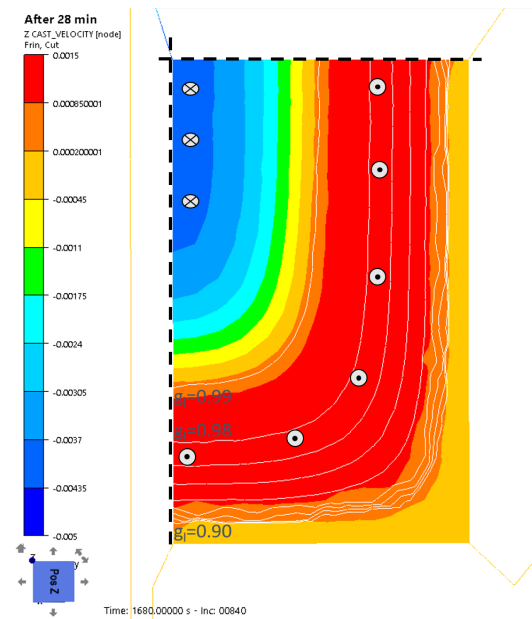


Figure 4.12: Horizontal cutting plane at 0.8 m height in the block with (color) the value of velocity vector over z-axis, (lines) the iso-fractions of liquid phase between 0.9 and 0.99 and (symbols) a summary of vector orientation after 28 min.

## 4.4 Macrosegregation inside a standard AZS block geometry

Numerical outputs of macrosegregation computations on standard block geometries are presented in this section.

### 4.4.1 Temperature history

As convection flows are computed with real liquid viscosity measured experimentally, the extra value of conductivity at high temperature ( $1\ 875^{\circ}\text{C} - 15\ \text{W m}^{-1}\ \text{K}^{-1}$ ) for AZS is removed and only measured thermal conductivity is kept as detailed in Figure 2.4.

In order to limit computation duration, only the first 12 h are simulated. At this time, every mesh element is below liquidus as shown in Figure 4.14 and convection becomes too weak to further modify the macrosegregation.

The temperature history deduced from the thermo-hydraulic solver remains close to the temperature results obtained with the thermal solver by default in THERCAST<sup>®</sup> during the first 5 hours as shown in Figure 4.13. The use of enthalpy instead of heat capacity tabulations requires a new temperature optimization to better retrieve measurements beyond the first 5 hours. In the riser, temperature predictions are still the worst. The riser temperature prediction are too cold at the beginning and the prediction for temperature peak is not even reached after 12h whereas it has been measured after 5h of annealing.

A well established temperature history is required to estimate the system composition. A new optimization of the temperature history should be performed for this new solver. However,

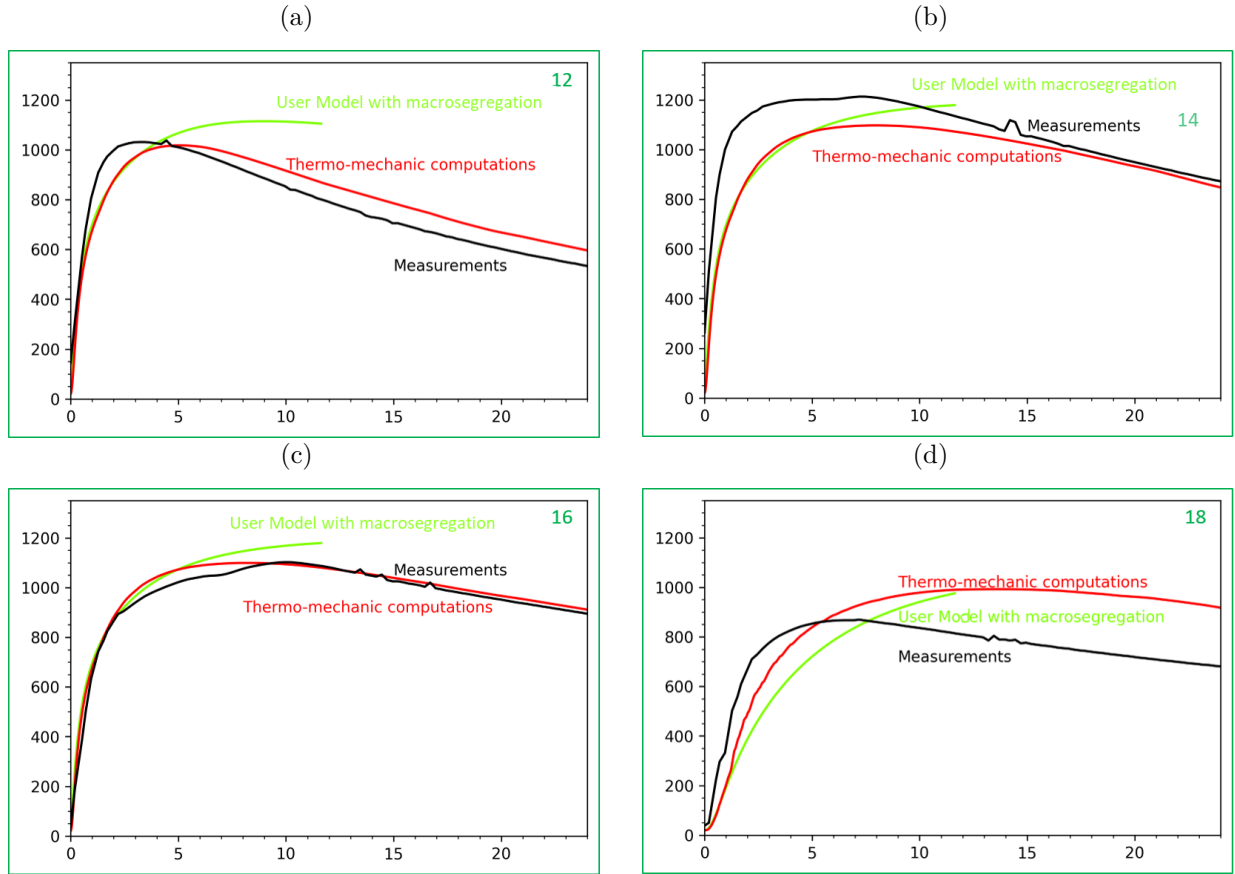


Figure 4.13: Comparison of temperature histories at different locations (see Figure 2.11) for (black) recorded data, (red) computed with default thermo-mechanical solver and (green) thermo-hydraulic solver with macrosegregation : (a) #12 bottom of the block, (b) #14 middle of the block, (c) #16 top of the block, (d) #18 riser.

due to lack of time, the adaptation of interface resistances has not been done. However, most of the macrosegregation occurs during the first hours, when temperature predictions are not far from experimental results.

#### 4.4.2 Convection predictions

The highest velocity predicted after 11h40 of annealing is  $0.5 \text{ mm s}^{-1}$  at the junction between block and riser. Most of the velocity norm are below  $10 \mu\text{m s}^{-1}$ . Macrosegregation can be considered as over especially because ladles of liquid are localized and not connected anymore as presented in Figure 4.16.

As discussed in Figure 4.11, just above liquidus, liquid goes up close to the skin of the block. Convection creates segregated channels of liquid depleted in zirconia. Such channels have a lower liquidus (as presented in Figure 4.4) so the liquid fraction pattern will also form channels (see Figure 4.14) even with temperature gradient perpendicular to the faces and oriented toward the core of the block (see Figure 4.17). Macrosegregation creates A-segregates patterns<sup>1</sup> close to external faces of the block as observed in metal [83, 90]. After 10h of annealing, V-patterns<sup>2</sup> are formed at the center of the block.

<sup>1</sup>long truncated going toward the riser cone [90]

<sup>2</sup>overlap of downward segregated channels [90]

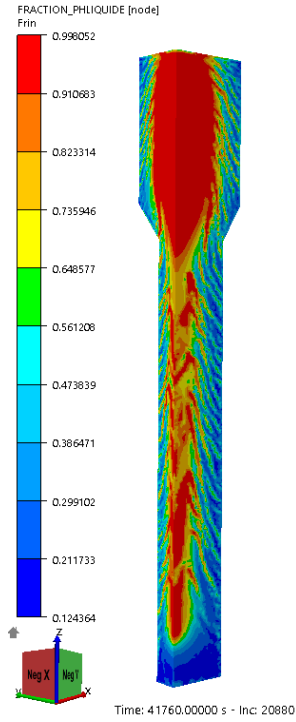


Figure 4.14: Map representing the liquid fraction inside the block after 11h40min.

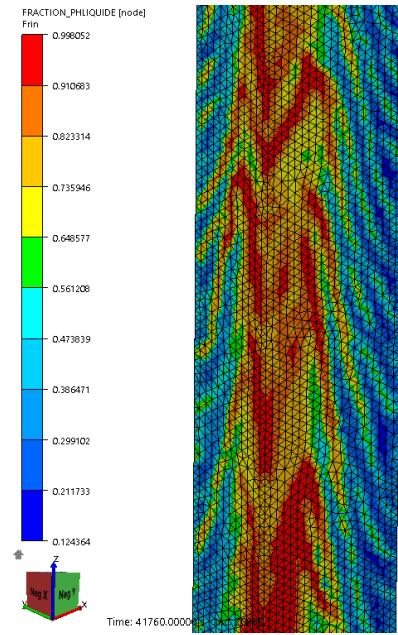


Figure 4.15: Zoom inside the block representing the liquid fraction and the segregation channels in A-pattern at the external part of the block and V-pattern at the core of the block after 11h40min.

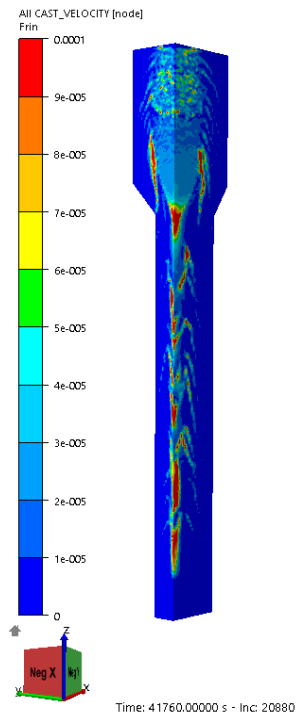


Figure 4.16: Map representing (color) velocity norm inside the block after 11h40min.

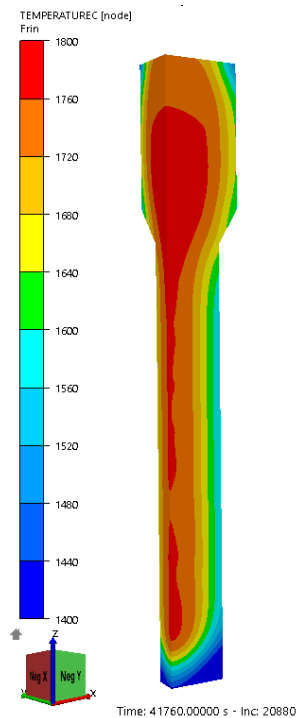


Figure 4.17: Map representing (color) temperature inside the block after 11h40min.

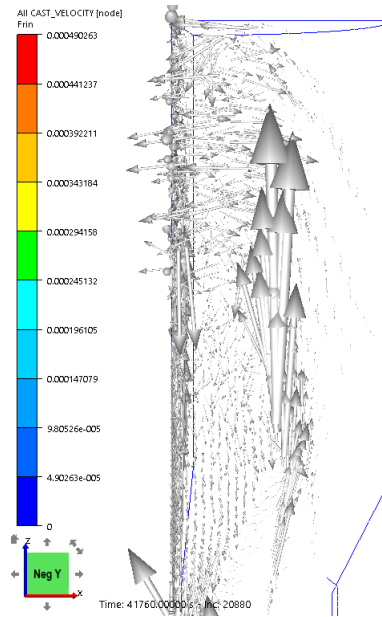


Figure 4.18: Zoom of the riser of the block showing the velocity vectors after 11h40 of annealing.

The velocity in the riser after 11h40 of annealing is presented in Figure 4.18. As mentioned in Figure 4.12, a single convection loop is observed with velocity upward close to the external faces and downward at the core of the block.

#### 4.4.3 Numerical map of macrosegregation

Pouring step is not modeled for AZS blocks. As the mold is not pre-heated, the AZS surface is quenched and macrosegregation has no time to settle. Quenching can be handled by thermal solvers and even if the first increments might present strong variations of temperature, stabilization occurs quickly (less than 10 increments). Composition is determined considering the temperature of the system. The instabilities over the first increments impact a lot the concentration that reaches irrelevant values (such as negative or above 100%). As the enthalpy is defined depending on the composition, such artifact in a mesh element degenerates as it will impact the thermo-hydraulic computations around and so on. Relevance of results is performed thanks to two actions : during the first 3 min, macrosegregation is not computed and concentration are contained in the range of the tabulations as detailed in § 4.2.1. The 3 min duration corresponds to the pouring duration and it gives time to the thermal solver to stabilize before considering macrosegregation. It is then possible to get stable results with the different solvers : thermal, hydraulic and solute solvers.

Macrosegregation is a chemical attribute due to the long range transport of chemical species, mostly by convection during the solidification process. The non-uniform distribution due to macrosegregation, taking place at the solid/liquid interface, is enhanced by convection flows and is propagated at the macro scale of the cast product. It is difficult to validate the mesh convergence for composition outputs, whereas mesh convergence has been checked for temperature outputs. The impact of mesh on concentration is plotted in Figure 4.19. Some channels are only one mesh element wide and the channel size decreases when the mesh grid is finer as in the top left corner of Figure 4.19.

Map of macrosegregation inside the block is presented for the four components of the AZS block in Figure 4.20 and Figure 4.21.  $\text{SiO}_2$  and  $\text{Na}_2\text{O}$  are in higher concentrations in the riser

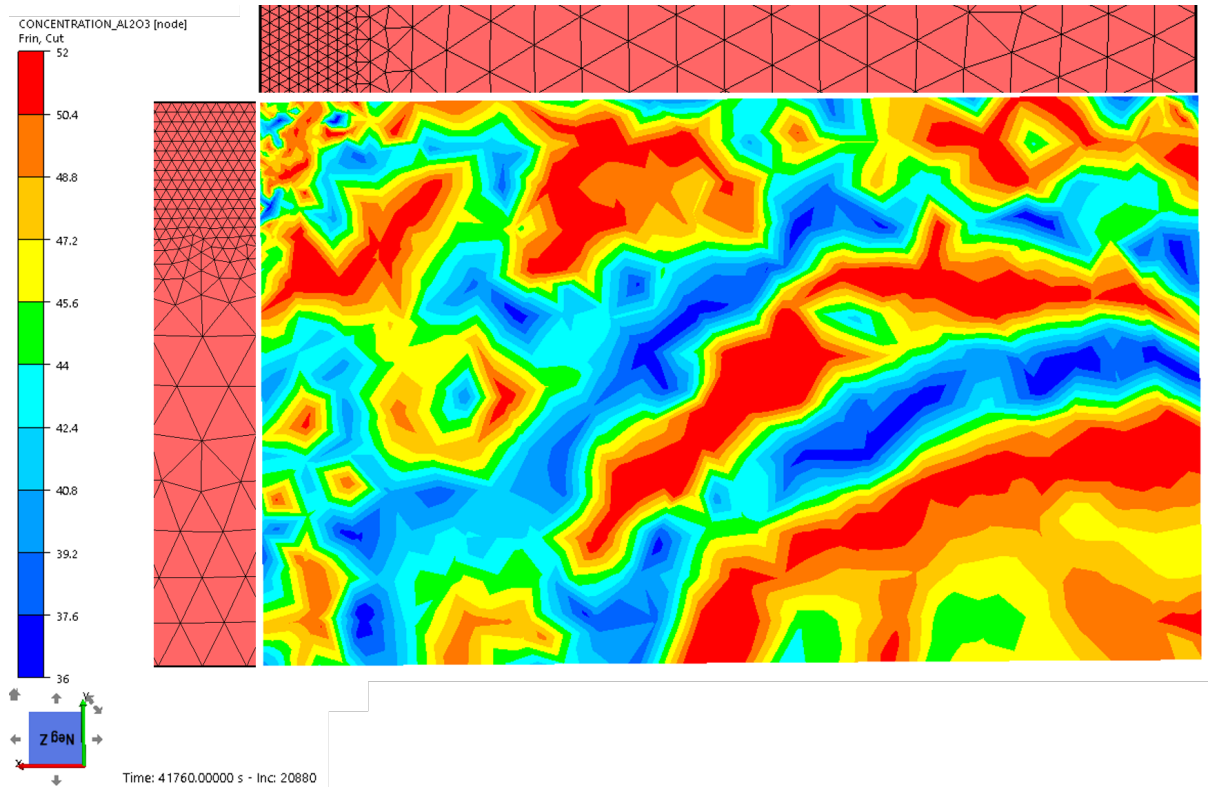


Figure 4.19: Horizontal cutting plane at 0.8m height showing the mesh size and the predicted global concentration of  $\text{Al}_2\text{O}_3$  after 11h40.

than in the block. Figure 4.21 shows that glassy phase compositions ( $\text{SiO}_2 - \text{Na}_2\text{O}$ ) are the closest to experimental results over the block height compare to the other compounds  $\text{Al}_2\text{O}_3$  and  $\text{ZrO}_2$ .  $\text{Al}_2\text{O}_3$  is present in high proportion at the bottom of the block and at the bottom of the riser. However, a depletion of  $\text{Al}_2\text{O}_3$  is measured in the block experimentally and only the first elements at the bottom of the block are depleted with results close to the experimental measurements. In simulation outputs,  $\text{ZrO}_2$  concentration in the block is depleted compare to nominal alloy composition whereas experimental results show an enriched block in  $\text{ZrO}_2$  over its entire height. The riser composition predictions get closer to experimental results where the block is indeed depleted in  $\text{ZrO}_2$  and enriched in  $\text{Al}_2\text{O}_3$ .

As the velocities estimations have been done for thermal convection in a fully liquid system, the hypothesis to neglect sedimentation might be too hard for the modeling of the industrial AZS blocks solidification. If sedimentation is considered,  $\text{ZrO}_2$  crystals would sink after their solidification, when liquid convection flows are still important and before solidification of the eutectic with corundum.

At the top of the riser, a depletion of  $\text{Al}_2\text{O}_3$  and  $\text{ZrO}_2$  is predicted by the numerical models. This phenomenon is predicted after the corundum has started to solidify. This might be due to the fact that the permeability in the mushy zone is too large and that the liquid depleted in  $\text{Al}_2\text{O}_3$  and  $\text{ZrO}_2$  condenses at the top of the block, pushing down the liquid enriched in  $\text{Al}_2\text{O}_3$ . A parameter study about the permeability is presented in the next section.

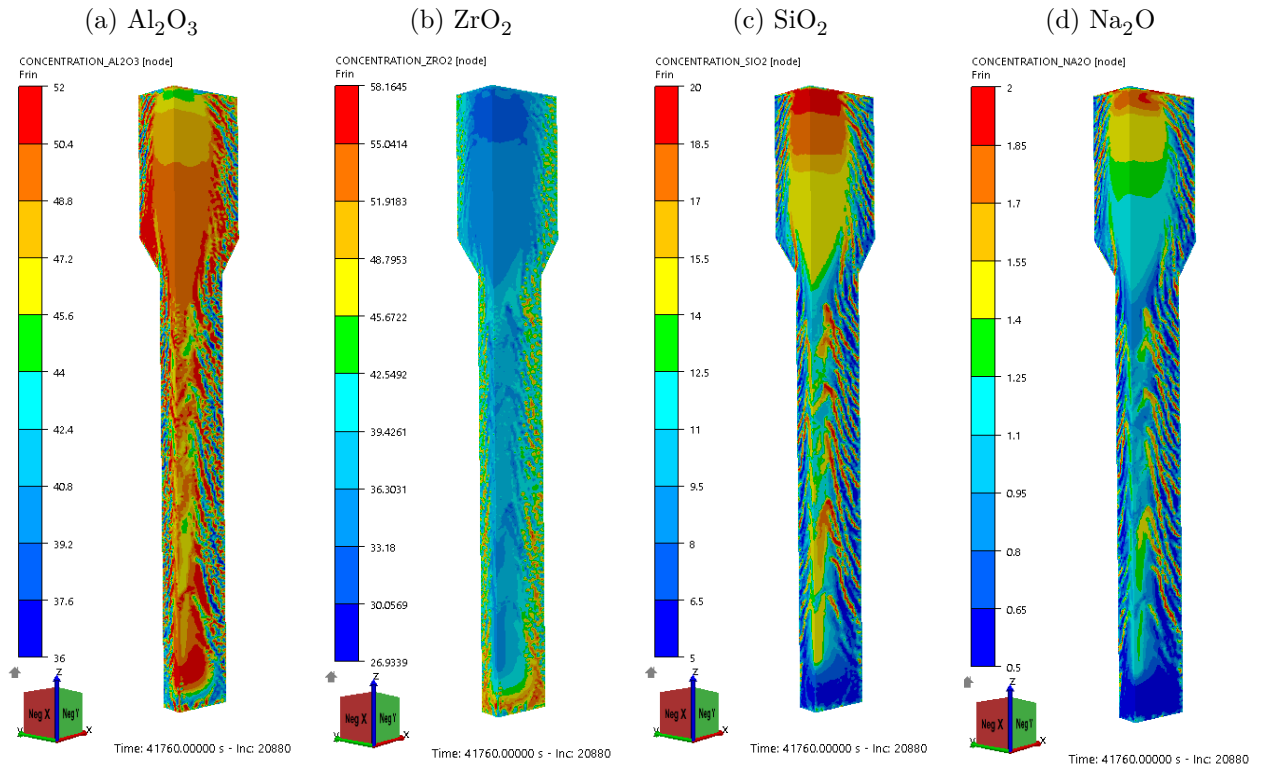


Figure 4.20: Map of composition for the different components of the AZS after 11h40 of annealing.

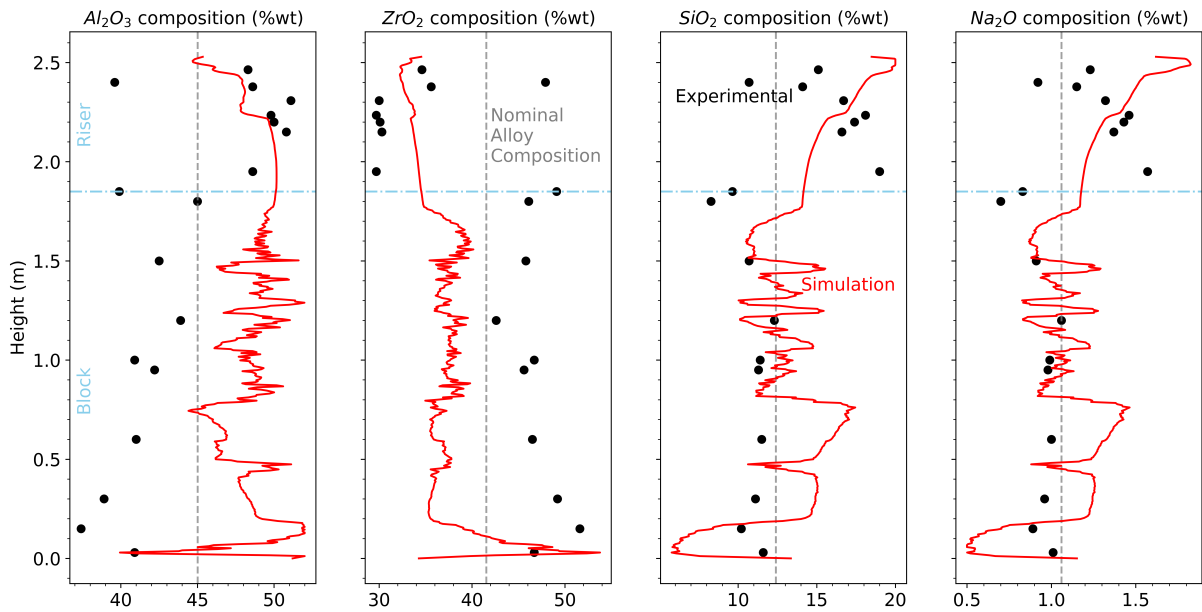


Figure 4.21: Composition profile along the block height (black) measured and (red) simulated at the center of the block. The limit with the riser (at 1.8 m high) is outlined by an horizontal dashed blue line. The nominal AZS composition is marked by a vertical dashed grey line.

#### 4.4.4 Impact of $\lambda_2$ parameter on permeability and macrosegregation results

The secondary dendrite arm spacing value,  $\lambda_2$ , for AZS material varies inside the block as the microstructure evolves depending on the distance to the skin of the block as observed in SEM observation in Figure 3.6. In THERCAST<sup>®</sup>, a single  $\lambda_2$  value is used in the current version. A tabulation of  $\lambda_2$  depending on the cooling rate requires a strong software development. As  $\lambda_2$  is used to determine the permeability in the mushy zone, it has a strong impact on convective flow and therefore solute redistribution within the block.

When  $\lambda_2 = 500 \mu\text{m}$ , the velocity one hour after casting is still close to  $1 \text{ cm s}^{-1}$  and temperature in the riser reaches the beginning of corundum solidification. Liquid depleted in zirconia and alumina becomes even lighter as shown in Figure 4.10. This liquid will stay at the top of the block and will push down the liquid enriched in  $\text{Al}_2\text{O}_3$  where corundum has not solidified yet. As velocity is still important over the entire block region, the liquid enriched in alumina sinks to the bottom of the block. This implies that the riser is depleted in alumina as shown in Figure 4.22d.

When  $\lambda_2$  is too small, the convection flow stops immediately below the liquidus. The segregation is less important between the block and the riser as shown in Figure 4.22a. In order to get a relevant concentration in the riser, a value of  $200 \mu\text{m}$  is considered in the next section, revealing a final segregation map with accumulation of  $\text{Al}_2\text{O}_3$  solute in the riser.

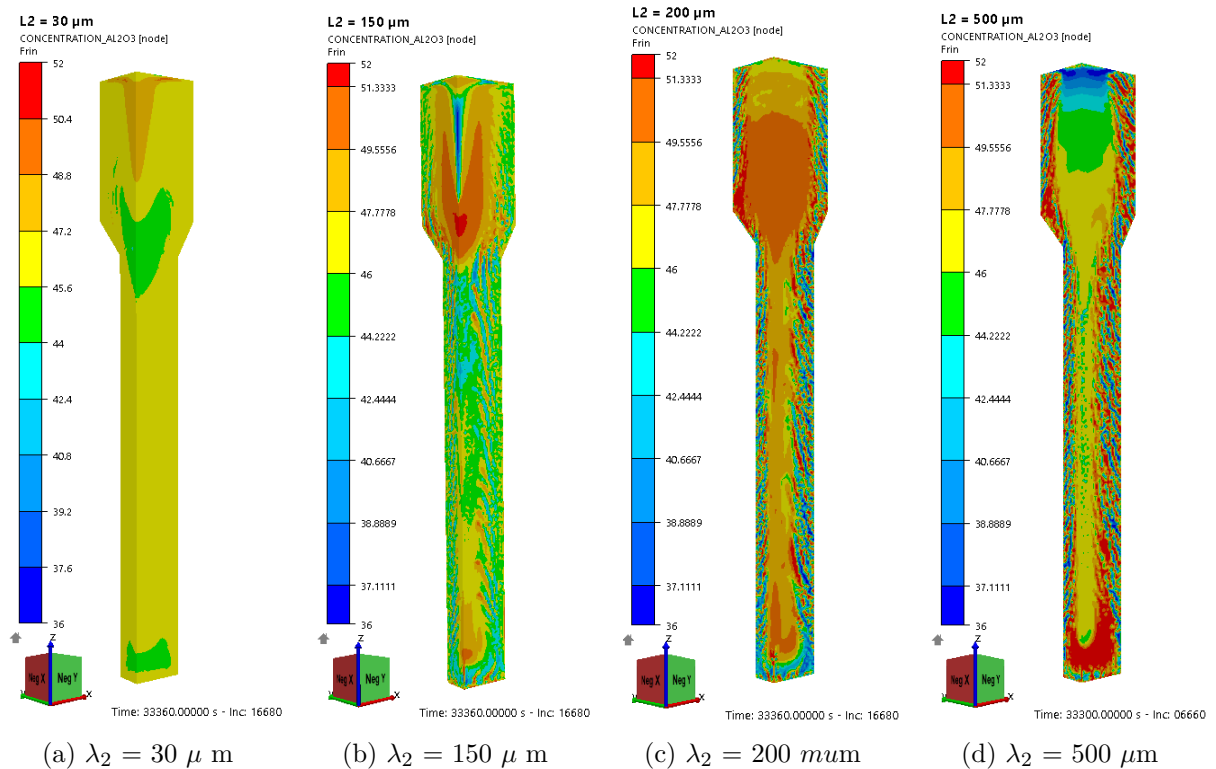


Figure 4.22: Global concentration in  $\text{Al}_2\text{O}_3$  inside block after 9h of annealing depending on the value of the secondary dendrite arm spacing value.

#### 4.4.5 Further work

The current stage of the project is not over and several axes could be suggested to improve the macrosegregation implementation for AZS blocks.

- The composition predicted by numerical simulations varies a lot from an element to another. In order to get a better representation of the map composition, numerical sensors should be located at the same height than the experimental measurements at few centimeters off the center line. The average of the composition of each element could then be compared with the experimental values. More generally, a full measurement of the segregation map is desirable for a more systematic comparison with simulated macrosegregation maps as it was presented for steels ingots by Ettrouidi [23].
- Benchmarks of different parameters would help to understand the key parameters that control the macrosegregation. For example, Brionne [22] models in THERCAST® the consequences of the cooling rate on steels macrosegregation. Similar study could be performed for AZS materials for several annealing medias. As the cooling rate impacts the microstructure, the permeability evolves inside the block. Such study for AZS materials requires to allow the variations of  $\lambda_2$  instead of keeping it constant over the entire block as it is the case currently.
- The sedimentation was neglected in the computations. Before implementing such phenomenon, as done for steel ingots by Ettrouidi [23], it would be useful to get experimental data about the structure and the size of the crystals especially at the bottom of the block. The presence of small equiaxed grains at the bottom implies the presence of sedimentation phenomenon [90]. If sedimentation is confirmed, adding more complexity to the simulations would be necessary.
- The study of another AZS composition with higher  $\text{Al}_2\text{O}_3$  proportion could validate the numerical models as having more  $\text{Al}_2\text{O}_3$  in the global AZS system implies getting more macrosegregation of this element and more corundum crystals.
- The current simulations are done considering an incompressible domain. The effect of macrosegregation on the shrinkage flow due to the formation of the macro-porosity at the top of the riser was one of the initial objective. The compressibility is currently being implemented with a level-set approach following Saad developments [20]. This approach consists in following the displacements of an AZS-air interface at the top of the block. Some experimental tests with small blocks should then be done to validate the models before going to the industrial block scale.
- Macrosegregation is currently predicted only considering a fluid-oriented approach. Another axis of research could be the coupling of macrosegregation with the mechanical resolution as done by Zhang [24] for steels. The mechanical properties for several AZS compositions will have to be characterized in order to quantify the impact of the macrosegregation on strain and stress distribution inside the block.

## 4.5 Conclusion about macrosegregation

In the previous chapter, local density was shown to be a key parameter for riser macro-porosity opening. This chapter presents the implementation of macrosegregation in an AZS block. First, experimental measurements of composition have been performed at the center of a block and its riser. The composition variations up to  $\pm 20\%$  implies variations of the liquid properties, i.e. density and enthalpy.

Some adaptations of the PY/PATH tool have been required to be able to tabulate such properties for concentrated oxide alloys. It has then been possible to call CIMLib® User Model

in THERCAST<sup>®</sup> to get the solute balance equation considered for each component in a fluid-oriented solver simulation.

Fluid-oriented solvers compute the convection flows from the experimental liquid density and viscosity. They impose a fixed solid hypothesis. Convection loop inverts its orientation when liquidus temperature is reached. Such inversion could inhibit gas bubbles elimination but gas distribution was not modeled in this study. To predict relevant convection flow velocity, that drives macrosegregation, a value of secondary dendrite arm spacing ( $\lambda_2$ ) has to be defined. Currently, a single value is implemented in THERCAST<sup>®</sup> whereas such value can evolve depending on the microstructure. The grain morphology should be taken in account to get relevant final component distribution. Experimental analysis should be performed to define precisely such value over the block and simulations could account for the variation of  $\lambda_2$  with the product. In a similar way, a study about permeability in the AZS mushy zone could be done to better anticipate the flows during the solidification of a block.

With the fluid-oriented solver called as "User Model", temperature is well predicted only for the first hours. A new optimization of parameters should be done to get a better representation of concentration over the block. It has not been performed in this study due to lack of time. Flows are predicted in agreement with the estimated velocity of the system in ideal conditions. Some compositions predicted in the block reach the tabulations boundaries for some components. For the other, composition is locally predicted in the same order of magnitude than experimental measurements of macrosegregation. If glassy phase is well predicted, more adjustments are required to improve the prediction for  $ZrO_2$  and  $Al_2O_3$  composition maps.

Sedimentation has not been considered as a fixed-solid hypothesis is used currently in the hydraulic solver. The consideration of grains transfer has been studied in steel ingot by Ettroudi [23]. To implement sedimentation, the perspective would be to add her developments into the model presented. Such consideration might improve the concentration prediction at the bottom of the block that is currently not enriched enough in  $ZrO_2$  and not sufficiently depleted in  $Al_2O_3$ .

In the future, it would also be necessary to implement compressibility to be able to predict the block shrinkage depending on macrosegregation. A wider opening in the riser is expected when macrosegregation is modeled. Such stage was not reached in this study. Saad [20] used a level-set approach to combine macrosegregation and compressibility for steel drops. The size of the AZS block is much larger and stabilization are in progress by Transvalor<sup>®</sup> to be able to get a representation of the macro-shrinkage in thermo-hydraulic computations. However, only the surface will be able to go down, internal cavities will not be computed as a single level-set would be used. The ideal situation would be to set-up the solver with small AZS block (lab scale) that could be fully analyzed and compared with simulations faster than the current one, also including enhanced investigations of macrosegregation, grain size and distribution of phases.

Finally, this study considered macrosegregation in a fluid-oriented approach. Mechanical resolution is not possible as it requires a solid-oriented solver. Zhang [24] combines both approaches for steel in the CEMEF CIMLib<sup>®</sup> internal library. The implementation of macrosegregation with a mechanical computation could be a way to determine the impact of macrosegregation on defects such as hot tears presented in the former chapter.

# Conclusion

This PhD project focuses on the production of electrofused refractory blocks made of Alumina-Zirconia-Silica (AZS) and its optimization. The main objectives for industrial refractory producers are, first, the prediction of defects occurrence, with a criterion characterizing the hot tear susceptibility, second, the optimization of riser geometry thanks to the prediction of solidification shrinkage after casting and third the distribution of chemical species within the block, known as macrosegregation. A visit at a Saint-Gobain SEPR plant was useful to fully understand the industrial production process of such blocks and to become familiar with the specificities and defects (especially edges cracks) observed at industrial scale. To optimize block quality or process productivity, this project aims at modeling the solidification of refractory blocks made of AZS in order to anticipate the impacts on quality of changes in industrial processes, to optimize the riser geometry and to anticipate the macrosegregation map at block scale. The guiding thread is to increase (or confirm) the quality of blocks and to reduce waste of material and energy during block casting.

A first stage is to collect relevant material properties. Some of them are collected in the literature, others are extracted from the thermodynamical database TCOX10 and some required more experimental investigations at Saint Gobain Research Provence (Cavaillon, France). To verify TCOX outputs, an investigation of the presence of mullite at thermodynamic equilibrium state was carried out using heat treatments. As mullite proportion is almost null in the core of the block casted and annealed, this phase has been rejected during tabulation of properties over temperature extracted with PhysalurgY<sup>®</sup>, confirming the role of Na<sub>2</sub>O against the kinetic of mullite phase formation. After the validation of material properties, numerical solver convergence in time step and in mesh size was also validated.

To fulfill industrial main objectives, it is also required to validate the temperature simulated with the numerical models by comparison with experimental data. Temperature history inside the AZS block is not possible with thermocouples due to the extreme high temperature conditions of casting. Temperature history is therefore collected at Saint-Gobain SEPR plant inside the mold or in the annealing media that surrounds it. The thermal history validation by computation, already performed for high zirconia type of refractory ceramics [5], is not found in the literature for AZS materials. This second stage required several adjustments of the parameters available in THERCAST<sup>®</sup> as many are not characterized experimentally over the full temperature range. Some settings are even completely arbitrary, as heat transfer resistance, to adjust numerical outputs to experimental results. When the temperature history is validated at sensors location, it was possible to perform thermo-mechanical analyses inside the AZS block during its solidification.

To respond to the first objective of predicting foundry defects, thermo-mechanical studies of the AZS block implies a better understanding of strain and stress build up, especially along the edges of the block. A couple of constitutive mechanical behavior laws for AZS have been

used, extrapolated when required from high zirconia refractory or steel materials that are more documented. The study shows that constitutive equations are a key parameter for mechanical response predictions as they impact a lot the deformation history during annealing. Strain evolution over temperature is used in several criteria detailed in literature to predict quantitatively the susceptibility to hot cracking. Such criteria also had to be adapted to ceramics as refractory materials present a strong proportion of glassy phase remaining at the end of the cooling process. A case study comparing four geometries retrieved industrial feedback about their hot tear susceptibility. While experimental tendencies have been numerically retrieved, real mechanical constitutive equations for AZS remain unknown, especially in the mushy zone. In the upcoming years, to optimize refractory production process, it will be required to determine the constitutive equations for AZS refractory material at high temperature and under stress conditions that are close to the data collected inside industrial blocks during their annealing. Slowing down annealing by reducing heat exchange and lower cooling rate will reduce the temperature gradient at the skin of the block and could reduce the stress generation but a longer annealing implies more macrosegregation. Coupled effects between hot tears and macrosegregation should also be investigated to go further with the first objective to reach relevant hot tears predictions.

The second objective is to model macro-porosity located inside the riser located above the AZS blocks. Thermo-mechanical computations, presented for hot tears prediction, predict currently an opening in the riser much smaller than experimental observations. Density has been proven to be a key parameter in macro-porosity opening, as lower liquid density in the riser increases the open volume predicted. It was also found that getting proper density evolution in the riser requires to take into account macrosegregation. Macro-segregation is implemented thanks to User-model called in THERCAST<sup>®</sup> that will perform computations of the thermo-solutal convection. Fluid-oriented mechanical solver is now taken called, with a fixed solid hypothesis (i.e. neglecting the sedimentation of equiaxed crystals and shrinkage flows). Properties are tabulated over temperature and concentrations. Thermodynamical information (as composition of phases all along the solidification path but also density and enthalpy) are extracted from the Thermo-Calc<sup>®</sup> TCOX10 database thanks to the PhysalurgY<sup>®</sup> library developed at CEMEF. To obtain relevant tabulations, it has been required to adapt PhysalurgY<sup>®</sup> to get properties for concentrate oxides alloys and not diluted metal alloys. After optimizing tabulations and the call of UserModels on an ideal case study with simplified geometry and composition, it has been possible to transpose the settings to the industrial block geometry and standard AZS refractory composition. However, implementation of macrosegregation could not be completely achieved during this project. After the confirmation of solver convergence with the call of such user models, adding compressibility is necessary to predict the macro-porosity opening with the lowering of an air/AZS interface. Finally when the model will retrieve the experimental observations in terms of concentration map and in terms of macro-porosity in the riser, it will be possible to determine the impact of the riser geometry on the AZS block "filling" quality.

In the future, several axes need to be investigated to better compute the AZS block annealing stage:

- Definition of key parameters that allow faster computations for industrial block annealing, especially when macrosegregation is computed;
- Combination of both a fluid-oriented solver for the liquid phase and a solid-oriented solver for the solid phases as it was developed for steel ingots by Zhang [24]. It will then be possible to model most of the phenomena occurring during the AZS block annealing. Coupling mechanical computations with macrosegregation would for example allow a quantification of macrosegregation impact on hot tear susceptibility;

- 
- Model sedimentation of equiaxed Zirconia crystals formed at the beginning of the solidification as it is done for steel ingots by Ettrouidi [23].

Thanks to numerical simulations, by adapting the composition of the AZS material (and therefore its thermal and mechanical properties) or by modifying the geometry of the block (and adapting the mold and media geometry too), it is possible to anticipate the impact on quality or productivity of different industrial processes. Such numerical models give answers to industrials without casting several blocks at 1:1 scale, which implies saving lots of time, human resources, storage place for the several days of annealing but moreover lots of raw materials and energy during block production.



# Bibliography

- [1] EUROFLOAT inaugure son nouveau four. *L’Echo de la Baie*, 112:124–125, 2016. URL <https://www.lechodelabaie.fr/wp-content/uploads/2017/09/zoom-112-eurofloat-inaugure-son-nouveau-four.pdf>. 1
- [2] MANFREDO, L.J. and et al. The corrosion resistance of high ZrO<sub>2</sub> fusion-cast Al<sub>2</sub>O<sub>3</sub>-ZrO<sub>2</sub>-SiO<sub>2</sub> glass refractories in soda lime glass. *Journal of Material Sciences*, 19:1272–1276, 1984. 1, 7
- [3] Edward R. Begley and Philip O. Herndon. 8 - zirconia-alumina-silica refractories. In Allen M. Alper, editor, *Refractory Glasses, Glass—Ceramics, and Ceramics*, volume 5 of *Refractory Materials*, pages 185–208. Elsevier, 1971. doi: <https://doi.org/10.1016/B978-0-12-053304-6.50016-3>. URL <https://www.sciencedirect.com/science/article/pii/B9780120533046500163>. 1
- [4] PETRONI, Laetitia, BOUSSUGE, Michel, and RYCKELYNCK, David. Numerical simulation of the cooling-down of high-zirconia fused-cast refractories. *Journal of the European Ceramic Society*, 32(15):3941–47, 2012. URL <https://doi.org/10.1016/j.jeurceramsoc.2012.06.004>. 2
- [5] ZHANG, Yang. *Etude des conséquences mécaniques de la transformation de phase dans les réfractaires électrofondus à très haute teneur en zircone*. PhD thesis, PSL Research University, 2017. 2, 32, 34, 59, 61, 115
- [6] Mines Paris PSL, ONERA, and Northwest Numerics and Modeling. Zebulon website. URL <http://www.zset-software.com/products/zebulon/>. 2
- [7] Transvalor. THERCAST website, 2022. URL <https://www.transvalor.com/en/thercast>. 2
- [8] COCKCROFT, Steven L., BRIMACOMBE, J. Keith, WALROD, Dennis G., and MYLES, Thomas A. Thermal Stress Analysis of Fused-cast AZS refractories during Production : Part I, Industrial Study. *Journal of the American Ceramic Society*, 77(6):1505–1511, 1994. 2, 8, 11, 62, 65
- [9] VERNEDE, Stephane. *A Granular Model of Solidification as Applied to Hot Tearing*. PhD thesis, Ecole Polytechnique Fédérale de Lausanne, Lausanne, 2007. 2
- [10] BELLET, Michel, CERRI, Olivier, BOBADILLA, Manuel, and CHASTEL, Yvan. Modeling Hot Tearing during Solidification of Steels: Assessment and Improvement of Macroscopic Criteria through the Analysis of Two Experimental Tests. *Metallurgical and Materials Transactions A*, 40A:2705–17, 2009. doi: 10.1007/s11661-009-9955-5. URL <https://link.springer.com/article/10.1007/s11661-009-9955-5>. 2, 11, 66

- [11] LATASTE, Emilie. *Comportement mécanique et endommagement de réfractaires électrofondus sous sollicitation thermomécanique*. PhD thesis, Ecole doctorale Matériaux de Lyon, GEMPPM – INSA de Lyon, 2005. 2, 32, 60, 64, 76
- [12] MASSARD, Ludovic. *Etude du fluage de réfractaires électrofondus du système alumine-zircone-silice*. PhD thesis, École Nationale Supérieure des Mines de Paris, 2005. URL <https://pastel.archives-ouvertes.fr/tel-00150692>. 8, 11, 13, 15, 18, 31, 57, 60, 61, 91
- [13] GOURAUD, Fanny. *Influence des transformations de phase de la zircone sur le comportement thermomécanique de réfractaires à très haute teneur en zircone*. PhD thesis, Université de Limoges, 2016. URL <http://www.theses.fr/2016LIM00110>. 13, 61
- [14] YEUGO-FOGAING, Edwige. *Caractérisation à haute température des propriétés d'élasticité de réfractaires électrofondus et de bétons réfractaires*. PhD thesis, Université de Limoges, Limoges, 2006. 2, 18, 32
- [15] CERRI, Olivier. *Rupture à chaud dans les aciers au cours de leur solidification : caractérisation expérimentale et modélisation thermo-mécanique*. PhD thesis, Ecole Nationale Supérieure des Mines de Paris, 2008. 2, 67
- [16] RAPPAZ, Michel, DREZET, Jean-Marie, and GREMAUD, Marco. A New Hot-tearing Criterion. *Metallurgical and Materials Transactions A*, 30A:449–455, February 1999. 25, 67
- [17] WON, Young Mok, YEO, Tae-jung, OH, Kyu Hwan, and SEOL, Dong Jin. A New Criterion for Internal Crack Formation in Continuously Cast Steels. *Metallurgical and Materials Transactions B*, 31B:779–794, August 2000. 11, 66, 67, 70, 71, 72
- [18] CLYNE, T.W., WOLF, C., and KURZ, W.;. The Effect of Melt Composition on Solidification Cracking of Steel, with Particular Reference to Continuous Casting. *Metallurgical and Materials Transactions B*, 13B:259–266, 1982. 2, 66, 67, 68
- [19] COSTES, Frédéric. Technical documentation - THERCAST, 2019. 2, 26, 54, 58, 59, 99
- [20] SAAD, Ali. *Numerical modelling of macrosegregation formed during solidification with shrinkage using a level set approach*. PhD thesis, PSL Research University, 2016. URL <https://pastel.archives-ouvertes.fr/tel-01566430>. 2, 43, 99, 113, 114
- [21] GOUTTEBROUZE, Sylvain, FACHINOTTI, Victor D., BELLET, Michel, and COMBEAU, Herve. 3D-FEM Modeling of Macrosegregation in Solidification of Binary Alloys. *International Journal of Forming Processes*, (8):203–217, 2005.
- [22] BRIONNE, Gary. *Influence de la vitesse de refroidissement sur l'évolution de la macrosegrégation dans les lingots de grande taille*. PhD thesis, Ecole de Technologie Supérieure, Québec, 2018. 113
- [23] ETTROUDI, Hanadi. *Modélisation numérique multi-échelle des structures de solidification, de la macrosegrégation et de la Transition Colonnaire-Equiaxe*. PhD thesis, PSL Research University, 2021. 2, 113, 114, 117
- [24] ZHANG Shaojie. *Numerical simulation of mechanical interactions between liquid and solid phase in solidification processes*. PhD thesis, Paris Sciences et Lettres, 2020. URL <https://pastel.archives-ouvertes.fr/tel-02897918/document>. 113, 114, 116

- 
- [25] MAGUIN, Vincent. *Simulation multiphysique de la macroségrégation et de la formation des freckles lors de la solidification d'aubes de turbines monocristallines*. PhD thesis, PSL Research University, 2020. 2
- [26] ASTM C0071-12R18. Standard Terminology Relating to Refractories, 2018. URL <https://www.astm.org/c0071-12r18.html>. 7
- [27] Barton, J. and Guillemet, C. *Le Verre, Science et Technologie*. EDP sciences, Paris, 2005. 7
- [28] FULCHER, Gordon S. Cast Refractory article and method of making the same, January 1927. URL <https://patentimages.storage.googleapis.com/09/c2/13/acbb4313c078cc/US1615751.pdf>. 7
- [29] FULCHER, Gordon S. Cast Refractory Product, January 1927. URL <https://patentimages.storage.googleapis.com/09/c2/13/acbb4313c078cc/US1615751.pdf>. 7
- [30] Pilkington, Lionel A. B. Manufacture of flat glass, August 1966. URL <https://patentimages.storage.googleapis.com/13/4c/4a/5a466d30c3be37/US3215516.pdf>. 7
- [31] CABODI, Isabelle and VESPA, Pierrick. Refractaires AZS pour Four Verriers. Internal report, Saint Gobain Internal report, SGR Provence, June 2019. 8
- [32] FARHI, Joseph. Coulée continue de brames minces. *Techniques de l'ingénieur*, October 1994. Ref M7814 v1. 8
- [33] LIDE, David R. , ed. *CRC Handbook of Chemistry and Physics - "Density of various solids" (15-29)*. Chemical Rubber Co. Press, Boca Raton, FL, USA, internet version edition, 2005. 8
- [34] Archives. Grande famille d'électrofondus pour l'industrie du verre. Technical report, Saint Gobain Internal report, SGR Provence, September 2001. 8, 9
- [35] FOURMENT, Jacques and FROMENTIN, Jean. Fours de verrerie. *Techniques de l'ingénieur Verres et céramiques*, base documentaire : TIP589WEB (ref. article : be8848), 2000. doi: 10.51257/a-v1-be8848. URL <https://www.techniques-ingenieur.fr/base-documentaire/materiaux-th11/sciences-et-technologies-du-verre-42573210/fours-de-verrerie-be8848/>. Editions T.I. 9
- [36] PECORARO, G.A. How the Properties of Glass Melts Influence the Dissolution of Refractory Materials. In *Properties of glass-forming melts*, pages 339–389. David Pye, Innocent Joseph, Angelo Montenero, crc press edition, 2005. ISBN 978-1-57444-662-3. 9
- [37] ORTEGA, André. Récupération et valorisation des réfractaires usagés. *L'industrie Céramique & Verrière*, (938):376–379, 1998. 10
- [38] VALOREF. Le recyclage des réfractaires. *Verre*, 4(5):28–29, 1998. 10
- [39] VALOREF. Safety Data Sheet VALORZAC® PR / N / T / CRB / ER, 2015. URL <https://www.valoref.com/secondary-raw-materials/valorzac>. 10
- [40] Thermo-Calc Software. CALPHAD methodology. URL <https://thermocalc.com/about-us/methodology/the-calphad-methodology/>. 12

- [41] KWON, Sun Young and JUNG, In-Ho. Thermodynamic assessment of the Al<sub>2</sub>O<sub>3</sub>-ZrO<sub>2</sub>, CaO-Al<sub>2</sub>O<sub>3</sub>-ZrO<sub>2</sub>, and Al<sub>2</sub>O<sub>3</sub>-SiO<sub>2</sub>-ZrO<sub>2</sub> systems. *Ceramics International*, 48(4):5413–5427, 2022. ISSN 0272-8842. doi: <https://doi.org/10.1016/j.ceramint.2021.11.085>. URL <https://www.sciencedirect.com/science/article/pii/S0272884221034969>. 12, 13
- [42] Thermo-Calc Software. Metal Oxide Solutions Database - TCOX10, 2020. 12, 16
- [43] GUILLEMOT, Gildas. Physalurgy website, 2017. URL <https://physalurgy.cemef.mines-paristech.fr>. 12, 24, 32
- [44] ASOKAN, T. Microstructural features of fusion cast Al<sub>2</sub>O<sub>3</sub>-ZrO<sub>2</sub>-SiO<sub>2</sub> refractories. *Journal of Material Sciences Letters*, 13:343–345, 1994. doi: <https://doi.org/10.1007/BF00420793>. URL <https://link.springer.com/article/10.1007/BF00420793>. 13
- [45] REA, Robert F. cone fusion study of mixtures of Zirconium silicate, Silica and Alumina. *Journal of the American Ceramic Society*, 9:95–96, 1939. doi: <https://doi.org/10.1111/j.1151-2916.1939.tb19434.x>. URL <https://ceramics.onlinelibrary.wiley.com/doi/10.1111/j.1151-2916.1939.tb19434.x>. 13
- [46] GRECA, Maria Conceicao, EMILIANO, Jose Vitorio, and SEGADAES, Ana Maria. Revised Phase Equilibrium Relationships in the System Al<sub>2</sub>O<sub>3</sub>-ZrO<sub>2</sub>-SiO<sub>2</sub>. *Journal of the European Ceramic Society*, 9(4):271–283, 1992. ISSN 0955-2219. doi: [https://doi.org/10.1016/0955-2219\(92\)90062-I](https://doi.org/10.1016/0955-2219(92)90062-I). URL <https://www.sciencedirect.com/science/article/pii/095522199290062I>. 13
- [47] VOROZHTECOV, V.A., YURCHENKO, D.A., ALMJASHEV, V. I., and STOLYAROVA, V.L. Phase Equilibria in the Al<sub>2</sub>O<sub>3</sub>-SiO<sub>2</sub>-ZrO<sub>2</sub> System: Calculation and Experiment. *Glass Physics and Chemistry*, 47(5):417–426, 2021. doi: 10.1134/S1087659621050175. 13
- [48] HEIDRICH, Roland. An update on fused cast AZS exudation. *Glass International*, 45: 41–42, 2022. 15, 32
- [49] COCKCROFT, Steven L., BRIMACOMBE, J. Keith, WALROD, Dennis G., and MYLES, Thomas A. Thermal Stress Analysis of Fused-Cast Refractories during Production : Part II, Development of Thermo-elastic Stress Model. *Journal of the American Ceramic Society*, 77(6):1512–1521, 1994. 15, 32, 65, 66
- [50] GAUBIL, Michel. *Etude de la solidification de matériaux réfractaires appartenant au système quaternaire Al<sub>2</sub>O<sub>3</sub>-ZrO<sub>2</sub>-SiO<sub>2</sub>-Na<sub>2</sub>O*. PhD thesis, Université d’Orléans, 1996. 15, 16
- [51] WISNIEWSKI, Wolfgang, THIEME, Christian, and RÜSSEL, Christian. The detailed microstructure of an alumina-zirconia-silica (AZS) fused cast refractory material from the cast skin into the bulk analyzed using EBSD. *Journal of the European Ceramic Society*, 39:2186–2198, 2019. 16, 63
- [52] PONS Gabriel. Study of mullite growth in AZS refractories. Master’s internship report, Polytech Montpellier, SGR Provence, 2022. 16
- [53] BRUKER. DIFFRACTION des rayons X (DRX) - D8 ENDEAVOR, . URL <https://www.bruker.com/fr/products-and-solutions/diffractometers-and-scattering-systems/x-ray-diffractometers/d8-endeavor.html>. 17

- 
- [54] BRUKER. X-ray Diffraction (XRD) - DIFFRAC.EVA, . URL <https://www.bruker.com/en/products-and-solutions/diffractometers-and-scattering-systems/x-ray-diffractometers/diffrac-suite-software/diffrac-eva.html>. 17
- [55] Malvern Panalytical. HighScore Plus. URL <https://www.malvernpanalytical.com/en/products/category/software/x-ray-diffraction-software/highscore-with-plus-option/>. 17
- [56] DANTZIG, Jonathan A. and RAPPAZ, Michel. *Solidification*. EPFL Press - distributed by CRC Press, 2nd edition edition, 2016. ISBN 978-2-940222-97-1. URL <http://www.solidification.org/>. 23, 24, 54, 65, 66, 98, 99
- [57] RAPPAZ, Michel, BELLET, Michel, and DEVILLE, Michel. *Modélisation numérique en science et génie des matériaux*. Ecole Polytechniques et universitaires romandes, Lausanne, première édition edition, 1998. ISBN 2-88074-365-6. 23, 24, 25, 53, 54, 55, 66, 100
- [58] ISHII, Mamoru and HIBIKI, Takashi. *Thermo-fluid Dynamics of Two-phase Flow*. Springer, Boston, MA, 1 edition, 2006. ISBN 978-0-387-29187-1. URL <https://doi.org/10.1007/978-0-387-29187-1>. 23
- [59] NI, J. and BECKERMANN, C. A volume-averaged two-phase model for transport phenomena during solidification. *Metallurgical and Materials Transactions B*, 22(3):349–361, 1991. doi: <https://doi.org/10.1007/BF02651234>. 23, 54
- [60] SUN, Y. and BECKERMANN, C. Diffuse interface modeling of two-phase flows based on averaging: mass and momentum equations. *Physica D: Non Linear*, 198(3):281–308, 2004. doi: 10.1016/j.physd.2004.09.003. 23
- [61] WHITAKER, Stephen. The transport equations for multi-phase systems. *Chemical Engineering Science*, 28:139–147, 1973. doi: [https://doi.org/10.1016/0009-2509\(73\)85094-8](https://doi.org/10.1016/0009-2509(73)85094-8). URL [https://www.academia.edu/14603279/The\\_transport\\_equations\\_for\\_multi\\_phase\\_systems](https://www.academia.edu/14603279/The_transport_equations_for_multi_phase_systems). 23
- [62] Transvalor. THERCAST® NxT 2.1 MANUEL DE L’UTILISATEUR Lingot. Technical report, Transvalor, December 2017. 29, 82, 83
- [63] BIRD, R. Byron, LIGHTFOOT, Edwin N., and STEWART, Warren R. *Transport phenomena*. John Wiley & Sons, Inc., New York, second edition, 2002. ISBN 0-471-41077-2. 29
- [64] CABODI, Isabelle. Media de recuisson. Technical report, Saint Gobain Internal report, 2020. 31
- [65] SHAO, Jian. India Groggs Test - Saint Gobain Internal report. Technical report, Saint Gobain Internal report, SGR Shanghai, 2020. 31
- [66] PETRONI, Laetitia. *Etude du comportement post-coulée de réfractaires électrofondus à très Haute Teneur en Zircône (THTZ)*. PhD thesis, Ecole Nationale Supérieure des Mines de Paris, 2011. URL <https://pastel.archives-ouvertes.fr/pastel-00657812>. 32, 59, 60, 61
- [67] CAROZZANI, Tommy. *Développement d’un modèle 3D Automate Cellulaire-Éléments Finis (CAFE) parallèle pour la prédiction de structures de grains lors de la solidification d’alliages métalliques*. PhD thesis, PSL Research University, 2012. 43, 45, 99

- [68] CHASSAING, Patrick. The Modeling of Variable Density Turbulent Flows. A review of first-order closure schemes. *Flow, Turbulence and Combustion*, 66(4):293–332, July 2001. ISSN 1573-1987. doi: 10.1023/A:1013533322651. URL <https://doi.org/10.1023/A:1013533322651>. 54
- [69] D A DREW. Mathematical Modeling of Two-Phase Flow. *Annual Review of Fluid Mechanics*, 15(1):261–291, January 1983. ISSN 0066-4189. doi: 10.1146/annurev.fl.15.010183.001401. URL <https://doi.org/10.1146/annurev.fl.15.010183.001401>. 54
- [70] BELLET, Michel, JAOUEN, Olivier, and POITRAULT, Isabelle. An ALE-FEM Approach to the Thermomechanics of Solidification Processes with Application to the Prediction of Pipe Shrinkage. *International Journal of Numerical Methods for Heat and Fluid Flow*, 15(2): 120–142, 2005. doi: 10.1108/09615530510578410. URL <https://hal-mines-paristech.archives-ouvertes.fr/hal-00517660>. 55, 56, 57, 58
- [71] R. J. Claxton. Aluminum alloy coherency. *JOM*, 27(2):14–16, February 1975. ISSN 1543-1851. doi: 10.1007/BF03355884. URL <https://doi.org/10.1007/BF03355884>. 55
- [72] HALPHEN, Bernard. Sur les matériaux standards généralisés. *Journal de Mécanique*, 14(1): 39–63, 1975. URL [https://www.researchgate.net/publication/260692929\\_Sur\\_les\\_Materiaux\\_Standards\\_Generalises](https://www.researchgate.net/publication/260692929_Sur_les_Materiaux_Standards_Generalises). 56
- [73] SARAMITO, Pierre. *Complex fluids : modeling and algorithms*. Number 79 in Mathématiques et Applications. Springer, 1 edition, 2016. ISBN 978-3-319-44361-4. URL <https://hal.archives-ouvertes.fr/hal-02077025>. 56
- [74] ERN, Alexandre and GUERMOND, Jean-Luc. *Theory and Practice of Finite Elements*. Springer, New York, NY, 1 edition, 2004. ISBN 978-0-387-20574-8. URL <https://doi.org/10.1007/978-1-4757-4355-5>. 57
- [75] LU, Tian Jian, EVANS, Anthony G., HUTCHINSON, John W., SRINIVASAN, Gajawalli V., and WINDER, Stephen M. Stress and Strain Evolution in Cast Refractory Blocks during Cooling. *Journal of the American Ceramic Society*, 81(4):917–925, 1998. 61
- [76] Dino-Lite France. Dino-Lite USB microscope. URL <https://www.dino-litefrance.fr/produits/la-gamme/microscopes/universel/am7515mt2a-microscope-numerique-usb-dino-lite/>. 63
- [77] KOSHIKAWA, Takao, BELLET, Michel, GANDIN, Charles-André, BOBADILLA, Manuel, and YAMAMURA, Hideaki. Study of hot tearing during steel solidification through ingot punching test and its numerical simulation. *Metallurgical and Materials Transactions A*, Springer Verlag / ASM International, 47(8):4053–4067, 2016. doi: 10.1007/s11661-016-3564-x. URL <https://hal-mines-paristech.archives-ouvertes.fr/hal-01354150>. 67
- [78] CAMPBELL, John. *Castings - The new metallurgy of cast metals*. Butterworth Heinemann, 2nd edition, 2003. ISBN 0-7506-4790-6. 67
- [79] YAMANAKA, A., NAKAJIMA, K., and OKAMURA, K. Critical Strain for internal crack formation in continuous casting. *Ironmaking and Steelmaking*, 22(6):508–512, 1995. ISSN 0301-9233. 69
- [80] RICHET, Pascal. Quelques aperçus sur la viscosité des silicates fondus. *Verre*, 14(3):62–66, 2008. URL [http://www.verreonline.fr/encyclopedie/doc/Visco\\_Richet.pdf](http://www.verreonline.fr/encyclopedie/doc/Visco_Richet.pdf). 76

- 
- [81] KOSHIKAWA, Takao. *Deformation of steel ingots by punch pressing during their solidification. Numerical modelling and experimental validation of induced hot cracking and macrosegregation phenomena*. PhD thesis, PSL Research University, 2017. 77
- [82] CABODI, Isabelle. *Analyse sedimentation*, 2017. 91
- [83] BECKERMANN, C. *Encyclopedia of Materials: Science and Technology - Macrosegregation*, 2001. 98, 107
- [84] CARMAN, P.C. Fluid Flow through Granular Beds. *Institution of Chemical Engineers*, 15:150–166, 1937. doi: [https://doi.org/10.1016/S0263-8762\(97\)80003-2](https://doi.org/10.1016/S0263-8762(97)80003-2). 99
- [85] RIVAUX, Benjamin. *Simulation 3D éléments finis des macroségrégations en peau induites par déformations thermomécaniques lors de la solidification d'alliages métalliques*. PhD thesis, Ecole Nationale Supérieure des Mines de Paris, 2011. 99
- [86] BROOKS Alexander N. and HUGHES Thomas J.R. Streamline upwind/Petrov-Galerkin formulations for convection dominated flows with particular emphasis on the incompressible Navier-Stokes equations. *Computer Methods in Applied Mechanics and Engineering*, 32(1): 199–259, 1982. doi: [https://doi.org/10.1016/0045-7825\(82\)90071-8](https://doi.org/10.1016/0045-7825(82)90071-8). 100
- [87] James A. Van Orman and Katherine L. Crispin. Diffusion in Oxides. *Reviews in Mineralogy and Geochemistry*, 72(1):757–825, January 2010. ISSN 1529-6466. doi: 10.2138/rmg.2010.72.17. URL <https://doi.org/10.2138/rmg.2010.72.17>. 100
- [88] STOUGH, M. A. and J. R. HELLMANN. Solid Solubility and Diffusivity in an Alumina/Zirconia System. *MRS Proceedings*, 365:41–46, 1994. doi: 10.1557/proc-365-41. 100
- [89] HENNET, Louis. *Propriétés thermophysiques AZS (Confidential). Résultats d'analyses*, CEMTHI, CEMHTI, 2019. 103, 104
- [90] LESOULT, Gérard. *Traité des matériaux 5 - Thermodynamique des matériaux - De l'élaboration des matériaux à la genèse des microstructures*. Presses polytechniques et universitaires romandes, Lausanne, 1ère édition edition, 2010. ISBN 978-2-88074-690-2. 104, 107, 113





Les blocs de cuve des fours verriers sont principalement composés de  $\text{Al}_2\text{O}_3 - \text{ZrO}_2 - \text{SiO}_2$ , d'où leur abréviation courante de blocs AZS. Ils sont produits par électrofusion. Cette étude porte sur la solidification de ces blocs une fois coulés dans leur moule. Un objectif est de prévoir la formation des criques à chaud au cours du refroidissement. Un second objectif est de prédire la géométrie de la retassure dans la masselotte.

Tout d'abord, une étude du matériau AZS a été réalisée pour valider les données thermodynamiques prédites par la base de données TCOX10. Celle-ci anticipe la présence de mullite, qui n'est pas observée expérimentalement. Des traitements thermiques à haute température valident cependant les résultats thermodynamiques et témoignent ainsi d'une cinétique de cristallisation. Pour la suite de l'étude, la mullite est suspendue pour extraire les données utiles pour les simulations, telles que le chemin de solidification, la composition, la densité et l'enthalpie des phases en présence (zircone, corindon, phase vitreuse ici assimilée au dernier liquide présent à basse température).

L'histoire thermique est mesurée sur des blocs industriels et est simulée avec le logiciel THERCAST<sup>®</sup>. Modéliser l'histoire thermique nécessite de tabuler les propriétés des différents domaines et d'ajuster les paramètres numériques.

Le comportement mécanique d'un bloc est ensuite modélisé pour prédire la formation de criques à chaud, défauts qui peuvent être présents sur les arêtes des blocs. Après des observations expérimentales, différents critères pouvant prédire la susceptibilité de leur formation sont comparés. La déformation cumulée sur un intervalle de température donné est retenue. Une analyse porte sur les variations des valeurs obtenues selon le domaine de température ou la consistance viscoplastique. Une fois optimisées, les simulations prédisent correctement la susceptibilité de fissuration à chaud sur les blocs industriels.

Pour prédire la retassure, des simulations thermomécaniques avec THERCAST<sup>®</sup> montrent que la composition, qui influence fortement la densité de la phase liquide, doit être connue localement. Cela nécessite donc de prédire la macroségrégation. Une cartographie expérimentale de la chimie du bloc est réalisée. Les tabulations des propriétés pour des oxydes à concentrations élevées nécessitent une adaptation de l'outil PATH de la librairie PhysalurgY<sup>®</sup>. En appliquant des solveurs de CIMLib<sup>®</sup> depuis THERCAST<sup>®</sup> pour les résolutions thermique, hydraulique et solutale (pour les solutés  $\text{Al}_2\text{O}_3$ ,  $\text{SiO}_2$  et  $\text{Na}_2\text{O}$  présents dans les phases liquide, zircone et corindon), il est alors possible de modéliser, en supposant un domaine incompressible, la convection thermo-solutale au cours du refroidissement, la sédimentation des cristaux étant négligée. Les simulations prédisent la formation de canaux ségrégués partant des parois du bloc et remontant vers le centre du bloc ainsi qu'un enrichissement de la masselotte en phase vitreuse. La compressibilité pour modéliser l'impact sur la retassure dans la masselotte n'a cependant pas pu être implémentée.

## MOTS CLÉS

---

solidification, criques à chaud, macroségrégation, AZS, THERCAST, simulation numérique

## ABSTRACT

---

Soldier blocks in glass furnaces are mainly composed of  $\text{Al}_2\text{O}_3 - \text{ZrO}_2 - \text{SiO}_2$ , they are therefore usually called AZS blocks. They are produced by electrofusion. This project concerns the solidification of those blocks in their mold. An objective is to anticipate the susceptibility of hot tears occurrence during the cooling down. A second objective is the prediction of the macro-porosity shape inside the riser.

First, a study of AZS material was carried out to validate the data obtained by the thermodynamic TCOX10 database. The latter predicts the formation of mullite, that is not observed experimentally. Heat treatments validate however the thermodynamic results, indicating a kinetic of crystallization. For this study, mullite is rejected to extract the relevant data for simulation of the solidification path, including the composition, the density and the enthalpy of the phases (zirconia, corundum and glassy phases, the latter being assimilated to the remaining liquid phase at low temperature).

Temperature history has been measured on industrial blocks and is simulated with THERCAST<sup>®</sup> software. To simulate the temperature history, it is required to tabulate the properties of the different domains and to adjust numerical settings. Block mechanical behavior is modelled to predict the risk of hot tears formation, defects that could be located at the edges of the blocks. After experimental observations, several criteria to predict the susceptibility of tear formation are compared. Cumulated strain over a given temperature range is considered as the most relevant. A study compares the values obtained depending on the temperature range or the visco-plastic consistency considered. After optimization, computations predict correctly the hot tears susceptibility for blocks at industrial scale.

To get a relevant shape of the macro-porosity, thermomechanical computations with the THERCAST<sup>®</sup> show that the composition, which impacts deeply the liquid phase density, has to be known locally. Macro-segregation needs therefore to be implemented. An experimental map of chemical compositions is performed. The tabulations of properties for concentrated oxide alloys required an adaptation of the PATH tool from the PhysalurgY<sup>®</sup> library. By calling CIMLib<sup>®</sup> solvers from THERCAST<sup>®</sup> for the thermal, hydraulic and solutal computations (for  $\text{Al}_2\text{O}_3$ ,  $\text{ZrO}_2$  and  $\text{Na}_2\text{O}$  present in zirconia, corundum and glassy phases), it is possible to model, considering an incompressible domain, the thermo-solutal convection during the cooling down, without sedimentation of crystals. Numerical models anticipate the formation of segregated channels going upward from the skin to the core of the block and also the enhancement of glassy phase proportion inside the riser. However, the compressibility, to model the impact on the riser macro-porosity shape, had not been implemented.

## KEYWORDS

---

solidification, hot tears, macrosegregation, AZS, THERCAST, numerical modeling